UCLA
UCLA Electronic Theses and Dissertations

Title

Synthesis of Tetraphenyl trans-3-Hexene-1,5-diyne Precursors for the Fabrication of Graphene Nanoribbons on Gold Surface

Permalink

https://escholarship.org/uc/item/8t06067k

Author

Bhagwandin, Dayanni Devi

Publication Date

2022

Peer reviewed|Thesis/dissertation

UNIVERSITY OF CALIFORNIA

Los Angeles

Synthesis of Tetraphenyl *trans*-3-Hexene-1,5-diyne Precursors

for the Fabrication of Graphene Nanoribbons on Gold Surface

A dissertation submitted in partial satisfaction

of the requirements for the degree

Doctor of Philosophy in Chemistry

by

Dayanni Bhagwandin

2022

ABSTRACT OF THE DISSERTATION

Synthesis of Tetraphenyl *trans*-3-Hexene-1,5-diyne Precursors

for the Fabrication of Graphene Nanoribbons on Gold Surface

by

Dayanni Bhagwandin

Doctor of Philosophy in Chemistry

University of California, Los Angeles 2022

Professor Yves F. Rubin, Chair

Carbon-based nanostructures are viewed as the next-generation components for advanced nanoelectronics. Offering exceptional properties such as low-current requirements and design-based optimization, these π-conjugated molecular structures show promise in outpacing the use of current transistor technologies. To fabricate and accurately study these molecules, it is necessary to utilize synthetic strategies that produce precise and defect-free structures. Thankfully, on-surface synthesis allows for the fabrication of defect-free conjugated polymers allowing in-situ visualization via scanning probe microscopies. This method typically uses a combination of polymerization and cyclization reactions to afford graphene-based nanostructures on a metal surface.

Through on-surface synthesis, a number of organic molecular precursors can be sublimed into gas phase and vapor-deposited onto a metal surface, usually gold(111), which is held at a constant temperature. Due to the catalytic activity and mobility of the selected metal, this annealing process often affords organized networks of organic building blocks. Further heating leads to the cleavage of C-X bonds in the aryl-halogen precursors, giving radicals that recombine to form covalent bonds that are typically uncontrolled in solution or gas-phase reactions.

Chapter 1 of this work is meant to outline the background of organic materials in electronic applications and introduce a timeline of graphene nanoribbons synthesized on metal surfaces.

Chapter 2 describes the synthesis of tetraphenyl-hex-3-en-1,5-diyne, a molecular model for the Hopf cyclization reaction leading to polycyclic aromatic compounds, here chrysene derivatives. We wanted to study the potential of this π-system as reaction pathway to chrysene and larger polycyclic aromatic compounds on Au(111), and ultimately, graphene nanoribbons. It was found that this molecule undergoes two sequential Hopf cyclizations at temperatures that are much lower than calculated or experimental Hopf cyclization reactions.

Chapter 3 expands on this work by discussing the synthesis of a diiodo derivative of tetraphenyl-hex-3-en-1,5-diyne. This molecular precursor is capable of pre-polymerizing on gold(111), providing an entry into the fabrication of graphene nanoribbons.

Chapter 4 of this works explores the possibilities of using combinatorial Ullman coupling and Hopf cyclization to generate graphene nanoribbons from annulated tetraphenyl-hex-3-en-1,5-diyne. Overall, this works aims to divulge new and exciting synthetic pathways for developing carbon-based materials for electronic applications.

Chapters 2 through 4 were conducted in collaboration with EMPA − Swiss Federal Laboratories for Materials Science and Technology, Dübendorf, Switzerland, and the University of Bern, Switzerland.

Chapter 5 of this work looks at the synthesis of a 1,4-butadiyne molecular precursors for the fabrication of graphene nanoribbons on Au(111)

Chapter 6 was motivated by the dramatic switch to remote-learning during the COVID-19 pandemic at UCLA. During this time, student interactions in online discussion sections were monitored to determine the best course characteristics for break-out room engagement. This work hopes to highlight important features that could be useful for in-person or remote courses in the future.

The dissertation of Dayanni Bhagwandin is approved.

Aradhna K. Tripati

William M. Gelbart

Richard B. Kaner

Yves F. Rubin, Committee Chair

University of California, Los Angeles

2022

DEDICATION

This work is dedicated to Mom, Dad, Umang Shah, Dodger,

and my guardian angel from above – Uncle Shak.

I would also like to recognize all my close family and friends that have been by my side throughout this journey. Thank you to Davendra Bhagwandin, Meleena Bhagwandin, Julianna Persaud, Valerie Alvarez, Tina Lee, Nayab Khan, Moontaha Syeda, and Ishika Saha.

Additionally, I would like to thank the members of the Rubin Lab. To Yolanda Li, thank you for being my mentor and friend when I needed it the most. To Julia Chang and Xinyu Liu, thank you for always supporting me. I wish you both the best. To Yves, thank you for giving me the opportunity to explore the world chemistry through your lab. It has been an honor being your student over these past five years.

Also, I would like to thank those who have continuously fostered an inclusive community and have made me feel welcomed throughout my academic journey. To Rachel Prado, Shanna Shaked, and Aradhna Tripati, thank you.

Lastly to my all mentors and peers from the High School for Mathematics, Science and Engineering and Hunter College's MARC and Yalow programs, thank you for making this journey possible.

TABLE OF CONTENTS

EXPERIMENTAL SPECTRA FOR ALL CHAPTERS

LIST OF FIGURES AND TABLES

ultraviolet light; armchair-8-GNR (top left) is obtained via heating in an argon tube furnace; ^{13}C solid-state NMR with cross polarization and magic angle spinning at different heating temperatures (300-600 °C), with color coded functional group shifts (right); aryl functional groups (green); alkyne functional groups (red); carbonyl functional groups (purple); alkyl functional groups (orange).. 50

ACKNOWLEDGEMENTS

VITA

EDUCATION

University of California, Los Angeles (UCLA)   *Los Angeles, CA*
M.S. Chemistry   Jun. 2019

City University of New York, Hunter College   *New York, NY*
B. S. Chemistry (Cum Laude)   Jun. 2019

High School for Mathematics, Science, and Engineering   *New York, NY*
High School Diploma   Jun. 2013

ACADEMIC TEACHING EXPERIENCE

University of California, Los Angeles   *Los Angeles, CA*
- *Graduate Teaching Fellow:* General Chemistry, Organic Chemistry   2017 - 2021
- *Graduate Assistant/Coordinator for Undergraduate Learning Assistants*   2020 - 2021

City University of New York, Hunter College   *New York, NY*
- *Undergraduate Teaching Assistant:* Organic Chemistry   2015 – 2017

SCHOLARSHIPS & SERVICE

University of California, Los Angeles   Los Angeles, CA
- *Physical Sciences Student Advisory Board on Diversity*   2020 – 2022
- *Center for Diverse Leadership in Science Fellow*   2018 – 2022
- *Center for Integration of Research, Teaching, and Learning Associate*   2020 – 2021

City University of New York, Hunter College   2015 – 2017
- *Maximizing Access to Research Careers Scholar* (Hunter College)   2013 – 2015
- *Yalow Cohort Scholar* (Hunter College)

RESEARCH EXPERIENCE

University of California, Los Angeles   *Los Angeles, CA*

1. *Tetraphenyl trans-3-Hexene-1,5-diyne Precursors for the Fabrication of*   2018 - 2022
    Graphene Nanoribbons on Au(111)
    Advisor: Dr. Yves Rubin

2. *Chemical Education Research: Structured Remote Classes Reflect High*   2020 – 2021
    Student Engagement In Discussion Sections Organic Materials:
    Synthesis of

City University of New York, Hunter College   *New York, NY*

3. *Carbohydrate Synthesis of Tetrahydrofuran Containing Acetogenins*   2015 - 2017
    Advisor: Dr. David R. Mootoo

<u>University of Washington</u>   *Seattle, WA*

4. *High Efficiency and Selectivity for Aldehyde-Water Shift Reaction with*   2016
    Ruthenium Catalyst
    Advisors: Dr. Karen Goldberg, Dr. D. Michael Heinekey

WORK EXPERIENCE

<u>Lost Spirits Distillery</u>   *Los Angeles, CA*
Distillery Laboratory Tour Guide   2019 - 2020
       .
<u>New York Hall of Science SCL (Science Career Ladder)</u>   *New York, NY*
Museum Floor Facilitator   2014 - 2016

PUBLICATIONS

- Zhao, C.; <u>Bhagwandin, D. D.</u>; Pignedoli, C. A.; Giovannantonio, M. D.; Fasel, R.; Rubin, Y.F.; "**Hopf Cyclization under Gold(111) Surface Catalysis: Dramatic Rate Enhancement Affording Chemically Tailored Nanostructures**," *in preparation*

- Shin, A. J.; <u>Bhagwandin, D. D.</u>, Prado, J. R.; Ghoshal, K; Mensah, S. T.; Shaked, S.; "**Breakout Room Design: Proposed Methods to Increase Student Engagement and Inclusion in Remote Learning**," *in preparation*

- Phearman.; Moore, J. M.; <u>Bhagwandin, D. D.</u>; Jonathan M. Goldberg, D. Michael Heinekey; Goldberg, Karen I. Goldberg; "**(Hexamethylbenzene)Ru Catalysts for the Aldehyde-Water Shift Reaction**," *Green Comm.* **2021**, 23, 1609 – 1615.

CHAPTER 1. INTRODUCTION TO GRAPHENE NANORIBBONS AND STATE-OF-THE-ART STRATEGIES FOR THEIR SYNTHESIS

1.1. Background

Advances in the semiconductor industry have been marked by technological achievements with ever-increasing miniaturization of the transistor.[1] In accordance with Moore's Law, the number of components on integrated circuits have continued to double over the years (Fig. 1).

Standard circuit technologies utilize complementary metal oxide semiconductors (CMOS), which are comprised of metal contacts, insulating oxides, and semiconducting materials. While the first circuits used germanium as the semiconducting material, silicon has been the primary material of choice since the 1960s for cost and technological reasons. Since switching to silicon, transistor technology has dramatically progressed with its ability to fabricate large area silicon wafers, allowing precise deposition of etched features. This technology has allowed for the transistor to become rapidly industrialized over time, while still being reliant primarily on silicon. Figure 1 shows that transistor development closely follows Moore's Law over time. The surface density of transistors has reached a point where new technology is required to build circuits at an ever-smaller level.
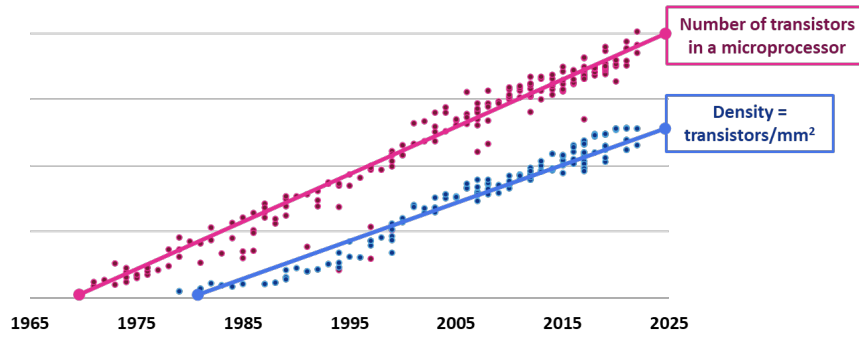
Figure 1. Projection of transistor technology over time. (red) Number of transistors in a microprocessor. (blue) Density = transistors/nm^2.

Although silicon technology has undergone rapid advancements over the years, existing research points to the need for alternate semiconductor materials, as the scaling of silicon is quickly reaching its limit.[2] Current practices allow for the fabrication of features down do 4 nm, but at this level, short-channel effects cause current leakage, leading to a difficulty in controlling the on/off state of transistors.[3,4] In addition, current industrial standards are immensely costly and energy consumptive. Silicon processing requires about 2% of annual consumed energy in the United States[4] and about 30% of total microchip fabrication cost,[3] indicating that miniaturization of silicon has become economically unfeasible.[5] In order to create the next generation of more sustainable electronics, new high performing and abundantly available semiconductor materials are necessary.[6]

One significant property that ultimately determines the optical and electronical performance of a device is the semiconductor bandgap.[7] This bandgap prevents the flow of electrons throughout the material and can thus create an on/off state in transistors. A drawback of silicon's current use is that its bandgap is reliant on its elemental composition, and therefore it can only be tuned through methods such as chemical doping, alloying, or intercalating.[8]

1.2. Organic Materials

Since the discovery of highly conducting polydiacetylene in 1979,[10] carbon-based organic materials have been of high interest for electronic applications due to their π-conjugated systems and tunable bandgap. Organic materials should afford cheaper and more sustainable electronics due to their lower cost, low-temperature processability,[11] and potential biodegradability.[12] In addition, organic materials can offer unsurpassed rheological properties such as high flexibility and softness, which are critical characteristics for next generation, biocompatible wearable electronics. Moreover, precise molecular tailoring allows for the tunability of device performance. Over the last 10 years, carbon-based nanostructures have proven to be important components for advanced nanoelectronics.[13,14] Offering new properties, such as flexibility[15,16] and biocompatibility,[17,18] these conjugated molecular structures show promise for outpacing the use of current transistor technologies. Examples in recent literature have pointed to their desirable use in new applications such as spintronics[19,20,21] and quantum computing.[22,23,24]

While much advancement has been made in the area of organic electronics, these molecular and polymeric materials still prove to be less than ideal for industrial processing due to low structural order, high number of defects, and high electron injection barriers. To bypass some of these problems, methods for increasing molecular order through spatially defined doping and supramolecular assembly have been investigated.[25]

1.3. Graphene Based Materials and Nanoribbons

Recent findings have pointed to graphene-based materials as a suitable replacement for silicon technology.[13] Graphene is a sheet of sp^2 hybridized carbon atoms; it has a zero bandgap, making it the best conductor of electricity ever known, and it is 100-300 times stronger than

stainless steel. However, forming different nanoscale architectures from graphene, such as ribbons or tubes, opens a bandgap in these materials, making them suitable for nanosized semiconducting applications. In addition, nanoscale carbon architectures can address the morphological and structural problems faced with most organic molecular and polymeric materials.[26]

In this realm, graphene nanoribbons (GNRs) are a versatile material with unique properties, such as high electrical conductivity, chemical stability, and a high surface to volume ratio.[27] Because of their tunable bandgap, graphene nanoribbons are a good material for efficient nanoelectronics materials, such as supercapacitors that would charge instantly and sustain multiple cycles of charging.[28] Furthermore, the bandgap of graphene nanoribbons can be finely tuned with modifications to the width and inner or edge structure.[29-30] This makes them ideal candidates for studying how bandgap engineering of organic molecules can affect device performance.

Graphene nanoribbons can mainly be characterized by their width and edge topology. A few examples of GNRs are armchair, zigzag, fjord, or chiral, which are all defined by different repeating units along the ends of the ribbon (Fig. 2a).[31] Additionally Fig. 2b shows the different types of synthetic strategies used to synthesized graphene nanoribbons. This is discussed in the next section.

1.4. Synthetic Strategies for Graphene Nanoribbons

Current synthesis methods involve making GNRs through mainly two methods: bottom-up and top-down approaches. Top-down unzipping methods require cutting graphene sheets with an

4

electron or ion beam, while bottom-up methods attempt to create GNRs from small molecular precursors.[32,33]

Bottom-up approaches have proven to be more successful, owing to the utilization of robust organic transformations. This produces GNRs with structurally precise edge and width structures. Bottom-up fabrication methods can be further categorized into subcategories: in solution, solid-state, and on-surface synthesis. Typically, the first step in these syntheses produces a conjugated polymer and the second step further cyclizes the backbone and pendant side chains to produce a fully fused GNR.
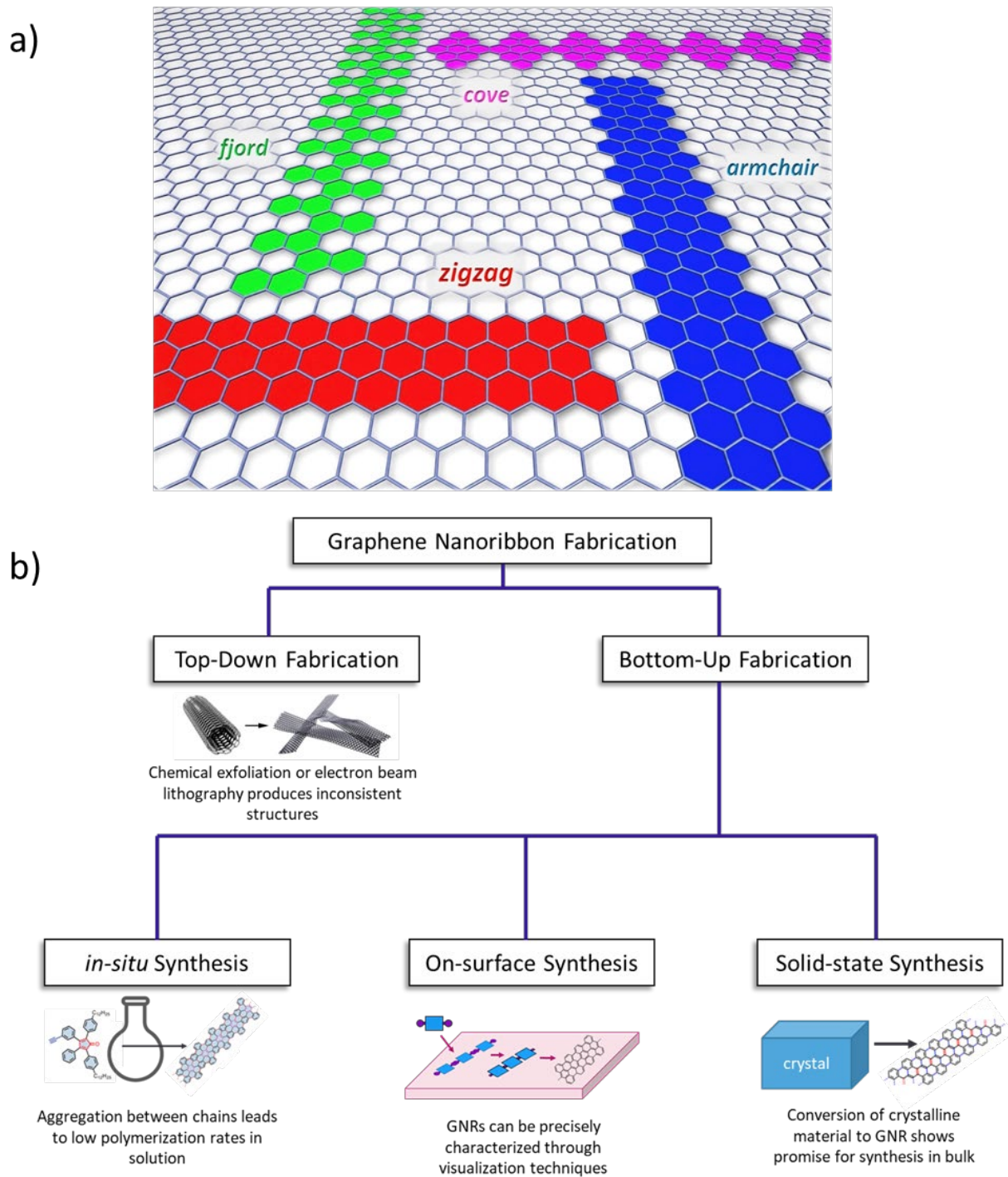
Figure 2. Diagram of Graphene Nanoribbons and Fabrication Methods. (a) fjord, cove, zigzag, and armchair edge topologies. (b) Two main types of fabrication consist of top-down and bottom-up. Bottom-up fabrication consists of *in-situ,* on-surface, and solid-state synthesis.

1.5. Solid-State Synthesis

The Rubin Lab has recently developed a new solid-state synthetic approach for producing GNRs. This approach shows that diaryl butadiyne monomers in the crystalline state can be converted into PDAs via topochemical polymerization with UV light (Fig. 3). The PDAs can then subsequently be converted into GNRs through cyclodehydrogenation under mild heating conditions (~350 ˚C) to afford GNRs.[34] By substituting different aryl side chains onto the butadiyne backbone different GNRs such as N=8 armchair[35] and N=8 (N_2) fjord-edge.[36]
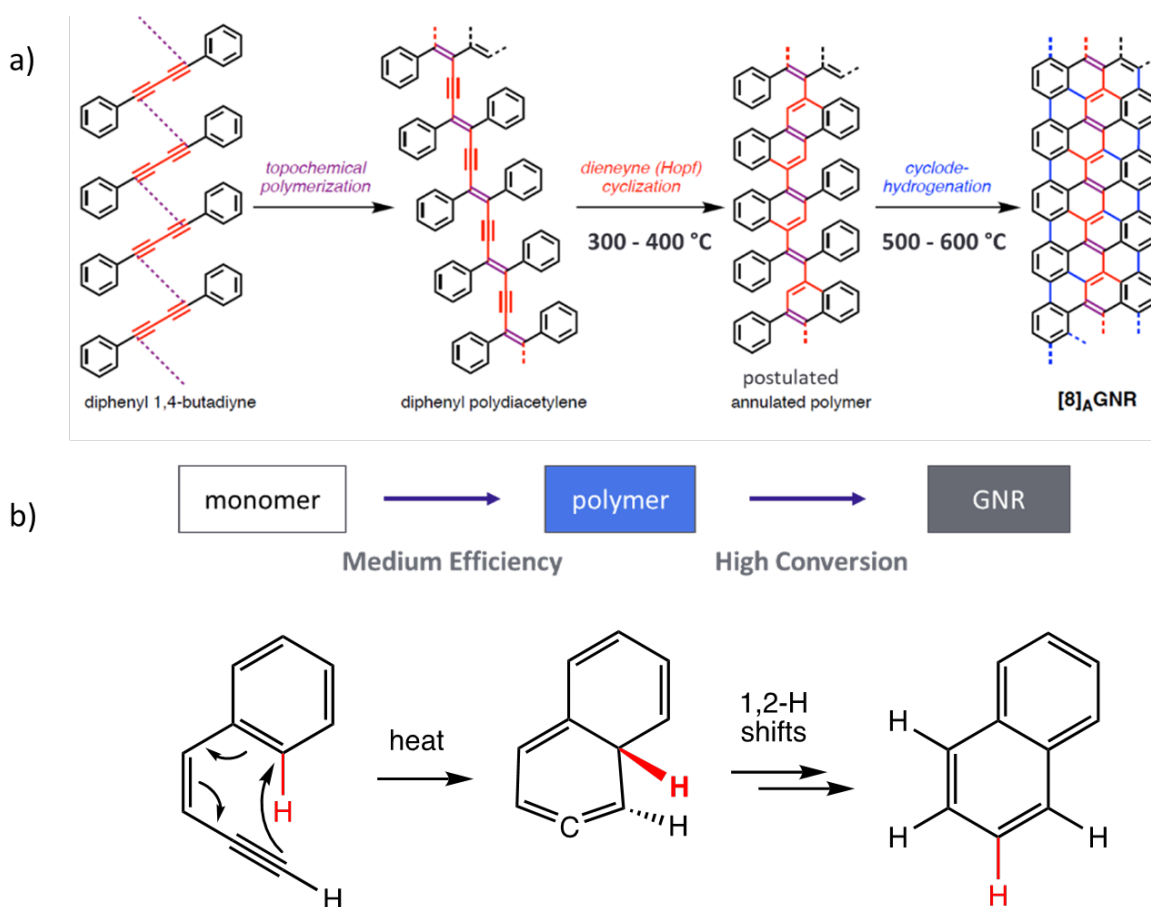
Figure 3. Solid State Synthesis of Graphene Nanoribbons via Hopf cyclization. (a) Rubin Lab's newly develop method which converts substituted diaryl 1,4-butadiynes (left) to diaryl polydiacetylenes (next) and [8]$_A$GNR (right); the postulated annulated polymer is obtained after a series of Hopf reactions of the diaryl polydiacetylene. (b) Hopf cyclization of a dienyne.

Although this method is robust at producing precisely defined GNRs in bulk material, it is hampered by an inefficient conversion of diphenyl 1,4-butadiyne to diphenyl polydiacetylene through topochemical polymerization in the crystal state. The second step, however, shows high conversion to the annulated polymer through a pericyclic reaction. This thermal cyclization is formally known as a Hopf cyclization reaction.

1.6. On Surface Synthesis

To fabricate and accurately study these molecules, it is necessary to utilize synthetic strategies that produce precise and defect-free structures.[37] Luckily, on-surface synthesis allows
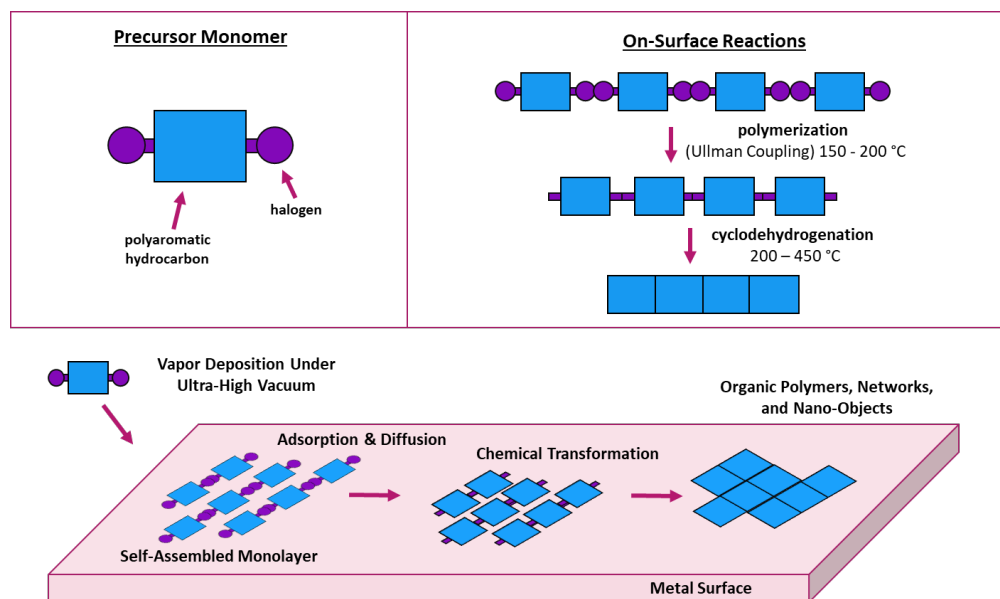
Figure 4. Synthesis of graphene-based materials on the surface of coinage metals (Au, Ag, Cu). Precursor monomers (aromatic hydrocarbons) with two halogen substituents (top left); on-surface self-assembly followed by polymerization of the aryl radicals obtained through homolytic C–X bond cleavages; subsequent cyclodehydrogenation of the polymer affords fused GNRs (top right). Precursor monomers are deposited onto a metal surface by sublimation, which forms a self-assembled monolayer, undergoes a chemical transformation to form polymers, networks, and nano objects (bottom).

for the fabrication of conjugated polymers[38] and *in-situ* visualization via scanning probe microscopies (Fig. 4).[39] This method typically uses a combination of polymerization and cyclization reactions to afford graphene-based nanostructures on a metal surface.

Through on-surface synthesis, organic molecular precursors are sublimed into the gas phase and deposited onto a coinage metal (Au, Ag, Cu) surface held at constant temperature. Due to the catalytic activity and mobility of these metals, the annealing process affords organized networks of organic building blocks. Further heating then leads to radical formation and ensuing covalent bond forming reactions[40] that are typically inaccessible by solution or gas-phase reactions.

Current methods for on-surface synthesis typically utilize Au(111) as both the substrate and reactive surface to produce GNRs. Gold allows for good mobility of the organic molecules on its surface while serving as a catalyst for the dehalogenation reactions. Typically, dibrominated or diiodinated PAHs are deposited on a surface through chemical vapor deposition (CVD) under ultra-high vacuum conditions (UHV).[41] Thermal activation causes the halogens to undergo homolytic C–X bond cleavage, resulting in surface-stabilized biradical intermediates that can diffuse across the metal surface. This gives these biradical intermediates enough thermal energy to produce a polymeric network linked entirely by carbon-carbon bonds.[42,43,44]

The first example of on-surface GNR work was described by Roman Fasel and his group. The synthesis of [7]$_A$GNR, as well as a chevron-GNR, from either 10,10'-dibromo-9,9'-bianthracene (DBBA) or 6,11-dibromo-1,2,3,4-tetraphenyltriphenylene, respectively, established the best proof that pristine graphene nanoribbons can be synthesized and image by scanning probe microscopies.[33] A number of groups have continued to use building blocks of a diverse array of bis-halogenated polyaromatic hydrocarbons (PAHs) to construct novel GNR structures. This is discussed in the next section.

1.6.1. Graphene Nanoribbons Synthesized on Au(111) and Useful Reactions

Graphene nanoribbons with various width and edge topologies have been fabricated throughout the past twenty years. Earlier methods fabricated GNRs through solution synthesis but produced inconsistent and short ribbons, usually fraught with insolubility issues. Solid-state synthesis in the Rubin Group, on the other hand, aims to bypass these problems by converting the starting material entirely in the crystal state. Although these methods have been very useful, on-surface synthesis has provided a direct and unequivocal route to convert a number of designed molecular precursors into GNRs.

The next section discusses the timeline of GNRs synthesized, starting with seminal work by Fasel *et al.* in 2010, and ending with the newest examples in 2022.

The first example of GNRs synthesized on-surface is described in Figure 5, entries 1 and 2. This work describes the first bottom-up approach to produce two different atomically precise GNRs. The molecular precursors, 10,10'-dibromo-9,9'-bianthryl (Figure 5, entry 1) and 6,11-dibromo-1,2,3,4-tetraphenyltriphenylene (Figure 5, entry 2) were used to produce an $N=7$ armchair edge GNR, as well as the alternating $N=6$ and $N=9$ chevron edge GNR.[33] By annealing to 200 °C, these precursors first undergo a thermal activation step which forms. A key point of this work was demonstrating that the subsequent cyclodehydrogenation step occurs when annealing at a higher temperature. Cyclodehydrogenation of both precursors occurs around 400 °C and affords a fully graphitized system. Scanning tunneling microscopy (STM) images and density functional theory (DFT) simulations were used to verify the structures by providing precise visualization of the formed structures.

Expanding on the aforementioned work, Fasel *et al.* demonstrated in 2014 that a nitrogen-based molecular precursor analogous to 6,11-dibromo-1,2,3,4-tetraphenyltriphenylene (Fig. 5,
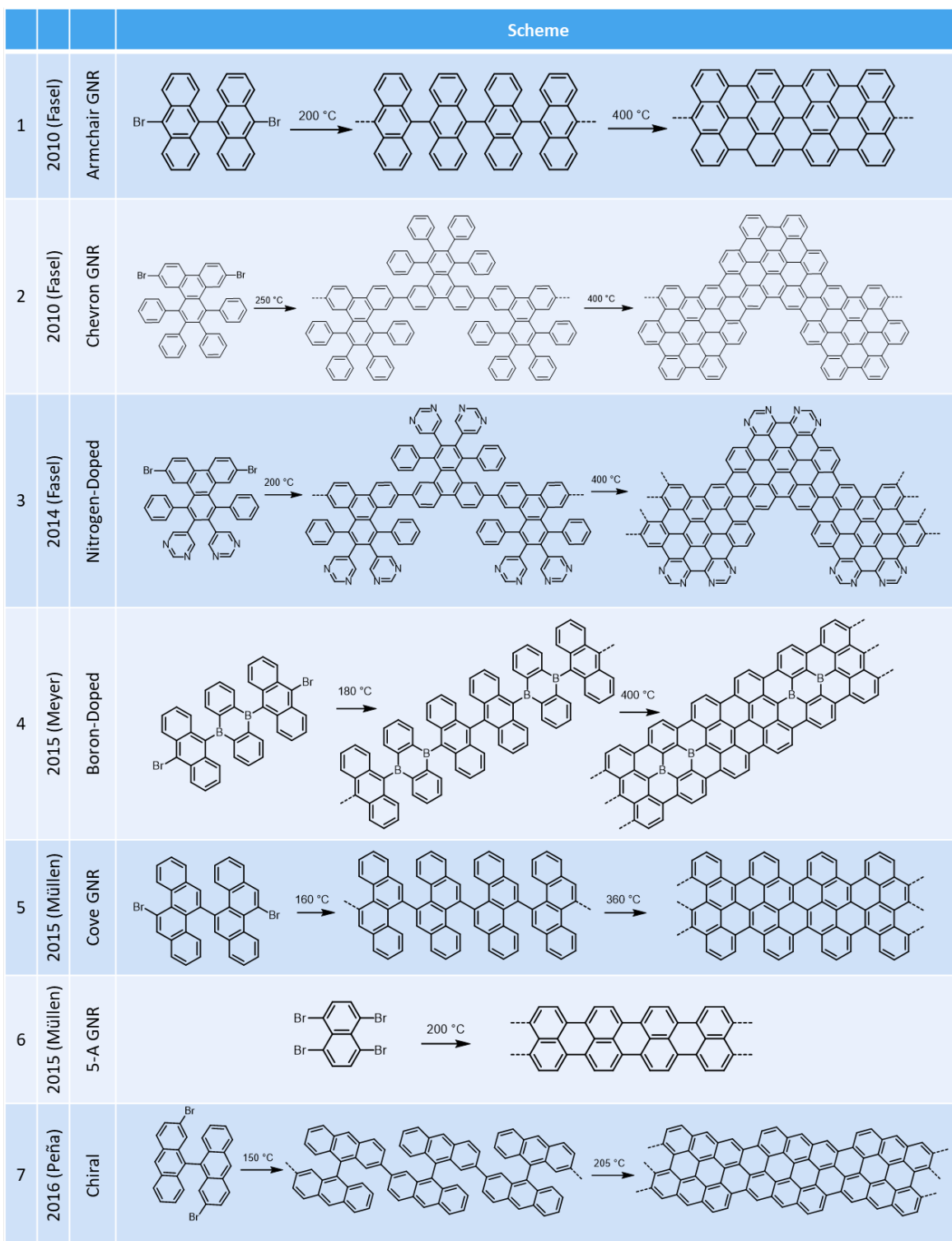
Figure 5. Graphene nanoribbons synthesized between 2010 - 2016. Armchair [7]GNR, Fasel, 2010 (1); Chevron GNR, Fasel, 2010 (2); Nitrogen-doped GNR, Fasel, 2014 (3); Boron-doped GNR, Meyer, 2015 (4); Cove-edge GNR, Müllen, 2015 (5); Armchair [5]GNR, Müllen, 2015 (6); Chiral GNR, Peña, 2016 (7).

entry 3) could generate N-doped GNRs.[45] This precursor has pyrimidinyl instead of phenyl rings and undergoes coupling similarly at 200 °C, with subsequent cyclodehydrogenation at 400 °C. It does however show a self-assembly pattern on the metal surface, similar to the analogous carbon precursor. Furthermore, both molecular precursors can also be deposited alternatingly to generate a "diblock copolymer," i.e., a polymer with alternating monomer units. Although both monomers are the same structurally, the presence of heteroatoms causes them to have different electronic structures. Thus, combining them into one polymer generates heterojunctions that could have applications in photovoltaics and electronics. Using this bottom-up method also proved that full control can be maintained over a dopant's position and concentration.

In 2015, Meyer and coworkers (Figure 5, entry 4) described the synthesis of boron-doped graphene nanoribbons through on-surface chemical reactions.[46] They obtained GNRs with widths of N=7, 14 and 21, and also described the achievement of a uniform texture of Lewis acidic sites. This is thanks to the particular design of the precursor, 9,10-bis(10-bromoanthracen-9-yl)-9,10-dihydro-9,10-diboraanthracene, which achieves boron-doping at designated internal positions, as well as a fixed doping ratio. The number of boron sites was determined by nitric oxide adsorption at thermal equilibrium. Ullman-type polymerization followed by cyclodehydrogenation was used to obtain the final structures. Also in 2015, Müllen *et al.* demonstrated that a *cove* edge periphery could be obtained for GNRs both in solution and on-surface (Figure 5, entry 5).[47] 11,11′-Dibromo-5,5′-bis-chrysene was used as a molecular precursor to afford this low bandgap *cove* edge GNR. Interestingly, comparison of both methodologies using the same precursor showed that longer and more uniform GNRs could be obtained via on-surface synthesis than in solution. GNR lengths up to 20 nm were obtained when synthesized on surface, while solution synthesis yielded torsionally twisted ribbons.

The narrowest armchair [5]GNR was synthesized by Müllen and coworkers in 2015 (Figure 5, entry 6).[48] They obtained this nanoribbon at low-temperature by using 1,4,5,8-tetrabromonaphthalene as the molecular precursor. Scanning tunnelling spectroscopy (STS) measurements reveal that the bandgap was larger than in previous studies predicted.[49] High resolution STM measurements also indicated the presence of organo-gold compounds, i.e., Au-naphthalene intermediates in the conversion to the final GNR. The carbon-gold bond was calculated to be about 2.2 Å, consistent with the reported literature value.[50]

In 2016, Peña and coworkers described the use of a 2,2′-dibromo-9,9′-bianthracene derivative for the development of a chiral GNR. When 10,10′-dibromo-9,9′-bianthracene was deposited on Au(111) or Ag(111), this molecular precursor afforded N=7 armchair GNR. However, when deposited on Cu(111), it afforded a chiral GNR (Figure 5, entry 7).[51,52] This GNR is described as "3,1" chiral because the length of one repeating unit is 3 aromatic rings, followed by one ring increase in height. Similarly, 2,2′-dibromo-9,9′-bianthracene was used to fabricate (3,1)-GNR. When deposited on gold or silver, this molecular precursor still produced (3,1)-GNR because of the relative positions of the two bromine atoms.

Figure 6 describes the synthesis of graphene nanoribbons on-surface between 2016 and 2020. In 2016, Fasel and coworkers reported the bottom-up synthesis of N=6 zigzag edge GNRs (Figure 6, entry 8).[53] Zigzag graphene nanoribbons are reported to host spin-polarized electronic edge states and can therefore be potentially used for key electronic applications.[54] This is because calculations predict that zigzag edge topology causes ribbons to couple ferromagnetically along the edge and antiferromagnetically between the edges.[29] A bis-halogenated "U-shaped" dibenzo-
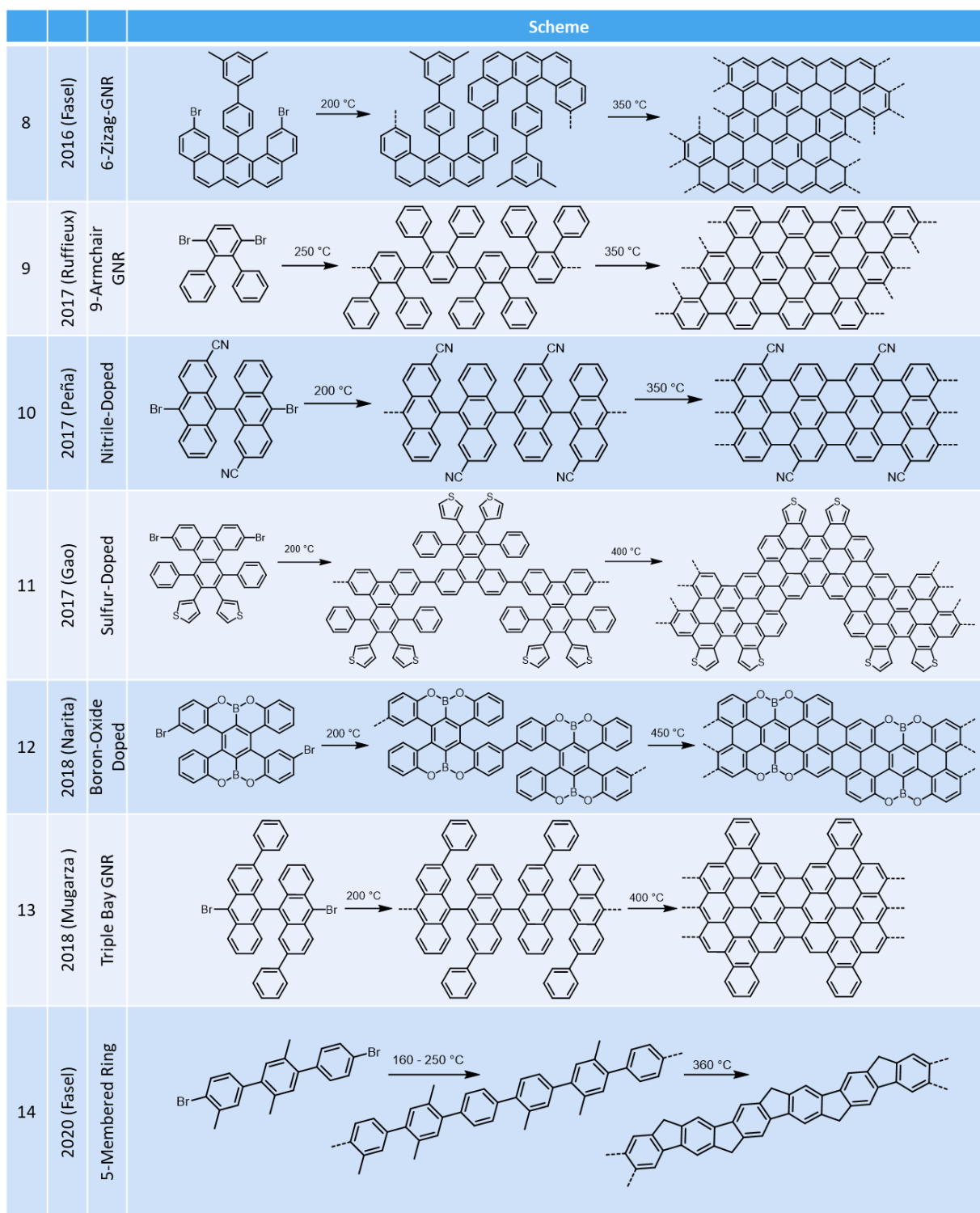
Figure 6. Graphene nanoribbons (GNR) synthesized between years 2016 to 2020. 6-Zigzag GNR, Fasel, 2016 (8); 9-Armchair GNR, Ruffieux, 2017 (9); Nitrile-Edge GNR, Peña 2017, (10); Sulfur-Edge GNR, Gao, 2017 (11); Boron-Oxide-Edge Doped GNR, Narita, 2018 (12); Triple-Bay-Edge GNR, Mugarza, 2018 (13); Five-Membered-Ring GNR, Fasel, 2020 (14).

anthracene monomer allowed for an initial polymerization of vacuum-deposited precursor to form a snake like structure. Additional methyl groups allowed for the oxidative ring closure of this structure, which formed the edge six-membered rings. This is a key step to zigzag GNR formation, where the methyl groups become dehydrogenatively incorporated into the graphitic system at 350 °C. Non-contact atomic force microscopy (nc-AFM) imaging with a CO-functionalized tip reveals a mono-hydrogen termination. This was determined by the absence of bending across the ribbon, which would occur from any bonding at the radical edges.[55] Scanning tunneling spectroscopy (STS) was used to show edge-localized states along with a large energy splitting of these states.

In 2017, Ruffieux and coworkers reported the synthesis of N=9 armchair GNR. This was done by using 3',6'-dibromo-1,1':2',1"-terphenyl as a molecular precursor (Figure 6, entry 9).[56] Surface-assisted dehalogenation and polymerization followed by cyclodehydrogenation afforded the final product. It should be noted that, across the literature for on-surface synthesis, this two-step reaction is often just deemed "Ullman coupling." Scanning probe microscopy and Raman spectroscopy were used to reveal the precise structure of this particular GNR, which has the potential to serve in room-temperature electronic and optoelectronic switching devices because of its low bandgap that is close to that of p-doped silicon (1.4 eV).

Also in 2017, Peña and coworkers demonstrated the synthesis of nitrile-doped N=7 armchair GNRs (Figure 6, entry 10).[57] This was done using a dicyano-substituted dibromo-bianthracene precursor, starting as previously discussed, from 2,2-dibromo-9,9-bianthracene. Rather than polymerizing from the 4' position, this synthesis installs bromines at the 9,9'-position. Polymerization in this direction affords N=7 armchair GNR, similar to the seminal work by Fasel *et al.* in 2010. Scanning tunnelling spectroscopy (STS) measurements reveal that the nitrile

groups behave as a very efficient n-dopants. This is because of the significant downshifting of bands and deep impurity levels from the lone pairs on the nitrogen atoms. Additionally, this work showed that while nitrile groups can tolerate high temperatures on surfaces, some of these groups cyclo-isomerize to produce pyridine rings. Further, similar cyclization reactions on-surface will be discussed later in this Chapter .

Furthermore, in 2017 Gao and coworkers demonstrated the synthesis of sulfur-doped GNRs on Au(111) (Figure 6, entry 11).[58] This was done by using sulfur-substituted oligophenylene monomers to afford a chevron backbone doped with sulfur end groups. This work shows that sulfur could tolerate high temperatures (400 °C) required for cyclodehydrogenation. The authors of this work reported that a tunable bandgap could be produced via the variable configurations and bond rotations of the precursor monomer. Meaning that depending on the combined relative positions of end groups, variable bandgap measurements (i.e., 1.53 eV, 1.55 eV, 1.64 eV) could be observed. STM and STS along with complementary theoretical DFT calculations were used to evaluate these results.

In 2018, Narita *et al.* showed that boron-oxide doped GNRs could be synthesized on surface (Figure 6, entry 12).[59] This was done by using 6,16-dibromo-9,10,19,20-tetraoxa-9a,19a-diboratetrabenzo[*a,f,j,o*]perylene as the molecular precursor to afford the first hetero-atom doped chiral (4,1) GNR. Boron-oxide doped (4,1)-chiral GNR also showed unique lateral self-assembly due to the presence of oxygen-boron-oxygen (OBO) segments on the edges. Such self-assembly characteristics is important for building smaller electronics in a highly robust manner. This GNR was characterized by STM, nc-AFM, and Raman spectroscopy. STS also reveals that OBO (4,1) chiral GNR segments have a larger bandgap than pristine (4,1) chiral GNR.

In 2018, Mugarza and coworkers described the synthesis of a nanoporous graphene (NPG) (Figure 6, entry 13).[60] This was achieved by using a similar precursor to that described by Fasel in 2010 which afforded N=7 armchair GNR in that earlier case. Instead, this molecular precursor had additional phenyl rings at the 4' position of the anthracene moieties. 2,2'-Diphenyl–10,10'-dibromo-9,9'-bianthracene was used in a three-step process to afford NPG. First, annealing to 200 °C allowed for the formation of polymers via debromination and subsequent Ullman coupling. Then, further heating to anneal at 400°C induced intramolecular cyclization, forming a GNR with a triple-bay region. These triple-bay regions cause the ribbons to have alternating widths of N=7 and N=13. Further heating of these GNRs to 450 °C induces *intermolecular* carbon-carbon bond formation between the ribbons. This results in nanoporous graphene with pore sizes of about 1 nm. Additionally, the authors of this work state that the electronic band structure of this material is confined to the pore sites, making it an interesting material for combined sieving and electrical sensing.

Expanding on the work done by Fasel in 2016, again Fasel and coworkers in 2020 utilized methyl-aryl coupling reactions to afford an oligo(indenoindene) GNR (Figure 6, entry 14).[61] Interestingly, this work showed that five-membered rings could be incorporated into a GNR synthesis on-surface. Numerous examples of solution synthesized conjugated organic polymers with five membered have been reported. However, conjugated ladder polymers that are more rigid have remained elusive through this method because of the high temperatures required for cyclodehydrogenation to form the fully fused GNR backbone. This work showed that methyl-aryl coupling can be used to afford five-membered rings on-surface at temperatures around 360 °C. Here, 4,4'-dibromo-trimethyl-p-terphenyl was used to fabricate this particular GNR. While segments of this GNR were pristine, some defects were observed by nc-AFM, which offered

insights into new possible edge structures. For example, methylene ($-CH_2-$) units were observed as brighter features, owing to the incomplete dehydrogenation of the cyclized structure.

The next set of examples detail GNRs that have been fabricated more recently, between the years of 2020 – 2021 (Figure 7). In 2020, Müllen and coworkers described the synthesis of an unprecedented cove-edge chiral GNR on Au(111) (Figure 7, entry 15).[62] This was achieved by using 2,6-dibromo-1,5-diphenylnaphthalene as the molecular precursor, and heating to about 300 °C. Non-planar structures were revealed via STM owing to the cove-edge structure. STS also revealed a small bandgap of about 1.6 eV. Due to the lack of enantiomeric selectivity when depositing molecules on surface, some polymeric structures with different chiralities and widths were also observed. This was verified by the change in ribbon structure when heating between 200-300°C. Ribbons lie uniformly at temperatures below 200 °C, stabilized by interactions of the GNR rings with the metal surface and bromine atoms underneath. This is because the estimated distance between monomers is larger than the expected carbon-carbon bond. Heating to 300 °C ultimately induced carbon-carbon bond formation and cyclodehydrogenation, causing the ribbons to separate from each other into twisted structures. It should be noted that the GNR obtained in this work is similar to the structures later discussed in Chapter 2 and Chapter 3.

In 2020, Feng *et al.* described the synthesis of a graphene nanoribbon doped with nitrogen and boron (Figure 7, entry 16).[63] Two N-B-N zigzag-GNRs, were synthesized using bis(para-iodophenyl)iodophenyl)-substituted NBN-dibenzophenalene monomers. These U-shaped mono-mers are based on similar work by Fasel in 2016, but instead incorporate nitrogen and boron heteroatoms and use iodine as the halogen for surface-assisted coupling. Although a seemingly more reactive halogen is used, this work describes the Ullman coupling process to still having to take place at 200 °C. It is stated that when these molecular precursors are sublimed onto Au(111)
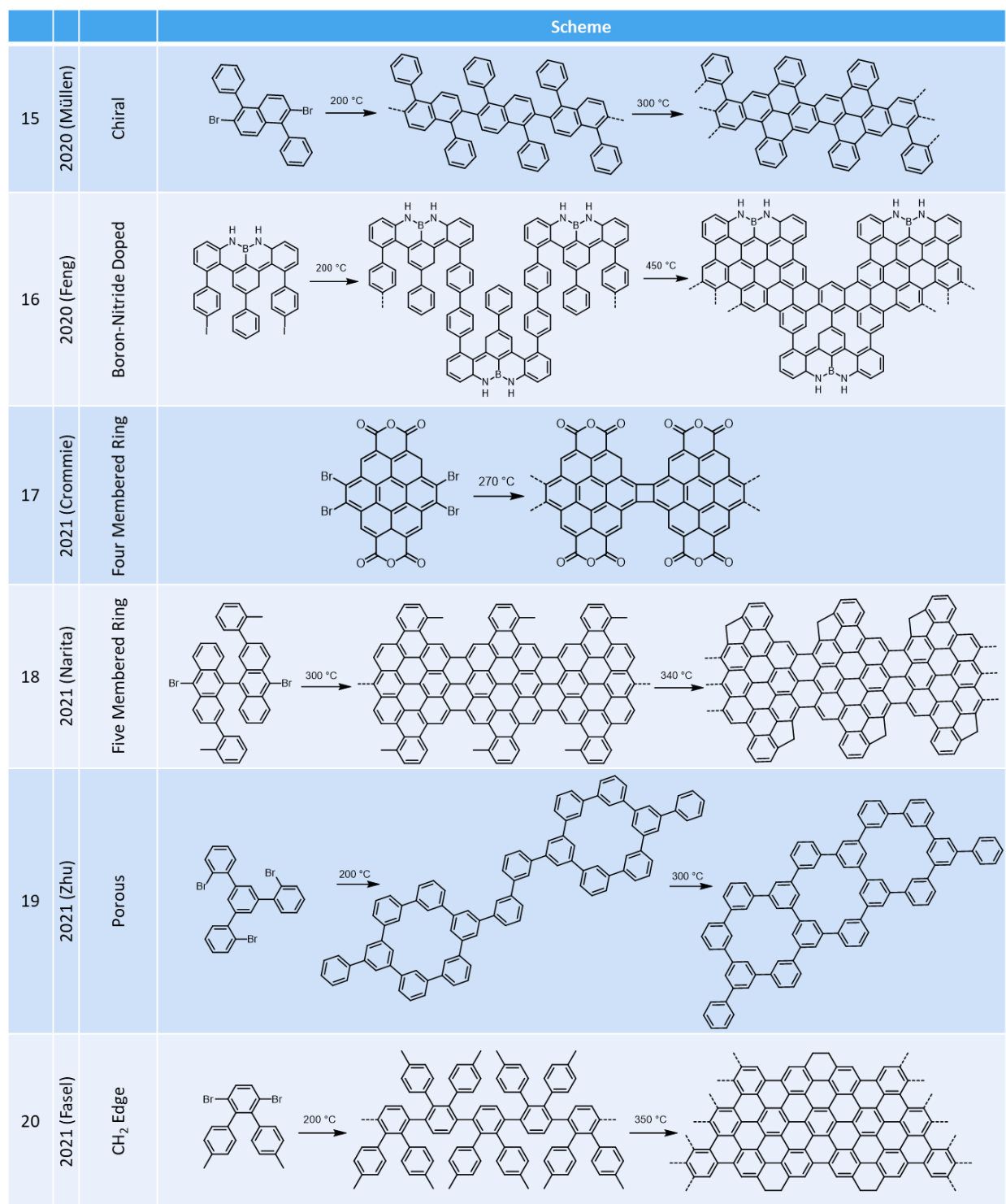
Figure 7. Graphene nanoribbons (GNRs) synthesized between the years 2020 to 2021. Chiral GNR, Müllen, 2020 (15); Boron-Nitrogen-Edge-Doped GNR, Feng, 2020 (16); Four-Membered Ring GNR, Crommie, 2021 (17); Five-Membered-Ring Edge GNR, Narita, 2021 (18); Porous GNR, Zhu, 2021 (19); CH_2-Edge GNR, Fasel, 2021 (20).

held at room temperature, they self-assemble in a tail-to-tail fashion facilitated by hydrogen-iodine interactions, and this can be noted via STM. This concept will be examined further in Chapter 2, as iodine is also used for the molecular precursor discussed there. STS measurements and DFT calculations revealed that the NBN GNRs have significantly larger bandgaps (1.5 eV and 1.9 eV) than their pristine carbon counterparts. Additionally, DFT calculations from this work showed that this GNR could be tuned to become gapless or metallic by oxidation, which could be an important way to alter the bandgap of doped GNR materials.

In 2021, Crommie and coworkers demonstrated that a four-membered ring could be incorporated into a GNR (Figure 7, entry 17).[64] Previously in 2017, Tran *et al.* showed that 4,5,9,10-tetrabromo-2,7-di-*tert*-butylpyrene could be used to form short-chain polymers that contain four-membered rings. The molecular precursor required the presence of four bromine atoms to simultaneously undergo a [2+2] cycloaddition and polymerization step. The polymers however were not long enough to characterize STM.[65] In the work by Crommie, linearly fused coronene-cyclobutadienoid GNRs (cor4GNRs) were synthesized. Incorporation of these four-membered rings resulted in a narrow 0.6 eV bandgap and novel electronic frontier states through pseudo-atomic orbitals. Overall, this work shows how incorporation of rings of different sizes into GNRs can be used to engineer localized electronic states, bandgaps, and magnetic properties.

In addition to the work by Fasel in 2020, Narita and coworkers, in 2021, showed that five-membered rings could also be incorporated into wider GNRs (Figure 7, entry 18).[66] This molecular precursor was based on the one used by Mugarza in 2018 to obtain triple-bay GNRs. Here instead, Narita incorporated a methyl group in the ortho position of the phenyl rings, creating ortho-tolyl-substituted dibromobianthryl. This precursor molecule was used to obtain an

armchair-edge GNR with five-membered rings incorporated throughout. This was achieved through C-H activation and cyclization of the benzylic methyl groups when the intermediate GNR was annealed at 300 °C. nc-AFM revealed methylene-bridged pentagons along the edges of the GNR. DFT calculations showed that the bandgap is 0.74 eV and that these five-membered rings do not contribute to the resonance. Additional heating between 320 - 340 °C causes partial dehydrogenation of the methylene groups, indicated by the new bright protrusions via nc-AFM. DFT calculations predicted this dehydrogenated GNR to have a bandgap of 0.41 eV.

In 2021, Zhu and coworkers reported the synthesis of nanoporous graphene (NPG) using 1,3,5-tris(2-bromophenyl)benzene on Cu(111) (Figure 7, entry 19).[67] They observed a difference in polymer formation when using two different annealing procedures. When step-annealed at room temperature, they reported dendritic structures thanks to the initial self-assembly of individual molecules. To bypass this and form the desired ordered porous structure, hot deposition was used.

Additionally in 2021, Fasel and coworkers described the synthesis of a N=9 armchair-edge extended GNR (Figure 7, entry 20).[68] At this point in time, methyl-aryl coupling had been explored as a method to form zigzag and armchair edges. However, in this work, the authors decided to explore the possibility of a methyl-methyl coupling reaction. Polymerization of U-shaped monomer, dimethyl substituted *o*-terphenyl, took place at 200 °C. Further heating to 350 °C caused cyclodehydrogenation to take place as well as the methyl-methyl coupling reaction. This produced three distinguishably different edge structures with (1) conjugated six-membered rings with sp^2 hybridized carbon atoms, (2) ethane-diyl bridges with sp^3 hybridized carbon atoms, and (3) defects caused by the loss of aryl units. The next section describes the most lately synthesized GNRs in 2022 (Figure 8).
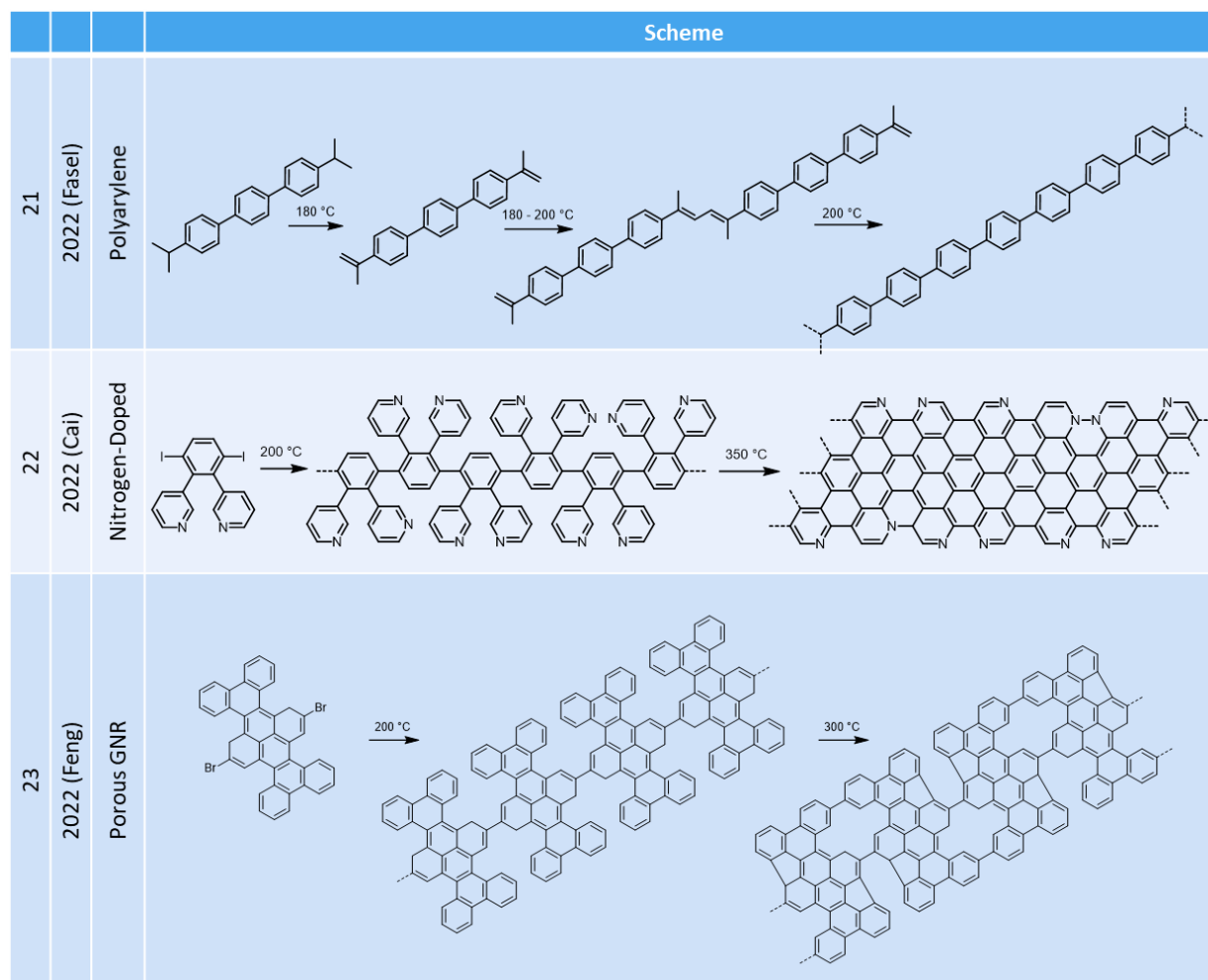
Figure 8. Graphene nanoribbons (GNR) synthesized in 2022. Polyarylene GNR, Fasel, 2022 (21); Nitrogen-Edge Doped GNR, Cai, 2022 (22); Porous GNR, Feng, 2022 (23).

In 2022, Fasel and coworkers described the synthesis of poly-*p*-phenylene on surface (Figure 8, entry 21).[69] This is done using a diisopropyl-*p*-terphenyl, which undergoes a novel [3+3]-type sp³-sp³ dimerization, which is considered a formal cycloisomerization. This precursor was chosen for the pre-installed isopropyl groups to initiate cyclization and polymerization. Initial heating at 180 °C induced a selective dehydrogenation of the isopropyl groups to form isopropenyl groups. This was verified by separate solution-synthesis and subsequent on-surface comparison of 4,4″-di-prop-2-enyl-*p*-terphenyl. Heating to 200 °C induces carbon-carbon bond

formation via coupling of the allylic carbon atoms in the subsequently formed methylene units. Further heating then causes the cycloaromatization step to take place. Overall, this works shows that incorporation of unique carbon-based functional groups, such as isopropyl units, can be used to explore the synthesis of novel GNR structures on surface. This type of unusual cyclization would be difficult to achieve in solution using classic synthesis.

In 2022, Cai et al. described the synthesis of a new nitrogen-doped GNR with differently substituted edges (Figure 8, entry 22).[70] Using 3,3'-(3,6-diiodo-1,2-phenylene) dipyridine (DIPDP) as the molecular precursor, N=9 armchair nitrogen-doped GNR was synthesized. Because of the inherent flexibility of the selected precursor monomer, three different adsorption conformations were observed. This ultimately produced a GNR that contained three different covalent bonds along the edges of the ribbon: (1) nitrogen-nitrogen, (2) carbon-carbon, and (3) nitrogen-carbon. DFT calculations from this study also predicted that the analogous carbon GNR would have a semiconductor character, while the nitrogen doped one should be metallic. There is no change to the bandgap from the pyridine ring for C-C bonds, however the C-N and N-N bonds greatly affect the band structure. This molecular precursor also uses iodine as the halogen for surface-assisted polymerization. The authors here report that removal of the iodine atom and polymerization took place at 200 °C while intact structures were observed on-surface at 25 ˚C.

Finally in 2022, Feng and coworkers described the synthesis of a porous graphene nanoribbon with five-membered rings (Figure 8, entry 23).[71] This non-planar GNR was synthesized using a 10,21-dibromohexabenzo[a,c,fg,j,l,o,p]tetracene molecular precursor with four cove sites. When deposited on Au(111) surface and annealed to 200 °C, the molecular precursor undergoes Ullman coupling. Further heating to 300 °C caused cyclodehydrogenation to take place, forming C–C bonds between the phenanthrene subunits of the polymers.

		Scheme
1	Intramolecular Dehydrogenation	400 °C → Fasel 2010
2	2 + 2 Cycloaddition	270 °C → Crommie 2021
3	Cycloaromatization of Isopropyl Groups	180 - 200 °C → Fasel 2022
4	Methyl-Methyl Coupling	350 °C → Fasel 2021
5	Methyl-Aryl Coupling	350 °C → Fasel 2016
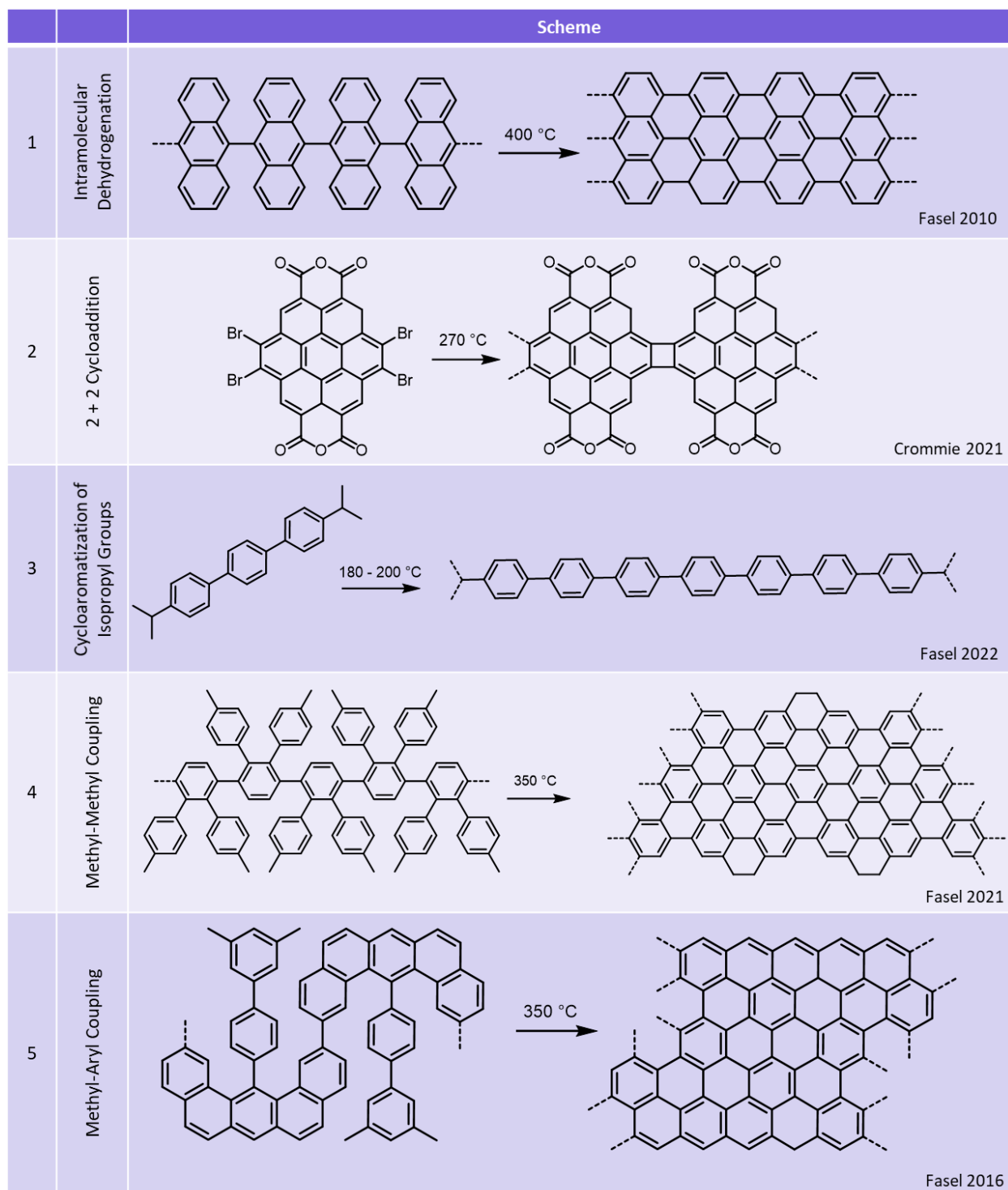
Figure 9. Examples of reactions used to synthesize graphene nanoribbons. Intramolecular dehydrogenation, Fasel, 2010 (1); 4+4 cycloaddition, Crommie, 2021 (2); Cycloaromatization of isopropyl groups, Fasel, 2022 (3); methyl-methyl coupling, Fasel, 2021 (4); methyl-aryl coupling, Fasel, 2016 (5).

Overall, these examples highlight the progression of on-surface graphene nanoribbon synthesis over the years (Figures 5 – 8). They show that GNRs can be synthesized with a variety of widths and edge structures. Additionally, heteroatoms can be used to alter their electronic structure. Inclusions of certain functional groups that are stable to on-metal reactions also offer novel avenues to electronic modulation.

The next part of this Chapter describes the general reactions that have been commonly or recently used to synthesize graphene nanoribbons on surface (Figure 9). The most used reaction is the Ullman coupling of dihalo biaryls.[72] This polymerization reaction requires two chemically equivalent halogens preinstalled on the molecular precursor. When heated, the halogens are homolitically split off, forming a biradical intermediate stabilized by the metal surface. Due to some mobility allowed by the selected metal, these diradicals move to couple with each other, forming carbon-carbon bonds. Further reactions occur with further heating to give a series of cyclization reactions. These reactions are of utmost importance to graphene nanoribbon synthesis because of the limited availability of defined dihalogenated polycyclic hydrocarbons. Cyclization reactions have been demonstrated in solution, but they oftentimes cannot be performed to form long chain polymers due to aggregation and poor solubility.

The most commonly used cyclization reaction is the intramolecular dehydrogenation (Figure 9, entry 1).[33] This reaction forms a carbon-carbon bond to afford either six or five-membered rings within a GNR. This typically requires temperatures above 300 °C to take place. Previous calculations have shown the effect of van der Waals interactions on surface-bound species in this reaction step.[73] This step is first initiated by hydrogen abstraction. It was found that, although most aromatic molecules are lying flat, slight tilting of aromatic rings causes some hydrogens to have a lower activation barrier for H· abstraction. This is because the transition state of the

abstraction step corresponds to a geometry where the hydrogen atom and the alpha carbon are bound to the metal surface. This abstraction then causes a slight rotation, where the dehydrogenated portion bends towards the neighboring C-H bond. A C–C bond is then formed through radical aromatic addition and subsequent metal-assisted removal of the beta-hydrogen.[74]

Various other cyclization reactions have been used to synthesize graphene nanoribbons on surface. This has been done by inclusion of different functional groups (Figure 9, entry 2). For example, [2+2] cycloaddition has been demonstrated by using molecular precursors containing four halogens (two chemically equivalent) in the 1,2 positions of the end-aryl rings. In 2021, Crommie showed that a four-membered ring in a GNR could be obtained via a [2+2] cycloaddition.[64] This work showed that coupling took place in areas of high surface density, meaning that no external hydrogen was required. Earlier examples of four-membered ring were only obtained via dimerization of alkenes or stepwise cyclodehydrogenation.[75,76] Previous work had been done to demonstrate [2+2] cycloaddition in polymers on surface, but only on smaller aromatic molecular precursors. This included using the following bromine substituted molecular precursors: 2,3,8,9-tetrabromotetracene,[77] 2,3,6,7,10,11-hexabromotriphenylene,[78] and 1,2,4,5-tetrabromo-3,6-dimethylbenzene.[79] This resulted in units with very little antiaromaticity due to the fusion pattern. Overall [2+2] cycloaddition could be achieved at temperatures around 270 °C.

In 2022, Fasel demonstrated that isopropyl groups could be used to facilitate a [3+3] cycloaddition, essentially creating a polymer with additional aromatic six-membered ring linkages created by the fusion of two isopropyl groups (Figure 9, entry 3).[69] This reaction is of utmost importance to graphene nanoribbon synthesis because it has demonstrated that unusual cyclization reactions can take place at temperatures below 200 °C. Low temperatures should allow for cheaper, safer, and overall more efficient synthesis of GNRs for electronic applications.

The next two examples take place because of the presence of methyl groups. Methyl-aryl coupling has been demonstrated for very few examples to date (Figure 9, entry 5).[19] This has been typically used to cyclize the edges of a nanoribbon to fabricate GNRs with a zigzag edge topology. Additionally, methyl-methyl coupling has been used to cyclize the edges of armchair GNRs (Figure 9, entry 4).[68] This forms methylene bridged edges of a GNR. These reactions are useful because in principle, they only require a methyl functional group to cyclize. However, they are limited because they still require high reaction temperatures (around 350 °C) to take place.

While current cyclization reactions are of interest for graphene nanoribbon synthesis, new functional groups should be investigated as components of this molecular toolbox. Alkynes offer some of the most versatile and useful reactions. The following reviews the surface reactions that have been demonstrated with alkynes.

In 2013, Fuchs and coworkers demonstrated that a Glaser-type coupling could take place on a metal surface.[80] In this experiment, 1,4-diethynylbenzene was coupled and polymerized on various metal surfaces (Figure 10, entry 1). Interestingly, while copper is the catalyst for Glaser couplings in solution,[81] this metal was not an efficient catalytic support for on-surface synthesis. Statistical analysis and theoretical results point to the role of the metal surface for aiding carbon-carbon bond formation. Theoretical DFT calculations from Fuchs and coworkers predict the reaction mechanism. Similar results to the process of Ullman Coupling were determined. Gold forms a complex, binding one of the alkynyl groups to two Au atoms on the substrate with a calculated energy of 0.5 eV. Next is the C-C coupling which has an energy of 0.79 eV. Additional calculations also reveal that the intermediates are more strongly bounded to the gold than the silver substrate, meaning use of a silver substrate would require less energy for a Glaser
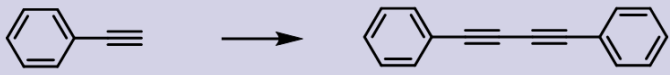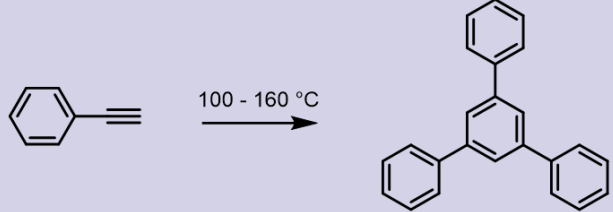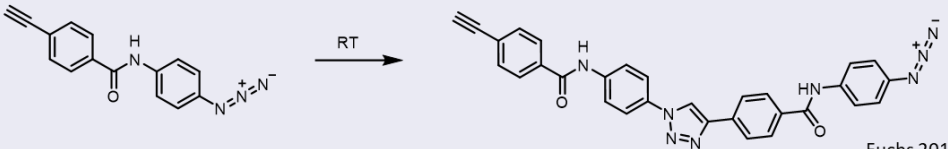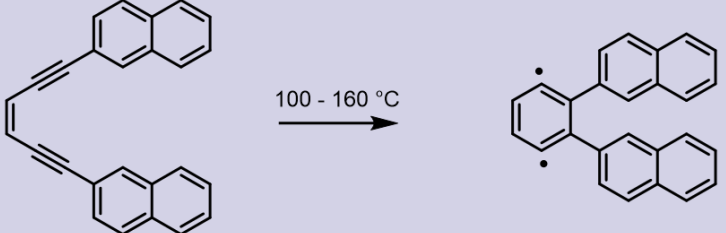
coupling. Dehydrogenation then occurs in two subsequent steps. This rection was found to take place at temperatures between 100 – 120 °C. This work also showed the possibility of non-dehydrogenative alkyne coupling as well as alkyne trimerization.

High-resolution bond-resolving scanning probe microscopies (BR-SPMs) has shown that non-dehydrogenative alkyne coupling can take place on metal surfaces. In 2021, de Oteyza *et al.* demonstrated that 1-bromo-2-ethynylpyrene favors Glaser coupling, while non-dehydrogenative head-to-head coupling took place when 2-ethynylpyrene was used (Fig. 10, entry 2). This is because the reaction was promoted by the presence of the vicinal radical formed from debromination. These reactions were found to take place at temperatures around 200 °C.[82]

In 2010, Lambert and coworkers demonstrated that a Sonogashira coupling could take place on a gold surface (Figure 10, entry 4).[83] In this experiment, they reacted phenylacetylene with iodobenzene to form diphenylacetylene and biphenyl. This was found to take place at around room temperature. Furthermore, in 2016 Xu and coworkers described the synthesis of acetylenic scaffolds through dehalogenative homocouplings of alkynyl bromides (Figure 10, entry 3).[84] This diyne moiety is a fundamental structure for organic materials, proving to be highly important in solid-state GNR synthesis. Studying these diynes on surface could lead to an understanding of new reactions. This is discussed further in Chapter 5.

In 2014, Fasel *et al.* reported the cyclotrimerization of arylalkynes on Au(111) (Figure 10, entry 5).[85] 1,3,5-Tris-(4-ethynylphenyl)benzene, a molecular precursor with a three-fold symmetrical aromatic core and three terminal alkyne groups, was deposited on surface and used

		Scheme
1	Glaser Coupling	Fuchs 2013
2	Non- dehydrogenative Coupling	De Oteyza 2021
3	Alkynyl Halide Coupling	Xu 2016
4	Sonogashira	Lambert 2010
5	Cyclotrimerization	Fasel 2014
6	Click Chemistry	Fuchs 2013
7	Bergman Cyclization	Xu 2013

Figure 10. Useful alkyne reactions for on-surface synthesis. Glaser coupling, Fuchs, 2013 (1); Non-dehydrogenative coupling, de Oteyza, 2021 (2); Alkynyl halide coupling, Xu, 2016 (3); Sonogashira reaction; Lambert, 2020 (4); Cyclotrimerization, Fasel, 2014 (5); Click reaction, Fuchs, 2013 (6); Bergman cyclization, Xu, 2013 (7).

to fabricate a two-dimensional honey-comb. In this process, three alkyne groups are thermally activated on the gold surface to form a benzene ring. This reaction was found to take place between 100-200 °C, which was a benefit for forming extended conjugated networks at low temperatures.

In 2013, Fuchs and coworkers described the occurrence of a [3+2] cycloaddition reaction (click reaction) between azides and alkynes on Au(111) under ultrahigh vacuum (Figure 10, entry 6).[86] The corresponding 1,4-triazole linkages can be formed at room temperature. The authors of this work state that the gold surface does not act as a catalyst for the reaction but instead serves as a scaffold. This is because it plays a crucial role in orienting the molecules and constraining them to a 2-dimensional environment. In addition to providing another low temp coupling reaction, this work details the importance of a metal scaffold in constraining the reaction environment, lowering the activation energy.

Finally, one important reaction involving the intramolecular cyclization of alkynes is discussed. In 2013, Xu and coworkers described the first use of a Bergman cyclization on-surface as a polymerization step to yield covalently linked conjugated carbon nanostructures (Figure 10, entry 7).[87] The Bergman reaction is the intramolecular thermal cyclization of hex-3-ene-1,5-diynes. In this this work, 1,6-di-2-naphthylhex-3-ene-1,5-diyne (DNHD) was used. This reaction takes place with heat, where the formed diradical intermediates couple to form an extended polymer. This was done on a copper surface. Low-temperature annealing results in intact, heart-shaped, molecular precursors. Molecules end up lying flat on the surface. When annealed to temperatures around 130 °C, the molecule underwent cyclization and one-dimensional chains were formed. This low temperature cyclization reaction is important to GNR formation, because it allows for more efficient processability. Low temperature processing is

highly desirable for electronic applications because it requires less harsh conditions. Additionally, low temperature formation of the final organic structures on-surface is desirable because high temperatures often result in molecules detaching from the surface.

From here, it is important to study other cyclization reactions that can be used to fabricate GNRs. Although the Bergman cyclization requires no external input other than heat, it forms highly reactive radicals which can simultaneously produce polymers with uncontrolled structure. To attain better control over GNR fabrication processes, stepwise reactions that can be modulated by different temperatures are necessary. Indeed, it is important to utilize a molecular precursor that can polymerize at a given temperature, then subsequently cyclize at a significantly higher temperature. Additionally, it is advantageous to utilize molecular precursors that require no external stimuli other than heat to take place. Chapter 2 of this thesis investigates such a system, using the Hopf cyclization of a tetraaryl *trans*-3-hexene-1,5-diyne precursor on gold(111) surface.

1.7. References

1)   Bourzac, K. The microprocessor turns 50. *C&EN News*. **2021**. *99*, 18.

2)   Liu, H.; Neal, A. T.; Ye, P. D. Channel Length Scaling of MoS$_2$ MOSFETs. *ACS Nano* **2012**, *6*, 8563–8569. https://doi.org/10.1021/nn303513c.

3)   Liu, C.; Chen, H.; Wang, S.; Liu, Q.; Jiang, Y.-G.; Zhang, D. W.; Liu, M.; Zhou, P. Two-Dimensional Materials for next-Generation Computing Technologies. *Nat. Nanotechnol.* **2020**, *15*, 545–557. https://doi.org/10.1038/s41565-020-0724-3.

4)   S. Chen, A. Gautam and F. Weig, *Bringing energy efficiency to the fab*, **2013**.

     https://www.mckinsey.com/~/media/mckinsey/dotcom/client_service/operations/pdfs/bringing_fabenergyefficiency.ashx

5)   Shalf, J. The Future of Computing beyond Moore's Law. *Phil. Trans. R. Soc. A.* **2020**, *378*, 20190061. https://doi.org/10.1098/rsta.2019.0061.

6)   Burmeister, D.; Trunk, M. G.; Bojdys, M. J. Development of Metal-Free Layered Semiconductors for 2D Organic Field-Effect Transistors. *Chem. Soc. Rev.* **2021**, *50*, 11559–11576. https://doi.org/10.1039/D1CS00497B.

7)   Chaves, A.; Azadani, J. G.; Alsalman, H.; da Costa, D. R.; Frisenda, R.; Chaves, A. J.; Song, S. H.; Kim, Y. D.; He, D.; Zhou, J.; Castellanos-Gomez, A.; Peeters, F. M.; Liu, Z.; Hinkle, C. L.; Oh, S.-H.; Ye, P. D.; Koester, S. J.; Lee, Y. H.; Avouris, Ph.; Wang, X.; Low, T. Bandgap Engineering of Two-Dimensional Semiconductor Materials. *NPJ 2D Mater Appl* **2020**, *4*, 29. https://doi.org/10.1038/s41699-020-00162-4.

8) Wang, H.; Yuan, H.; Sae Hong, S.; Li, Y.; Cui, Y. Physical and Chemical Tuning of Two-Dimensional Transition Metal Dichalcogenides. *Chem. Soc. Rev.* **2015**, *44*, 2664–2680. https://doi.org/10.1039/C4CS00287C.

9) Chiang, C. K.; Fincher, C. R.; Park, Y. W.; Heeger, A. J.; Shirakawa, H.; Louis, E. J.; Gau, S. C.; MacDiarmid, A. G. Electrical Conductivity in Doped Polyacetylene. *Phys. Rev. Lett.* **1977**, *39*, 1098–1101. https://doi.org/10.1103/PhysRevLett.39.1098.

10) Young, R. J.; Read, R. T.; Bloor, D.; Ando, D. Structure and Morphology of Polydiacetylene Single Crystals. *Faraday Discuss. Chem. Soc.* **1979**, *68*, 509. https://doi.org/10.1039/dc9796800509.

11) Fukuda, K.; Someya T. Recent Progress in the Development of Printed Thin-Film Transistors and Circuits with High-Resolution Printing Technology, *Adv. Mater.* **2017**, *29*, 1602736. https://doi.org/10.1002/adma.201602736

12) Xiong, R.; Grant, A. M.; Ma, R.; Zhang, S.; Tsukruk, V. V. Naturally-Derived Biopolymer Nanocomposites: Interfacial Design, Properties and Emerging Applications. *Materials Science and Engineering: R: Reports* **2018**, *125*, 1–41. https://doi.org/10.1016/j.mser.2018.01.002.

13) Shulaker, M. M.; Hills, G.; Patil, N.; Wei, H.; Chen, H.-Y.; Wong, H.-S. P.; Mitra, S. Carbon Nanotube Computer. *Nature* **2013**, *501*, 526–530. https://doi.org/10.1038/nature12502.

14) Zhai, L.; Khondaker, S. I.; Thomas, J.; Shen, C.; McInnis, M. Ordered Conjugated Polymer Nano- and Microstructures: Structure Control for Improved Performance of Organic Electronics. *Nano Today* **2014**, *9*, 705–721. https://doi.org/10.1016/j.nantod.2014.10.004.

15) Siegel, Joel. F.; Dwyer, J. H.; Suresh, A.; Safron, N. S.; Fortman, M. A.; Wan, C.; Choi, J. W.; Wei, W.; Saraswat, V.; Behn, W.; Kats, M. A.; Arnold, M. S.; Gopalan, P.; Brar, V. W. Using Bottom-Up Lithography and Optical Nonlocality to Create Short-Wave Infrared Plasmonic Resonances in Graphene. *ACS Photonics* **2021**, *8*, 1277–1285. https://doi.org/10.1021/acsphotonics.1c00149.

16) Bao, Z.; Chen, X. Flexible and Stretchable Devices. *Adv. Mater.* **2016**, *28*, 4177–4179. https://doi.org/10.1002/adma.201601422.

17) Pinto, A. M.; Gonçalves, I. C.; Magalhães, F. D. Graphene-Based Materials Biocompatibility: A Review. *Colloids and Surfaces B: Biointerfaces* **2013**, *111*, 188–202. https://doi.org/10.1016/j.colsurfb.2013.05.022.

18) Someya, T.; Bao, Z.; Malliaras, G. G. The Rise of Plastic Bioelectronics. *Nature* **2016**, *540*, 379–385. https://doi.org/10.1038/nature21004.

19) Ruffichez-Sánchez, C.; Liu, J.; Dienel, T.; Talirz, L.; Shinde, P.; Pignedoli, C. A.; Passerone, D.; Dumslaff, T.; Feng, X.; Müllen, K.; Fasel, R. On-Surface Synthesis of Graphene Nanoribbons with Zigzag Edge Topology. *Nature* **2016**, *531*, 489–492. https://doi.org/10.1038/nature17151.

20) Kong, X.; Cui, B.; Zhao, W.; Zhao, J.; Li, D.; Liu, D. Spin Negative Differential Resistance and High Spin Filtering Behavior Realized by Devices Based on Graphene Nanoribbons and Graphitic Carbon Nitrides. *Organic Electronics* **2014**, *15*, 3674–3680.

https://doi.org/10.1016/j.orgel.2014.10.016.

21) Li, T.; Xu, L.; Xiao, X.; Chen, F.; Cao, L.; Wu, W.; Tong, W.; Zhang, F. Enhanced Spin Transport of Conjugated Polymer in the Semiconductor/Insulating Polymer Blend. *ACS Appl. Mater. Interfaces* **2020**, *12*, 2708–2716. https://doi.org/10.1021/acsami.9b16602.

22) Guo, G.-P.; Lin, Z.-R.; Tu, T.; Cao, G.; Li, X.-P.; Guo, G.-C. Quantum Computation with Graphene Nanoribbon. *New J. Phys.* **2009**, *11*, 123005. https://doi.org/10.1088/1367-2630/11/12/123005.

23) Tan, Y.; Xia, X.-S.; Liao, X.-L.; Li, J.-B.; Zhong, H.-H.; Liang, S.; Xiao, S.; Liu, L.-H.; Luo, J.-H.; He, M.-D.; Chen, L.-Q. A Highly-Flexible Bistable Switch Based on a Suspended Monolayer Z-Shaped Graphene Nanoribbon Nanoresonator. *Carbon* **2020**, *157*, 724–730. https://doi.org/10.1016/j.carbon.2019.10.103.

24) Chen, C.-C.; Chang, Y.-C. Theoretical Studies of Graphene Nanoribbon Quantum Dot Qubits. *Phys. Rev. B* **2015**, *92*, 245406. https://doi.org/10.1103/PhysRevB.92.245406.

25) Li, J.; Rochester, C. W.; Jacobs, I. E.; Friedrich, S.; Stroeve, P.; Riede, M.; Moulé, A. J. Measurement of Small Molecular Dopant F4TCNQ and $C_{60}F_{36}$ Diffusion in Organic Bilayer Architectures. *ACS Appl. Mater. Interfaces* **2015**, *7*, 28420–28428. https://doi.org/10.1021/acsami.5b09216.

26) Cesano, F.; Uddin, M. J.; Lozano, K.; Zanetti, M.; Scarano, D. All-Carbon Conductors for Electronic and Electrical Wiring Applications. *Front. Mater.* **2020**, *7*, 219. https://doi.org/10.3389/fmats.2020.00219.

27) Novoselov, K. S.; Fal′ko, V. I.; Colombo, L.; Gellert, P. R.; Schwab, M. G.; Kim, K. A Roadmap for Graphene. *Nature* **2012**, *490*, 192–200. https://doi.org/10.1038/nature11458.

28) Tour, J. M. Top-Down versus Bottom-Up Fabrication of Graphene-Based Electronics. *Chem. Mater.* **2014**, *26*, 163–171. https://doi.org/10.1021/cm402179h.

29) Nakada, K.; Fujita, M.; Dresselhaus, G.; Dresselhaus, M. S. Edge State in Graphene Ribbons: Nanometer Size Effect and Edge Shape Dependence. *Phys. Rev. B* **1996,** *54*, 17954-17961. https://journals.aps.org/prb/abstract/10.1103/PhysRevB.54.17954

30) Son, Y.-W.; Cohen, M. L.; Louie, S. G. Energy Gaps in Graphene Nanoribbons. *Phys. Rev. Lett.* **2006**, *97*, 216803. https://doi.org/10.1103/PhysRevLett.97.216803.

31) Dutta, S.; Pati, S. K. Novel Properties of Graphene Nanoribbons: A Review. *J. Mater. Chem.* **2010**, *20*, 8207. https://doi.org/10.1039/c0jm00261e.

32) Gao, J.; Uribe-Romo, F. J.; Saathoff, J. D.; Arslan, H.; Crick, C. R.; Hein, S. J.; Itin, B.; Clancy, P.; Dichtel, W. R.; Loo, Y.-L. Ambipolar Transport in Solution-Synthesized Graphene Nanoribbons. *ACS Nano* **2016**, *10*, 4847–4856. https://doi.org/10.1021/acsnano.6b00643.

33) Cai, J.; Ruffieux, P.; Jaafar, R.; Bieri, M.; Braun, T.; Blankenburg, S.; Muoth, M.; Seitsonen, A. P.; Saleh, M.; Feng, X.; Müllen, K.; Fasel, R. Atomically Precise Bottom-up Fabrication of Graphene Nanoribbons. *Nature* **2010**, *466*, 470–473. https://doi.org/10.1038/nature09211.

34) Jordan, R. S.; Wang, Y.; McCurdy, R. D.; Yeung, M. T.; Marsh, K. L.; Khan, S. I.; Kaner, R. B.; Rubin, Y. Synthesis of Graphene Nanoribbons via the Topochemical Polymerization and Subsequent Aromatization of a Diacetylene Precursor. *Chem* **2016**, *1*, 78–90. https://doi.org/10.1016/j.chempr.2016.06.010.

35) Jordan, R. S.; Li, Y. L.; Lin, C.-W.; McCurdy, R. D.; Lin, J. B.; Brosmer, J. L.; Marsh, K. L.; Khan, S. I.; Houk, K. N.; Kaner, R. B.; Rubin, Y. Synthesis of $N = 8$ Armchair Graphene Nanoribbons from Four Distinct Polydiacetylenes. *J. Am. Chem. Soc.* **2017**, *139*, 15878–15890. https://doi.org/10.1021/jacs.7b08800.

36) Li, Y. L.; Zee, C.-T.; Lin, J. B.; Basile, V. M.; Muni, M.; Flores, M. D.; Munárriz, J.; Kaner, R. B.; Alexandrova, A. N.; Houk, K. N.; Tolbert, S. H.; Rubin, Y. Fjord-Edge Graphene Nanoribbons with Site-Specific Nitrogen Substitution. *J. Am. Chem. Soc.* **2020**, *142* (42), 18093–18102. https://doi.org/10.1021/jacs.0c07657.

37) Wang, X.-Y.; Narita, A.; Müllen, K. Precision Synthesis versus Bulk-Scale Fabrication of Graphenes. *Nat Rev Chem* **2018**, *2*, 0100. https://doi.org/10.1038/s41570-017-0100.

38) Barth, J. V.; Costantini, G.; Kern, K. Engineering Atomic and Molecular Nanostructures at Surfaces. *Nature* **2005**, *437*, 671–679. https://doi.org/10.1038/nature04166.

39) Gross, L.; Mohn, F.; Moll, N.; Liljeroth, P.; Meyer, G. The Chemical Structure of a Molecule Resolved by Atomic Force Microscopy. *Science* **2009**, *325*, 1110–1114. https://doi.org/10.1126/science.1176210.

40) Barth, J. V.; Costantini, G.; Kern, K. Engineering Atomic and Molecular Nanostructures at Surfaces. *Nature* **2005**, *437*, 671–679. https://doi.org/10.1038/nature04166.

41) Eder, G.; Smith, E. F.; Cebula, I.; Heckl, W. M.; Beton, P. H.; Lackinger, M. Solution Preparation of Two-Dimensional Covalently Linked Networks by Polymerization of 1,3,5-Tri(4-Iodophenyl) Benzene on Au(111). *ACS Nano* **2013**, *7*, 3014–3021. https://doi.org/10.1021/nn400337v.

42) Grill, L.; Dyer, M.; Lafferentz, L.; Persson, M.; Peters, M. V.; Hecht, S. Nano-Architectures by Covalent Assembly of Molecular Building Blocks. *Nature Nanotech* **2007**, *2*, 687–691. https://doi.org/10.1038/nnano.2007.346.

43) Gourdon, A. On-surface Covalent Coupling in Ultrahigh Vacuum. *Angew. Chem. Int. Ed. Engl.* **2008**, *47*, 6950–6953. https://doi.org/10.1002/anie.200802229.

44) Eichhorn, J.; Nieckarz, D.; Ochs, O.; Samanta, D.; Schmittel, M.; Szabelski, P. J.; Lackinger, M. On-Surface Ullmann Coupling: The Influence of Kinetic Reaction Parameters on the Morphology and Quality of Covalent Networks. *ACS Nano* **2014**, *8*, 7880–7889. https://doi.org/10.1021/nn501567p.

45) Cai, J.; Pignedoli, C. A.; Talirz, L.; Ruffieux, P.; Söde, H.; Liang, L.; Meunier, V.; Berger, R.; Li, R.; Feng, X.; Müllen, K.; Fasel, R. Graphene Nanorobot Heterojunctions. *Nature Nanotech* **2014**, *9*, 896–900. https://doi.org/10.1038/nnano.2014.184.

46) Kawai, S.; Saito, S.; Osumi, S.; Yamaguchi, S.; Foster, A. S.; Spijker, P.; Meyer, E. Atomically Controlled Substitutional Boron-Doping of Graphene Nanoribbons. *Nat. Commun.* **2015**, *6*, 8098. https://doi.org/10.1038/ncomms9098.

47) Liu, J.; Li, B.-W.; Tan, Y.-Z.; Giannakopoulos, A.; Sanchez-Sanchez, C.; Beljonne, D.; Ruffieux, P.; Fasel, R.; Feng, X.; Müllen, K. Toward Cove-Edged Low Band Gap Graphene Nanoribbons. *J. Am. Chem. Soc.* **2015**, *137*, 6097–6103. https://doi.org/10.1021/jacs.5b03017.

48) Zhang, H.; Lin, H.; Sun, K.; Chen, L.; Zagranyarski, Y.; Aghdassi, N.; Duhm, S.; Li, Q.; Zhong, D.; Li, Y.; Müllen, K.; Fuchs, H.; Chi, L. On-Surface Synthesis of Rylene-Type Graphene Nanoribbons. *J. Am. Chem. Soc.* **2015**, *137*, 4022–4025.

https://doi.org/10.1021/ja511995r.

49) Yang, L.; Park, C.-H.; Son, Y.-W.; Cohen, M. L.; Louie, S. G. Quasiparticle Energies and Bandgaps in Graphene Nanoribbons. *Phys. Rev. Lett.* **2007**, *99*, 186801. https://doi.org/10.1103/PhysRevLett.99.186801.

50) Fernandez, E. J.; Jones, P. G.; Laguna, A.; Lopez-de-Luzuriaga, J. M.; Monge, M.; Perez, J.; Olmos, M. E. Strong Activation of the Double Bond in (PPh2)2CCH2. Novel Synthesis of gold(III) Methanide Complexes by Michael Addition Reactions. *ACS Organometallics.* **1997**, *16*, 1130 – 1136. https://doi.org/10.1021/om9609832

51) de Oteyza, D. G.; García-Lekue, A.; Vilas-Varela, M.; Merino-Díez, N.; Carbonell-Sanromà, E.; Corso, M.; Vasseur, G.; Rogero, C.; Guitián, E.; Pascual, J. I.; Ortega, J. E.; Wakayama, Y.; Peña, D. Substrate-Independent Growth of Atomically Precise Chiral Graphene Nanoribbons. *ACS Nano* **2016**, *10*, 9000–9008. https://doi.org/10.1021/acsnano.6b05269.

52) Sánchez-Sánchez, C.; Dienel, T.; Deniz, O.; Ruffieux, P.; Berger, R.; Feng, X.; Müllen, K.; Fasel, R. Purely Armchair or Partially Chiral: Noncontact Atomic Force Microscopy Characterization of Dibromo-Bianthryl-Based Graphene Nanoribbons Grown on Cu(111). *ACS Nano* **2016**, *10*, 8006–8011. https://doi.org/10.1021/acsnano.6b04025.

53) Ruffieux, P.; Wang, S.; Yang, B.; Sánchez-Sánchez, C.; Liu, J.; Dienel, T.; Talirz, L.; Shinde, P.; Pignedoli, C. A.; Passerone, D.; Dumslaff, T.; Feng, X.; Müllen, K.; Fasel, R. On-Surface Synthesis of Graphene Nanoribbons with Zigzag Edge Topology. *Nature* **2016**, *531*, 489–492. https://doi.org/10.1038/nature17151.

54) Han, W.; Kawakami, R. K.; Gmitra, M.; Fabian, J. Graphene Spintronics. *Nature Nanotech* **2014**, *9*, 794–807. https://doi.org/10.1038/nnano.2014.214.

55) Li, Y., Zhang, W., Morgenstern, M. & Mazzarello, R. Electronic and Magnetic Properties Of Zigzag Graphene Nanoribbons on the (111) Surface of Cu, Ag, and Au. *Phys. Rev. Lett.* **2013**, *110*, 216804. 10.1103/PhysRevLett.110.216804

56) Talirz, L.; Söde, H.; Dumslaff, T.; Wang, S.; Sanchez-Valencia, J. R.; Liu, J.; Shinde, P.; Pignedoli, C. A.; Liang, L.; Meunier, V.; Plumb, N. C.; Shi, M.; Feng, X.; Narita, A.; Müllen, K.; Fasel, R.; Ruffieux, P. On-Surface Synthesis and Characterization of 9-Atom Wide Armchair Graphene Nanoribbons. *ACS Nano* **2017**, *11*, 1380–1388. https://doi.org/10.1021/acsnano.6b06405.

57) Carbonell-Sanromà, E.; Hieulle, J.; Vilas-Varela, M.; Brandimarte, P.; Iraola, M.; Barragán, A.; Li, J.; Abadia, M.; Corso, M.; Sánchez-Portal, D.; Peña, D.; Pascual, J. I. Doping of Graphene Nanoribbons *via* Functional Group Edge Modification. *ACS Nano* **2017**, *11*, 7355–7361. https://doi.org/10.1021/acsnano.7b03522.

58) Zhang, Y.-F.; Zhang, Y.; Li, G.; Lu, J.; Que, Y.; Chen, H.; Berger, R.; Feng, X.; Müllen, K.; Lin, X.; Zhang, Y.-Y.; Du, S.; Pantelides, S. T.; Gao, H.-J. Sulfur-Doped Graphene Nanoribbons with a Sequence of Distinct Bandgaps. *Nano Res.* **2017**, *10*, 3377–3384. https://doi.org/10.1007/s12274-017-1550-2.

59) Wang, X.-Y.; Urgel, J. I.; Barin, G. B.; Eimre, K.; Di Giovannantonio, M.; Milani, A.; Tommasini, M.; Pignedoli, C. A.; Ruffieux, P.; Feng, X.; Fasel, R.; Müllen, K.; Narita, A. Bottom-Up Synthesis of Heteroatom-Doped Chiral Graphene Nanoribbons. *J. Am. Chem. Soc.* **2018**, *140*, 9104–9107. https://doi.org/10.1021/jacs.8b06210.

60) Moreno, C.; Vilas-Varela, M.; Kretz, B.; Garcia-Lekue, A.; Costache, M. V.; Paradinas, M.; Panighel, M.; Ceballos, G.; Valenzuela, S. O.; Peña, D.; Mugarza, A. Bottom-up Synthesis of Multifunctional Nanoporous Graphene. *Science* **2018**, *360*, 199–203. https://doi.org/10.1126/science.aar2009.

61) Di Giovannantonio, M.; Chen, Q.; Urgel, J. I.; Ruffieux, P.; Pignedoli, C. A.; Müllen, K.; Narita, A.; Fasel, R. On-Surface Synthesis of Oligo(Indenoindene). *J. Am. Chem. Soc.* **2020**, *142*, 12925–12929. https://doi.org/10.1021/jacs.0c05701.

62) Keerthi, A.; Sánchez-Sánchez, C.; Deniz, O.; Ruffieux, P.; Schollmeyer, D.; Feng, X.; Narita, A.; Fasel, R.; Müllen, K. On-surface Synthesis of a Chiral Graphene Nanoribbon with Mixed Edge Structure. *Chem. Asian J.* **2020**, *15*, 3807–3811. https://doi.org/10.1002/asia.202001008.

63) Fu, Y.; Yang, H.; Gao, Y.; Huang, L.; Berger, R.; Liu, J.; Lu, H.; Cheng, Z.; Du, S.; Gao, H.; Feng, X. On-Surface Synthesis of NBN-Doped Zigzag-Edged Graphene Nanoribbons. *Angew. Chem.* **2020**, *132*, 8958–8964. https://doi.org/10.1002/ange.202000488.

64) Jacobse, P. H.; Jin, Z.; Jiang, J.; Peurifoy, S.; Yue, Z.; Wang, Z.; Rizzo, D. J.; Louie, S. G.; Nuckolls, C.; Crommie, M. F. Pseudo-Atomic Orbital Behavior in Graphene Nanoribbons with Four-Membered Rings. *Sci. Adv.* **2021**, *7*, eabl5892. https://doi.org/10.1126/sciadv.abl5892.

65) Tran, B. V.; Pham, T. A.; Grunst, M.; Kivala, M.; Stöhr, M. Surface-Confined [2 + 2] Cycloaddition towards One-Dimensional Polymers Featuring Cyclobutadiene Units. *Nanoscale* **2017**, *9*, 18305–18310. https://doi.org/10.1039/C7NR06187K.

66) Xu, X.; Di Giovannantonio, M.; Urgel, J. I.; Pignedoli, C. A.; Ruffieux, P.; Müllen, K.; Fasel, R.; Narita, A. On-Surface Activation of Benzylic C-H Bonds for the Synthesis of Pentagon-Fused Graphene Nanoribbons. *Nano Res.* **2021**, *14*, 4754–4759. https://doi.org/10.1007/s12274-021-3419-2.

67) Huang, J.; Pan, Y.; Wang, T.; Cui, S.; Feng, L.; Han, D.; Zhang, W.; Zeng, Z.; Li, X.; Du, P.; Wu, X.; Zhu, J. Topology Selectivity in On-Surface Dehydrogenative Coupling Reaction: Dendritic Structure *versus* Porous Graphene Nanoribbon. *ACS Nano* **2021**, *15*, 4617–4626. https://doi.org/10.1021/acsnano.0c08920.

68) Qiu, Z.; Sun, Q.; Wang, S.; Barin, G. B.; Dumslaff, B.; Ruffieux, P.; Müllen, K.; Narita, A.; Fasel, R. Exploring Intramolecular Methyl–Methyl Coupling on a Metal Surface for Edge-Extended Graphene Nanoribbons. *Organic Materials* **2021**, *03*, 128–133. https://doi.org/10.1055/s-0041-1726295.

69) Kinikar, A.; Di Giovannantonio, M.; Urgel, J. I.; Eimre, K.; Qiu, Z.; Gu, Y.; Jin, E.; Narita, A.; Wang, X.-Y.; Müllen, K.; Ruffieux, P.; Pignedoli, C. A.; Fasel, R. On-Surface Polyarylene Synthesis by Cycloaromatization of Isopropyl Substituents. *Nat. Synth* **2022**, *1*, 289–296. https://doi.org/10.1038/s44160-022-00032-5.

70) Zhang, Y.; Lu, J.; Li, Y.; Li, B.; Ruan, Z.; Zhang, H.; Hao, Z.; Sun, S.; Xiong, W.; Gao, L.; Chen, L.; Cai, J. On-Surface Synthesis of a Nitrogen-Doped Graphene Nanoribbon with Multiple Substitutional Sites. *Angew Chem Int Ed* **2022**, *61*, e202204736. https://doi.org/10.1002/anie.202204736.

71) Ajayakumar, M. R.; Di Giovannantonio, M.; Pignedoli, C. A.; Yang, L.; Ruffieux, P.; Ma, J.; Fasel, R.; Feng, X. On-surface Synthesis of Porous Graphene Nanoribbons Containing Nonplanar [14]Annulene Pores. *Journal of Polymer Science* **2022**, *60*, 1912–1917. https://doi.org/10.1002/pol.20220003.

72) Lackinger, M. Surface-Assisted Ullmann Coupling. *Chem. Commun.* **2017**, *53*, 7872–7885. https://doi.org/10.1039/C7CC03402D.

73) Kraus, S.; Herman, A.; Huttmann, F.; Krämer, C.; Amsharov, K.; Tsukamoto, S.; Wende, H.; Atodiresei, N.; Michely, T. Selecting the Reaction Path in On-Surface Synthesis through the Electron Chemical Potential in Graphene. *J. Am. Chem. Soc.* **2022**, *144*, 11003–11009. https://doi.org/10.1021/jacs.2c04359.

74) Treier, M.; Pignedoli, C. A.; Laino, T.; Rieger, R.; Müllen, K.; Passerone, D.; Fasel, R. Surface-Assisted Cyclodehydrogenation Provides a Synthetic Route towards Easily Processable and Chemically Tailored Nanographenes. *Nature Chem* **2011**, *3*, 61–67. https://doi.org/10.1038/nchem.891.

75) Cirera, B.; Giménez-Agulló, N.; Björk, J.; Martínez-Peña, F.; Martin-Jimenez, A.; Rodriguez-Fernandez, J.; Pizarro, A. M.; Otero, R.; Gallego, J. M.; Ballester, P.; Galan-Mascaros, J. R.; Ecija, D. Thermal Selectivity of Intermolecular versus Intramolecular Reactions on Surfaces. *Nat Commun* **2016**, *7*, 11002. https://doi.org/10.1038/ncomms11002.

76) Liu, M.; Liu, M.; She, L.; Zha, Z.; Pan, J.; Li, S.; Li, T.; He, Y.; Cai, Z.; Wang, J.; Zheng, Y.; Qiu, X.; Zhong, D. Graphene-like Nanoribbons Periodically Embedded with Four- and Eight-Membered Rings. *Nat Commun* **2017**, *8*, 14924. https://doi.org/10.1038/ncomms14924.

77) J. Liu, X. Feng, K. Mullen, J. R. Sanchez-Valencia, O. Groning, P. Ruffieux, R. Fasel, On-surface synthesis and characterization of acene-based nanoribbons incorporating four-membered rings. *Chem. A Eur. J.* **2019**. 25, 12074–12082. https://doi.org/10.1002/chem.201901410

78) R. Zhang, B. Xia, H. Xu, N. Lin, Kinetically controlled synthesis of four- and six-member cyclic products via sequential aryl-aryl coupling on a Au(111) surface. *ChemPhysChem.* **2019**, 20, 2292–2296. https://doi.org/10.1002/cphc.201900256

79) Li, D.-Y.; Qiu, X.; Li, S.-W.; Ren, Y.-T.; Zhu, Y.-C.; Shu, C.-H.; Hou, X.-Y.; Liu, M.; Shi, X.-Q.; Qiu, X.; Liu, P.-N. Ladder Phenylenes Synthesized on Au(111) Surface via Selective [2+2] Cycloaddition. *J. Am. Chem. Soc.* **2021**, *143*, 12955–12960. https://doi.org/10.1021/jacs.1c05586.

80) Gao, H.-Y.; Franke, J.-H.; Wagner, H.; Zhong, D.; Held, P.-A.; Studer, A.; Fuchs, H. Effect of Metal Surfaces in On-Surface Glaser Coupling. *J. Phys. Chem. C* , **2013**, *117*, 18595–18602. https://doi.org/10.1021/jp406858p.

81) Sindhu, K. S.; Anilkumar, G. Recent Advances and Applications of Glaser Coupling Employing Greener Protocols. *RSC Adv.* **2014**, *4*, 27867–27887. https://doi.org/10.1039/C4RA02416H.

82) Lawrence, J.; Mohammed, M. S. G.; Rey, D.; Aguilar-Galindo, F.; Berdonces-Layunta, A.; Peña, D.; de Oteyza, D. G. Reassessing Alkyne Coupling Reactions While Studying the Electronic Properties of Diverse Pyrene Linkages at Surfaces. *ACS Nano* **2021**, *15*, 4937–4946. https://doi.org/10.1021/acsnano.0c09756.

83) Kanuru, V. K.; Kyriakou, G.; Beaumont, S. K.; Papageorgiou, A. C.; Watson, D. J.; Lambert, R. M. Sonogashira Coupling on an Extended Gold Surface in Vacuo: Reaction of Phenylacetylene with Iodobenzene on Au(111). *J. Am. Chem. Soc.* **2010**, *132*, 8081–8086. https://doi.org/10.1021/ja1011542.

84) Sun, Q.; Cai, L.; Ma, H.; Yuan, C.; Xu, W. Dehalogenative Homocoupling of Terminal Alkynyl Bromides on Au(111): Incorporation of Acetylenic Scaffolding into Surface Nanostructures. *ACS Nano* **2016**, *10*, 7023–7030. https://doi.org/10.1021/acsnano.6b03048.

85) Liu, J.; Ruffieux, P.; Feng, X.; Müllen, K.; Fasel, R. Cyclotrimerization of Arylalkynes on Au(111) . *Chem. Commun.* **2014**, *50*, 11200–11203. https://doi.org/10.1039/C4CC02859G.

86) Díaz Arado, O.; Mönig, H.; Wagner, H.; Franke, J.-H.; Langewisch, G.; Held, P. A.; Studer, A.; Fuchs, H. On-Surface Azide–Alkyne Cycloaddition on Au(111). *ACS Nano* **2013**, *7*, 8509–8515. https://doi.org/10.1021/nn4022789.

87) Sun, Q.; Zhang, C.; Li, Z.; Kong, H.; Tan, Q.; Hu, A.; Xu, W. On-Surface Formation of One-Dimensional Polyphenylene through Bergman Cyclization. *J. Am. Chem. Soc.* **2013**, *135*, 8448–8451. https://doi.org/10.1021/ja404039t.

CHAPTER 2. SEQUENTIAL DOUBLE HOPF CYCLIZATION OF TETRAPHENYL

TRANS-3-HEXENE-1,5-DIYNE ON GOLD(111)

2.1. Background

The previous Chapter of this thesis introduced and described the purpose of graphene nanoribbons in the field of electronic materials. To contribute to state-of-the-art research in this field, enhancements to the already existing reaction toolkit should be considered. Thus, to expand on the available reactions for graphene nanoribbon synthesis, molecules with reactive moieties should be explored as potential precursors. To date, numerous reactions exist,[1] however they are limited by requirement of high temperatures and propensity to produce side reactions. Chapter 2 discusses the investigation of tetraphenyl *trans*-3-hexene-1,5-diyne (TPE) as a potential precursor molecule. TPD was synthesized and reacted under ultra-high vacuum (UHV) on Au(111) through thermal activation. It was found that this molecule undergoes two subsequent Hopf cyclizations as expected thanks to the conjugated enediyne backbone.

To date, numerous organic on-surface reactions have been demonstrated. Dehalogenative cross-linking reactions include Ullman-like coupling,[2,3] coupling of alkyl,[4] alkenyl,[5] alkynyl bromides,[6] while other cross-linking reactions have been achieved through alkene dimerization,[7] direct C-H activation,[8,9] and condensation,[10,11,12] and no dehydrogenative coupling.[13] Furthermore, numerous cyclization reactions have been demonstrated. Examples include intermolecular dehydrogenative cyclization (300 – 400 °C),[14] 2+2 cycloaddition (270 °C),[15] cycloaromatization of isopropyl groups (200 °C),[16] methyl-methyl coupling (350 °C),[17] and methyl-aryl (350 °C) oxidative ring closure.[18,19,20] Although these organic reactions are effective, alkynyl derivatives should offer a more robust reactivity on-surface and would avoid the need to cleave aryl C–X bonds. Alkyne coupling chemistry is commonly used in Glaser couplings[21],

click-chemistry[22], Sonogashira reactions[23], cyclotrimerizations[24], and Bergman cyclizations.[25] Furthermore, some enediynes are capable of cyclizing under two competing mechanisms in solution, i.e., between carbons C1-C5 or C1-C6 (Bergman). The Bergman cyclization has been previously reported on Au(111).[26] The authors reported that the C1-C5 mechanism is suppressed while C1-C6 takes place to form a highly strained bicyclic olefin.

To further understand on-surface chemistry and ultimately fabricate libraries of graphene-based molecules based on acetylenic precursors, low-barrier (<200 °C) intramolecular cyclization reactions that afford further annulated products should be developed. In this context, alkyne transformations have been explored experimentally in solution, gas, or solid-state could be potentially valuable.

Herein we report the first example of a Hopf cyclization on a metal surface as a model for the conversion of a dienyne into the corresponding nanographene segment (Figures 11 and 13). Tetraphenyl *trans*-3-hexene-1,5-diyne (TPE, **2c**) was synthesized and deposited on Au(111). Scanning tunnelling microscopy (STM) and non-contact atomic force microscopy (nc-AFM) revealed unexpectedly efficient conversion. This study was complemented by density functional theory (DFT) and cyclization barrier calculations to analyze the mechanism of this reaction.

Two sequential Hopf cyclizations of tetraphenyl *trans*-3-hexene-1,5-diyne are observed, with the first entirely completed at ~150 °C, and the second nearly entirely at ~190 °C. We demonstrate by DFT and charge distribution calculations that a gold-alkyne interaction stabilizes intermediates in the Hopf reaction, significantly lowering the reaction barrier for both cyclizations. We also conclude that the second cyclization has to be induced at higher temperatures due to a necessary break in aromaticity within the first cyclized ring.

2.1.1. The Hopf Cyclization

A reaction of particular interest is the Hopf cyclization. First discovered over half a century ago, this reaction achieves the thermal cycloaromatization of *cis*-hexa-1,3-dien-5-ynes to produce benzene in the gas phase transforms hexa-1,3-dien-5-yne to benzene through two consecutive 1,2-hydrogen shifts (Figure 11).[27] Unlike the Bergman cyclization, the Hopf mechanism does not require an external hydrogen source and takes place intramolecularly. Although the Hopf cyclization was discovered about a half century ago, this reaction has not been extensively used because of the high barrier of this reaction (>45 kcal/mol) and corresponding high temperatures (>300 ˚C) required for solution synthesis.
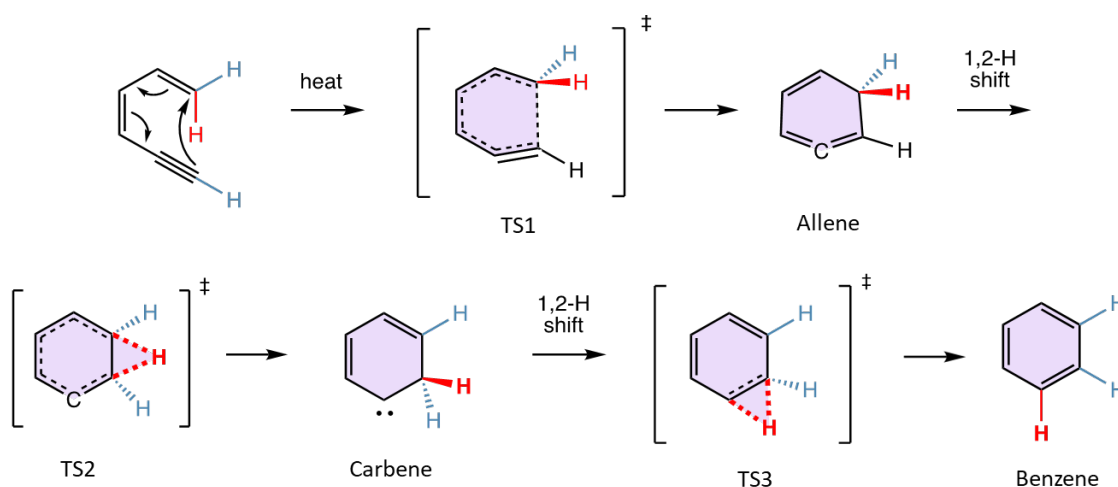
Figure 11. Mechanistic Hopf cyclization of *cis*-hexa-1,3-dien-5-yne to afford benzene. Left-to-right: Starting compound, transition state TS1, allene, first 1,2-hydrogen shift (top left to right); transition state TS2, carbene, second 1,2-hydrogen shift, transition state TS3, benzene.

Figure 11 details the mechanism of the Hopf cyclization, which proceeds through two intermediates and three transition states as postulated and calculated by Hopf *et al.*[28,29] The first step involves an intramolecular 6π-electrocyclization. This is completed by the alkyne triple bond forming a cyclic resonance structure with the two adjacent double bonds in the first

transition state (TS1). From here, a highly strained allene intermediate is formed, in which the internal alkyne carbon becomes flanked by two double bonds. Subsequently, a 1,2-hydrogen shift takes place, where the hydrogen highlighted in red moves towards the newly formed bond, passing through the second transition state (TS2). This then forms a carbene intermediate, in which the internal alkyne carbon obtains a lone pair. After this, a second 1,2-hydrogen takes place, during which the same hydrogen highlighted in red moves towards the carbene carbon. This structure then constitutes the third and final transition state (TS3). Benzene is then formed as the final compound, thus completing the Hopf cyclization.

The Hopf cyclization has been exploited in solid-state GNR synthesis. The Rubin group had hypothesized that the transformation of poly(diphenyl butadiynes) to graphene nanoribbons could take place via a series of Hopf cyclizations in the solid state (Fig. 12).[30,31,32] Although this process would require high temperatures, this pathway serves as a scaffold for different methods of induced Hopf cyclizations. As a result, it was of interest to study similar molecular precursors on noble metal surfaces to clearly substantiate that hypothesis. In addition, when compared to reactions in the gas phase or in solution, surface confinement can provide catalytic and charging effects, thus modifying the reaction mechanism and barriers.[33,34,35]

The conversion of poly(diphenyl butadiynes) to graphene nanoribbons is done in the crystal state.[36,37,38] This reaction uses photochemical activation and produces a deep blue polymer, i.e., a polydiacetylene (PDA) derivative. The second step of this procedure involves heating the produced PDAs to form a fully annulated system of GNRs with precise structure. This second step involves an initial Hopf cyclization step where the enediyne backbone cyclizes via two subsequent 1,2-hydrogen shifts. Progression of this reaction was followed by solid-state nuclear magnetic resonance spectroscopy (ss-NMR) and Raman spectroscopy. The right side of Figure

12 shows the functional groups present at each temperature point. The data shows that the initial disappearance of alkyne absorptions and the broadening of sp^2-carbon absorptions. Further heating above 500 ˚C results in the carbonyl and alkyl functional groups being replaced by hydrogen atoms.
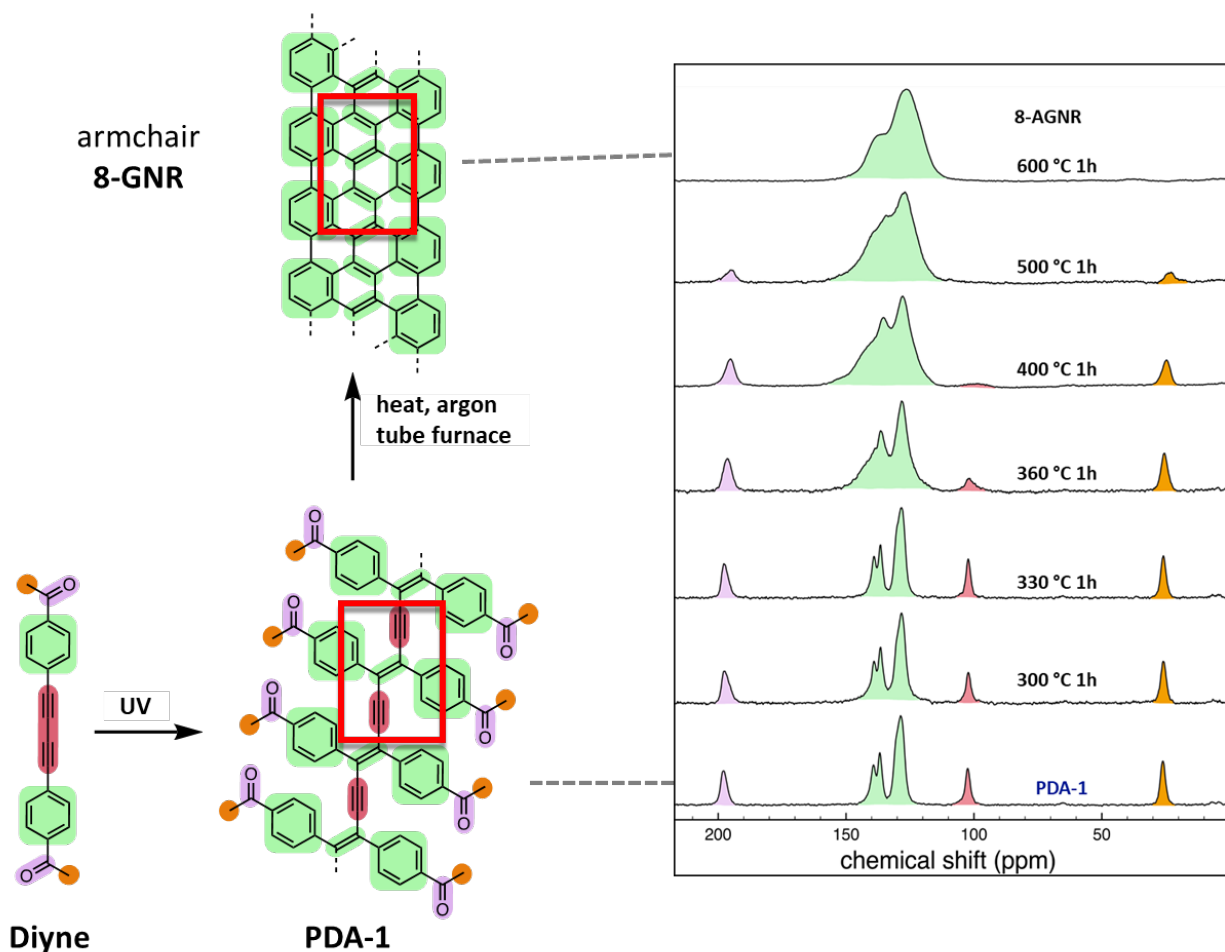
Figure 12. Solid-state conversion of poly(diacetylenes) (PDAs) to graphene nanoribbons. Poly(diphenyl butadiynes) (bottom left) convert into polydiacetylenes (bottom middle) under ultraviolet light; armchair-8-GNR (top left) is obtained via heating in an argon tube furnace; ^{13}C solid-state NMR with cross polarization and magic angle spinning at different heating temperatures (300-600 °C), with color coded functional group shifts (right); aryl functional groups (green); alkyne functional groups (red); carbonyl functional groups (purple); alkyl functional groups (orange).

2.1.2. Proposed Synthesis of the Model Precursor

These results obtained in the bulk confirmed the desired production of graphene nanoribbons through subsequent cyclization steps. They revealed that these designed precursors can effectively produce GNRs with precise width and edge structures. However, it was not clear to what extent this reaction proceeds in the solid, i.e., how effective it is at preventing the presence of defects and partially closed rings. The CP-MAS ^{13}C solid-state NMR spectra of armchair-8-GNR are broad, due to the tendency of all GNRs to strongly aggregate in the solid, and thus cannot confirm unequivocal full conversion. Hence, it was necessary to demonstrate that the Hopf cyclization is effective on a model system.

To closely study and demonstrate the mechanistic progression of this system, a precursor monomer that closely mimics portions of the polymer was devised. Thus, a precursor monomer that incorporates the *trans*-3-hexene-1,5-diyne portion of our PDAs was prepared. It should undergo two Hopf cyclizations to afford a chrysene unit. Studying this system through a method that allows for precise and accurate visualization was critical. Thus, we decided to study this molecule's ability to react on gold surfaces and use scanning tunneling microscopy, non-contact atomic force microscopy, and density functional theory to analyze the results.

The diphenyl *trans*-3-hexene-1,5-diyne model compound DPE, first synthesized by Matthews *et al.*, was a possible target (Fig. 13a). This compound should undergo the same Hopf cyclization to obtain a fully annulated polyaromatic hydrocarbon, chrysene.[39] To synthesize DPE, (triisopropylsilyl)acetylene was deprotonated using *n*-butyllithium (Fig. 14). The corresponding acetylide was then reacted with benzaldehyde to form the corresponding propargyl alcohol. From here, subsequent conversion of the propargylic alcohol function to its bromide was followed by a deprotonation-nucleophilic dimerization step to obtain the final

compound equipped with the TIPS-stabilizing protecting groups. These silyl groups can then be removed via a final deprotection step before evaporation on gold(111). However, all attempts to synthesize this first compound were unsuccessful. Furthermore, terminal alkynes would likely undergo side-reactions on gold(111), such as Glaser coupling.[40,41] Thus, it was decided that an analogous, more stable molecule should be designed. This molecule should have non-terminal alkyne moieties. A simple solution would be to use additional phenyl groups instead of TIPS.

.
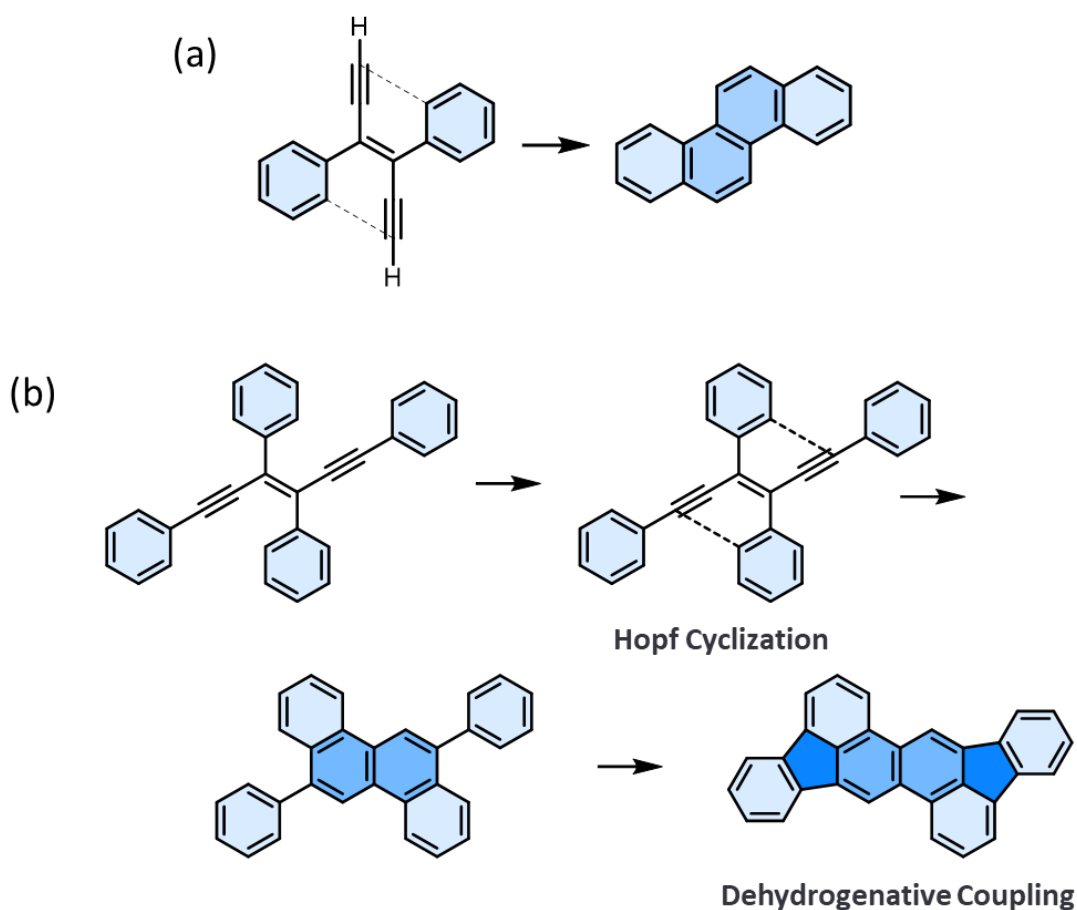
Figure 13. Proposed on-surface cyclization of *trans*-diphenyl 3-hexene-1,5-diyne (DPE) and tetraphenyl *trans*-3-hexene-1,5-diyne (TPE). Both DPE (a) and TPE (b) can undergo Hopf cyclization (cyan blue), while TPE (b) can undergo an additional dehydrogenative coupling step (dark blue).

Tetraphenyl *trans*-3-hexene-1,5-diyne (TPE) should undergo two Hopf cyclization sequences after deposition on gold(111) (Fig. 13b). The initial Hopf cyclization steps between the alkynyl and phenyl groups should take place upon heating, forming a chrysene backbone. From here, further heating could induce a cyclodehydrogenative step, which would result in further ring fusions by forming 5-membered rings.

TPE has been previously synthesized using several methods. Work by Bharathi and co-workers in 1999 showed that TPE can synthesized via reductive coupling of aromatic propargyl ketones using low valent titanium species (McMurry coupling).[42] In that study, TPE was obtained in 43% yield by treating 1,3-diphenylprop-2-yn-1-one with titanium tetrachloride (TiCl$_4$) and triethylamine (Et$_3$N). In 2001, Kamigata and co-workers reported the synthesis of TPE through a thermal reaction of a selenium substituted allene.[43] Here, a *p*-xylene solution of 1,3-bis(methylseleno)allene was refluxed for three days to produce TPE in 34% yield, as well as its *cis* isomer in 7% yield. Later, Tomás and co-workers in 2005 showed that TPE could be synthesized via a tungsten-carbene complex.[44] A tungsten phenyl(methoxy)carbene complex was treated with 1) lithium phenylacetylide in THF, 2) trimethylsilyl triflate (TMSOTf), and 3) pyridine to afford TPE in 45% yield. In 2006, Bharathi and co-workers again showed that TPE could be synthesized with the same reagent system as they reported before, but instead used the aromatic propargyl alcohol, 1,3-diphenyl-2-propyn-1-ol.[45] Here, TPE was synthesized in 68%.

2.2. Methods

TPE was synthesized according to the coupling procedure described by Matthews and co-workers.[39]

2.2.1. Synthesis of tetraphenyl *trans*-3-hexene-1,5-diyne (TPE) 2c.

Synthesis of **TPE (2c)** was achieved over three steps (Figure 14). Firstly, phenylacetylene was deprotonated using *n*-butyllithium. The formed acetylide anion was added to benzaldehyde in one pot. Critical aspects of this reaction were temperature and dryness. The entire reaction did not proceed when deprotonation of the terminal alkyne was done at room temperature. Overall, propargyl alcohol **2a** was produced in 70% yield.
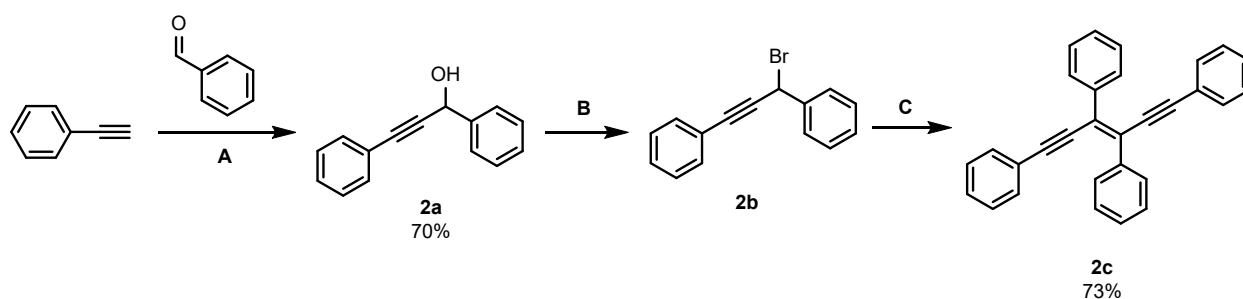
Figure 14. Synthetic scheme for tetraphenyl *trans*-3-hexene-1,5-diyne (TPE). (A) 1) *n*-BuLi, THF 0 °C, 30 min, 2) Benzaldehyde, 2 h (2a, 70%); (B) PBr₃, Et₂O, 0 °C, 30 min, (2b, not isolated); 3) LiHMDS, HMPA, THF, -90 °C to RT, (2c, 73%).

From here, the propargyl bromide **2b** was obtained. It should be noted that this compound was never isolated. Any purification attempts on different chromatographic supports resulted in decomposition of this highly sensitive propargylic halide, likely due to the easy formation of a stabilized cation. Following the workup step, the crude propargyl bromide was left to dry under vacuum overnight.

Figure 15. Crystal structure of tetraphenyl *trans*-3-hexene-1,5-diyne (TPE). (a) TPE; (b) white crystals obtained by slow evaporation of chloroform; (c) Representation of the crystal structure using Cambridge Crystallographic Database software called Mercury.

For the next step, the crude material was dissolved into dry THF under argon. In a separate flask cooled to 0 °C, THF, lithium bis(trimethylsilyl)amide (LiHMDS), and hexamethylphosphoramide (HMPA) were added under argon. The crude material flask was cooled to –90 °C using a bath of hexanes slurry prepared by cooling with liquid nitrogen. In this step, it was crucial to keep the crude material stirring vigorously. If the stirring bar was too slow, it was likely to cause any undissolved material to precipitate out and freeze on the sides of the flask. To prevent this, a larger stirring bar was used. Additionally, the freezing point of THF is –108 °C, so proper care was taken to maintain the bath at a temperature which would not cause the THF to freeze. This was done by using a thermometer submerged in the bath. After the work-up step, the final compound, tetraphenyl *trans*-3-hexene-1,5-diyne (TPE) **2c,** was obtained in 73% yield after purification on silica gel. Additionally, it was found that this compound could be precipitated out of chloroform by the addition of hexanes. By dissolving in chloroform and slowly evaporating the solvent, pure crystals were obtained that were suitable for single-crystal X-ray diffraction. Figure 15 shows a comparison of chemical structure, the habit of the pure crystals, and the single crystal structure.

2.3. Results and Discussion

2.3.1. Deposition and Reactivity of TPE

Tetraphenyl *trans*-3-hexene-1,5-diyne **2c** was deposited on Au(111) under ultrahigh vacuum (UHV) conditions. This was done by subliming **2c** into the gas phase, and then cooling to a certain temperature to subsequently anneal the molecules to the gold surface. Figure 16 shows scanning tunnelling microscope (STM) images obtained at different annealing temperatures.

STM is a type of microscopy method used for imaging surfaces at the atomic level. It can be used to distinguish features to approximately 0.1 nm and can resolve height differences of 0.01 nm (depth resolution). STM works by scanning a metal tip over the surface. This tip uses an applied electrical voltage (V, described in the top right corner, first number) and is brought very close to the surface. This causes electrons to tunnel, which is a quantum mechanical phenomenon that occurs when the tip is brought close to the surface. Here, the wavelike properties of electrons cause them to "tunnel" through the solid regions of the surface. The variance in tunneling current, which is measured by feedback loop, allows us to scan the surface to angstrom-level definition. The feedback loop maintains a current setpoint, allowing for the generation of a 3D image of the electronic topography. The tunneling current (top right, right number) measures the density of electrons at the surface of the sample. Therefore, the density maxima, or areas with lower electron density (empty orbitals), appear as brighter spots in the image. From here, we can clearly deduce any resulting reactions from changes in the images obtained.

Fig. 16a shows **2c** after being epitaxially deposited on Au(111) surface at room temperature (RT) in an ultra-high vacuum chamber with a base pressure of 1×10^{-10} mbar. The as-grown sample surface is shown, where most molecules are isolated and show a preference for residing

in between the herringbone stripes of Au(111). All the molecules are seen in the *trans*-configuration, indicating that their original configuration is retained, as expected.
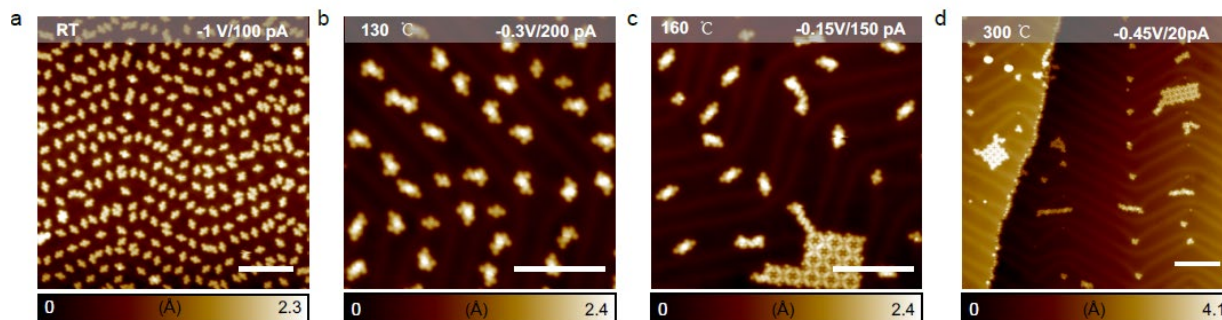
Figure 16. STM topographic images of the on-surface evolution of tetraphenyl *trans*-3-hexene-1,5-diyne (TPE, 2c) with stepwise annealing. The white scale bars indicate a length of 10 nm. Top right data indicate bias voltage and current. The scale bar at the bottom depicts height. (a) room temperature (RT) with intact molecules; (b) After heating to 130 °C, single Hopf cyclization has occurred; (c) After heating to 160 °C, single and double Hopf cyclizations have occurred; (d) 300 °C, all starting enediyne molecules have fully cyclized.

After depositing **2c** on Au(111) held at 130 °C (Fig. 16b), molecules appear to no longer lie across the herringbone pattern. A change in the brightness of the image can be observed, indicating that a conversion has taken place. Some self-assembled islands are observed as well. After depositing **2c** on Au(111) held at 160 °C (Fig. 16c), another change in molecular structure can be observed from some of the molecules, together with a large self-assembly island appearing at the bottom of the figure. After depositing **2c** on to Au(111) held at 300 °C (Fig. 16d), a lesser number of molecules are observed; thus, heating at this higher temperature provides enough energy for a good number of molecules to be desorbed from the surface.

Figure 17 (top) shows the STM images of different individually observed electronic structures at the 500 pm scale (i.e., changes from enediyne **2c**). These images are overlayed with

57
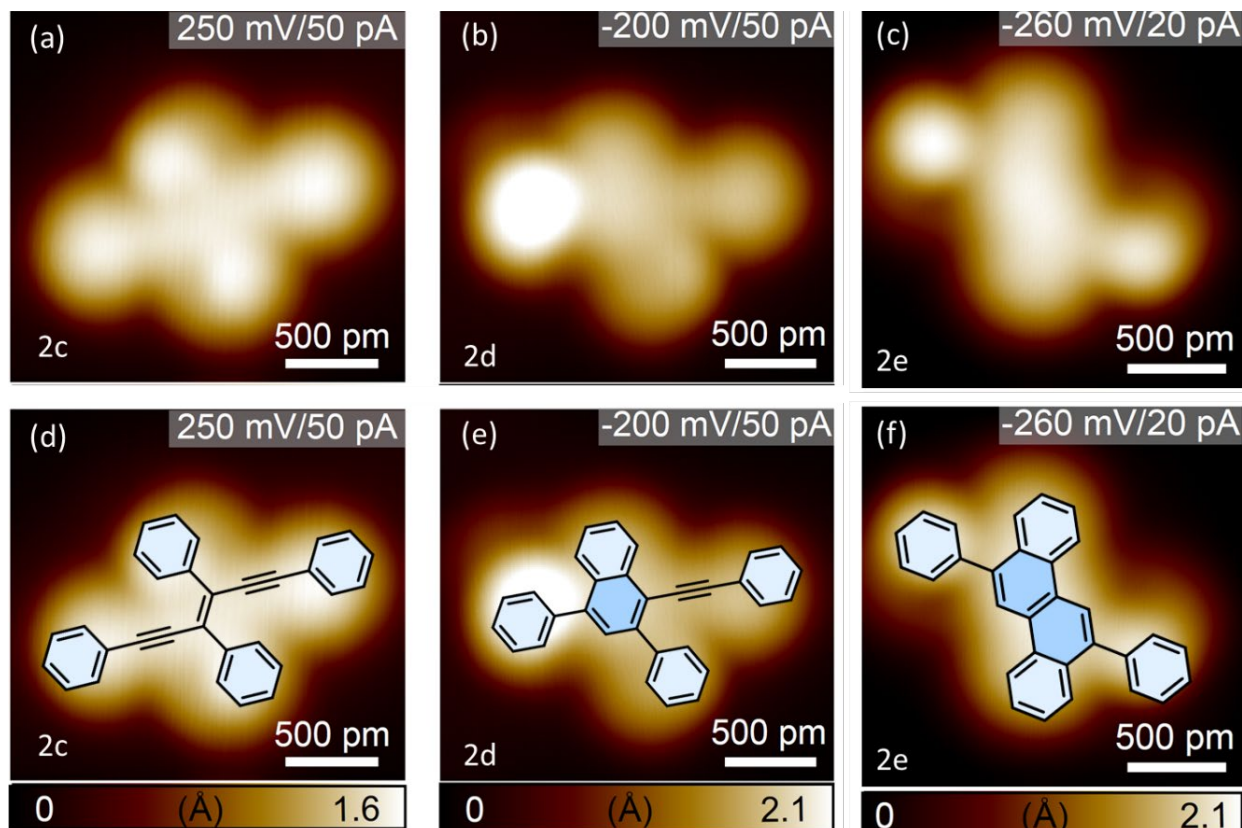
Figure 17. STM images of individual TPE (2c), mono-cyclized TPE (2d), and doubly cyclized TPE (2c) molecules. White scale bar is 500 pm. Top right is bias voltage and current. Bottom bar depicts relative height. STM image and overlay of topographical structure: TPE, 2c (a and d); mono-cyclized TPE, 2d (b and e); doubly cyclized TPE, 2e (c and f).

the predicted resultant structures from the Hopf-cyclization (Fig. 17 bottom). Figure 17 (a and d) clearly depict the intact enediyne structure of the precursor molecule **2c**. This can be determined by the symmetry of the bright protrusions and the spatial arrangement of all the indicated phenyl groups. This structure appears throughout in Fig. 16a (heating at room temperature). Fig. 17 (b and e) show a change in the equivalent brightness of the phenyl groups as well as a change in the spatial arrangement. Here a brighter protrusion is seen on the left side of the molecule. This would mean that the phenyl group now appears closer to the tip or further away from the gold surface. This structure is presumed to be **2d**, formed after a single Hopf cyclization. This means that the phenyl ring in the 4' position of the formed naphthyl ring ("para" to the alkyne) rotates

out of planarity to avoid steric hindrance of the newly formed ring. This formation can be observed in Fig. 16b after heating at 130 °C.

The two panels in Fig. 17c and f show that the symmetry of the molecule has again changed. Now the phenyl rings on the left and right sides appear slightly brighter in comparison to the top and bottom. This structure corresponds to a molecule after two Hopf cyclizations.

2.3.2. Temperature Controlled Sequential Hopf Cyclizations
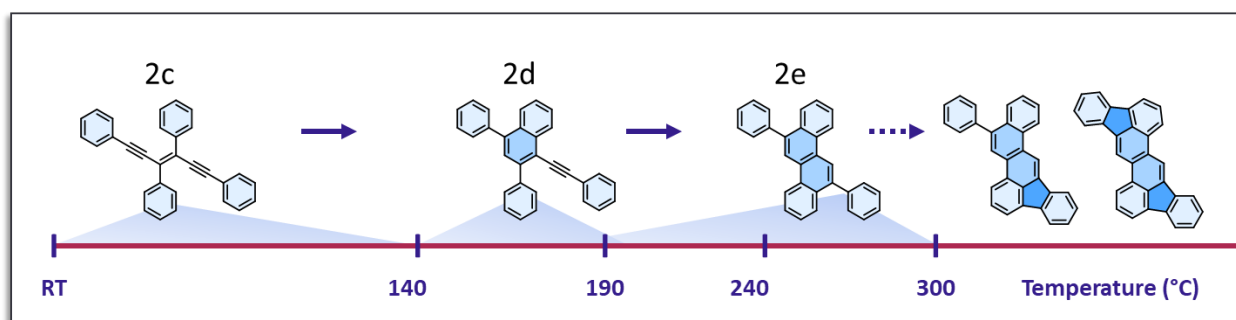
Figure 18. Transformation of tetraphenyl *trans*-3-hexene-1,5-diyne (TPE, 2c) through thermodynamically activated stepwise cyclization. TPE (2c) observed between room temperature (RT) and 140 °C; half-cyclized TPE (2d) observed between 140 °C and 190 °C; fully cyclized TPE (2e) observed between 190 °C and 300 °C; further cyclizations observed past 300 °C (rightmost structure).

Figure 18 shows the reaction progression as heating takes places. The bottom of the figure shows nc-AFM images obtained from each temperature interval above. Heating of the tetraphenyl *trans*-3-hexene-1,5-diyne **3c** on surface reveals that the Hopf cyclization does in fact occur on Au(111). Interestingly, the two Hopf cyclizations occur at different temperatures, where a majority of the molecules having undergone a single Hopf cyclization can be observed between 140 – 190 °C. Further heating between 190 – 300 ˚C causes these molecules to undergo a second Hopf cyclization, forming annulated chrysene molecules with two phenyl substituents. Further

heating to 300 ˚C results in some molecules undergoing a cyclodehydrogenation step. However, the high temperature involved made nc-AFM imaging difficult.

2.3.3. Distribution of TPE at Increasing Temperatures
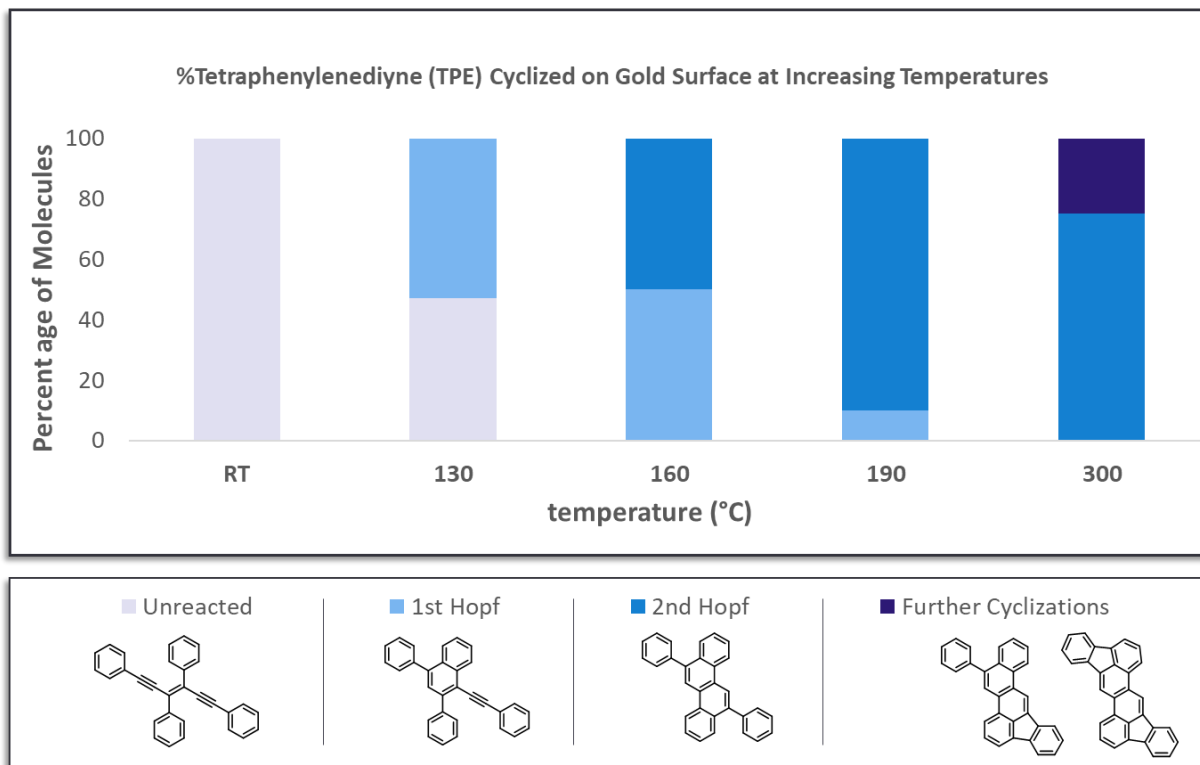
Figure 19. Statistical ratio of product formed on Au(111). All molecules after room temperature (RT) annealing are intact, 100% TPE, 2c (light purple); annealing to 130 °C, 45% TPE, 55% 2d (light blue); annealing to 160 °C, 50% 2d, 50% 2e (blue); annealing to 190 °C, 10% 2d, 90% 2e; annealing to 300 °C, 78% 2e, 22% cyclodehydrogenation product.

Figure 19 shows an estimation of the reacted products at interval temperatures. This is done by counting the number of molecules that match the corresponding DFT calculated structure. At room temperature 100% of the molecules are unreacted. At 130 °C about 45% of the molecules have reacted to produce the first Hopf cyclization product depicted in the key of Figure 19. When the temperature was increased to 160 °C, all molecules had undergone at least one Hopf

cyclization. At least 50% of the molecules at this point had undergone two cyclizations. When the temperature was increased to 190 °C, a majority of TEP molecules were observed to have undergone the second Hopf cyclization, with about 10% of the single cyclized Hopf product remaining intact. Further heating to 300 °C resulted in cyclizations between the phenyl rings. This cyclodehydrogenative step is typical with most graphene nanoribbon syntheses on surface. Some molecules were observed to have undergone either one or two more cyclization to form five-membered rings. At this point, further heating resulted in difficulty of characterization.

2.3.4. Experimental Results and Complementary Calculations and Simulations

To further verify that these were in fact the resultant structures of the Hopf cyclization, analogous DFT calculations along with non-contact atomic force microscopy (nc-AFM) and simulated AFM were completed.

nc-AFM is similar to STM in that it is a type of scanning microscopy method. In AFM, a probe is used to physically touch the sample to measure the features along the surface. The cantilever beam taps the surface of a substrate and can contain different molecular tips (in this case C=O). A laser then detects any movement of the cantilever. A feedback loop in this system and generates a high-resolution topographic map. Intermolecular attraction between the tip and the surface causes the cantilever to move closer towards the surface.

In nc-AFM, the tip never touches the surface of the material. Instead, the tip vibrates at the resonance frequency of the sample. This achieves control of the tip-to-sample distance and allows for precise measurement of fluctuations. AFM does not require a conductive sample and shows molecular resolution, while STM shows the electronic structure.
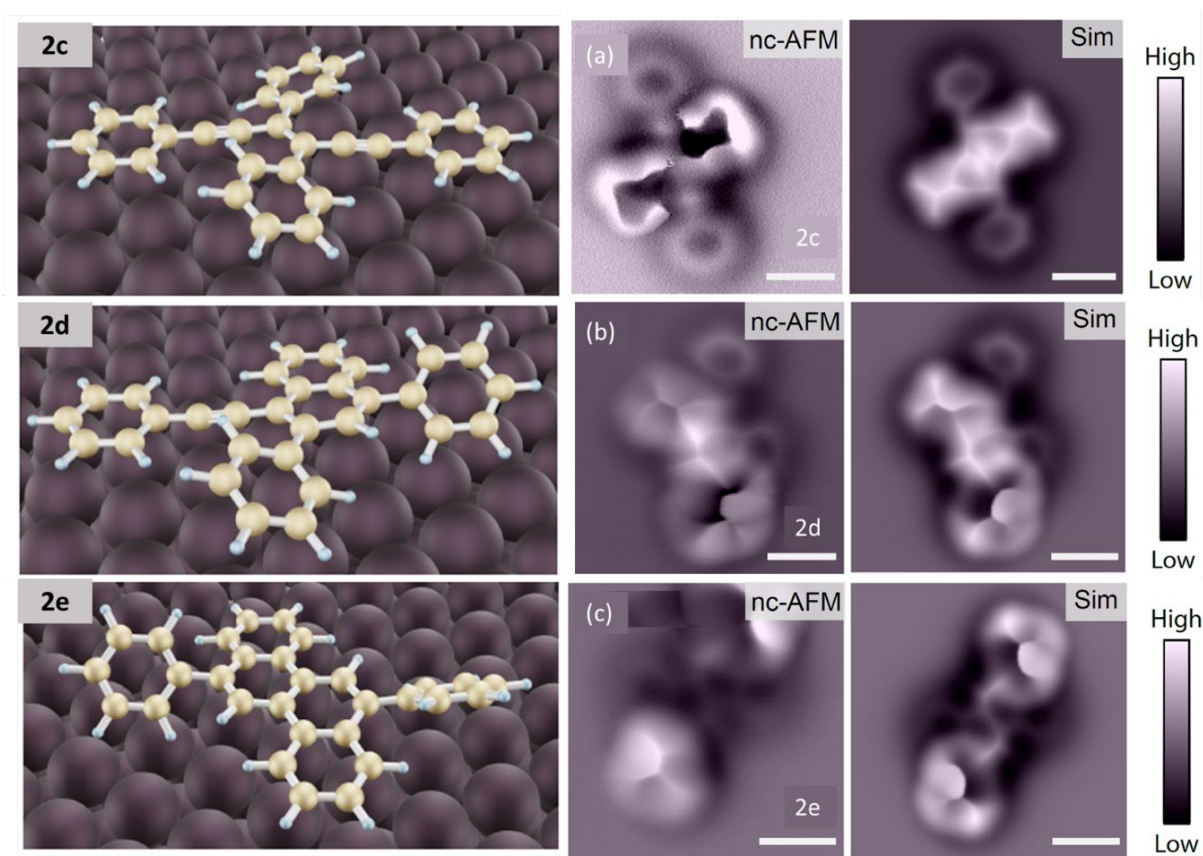
Figure 20. Relaxed geometries of 2c, 2d, and 2e on Au(111) substrate and corresponding non-contact atomic force microscopy (nc-AFM) and simulated AFM images. White scale bars indicate 1 nm, uncyclized TPE (2c), nc-AFM image and simulated on right, geometry shows rings are more planar (a); first cyclization product (2d), nc-AFM and simulated image on the right, phenyl ring on right up from cyclized ring (b); second cyclization product (2e), nc-AFM and simulated image on right (inverse structure to a and b), phenyl ring on left flips opposite to the phenyl ring on the right (c).

To understand the reaction route, systematic density functional theory (DFT) calculations were performed based on the structures observed in experiments. Fig. 20 depicts the relaxed geometries of **2c**, **2d**, and **2e** on Au(111) substrate (left) and the corresponding non-contact atomic force microscopy (nc-AFM) and simulated SFM images (right). A 4-layer Au supercell with a size of 38.3 × 32.4 ˚A2 (768 gold atoms) is constructed to mimic the surface environment (see Methods for details) and all the reactions are considered on this slab. We first confirmed the

feasibility of our model by reproducing the adsorptional configurations of experimentally observed structures **2c**, **2d**, and **2e**. Starting from **2c**, its constrained optimized geometry on Au(111) is shown in Fig. 20 (left), where the phenyl groups on the top and bottom are nearly planar while phenyl groups on the right and left are tilted out-of-plane. The simulated AFM image using the relaxed geometry is compared with the experimental observed nc-AFM image of **2c** (Fig. 20a), showing good consistency with each other. The minor difference is that the experimental image fails to simultaneously and clearly characterize the main chain and the tilting side phenyl groups, but a series of nc-AFM images with different tip-molecule distances in the experiment overcome this difficulty. Similarly, both singly cyclized species **2d** and fully cyclized species **2e** are also reproduced by on-surface geometrical relaxation, confirmed by the consistency between simulated and experimental observed AFM images (Fig. 20 b and c). Ultimately these results show that, in order for the molecule to form the cyclized structures, the phenyl rings on the side must flip accordingly.

Overall, these results show a few important observations: First, the Hopf cyclization on both sides of the molecule can be obtained at temperatures below 200 °C, which is at least 150 ˚C below what the Rubin group have observed for the conversion of PDAs incorporating enediyne moieties in the solid state.[31,37] Even more importantly, the first Hopf cyclization starts to take place at temperatures as low as 130 °C. This is surprising, because previous work had shown this cyclization to take place at temperatures nearly double of that observed on-surface. Secondly, the second Hopf cyclization requires higher temperatures to occur. It could be expected that both sides of the molecule would undergo both Hopf cyclization at similar temperatures based on the structure of the starting material, however the results show this differently. While most of the molecules complete one cyclization at lower temperatures, an increase in temperature is required

to induce the second cyclization. The reasons for this are discussed in the next section, where DFT calculations were carried out to determine the origins of this bias.

2.3.5. Calculations on the Sequential Hopf Cyclization

First Hopf Cyclization
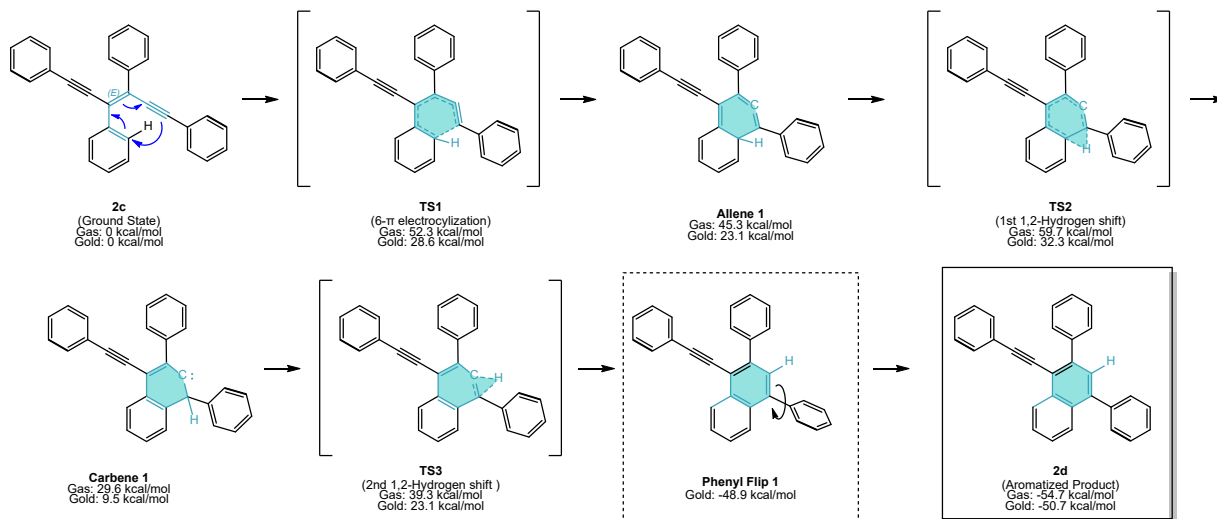
Figure 21. Comparison of the DFT calculated ground state and transition state energies for the first Hopf cyclization in the gas phase (B3LYP-D3/6-31G(d), with single-point energies at the M06-2X/6-311+G(d,p) level) and on gold(111). TPE, 2c (ground state), Gas: 0, Gold: 0; TS1 (6-π electrocyclization), Gas: 52.3 Gold: 28.6; Allene 1 Intermediate, Gas: 45.3, Gold: 23.1; TS2 (1st 1,2-Hydrogen shift), Gas: 59.7, Gold 32.2; Carbene 1 Intermediate, Gas: 29.6, Gold: 9.5; TS3 (2nd 1,2-Hydrogen shift), Gas: 39.3, Gold: 23.1; Phenyl Flip 1 (only occurs on-surface), Gold: -48.9; Half-cyclized, 2d (aromatized product), Gas: -54.7, Gold: -50.7.

Based on STM images and complementary DFT calculations, the entire mechanism from **2c** to **2d**, then to **2e**, is detailed in Figures 21 and 22. Figure 21 shows the first Hopf cyclization and conversion steps to the mono-cyclized product. Compound **2c** (TPE, tetraphenyl *trans*-3-hexene-1,5-diyne) is the ground state of this mechanism with a relative energy level of 0 kcal/mol. From here, a 6π-electrocyclization first takes place, during which transition state 1 (TS1) is involved. Gas phase DFT calculations of TS1 show that it has a barrier of 52.3 kcal/mol, while on-gold surface calculations show a value of only 28.6 kcal/mol. This shows that the value for the first

transition state is almost halved in energy when on-surface in comparison to gold. Further discussion will detail precisely how the gold surface contributes to this. From here the first allene is formed. Gas phase calculations show a value of 45.3 kcal/mol, while on-surface calculations show 23.1 kcal/mol. The first 1,2-hydrogen shift takes place by going through the second transition state (TS2), and again, the on-surface calculations show that the value is almost half of that of the gas phase calculation (gas: 59.7 kcal/mol *vs*. gold: 32.2 kcal/mol). After the transition to the neighboring phenyl ring, the first carbene is formed. The calculation reveal that on-gold has just a third of the value of that of the gas phase calculation, thus significantly less than in the previous structures (gas: 29.6 kcal/mol *vs*. gold: 9.5 kcal/mol). From here, the second 1,2-hydrogen shift takes place, and again, the results show that the on-surface value is nearly half that of the gas phase calculations (gas: 39.3 kcal/mol; gold: 23.1 kcal/mol).

One thing to note from here, is that the mechanisms do not necessarily follow the same route. In the free-gas calculations, molecules can freely rotate in order to form the lowest energy state. However, when on-surface, molecules are constricted to a 2-dimensional surface by relatively strong π-to-gold interactions. DFT calculations reveal that, in order to relax after the second hydrogen shift (Fig. 20), the phenyl ring (bottom right ring) must flip (dashed line box). Originally starting from **2c**, the bottom right phenyl ring remains tilted away from the top phenyl ring (bold line indicates bond furthest away from gold surface). After the phenyl flip, the bottom right ring now points towards the top phenyl ring. This is calculated to be relatively low in energy in comparison to other steps for the on-surface conversion (gold: -48.9 kcal/mol; difference: -72 kcal/mol). This phenyl flip then leads to the aromatized product with **2d**, having similar values to the gas phase calculation (gas: -54.7 kcal/mol, gold: -50.7 kcal/mol). This follows the same DFT model results that were depicted in Fig. 20.

Second Hopf Cyclization

2d
(Ground State)
Gas: 0 kcal/mol
Gold: 0 kcal/mol

TS4
(6-π electrocylization)
Gas: 60.0 kcal/mol
Gold: 29.9 kcal/mol

Allene 2
Gas: 56.3 kcal/mol
Gold: 27.6 kcal/mol

TS5
(1st 1,2-Hydrogen shift)
Gas: 64.2 kcal/mol
Gold: 35.7 kcal/mol

Carbene 2
Gas: 33.9 kcal/mol
Gold: 13.3 kcal/mol

TS6
(2nd 1,2-Hydrogen shift)
Gas: 39.3 kcal/mol
Gold: 27.6 kcal/mol

Phenyl Flip 2
Gold: -40.1 kcal/mol

2e
(Aromatized Product)
Gas: -45.9 kcal/mol
Gold: -44.3 kcal/mol

Figure 22. Comparison of the DFT calculated ground state and transition state energies for the second Hopf cyclization in the gas phase (B3LYP-D3/6-31G(d) with single-point energies at the M06-2X/6-311+G(d,p) level). Mono-cyclized 2d (GS), Gas: 0, Gold: 0; TS4 (6-π electrocylization), Gas: 60.0 Gold: 29.9; Allene 2 Intermediate, Gas: 56.3, Gold: 27.6; TS5 (1st 1,2-Hydrogen shift), Gas:64.2, Gold 35.7; Carbene 2 Intermediate, Gas: 33.9, Gold: 13.3; TS5 (2nd 1,2-Hydrogen shift), Gas: 39.3, Gold: 27.6; Phenyl Flip 2 (only occurs on-surface), Gold: -40.1; Fully-cyclized, 2e (aromatized product), Gas: -45.9, Gold: -44.3.

Fig. 22 shows the progression for the second Hopf cyclization, i.e., conversion to the fully-cyclized product from the half. Compound **2d** (tetraphenyl *trans*-3-hexene-1,5-diyne having undergone one Hopf cyclization) is the ground state of this mechanism with energy levels of 0 kcal/mol. From here, a second 6π-electrocylization takes place in which transition state 4 (TS4) is actually below the kinetic barrier for this reaction (see TS 5). Gas phase DFT calculations of TS4 show that it has energy value of 60.0 kcal/mol, while on-gold surface calculations show and energy value of 29.9 kcal/mol. This shows that the value for the fourth transition state is almost halved in energy when on-surface in comparison to gold. Again, further discussion below will detail precisely how the gold surface contributes to this. From here on, a second allene structure is formed. Gas phase calculations show a value of 56.3 kcal/mol while on-surface calculations

show 27.6 kcal/mol. The third 1,2-hydrogen shift takes place forming the fifth transition state (TS5), which is the rate-determining step. Again, on-surface calculations show that the value is almost half to that in the gas phase (gas: 64.2 kcal/mol; gold: 35.7 kcal/mol). After transfer to the neighboring phenyl ring, the second carbene is formed. Again, the calculations reveal that on-gold has just a third of the value as gas phase calculations, even more significant than previous structures discussed (gas: 33.9 kcal/mol; gold: 13.3 kcal/mol). From here, the last 1,2-hydrogen takes place. Again, to form transition state 6 (TS6), the results show that the on-surface value is nearly half that of the gas phase calculations (gas: 39.3 kcal/mol; gold: 27.6 kcal/mol).

Once more, this pathway requires a second phenyl flip to occur (dashed box). On-gold calculations show this to be -40.1 kcal/mol (difference: -67.7 kcal/mol). Finally, the aromatized product **2d** is formed. Calculations show that, in the gas phase, the value is -45.9 kcal/mol, while on-gold, it has a rather similar value of -44.3 kcal/mol.

Figure 23 shows plotted relative energies for the transition states and intermediates of the reaction mechanism. The top portions show the first Hopf cyclization while the bottom shows the second Hopf cyclization. Overall, a few things can be deduced from this overall comparison. Arrows B and D (on-gold) are about half the value of arrows A and C (free gas). These calculations show that gold does indeed help lower the barrier to cyclization. Furthermore, the second Hopf cyclization shows the same, where arrows F and H (on-gold) are about half the value of arrows (E and G). Once again this shows that the gold surface helps lower the barrier to cyclization. In addition to this, when comparing free gas calculation arrows, A (52.3 kcal/mol) and E (60.0 kcal/mol) to each other, E is slightly higher with a difference of about 8 kcal/mol. This definitively proves that the first cyclization (arrow A) requires less energy than the second cyclization (arrow B) for free gas calculations. Furthermore, when comparing arrows B (28.5
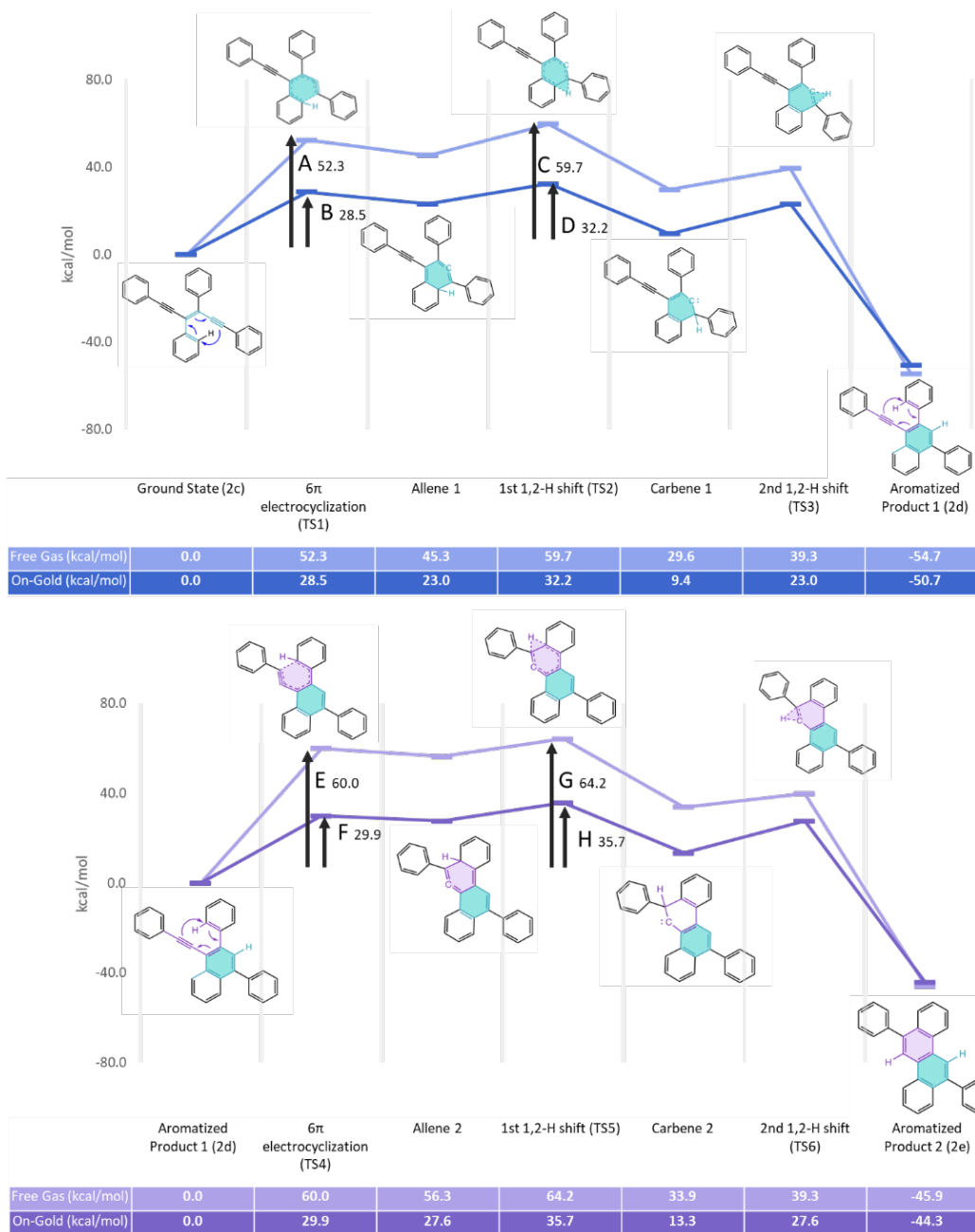
Figure 23. Plotted energies (kcal/mol) for the cyclizations of tetraphenyl *trans*-3-hexene-1,5-diyne (2c). Plotted energies for the cyclization of TPE (2c) in free gas state and on-gold surface. Arrows detail specific energy differences. (arrows A-D: First Hopf); (arrows E-H: Second Hopf); (A) Free gas energy for 6-π electrocyclization: 52.3 kcal/mol; (B) On-gold surface energy for 6-π electrocyclization: 28.5 kcal/mol; (C) Free gas energy for 1st 1,2-hydrogen shift: 59.7 kcal/mol; (D) On-gold surface energy for 2nd 1,2-hydrogen shift: 32.2 kcal/mol; (E) Free gas energy for 6-π electrocyclization: 60.0 kcal/mol; (F) On-gold surface energy for 6-π electrocyclization: 29.9 kcal/mol; (G) Free gas energy for 1st 1,2-hydrogen shift: 64.2 kcal/mol; (H) On-gold surface energy for 2nd 1,2-hydrogen shift: 35.7.

kcal/mol) and F (29.9 kcal/mol), F is higher with a difference of about 1.5 kcal/mol. Again, this proves that the second cyclization requires more energy to takes place. This further explains why the higher temperature is needed to make the second cyclization take place.

To accurately determine why these values differ, a close look at the exact mechanism of **2c** is required. In the first Hopf reaction, the phenyl ring on the bottom must break its aromaticity in order to induce the 6π-electrocyclization and cause the reaction to take place. While this is energetically costly, the second cyclization actually costs more energy. This is because, in order to induce the 6π-electrocyclization of the second Hopf reaction, the newly formed naphthalene ring must break its aromaticity in addition to that of the involved phenyl ring substituent. This is also apparent when comparing arrows C (59.7 kcal/mol) and G (64.2 kcal/mol) for TS2 and TS4 in free gas calculations. These values have a difference of about 4 kcal/mol, with TS4 requiring more energy. Additionally, arrows D (32.2 kcal/mol) and H (35.7 kcal/mol) for on-gold calculations have a difference of about 3 kcal/mol, with TS5 requiring more energy than TS2. Overall, the second cyclization requires more energy input, and therefore results in the second Hopf cyclization of **2c** requiring higher temperatures. Thus, **2c** can be converted into **2d** via the first Hopf cyclization, and **2d** can be converted to **2e** through the second and more energetically costly Hopf cyclization. This is apparent for both free-gas and on-gold calculation because all the steps of the second cyclization require slightly more energy than their analogous steps in the first cyclization. Furthermore, all on-gold calculations have lower relative values than for the on-surface calculations, meaning that the gold surface greatly enhances the cyclization of **2c** to **2d**, and of **2d** to **2e**.

2.3.6. Charge Analysis Between TPE and Gold Surface

From here, one important question remains for this system. Exactly, how does gold help in the double Hopf cyclizations of tetraphenyl *trans*-3-hexene-1,5-diyne (TPE, **2c**)? This is discussed in the next section.

Using **2c – 2e** as the cornerstones, we propose a novel mechanism for the double Hopf cyclization of **2c** on the gold(111) surface. Generally speaking, the full reaction can be rationalized by a sequence of three steps depicted in Figures 21 to 23: (i) triple bond breaking on one side and radical electrocyclization (**TS1** and **TS4**); (ii) aromatization by H-migration (**TS2, TS3, TS5, TS6**); (iii) flip of a phenyl group (**Phenyl Flip 1, Phenyl Flip 2**).

Thus, the triple bond on one side of **2c** tends to form two radical sites under thermal excitation, which are localized mainly at the C_1 and C_2 carbons. Both play different roles during the cyclization process (Fig. 24a). The radical at the C_1 site is eager to be passivated by cyclizing with C_{14}, while radical at C_2 site is readily passivated by the Au atom from the substrate. Based on the calculation, an energy barrier of 28.6 kcal/mol should be conquered for this step, and the resulted structure **TS1** is transient due to its higher energy. The observation of five-membered species, despite very rare, confirms this diradical cyclization path on-surface rather than the 6 π electrocyclization that occurs in the gas phase.

A 1,2-hydrogen migration (between carbons 14 and 2) is spontaneously triggered to stabilize the molecule, by which the energy of the system is drastically reduced. It should be noted that
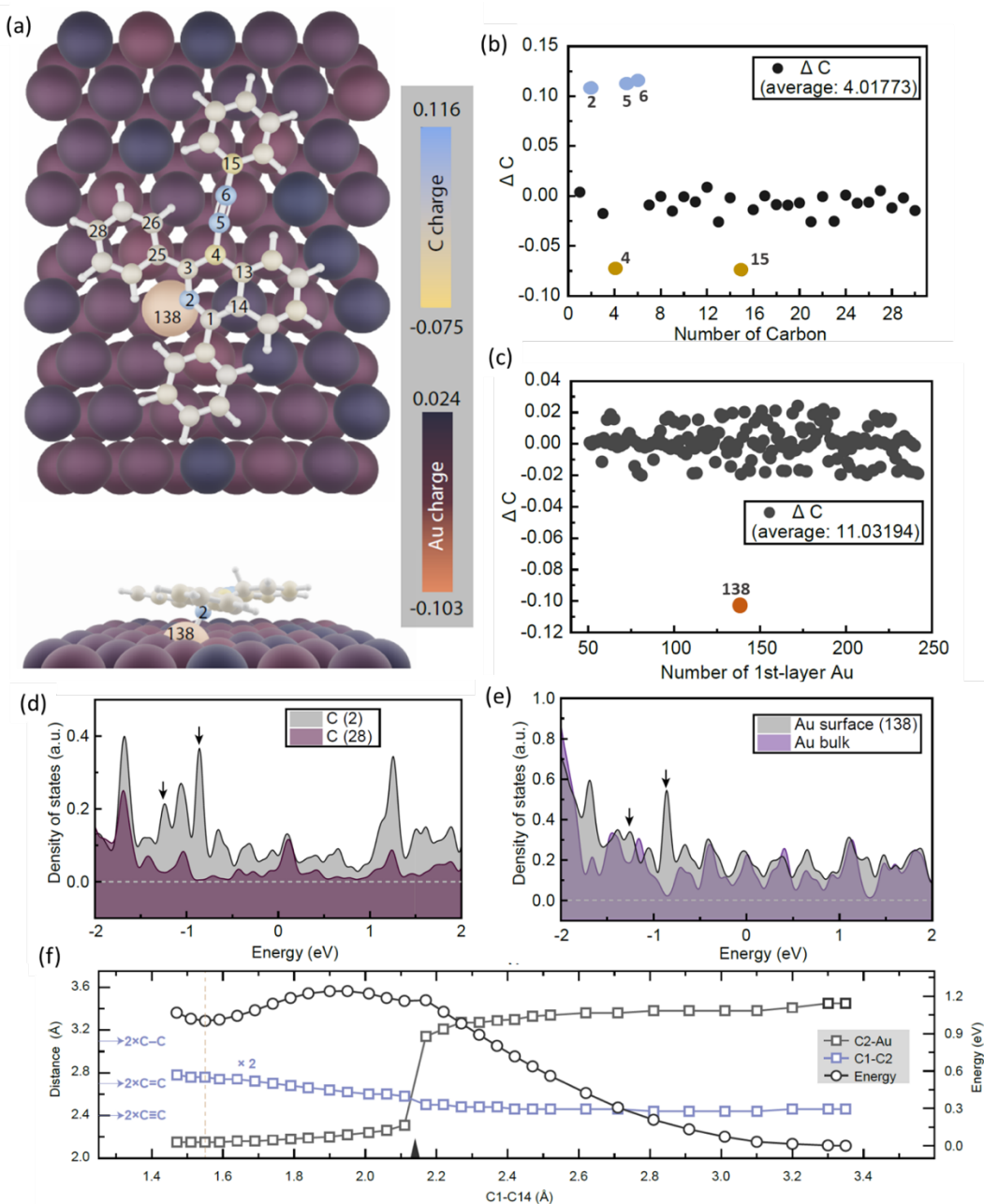
Figure 24. Electronic structure and charge analysis. Results calculated using DFT and Bader's theory. a) Spatially resolved charge values of both carbon (C) and gold (Au) atoms. Only partial gold atoms close to the TPE molecule are shown here. The numbers show the atomic order in the calculational model; b) charge values of all carbon atoms; d) charge values of all gold atoms in first layer of surface; d) calculated partial density of states (PDOS) for carbon atoms, arrows indicate new peaks, carbon atom 2 (grey), all 28 carbons (maroon); e) calculated PDOS for gold atoms, arrows indicate new peaks, gold surface atom 138 (grey), bulk gold surface (purple); comparison between C atoms bonded/non-bonded with Au substrate. F) variations of bond lengths (Å) for C2-gold(grey square) and C1-C2 (blue square) and energy (eV) of the whole system during the cyclization.

71

this hydrogen will transfer at C_1 during the migration, giving a two-step migration process. The relaxed structure after the H-migration is still different to that in the gas phase with the flipping of a phenyl group. This flip further lowers the energy of the molecule by 3.9 kcal/mol. Finally, the single-Hopf cyclization of **2c** to obtain **2d** is completed. Likewise, such a cyclization on the other side would occur by a slightly higher thermal excitation, corresponding to the higher energy barrier. The slightly enhanced energy barrier for the remaining side can be explained by its structural stretching and the enhanced tilting of the phenyl group after one-side cyclization. Specifically, the distance between C_6 and C_{26} is 3.40 Å in structure **2d**, larger than the 3.35 Å between C_1 and C_{14} in structure **2c**.

Figure 24 shows the geometry and charge analysis using DFT and Bader's Theory. Figure 24a shows the spatially resolved charge values of both the carbon and gold atoms. Bader theory uses zero flux, a 2-D surface on which the charge density is a minimum perpendicular to the surface. Calculating the charge enclosed within a Bader volume is a way to approximate the total electronic charge of an atom. The charge distribution (Figs. 24b,c) can be used to determine multipole moments, defining a charge transfer between atoms.[46,47,48] Note that the values for the charge transfer appear positive to denote the "acceptance" of electrons. The blue dots that appear higher on Fig. 24b signify carbons that contain more electrons than the average value for all carbons in the system (4.02). Additionally, Fig. 24c shows the average electron count for all gold atoms in the calculated system (11.0). This means that one gold atom (Au-138) becomes positively charged by stabilizing the reaction intermediate.

To get a clearer view of how the catalytic process is implemented, we analyzed the geometrical evolution by shortening the distance between C_1 and C_{14} (Fig. 24a) step by step, and then checked charge transfer between Au and C atoms after the radical cyclization. The

optimized structure at different steps implicates two crucial variations: 1) the lengthening of the C_1-C_2 bond length implies triple bond breaking, and the shortening of bond length between C_2-Au reflects the passivation of the radical at C_2. Both bond lengths exhibit an abrupt change at the same C_1-C_{14} distance (2.13 Å). The energy of the whole system is also calculated at each step and is shown by the black circles in Fig. 24f. The saddle point at the C_1-C_{14} distance (1.55 Å) implies an end to the electrocyclization, in which the C_1-C_2 bond length is enlarged to 1.38 Å, which is close to the default C=C bond length (1.34 Å). Additionally, the C_2-Au distance is decreased to 2.15 Å, although slightly larger than the Au-C bond length reported in previous literature,[30] suggesting an Au-C bond formation. Concomitantly, the original *sp*-hybridization between C_1 and C_2 deforms into a distorted sp^2-like hybridization.

Charge transfer between the substrate and the molecule is also estimated by calculating the charge value at each atom using Bader's theory (Fig. 24), which spatially visualizes charge deviations from the average value for C atoms and part of the first layer of Au atoms. Within the molecule, C_2, C_4, C_5, C_6, and C_{15} show obvious charge deviation from the average value, as shown in Fig. 24b. C_2 is negatively charged and is the site that gets potentially bonded to the Au substrate based on geometry. Aside from C_2, other carbon atoms are only involved by resonance within the molecule in relation to the remaining triple bond. Correspondingly, the Au atom adjacent to C_2 exhibits a complementary positive charge, resulting from the formation of the Au-C bond. The partial density of states (PDOSs) of individual atoms shown in Fig. 24d and 24e also give clear evidence for the Au-C bond formation between C_2 and Au_{138}, manifested by the emergence of new electronic states marked by black arrows. Based on the above analysis, we conclude that Au-C bonding and charge transfer are key to lowering the barrier of the Hopf cyclization on the Au(111) surface.

2.3.7. Self-Assembly of Cyclized Product
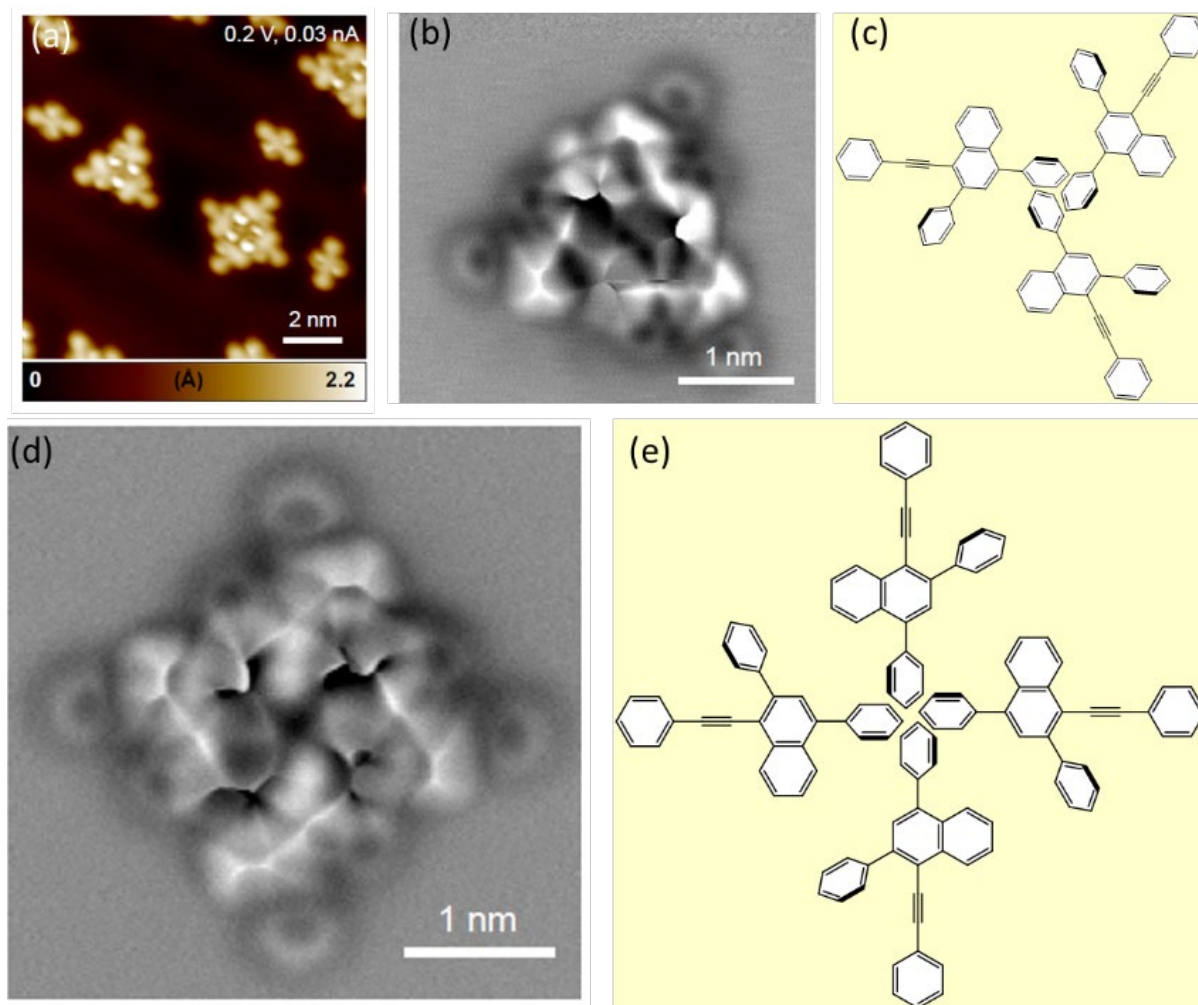
Figure 25. Self-assembled islands of mono-Hopf cyclized product 3d. (a) STM image of self-assembled structures observed after first Hopf cyclization, white scale bar (2 nm), cluster of three or four molecules observable; (b) nc-AFM image of self-assembly of three half-Hopf cyclized molecules; (c) schematic of self-assembly of three half-Hopf cyclized molecules; (d) nc-AFM image of four half-Hopf cyclized molecules; (e) schematic of self-assembly of four half-Hopf cyclized molecules.

In addition to the topics discussed earlier in this Chapter, the self-assembly of converted molecules is discussed here. This is an important topic in consideration of the formation of nano-objects when deposited on surface. Figs. 25 and 26 show different types of self-assembled

islands that occur after cyclization. After the first Hopf cyclization, Fig. 25 shows self-assembly of three and four molecules in separate, well-formed islands. Fig. 25a shows an STM image of the structures observed from one cyclization. In this image you can see triangular and square shaped structures. Fig. 25b and 25d show the nc-AFM image of a close-up view of each of these structures. Here, one can observe lighter regions that represent areas closer to the tip (further away from the surface). Fig. 25c shows the schematic assembly of three of the Half-cyclized products (**2d**). In this schematic, the bold lines point up or away from the gold surface. Through this positioning in the middle, three molecules are coming together.
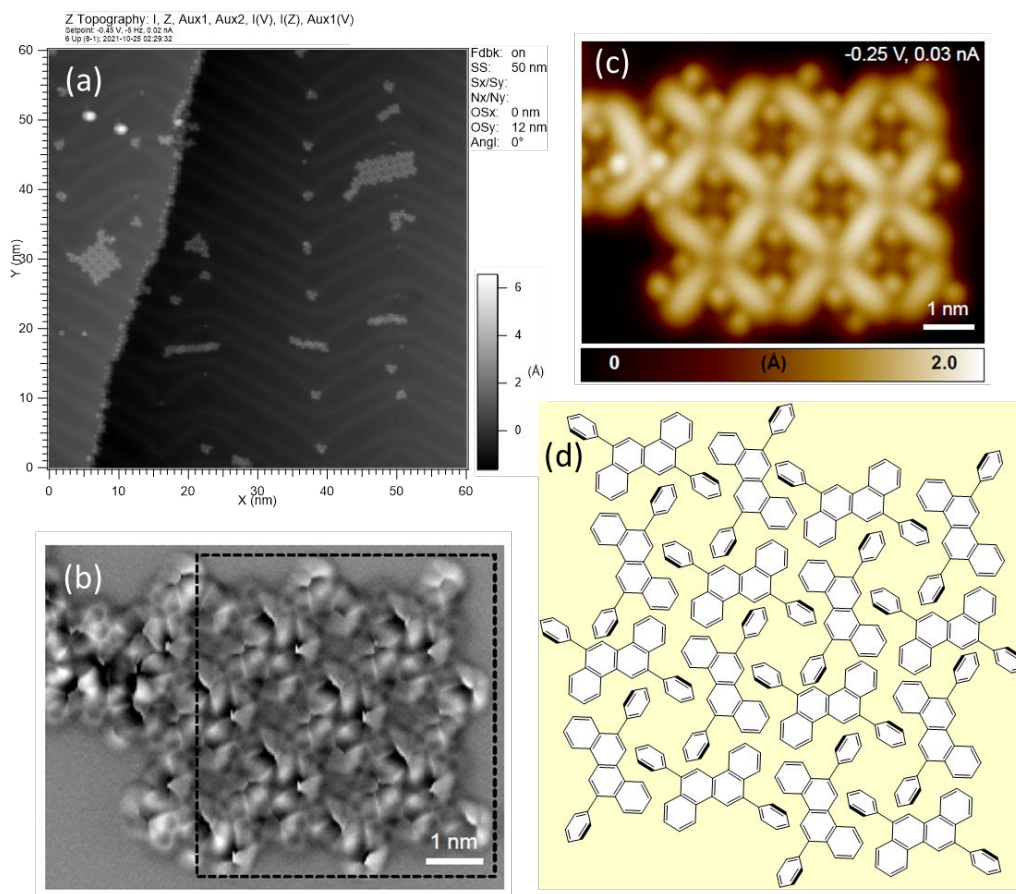
Figure 26. Self-assembly of molecules after second Hopf cyclization. (a) nc-AFM image of clusters from self-assembled molecules after second Hopf cyclization; (b) nc-AFM image of self-assembled structures, white scale bar (1 nm); (c) STM image of self-assembled structures, white scale bar (1 nm); (d) schematic view of self-assembled structures with defined rotation around phenyl groups.

In addition, Fig 26 shows the self-assembly of the doubly Hopf cyclized product (**2e**). When the molecules doubly cyclize, the phenyl rings at the ends are pointing diagonally. This causes them to interlock into the observed self-assembled structures. Fig. 26a shows the overall nc-AFM image of clusters that are observed. However, when heating to high-enough temperatures to cyclize at both ends of the molecule, only a few molecules remain on the surface. Fig. 25b shows a zoomed-in version of the nc-AFM image, in which a beautiful grid-like pattern is observed. Fig. 25c also shows an analogous STM image of the grid-like structure. Fig. 25d shows the schematic representation of how the fully cyclized molecules can assemble into a grid-like fashion.

2.3.8. Post Hopf Species
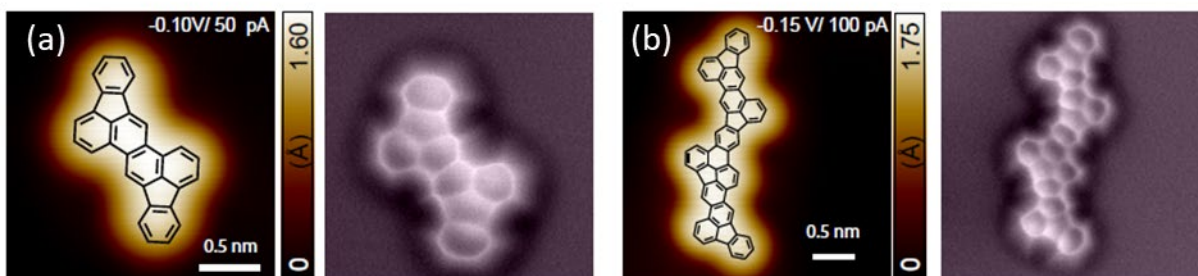
Figure 27. Cyclodehydrogenation products and oligomers formed from TPE. (a) STM image of cyclodehydrogenation product (left), white scale bar (0.5 nm), simulated AFM image of cyclodehydrogenation product (right); (b) STM image of oligomers formed from cyclodehydrogenation product (left), white scale bar (0.5 nm), simulated AFM image of oligomers formed from cyclodehydrogenation product (right).

In addition to the self-assembled structures observed, post-Hopf species that have undergone cyclodehydrogenation can be observed. These species are not detailed in the main discussion of this work because of the low occurrence of these conversions. Heating past 300 °C induces

formation of the cyclodehydrogenation product, but at this temperature, molecules begin to detach from the surface and evaporate into the ultra-high vacuum of the setup. Fig. 27a shows an STM image of the cyclodehydrogenation product and to the right of that is the analogous AFM image. Fig. 27b shows a dimer of the cyclodehydrogenation product that formed, and on the right is the analogous AFM image. This figure indicates that cyclodehydrogenation can take place between neighboring atoms, causing them to bond together through a six membered ring. Bottom right of the figures indicates the scale bar (0.5 nm). These results show that this method can be exploited to produce carbon structures with graphene nanoribbon morphology. The only issue to note is that molecules will detach from the surface at temperatures high enough for the cyclodehydrogenation to occur. To bypass this, polymers of tetraphenyl *trans*-3-hexene-1,5-diyne will be explored in the next Chapter.

2.3.9. Five-Membered Ring Formation of TPE

TPE molecules that have undergone a five-membered ring cyclization rather than an initial Hopf cyclization are also observed, through infrequently, These molecules make up a very small portion of the overall Hopf cyclized structures (~1%), but nevertheless they provide insight into why the Hopf cyclization to form a six-membered ring occurs on gold and why other pathways are less likely. Figure 28a shows the five-membered ring product. The blue and red lines indicate different up down positions (blue is pointing down towards the surface and red pointing up and away from the surface). The resultant positioning can be seen in Fig. 28b which shows the nc-AFM image and the analogous simulated image. Fig. 29 shows the energy diagram for a cyclization to form a six-membered ring versus the five-membered ring formation. In this mechanism, TPE **2c** is converted into 2f-IM1, which is stabilized by gold via a radical reaction.
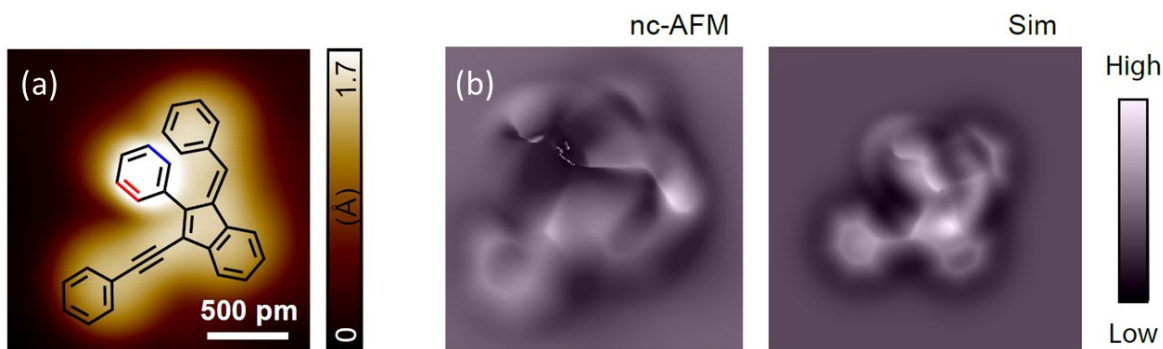
Figure 28. Five-membered ring formation of TPE. (a) STM image of five-membered ring product with phenyl ring rotated, down position close to gold surface (blue), up position away from gold surface (red), white scale bar (500 pm); (b) nc-AFM image of five-membered ring product (left), simulated AFM image of five-membered ring product (right).
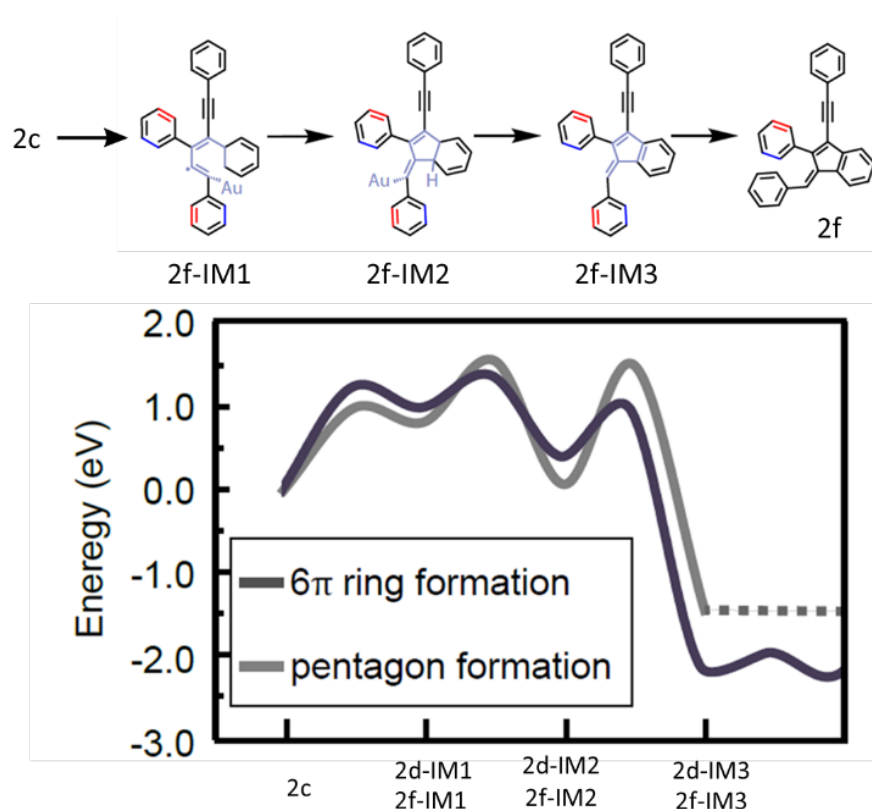
Figure 29. Energy diagram for the 6π-electrocyclization pathway vs. five-membered ring formation. *Trans*-tetraphenyl hexenediyne (2c) is converted to 5-membered ring product (2f) through 2f-IM1, 2f-IM2, and 2f-IM3, which details gold-stabilized intermediates, DFT calculated energy diagram for on-gold reactivity (bottom), comparison shows 5-membered ring formation is unfavorable due to higher energy requirement than 6-π electrocyclization.

reaction. In comparison to the first intermediate of the 6-π electrocyclization (2d-IM1), 2f-IM1 actually requires less energy to take place. However, 2f-IM2 and 2f-IM3, the second and third intermediates in this pathway, require more energy than the second and third intermediates for the 6-π electrocyclization (2d-IM2 and 2d-IM3). This therefore shows why the **2f** pathway is less favorable in comparison to the **2d** pathway. This pathway still points to the fact that gold helps stabilize the molecules for the reaction.

2.4. Conclusion

In conclusion, the results from this work highlight two important points: 1) Hopf cyclization occurs on gold surface at energies about half those required in the gas phase. This is the first ever observed occurrence of such a low temperature required for a Hopf cyclization without ring-strain designed into the dienyne system.[49] 2) Furthermore, a gold atom from the surface helps stabilize intermediates in the Hopf cyclization through charge transfer. Overall STM, nc-AFM, and simulated AFM images help define TPE **2c** on surface and its conversion to mono-cyclized (**2d**) or doubly cyclized (**2e**) products. DFT analysis and Bader theory calculations reveal the exact mechanism of the cyclization. Calculations show that a charge is transferred between the gold and alkyne carbon, causing the alkyne to become negatively charged in the intermediate structures. Calculations also reveal that the second Hopf cyclization (conversion from **2d** to **2e**) requires more energy, as it involves breaking the aromaticity of the newly formed naphthalene ring in addition to that of the phenyl substituent involved in the reaction.

Additionally, mon-cyclized molecules (**2d**) have been observed to self-assemble and cause the appearance of triangular and square shaped islands. Fully cyclized molecules (**2e**) have also

been observed to self-assemble into a square/grid-like fashion. Five-membered ring formation was also observed, however in low occurrence.

Overall, these results show that Hopf cyclizations are a potentially beneficial reaction to be utilized for on-surface aromatic molecule synthesis. Cyclization reactions are important to graphene nanoribbon synthesis, and only very few, such as cycloaromatization of isopropyl groups have been reported to occur at such low temperatures (130 °C).[50] Creating such specifically designed precursors incorporating (*E*)-hex-3-en-1,5-diyne moieties could provide access to unprecendented aromatic structurs and graphene nanoribbons at low temperatures. The next Chapter will discuss how polymers of this form can be generated

2.5. Experimental

Synthetic Preparation Techniques

Drying of Tetrahydrofuran (THF)

Commercial THF was dried according to the following. Molecular sieves were added to a round bottom flask. A septum was placed on top and parafilmed to prevent any leakages. The sieves were activated by heating to 180 °C in a round bottom flask under vacuum overnight. THF was then added to this flask and left to sit for three days. When dry THF was used in synthetic reactions, solvent was transferred under air free conditions.

Transferring of Solvent Under Air-Free Conditions

To transfer solvent without exposure to air, either a cannula transfer or a syringe was used. The flask containing the solvent was placed under positive pressure by adding a septum and needle connected to the in-hood argon line. When transferring using a syringe, adequate volume size, to not exceed more than 50% of the syringe volume was used. The syringe was also flushed by drawing argon through the flask into the needle and expelling it three times. When using a canula, the needle was connected to the first flask and the receiving flask. To start the desired flow of solvent, a venting needle or vacuum line needle was also connected to the receiving flask. In cases of small amounts of solvent, a venting needle was adequate. However, in cases of volume exceeding 50 mL, a vacuum line was used to generate a faster flow.

Running Reactions Under Air-Free Conditions

To prevent the interference of air in most reactions, unless explicitly noted, reactions were capped with a septum and a needle connected to continuous argon flow was connected. Argon was allowed to flow over the reaction at all times, thus preventing air from entering the reactions.

STM and nc-AFM measurements

STM and nc-AFM measurements were performed in a commercial low-temperature STM from Scienta Omicron operating at a temperature of 4.5 K and a base pressure below $2\rightarrow10^{-11}$ mbar. A gold(111) single-crystal surface was prepared by Ar-ion sputtering, followed by annealing at 430 ˚C. Molecule **2c** was deposited on the clean Au(111) surface via molecule beam epitaxy at 112 ˚C, with a rough rate of 0.45 Å /min. *In-situ* cold deposition of CO molecules was performed to get a CO-functionalized tip for nc-AFM.

Computational details

All DFT calculations for gold(111) surface reactions were performed using the AiiDAlab platform[51] based on the AiiDA infra-structure[52] and the CP2K code[53]. The surface–adsorbate systems were modelled in the repeated slab scheme. The simulation cell consisted of four atomic layers of gold along the [111] direction. A layer of hydrogen atoms was used to passivate one side of the slab to suppress the Au(111) surface state. A vacuum of 40 Å was included in the simulation cell to decouple the system from its periodic replicas in the direction perpendicular to the surface. The electronic states were expanded using a TZV2P Gaussian basis set[54] for carbon and hydrogen species and a DZVP basis set for gold species. A cutoff of 600 Ry was used for the plane-wave basis set. Norm-conserving Goedecker–Teter–Hutter pseudo-potentials[55] were used to represent the frozen core electrons of the atoms. We used the Perdew–Burke–Ernzerhof parameterization for the generalized gradient approximation of the exchange-correlation functional[56]. To account for van der Waals interactions, we used the D3 scheme proposed by Grimme57. The gold surface was modelled using a super-cell, with a size of 38.3 × 32.4 Å ^{2} (768 gold atoms). The Au(111) slab was planar, and the herringbone reconstruction associated with

this surface was not considered as it would greatly expand the supercell and not substantially change the chemical activity of the surface.[58] To obtain the equilibrium geometries, we kept the atomic positions of the bottom two layers of the slab fixed to the ideal bulk positions, and all other atoms were relaxed until forces were lower than 0.005 eV Å or nc-AFM simulations using AiiDAla. The equilibrium geometries and the electrostatic potential obtained using CP2K were used in combination with the probe particle code developed by Hapala.[59]

For the characterization of the reaction path of the cycloaromatization reaction, using advanced sampling methods such as meta-dynamics[60] would be computationally prohibitive due to the large number of atoms involved. Also relying on the nudged elastic band (NEB)[61] or string method[62] for such a long series of reaction steps would have a computational cost that we cannot afford. In order to nevertheless obtain a reasonable estimate of the reaction barriers, we used constrained geometry optimizations by defining a collective variable (length of a bond between two atoms or amplitude of a dihedral angle) for each step of the reaction pathway based on experimentally verified structures (**2c, 2d, 2e**), varied with a fine step size to sample the potential energy with adequate accuracy. Each intermediate geometry is optimized without constraints. The energy profile resulting from such a series of constrained geometry optimizations, where all atomic degrees of freedom are allowed to relax subject to the constraint of the collective variable, provides a reasonable estimate of the reaction barrier.

Synthetic Procedures for tetraphenyl *trans*-3-hexene-1,5-diyne 2c (TPE)

2a
70%

2b

2c
73%
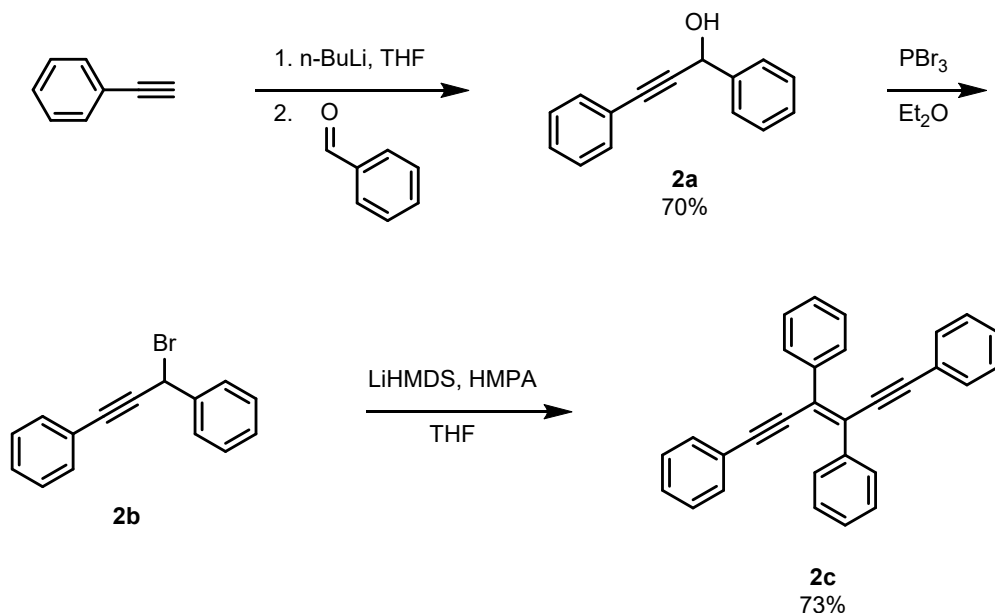
1,3-Diphenylprop-2-yn-1-ol (2a).[63]

Dry THF (15 mL) was added to a flame-dried 50 mL round bottom flask containing a magnetic stirring bar and placed under argon. Phenylacetylene (1.0 mL, 9.1 mmol, 1.0 eq) was added via syringe. The reaction was cooled to 0 ˚C to generate the lithium acetylide. A total of 6.7 mL (10.0 mmol, 1.1 eq) of 1.5 M *n*-BuLi was added dropwise via syringe. The bath was removed, allowing the reaction to warm up to room temperature. After 30 minutes, the reaction was cooled back down to –78 ˚C. Benzaldehyde (0.93 mL, 9.1 mmol, 1.0 eq) was added dropwise via syringe. Once added, the bath was removed, and the reaction was left stirring at RT for 2 hours. The reaction was quenched with saturated NH$_4$Cl (20 mL). The crude organic

product was extracted with EtOAc, washed with brine, dried with anh. MgSO$_4$, and then evaporated on the Rotavap. The residual oil was dried under vacuum overnight. The final product was purified as an oil via column chromatography (100% hexanes to 100% DCM; rf = 0.50, 100% DCM) to give 1.3 gram of pure 1,3-diphenylprop-2-yn-1-ol in 70% yield. ^{1}H NMR (500 MHz, CDCl$_3$) δ (ppm) 7.62 (d, J = 7.7 Hz, 2H), 7.49 – 7.46 (m, 2H), 7.41 (t, J = 7.4 Hz, 2H), 7.38 – 7.30 (m, 4H), 1.99 (bs, 1H). ^{13}C-NMR (500 MHz, CDCl$_3$) δ (ppm) 140.6, 131.7, 128.7 128.6, 128.4, 128.3, 126.7, 122.4, 88.7, 86.6, 65.1.
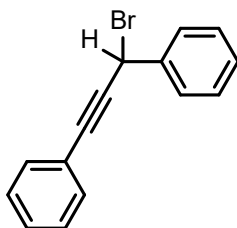
1,3-Diphenylprop-2-yn-1-bromide (2b)[64]

Dry Et$_2$O (150 mL) was added to a flame-dried 500 mL round bottom flask containing a magnetic stirring bar and **2a** (1.0 g, 4.8 mmol, 1 eq). The flask was cooled to 0 ˚C using an ice bath. PBr$_3$ (0.91 mL, 9.6 mmol, 2 eq) was added dropwise via syringe under argon and the reaction was stirred for 30 minutes. The reaction was quenched with sat. NaHCO$_3$, (30 mL). The crude organic product was extracted with Et$_2$O, washed with brine, the separated organic layer dried with anh. MgSO$_4$, and the residual oil dried overnight under high vacuum. Compound **2b** is unstable on silica gel. The crude material was carried onto the next step due to its extreme sensitivity.
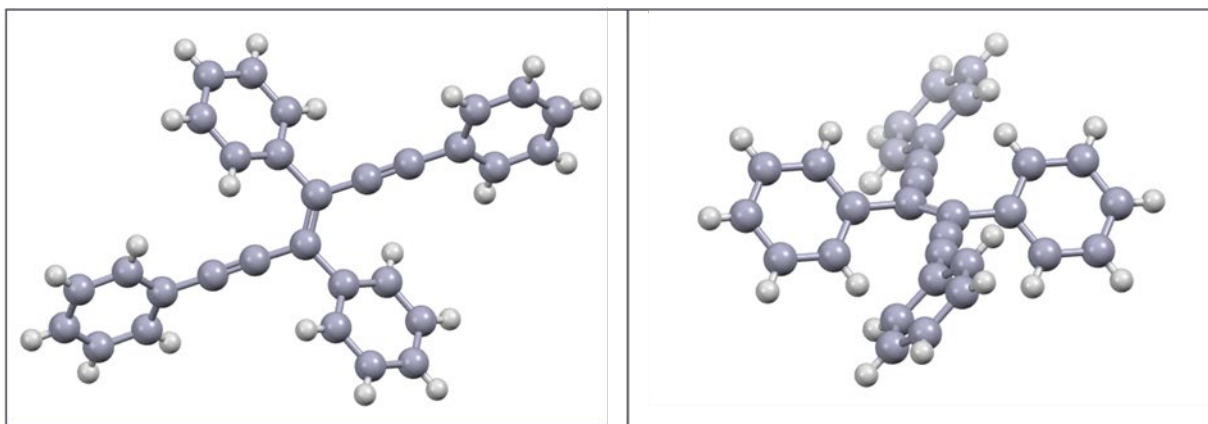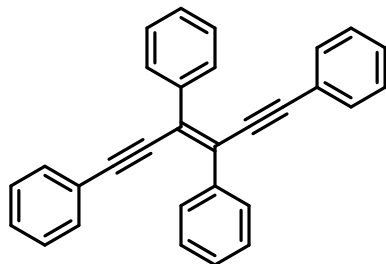
(*E*)-1,3,4,6-tetraphenyl-hex-3-en-1,5-diyne (2c) (TPE)

Dry THF (45 mL) and a magnetic stirring bar were added to the flask containing 1.3 gram of crude propargylic bromide (**2b**). Dry THF (20 mL) was added to a separate flame-dried 250 mL round bottom flask containing a magnetic stirring bar. The reaction was cooled to –10 ˚C and LiHMDS (0.8 mL, 4.1 mmol, 1.1 eq) and HMPA (0.7 mL, 4.1 mmol, 1.1 eq) were added via syringe. The reaction containing the starting material was cooled to –90 ˚C using a frozen hexanes slurry generated with liquid nitrogen. The LiHMDS and HMPA mixture was added dropwise over 30 minutes and the reaction was left to stir and warm to room temperature. The reaction was quenched with saturated NH4Cl (100 mL). The crude organic product was extracted with chloroform, washed with brine, and dried under vacuum. Pure iridescent white crystals of **2c** were isolated by slow evaporation from chloroform, 510 mg (73% yield). ^{1}H NMR (500 MHz, CDCl3): δ (ppm) 8.01 (d, *J* = 7.1 Hz, 4H), 7.49 (t, *J* = 7.5 Hz, 4H), 7.42 (t, *J* = 7.9 Hz,

2H), 7.38 (s, 2H), 7.34 – 7.28 (s, 10H). ^{13}C-NMR (500 MHz, CDCl$_3$): δ (ppm) 139.0, 131.4, 129.2, 128.6, 128.4, 128.3, 127.8, 123.3, 98.5, 90.9.

nc-AFM images of TPE with different tip-molecule distance
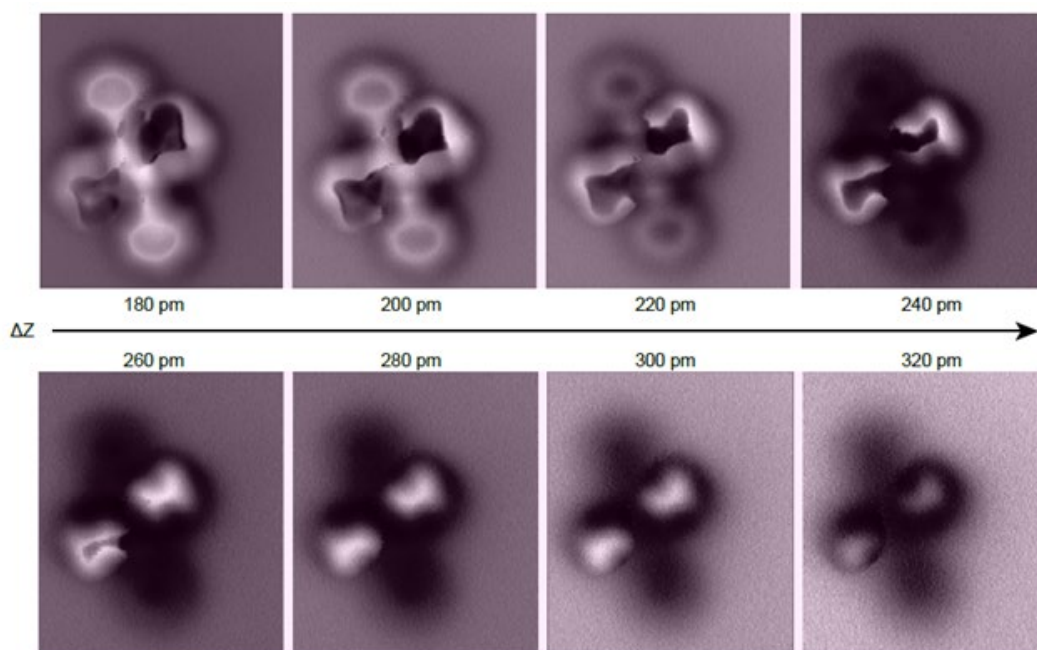
Comparison of the different phenyl rotamers after H-migration.
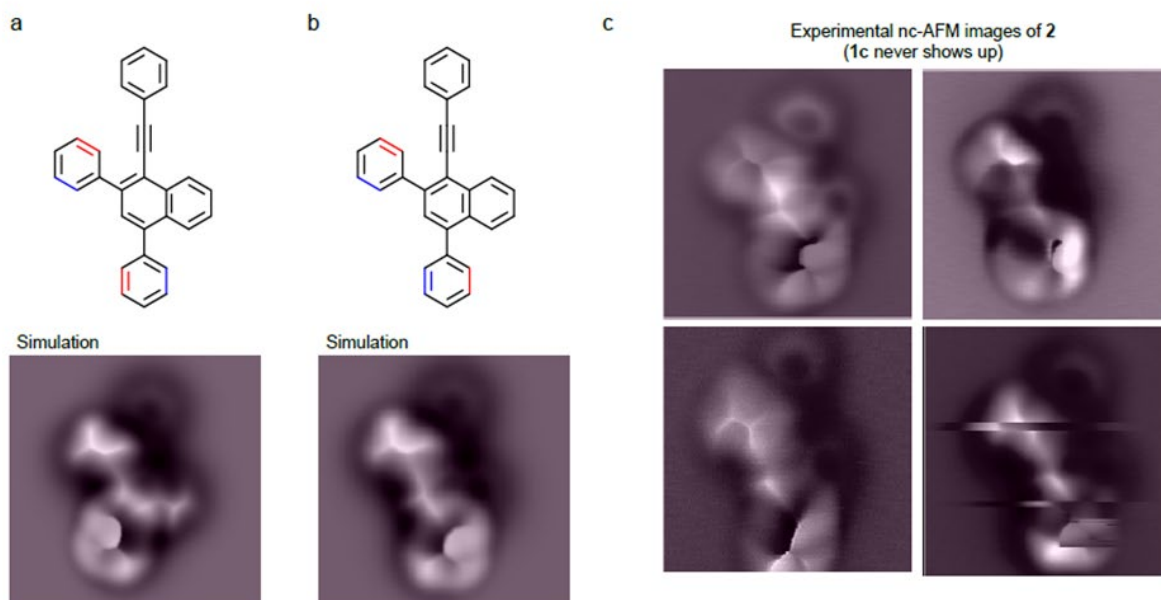
2.6. References

1) Chen, Z.; Narita, A.; Müllen, K.; Graphene Nanoribbons: On-Surface Synthesis and Integration into Electronic Devices. *Adv. Mat.,* **2020**, *32*, 2001893. https://doi.org/10.1002/adma.20200189.

2) Xi, M.; Bent, B. E. Iodobenzene on Cu(111): Formation and Coupling of Adsorbed Phenyl Groups. 14. *Surface Science*. **1992**, *278*, 19-32. https://doi.org/10.1016/0039-6028(92)90580-Y

3) Xi, M.; Bent, B. E. Mechanisms of the Ullmann Coupling Reaction in Adsorbed Monolayers. *J. Am. Chem. Soc.* **1993**, *115*, 7426–7433. https://doi.org/10.1021/ja00069a048.

4) Sun, Q.; Cai, L.; Ma, H.; Yuan, C.; Xu, W. Dehalogenative Homocoupling of Terminal Alkynyl Bromides on Au(111): Incorporation of Acetylenic Scaffolding into Surface Nanostructures. *ACS Nano* **2016**, *10* (7), 7023–7030. https://doi.org/10.1021/acsnano.6b03048.

5) Sun, Q.; Cai, L.; Ma, H.; Yuan, C.; Xu, W. The Stereoselective Synthesis of Dienes through Dehalogenative Homocoupling of Terminal Alkenyl Bromides on Cu(110). *Chem. Commun.* **2016**, *52*, 6009–6012. https://doi.org/10.1039/C6CC01059H.

6) Sun, Q.; Cai, L.; Ma, H.; Yuan, C.; Xu, W. Dehalogenative Homocoupling of Terminal Alkynyl Bromides on Au(111): Incorporation of Acetylenic Scaffolding into Surface Nanostructures. *ACS Nano* **2016**, *10*, 7023–7030. https://doi.org/10.1021/acsnano.6b03048.

7) Zhang, C.; Sun, Q.; Kong, H.; Yuan, C.; Xu, W. On-Surface Stereoconvergent Synthesis, Dimerization and Hybridization of Organocopper Complexes. *Sci. China Chem.* **2019**, *62*, 126–132. https://doi.org/10.1007/s11426-018-9355-8.

8) Sun, Q.; Zhang, C.; Kong, H.; Tan, Q.; Xu, W. On-Surface Aryl–Aryl Coupling via Selective C–H Activation. *Chem. Commun.* **2014**, *50*, 11825–11828. https://doi.org/10.1039/C4CC05482B.

9) Zhong, D.; Franke, J.-H.; Podiyanachari, S. K.; Blömker, T.; Zhang, H.; Kehr, G.; Erker, G.; Fuchs, H.; Chi, L. Linear Alkane Polymerization on a Gold Surface. *Science* **2011**, *334*, 213–216. https://doi.org/10.1126/science.1211836.

10) Clair, S.; Abel, M.; Porte, L. Growth of Boronic Acid Based Two-Dimensional Covalent Networks on a Metal Surface under Ultrahigh Vacuum. *Chem. Commun.* **2014**, *50*, 9627–9635. https://doi.org/10.1039/C4CC02678K.

11) Zwaneveld, N. A. A.; Pawlak, R.; Abel, M.; Catalin, D.; Gigmes, D.; Bertin, D.; Porte, L. Organized Formation of 2D Extended Covalent Organic Frameworks at Surfaces. *J. Am. Chem. Soc.* **2008**, *130*, 6678–6679. https://doi.org/10.1021/ja800906f.

12) Xu, L.; Zhou, X.; Yu, Y.; Tian, W. Q.; Ma, J.; Lei, S. Surface-Confined Crystalline Two-Dimensional Covalent Organic Frameworks *via* on-Surface Schiff-Base Coupling. *ACS Nano* **2013**, *7*, 8066–8073. https://doi.org/10.1021/nn403328h.

13) Klappenberger, F.; Zhang, Y.-Q.; Björk, J.; Klyatskaya, S.; Ruben, M.; Barth, J. V. On-Surface Synthesis of Carbon-Based Scaffolds and Nanomaterials Using Terminal Alkynes. *Acc. Chem. Res.* **2015**, *48*, 2140–2150. https://doi.org/10.1021/acs.accounts.5b00174.

14) Treier, M.; Pignedoli, C. A.; Laino, T.; Rieger, R.; Müllen, K.; Passerone, D.; Fasel, R. Surface-Assisted Cyclodehydrogenation Provides a Synthetic Route towards Easily Processable and Chemically Tailored Nanographenes. *Nature Chem* **2011**, *3*, 61–67. https://doi.org/10.1038/nchem.891.

15) Jacobse, P. H.; Jin, Z.; Jiang, J.; Peurifoy, S.; Yue, Z.; Wang, Z.; Rizzo, D. J.; Louie, S. G.; Nuckolls, C.; Crommie, M. F. Pseudo-Atomic Orbital Behavior in Graphene Nanoribbons with Four-Membered Rings. *Sci. Adv.* **2021**, *7*, eabl5892. https://doi.org/10.1126/sciadv.abl5892.

16) Kinikar, A.; Di Giovannantonio, M.; Urgel, J. I.; Eimre, K.; Qiu, Z.; Gu, Y.; Jin, E.; Narita, A.; Wang, X.-Y.; Müllen, K.; Ruffieux, P.; Pignedoli, C. A.; Fasel, R. On-Surface Polyarylene Synthesis by Cycloaromatization of Isopropyl Substituents. *Nat. Synth* **2022**, *1*, 289–296. https://doi.org/10.1038/s44160-022-00032-5.

17) Qiu, Z.; Sun, Q.; Wang, S.; Barin, G. B.; Dumslaff, B.; Ruffieux, P.; Müllen, K.; Narita, A.; Fasel, R. Exploring Intramolecular Methyl–Methyl Coupling on a Metal Surface for Edge-Extended Graphene Nanoribbons. *Org. Mat.* **2021**, *03*, 128–133. https://doi.org/10.1055/s-0041-1726295.

18) Xu, X.; Di Giovannantonio, M.; Urgel, J. I.; Pignedoli, C. A.; Ruffieux, P.; Müllen, K.; Fasel, R.; Narita, A. On-Surface Activation of Benzylic C-H Bonds for the Synthesis of Pentagon-Fused Graphene Nanoribbons. *Nano Res.* **2021**, *14*, 4754–4759. https://doi.org/10.1007/s12274-021-3419-2.

19) Di Giovannantonio, M.; Chen, Q.; Urgel, J. I.; Ruffieux, P.; Pignedoli, C. A.; Müllen, K.; Narita, A.; Fasel, R. On-Surface Synthesis of Oligo(Indenoindene). *J. Am. Chem. Soc.* **2020**, *142*, 12925–12929. https://doi.org/10.1021/jacs.0c05701.

20) Ruffieux, P.; Wang, S.; Yang, B.; Sánchez-Sánchez, C.; Liu, J.; Dienel, T.; Talirz, L.; Shinde, P.; Pignedoli, C. A.; Passerone, D.; Dumslaff, T.; Feng, X.; Müllen, K.; Fasel, R. On-Surface Synthesis of Graphene Nanoribbons with Zigzag Edge Topology. *Nature* **2016**, *531*, 489–492. https://doi.org/10.1038/nature17151.

21) Gao, H.-Y.; Franke, J.-H.; Wagner, H.; Zhong, D.; Held, P.-A.; Studer, A.; Fuchs, H. Effect of Metal Surfaces in On-Surface Glaser Coupling. *J. Phys. Chem. C* **2013**, *117*, 18595–18602. https://doi.org/10.1021/jp406858p.

22) Díaz Arado, O.; Mönig, H.; Wagner, H.; Franke, J.-H.; Langewisch, G.; Held, P. A.; Studer, A.; Fuchs, H. On-Surface Azide–Alkyne Cycloaddition on Au(111). *ACS Nano* **2013**, *7*, 8509–8515. https://doi.org/10.1021/nn4022789.

23) Zhang, R.; Lyu, G.; Li, D. Y.; Liu, P. N.; Lin, N. Template-Controlled Sonogashira Cross-Coupling Reactions on a Au(111) Surface. *Chem. Commun.* **2017**, *53*, 1731–1734. https://doi.org/10.1039/C6CC10091K.

24) Liu, J.; Ruffieux, P.; Feng, X.; Müllen, K.; Fasel, R. Cyclotrimerization of Arylalkynes on Au(111). *Chem. Commun.* **2014**, *50*, 11200–11203. https://doi.org/10.1039/C4CC02859G.

25) de Oteyza, D. G.; Pérez Paz, A.; Chen, Y.-C.; Pedramrazi, Z.; Riss, A.; Wickenburg, S.; Tsai, H.-Z.; Fischer, F. R.; Crommie, M. F.; Rubio, A. Noncovalent Dimerization after Enediyne Cyclization on Au(111). *J. Am. Chem. Soc.* **2016**, *138*, 10963–10967. https://doi.org/10.1021/jacs.6b05203.

26) Sun, Q.; Zhang, C.; Li, Z.; Kong, H.; Tan, Q.; Hu, A.; Xu, W. On-Surface Formation of One-Dimensional Polyphenylene through Bergman Cyclization. *J. Am. Chem. Soc.* **2013**, *135*, 8448–8451. https://doi.org/10.1021/ja404039t.

27) H. Hopf, H. Musso, Preparation of Benzene by Pyrolysis of cis- and trans-1,3-Hexadien-5-yne. *Angew. Chem.* **1969**, *81*, 704. https://doi.org/10.1002/anie.196906801

28) Prall, M.; Krüger, A.; Schreiner, P. R.; Hopf, H. The Cyclization of Parent and Cyclic Hexa-1,3-Dien-5-Ynes—A Combined Theoretical and Experimental Study. *Chem. Eur. J.* **2001**, *7*, 4386–4394.

https://doi.org/10.1002/1521-3765(20011015)7:20<4386::AID-CHEM4386>3.0.CO;2-S.

29) Hopf, H.; Krüger, A. Synthesis of Cyclo-1,3-Dien-5-Ynes. *Chem. Eur. J.* **2001**, *7*, 4378–4385.

https://doi.org/10.1002/1521-3765(20011015)7:20<4378::AID-CHEM4378>3.0.CO;2-I.

30) Jordan, R. S.; Wang, Y.; McCurdy, R. D.; Yeung, M. T.; Marsh, K. L.; Khan, S. I.; Kaner, R. B.; Rubin, Y. Synthesis of Graphene Nanoribbons via the Topochemical Polymerization and Subsequent Aromatization of a Diacetylene Precursor. *Chem* **2016**, *1*, 78–90. https://doi.org/10.1016/j.chempr.2016.06.010.

31) Jordan, R. S.; Li, Y. L.; Lin, C.-W.; McCurdy, R. D.; Lin, J. B.; Brosmer, J. L.; Marsh, K. L.; Khan, S. I.; Houk, K. N.; Kaner, R. B.; Rubin, Y. Synthesis of $N = 8$ Armchair Graphene Nanoribbons from Four Distinct Polydiacetylenes. *J. Am. Chem. Soc.* **2017**, *139*, 15878–15890. https://doi.org/10.1021/jacs.7b08800.

32) Li, Y. L.; Zee, C.-T.; Lin, J. B.; Basile, V. M.; Muni, M.; Flores, M. D.; Munárriz, J.; Kaner, R. B.; Alexandrova, A. N.; Houk, K. N.; Tolbert, S. H.; Rubin, Y. Fjord-Edge

Graphene Nanoribbons with Site-Specific Nitrogen Substitution. *J. Am. Chem. Soc.* **2020**, *142*, 18093–18102. https://doi.org/10.1021/jacs.0c07657.

33) Treier, M.; Pignedoli, C. A.; Laino, T.; Rieger, R.; Müllen, K.; Passerone, D.; Fasel, R. Surface-Assisted Cyclodehydrogenation Provides a Synthetic Route towards Easily Processable and Chemically Tailored Nanographenes. *Nature Chem.* **2011**, *3*, 61–67. https://doi.org/10.1038/nchem.891.

34) Lackinger, M. Surface-Assisted Ullmann Coupling. *Chem. Commun.* **2017**, *53*, 7872–7885. https://doi.org/10.1039/C7CC03402D.

35) Liu, W.; Luo, X.; Bao, Y.; Liu, Y. P.; Ning, G.-H.; Abdelwahab, I.; Li, L.; Nai, C. T.; Hu, Z. G.; Zhao, D.; Liu, B.; Quek, S. Y.; Loh, K. P. A Two-Dimensional Conjugated Aromatic Polymer via C–C Coupling Reaction. *Nature Chem.* **2017**, *9* (6), 563–570. https://doi.org/10.1038/nchem.2696.

36) Li, Y. L.; Zee, C.-T.; Lin, J. B.; Basile, V. M.; Muni, M.; Flores, M. D.; Munárriz, J.; Kaner, R. B.; Alexandrova, A. N.; Houk, K. N.; Tolbert, S. H.; Rubin, Y. Fjord-Edge Graphene Nanoribbons with Site-Specific Nitrogen Substitution. *J. Am. Chem. Soc.* **2020**, *142* (42), 18093–18102. https://doi.org/10.1021/jacs.0c07657.

37) Jordan, R. S.; Li, Y. L.; Lin, C.-W.; McCurdy, R. D.; Lin, J. B.; Brosmer, J. L.; Marsh, K. L.; Khan, S. I.; Houk, K. N.; Kaner, R. B.; Rubin, Y. Synthesis of *N* = 8 Armchair Graphene Nanoribbons from Four Distinct Polydiacetylenes. *J. Am. Chem. Soc.* **2017**, *139* (44), 15878–15890. https://doi.org/10.1021/jacs.7b08800.

38) Jordan, R. S.; Wang, Y.; McCurdy, R. D.; Yeung, M. T.; Marsh, K. L.; Khan, S. I.; Kaner, R. B.; Rubin, Y. Synthesis of Graphene Nanoribbons via the Topochemical Polymerization

and Subsequent Aromatization of a Diacetylene Precursor. *Chem* **2016**, *1* (1), 78–90. https://doi.org/10.1016/j.chempr.2016.06.010

39) Jones, G. B.; Wright, J. M.; Plourde, G. W.; Hynd, G.; Huber, R. S.; Mathews, J. E. A Direct and Stereocontrolled Route to Conjugated Enediynes. *J. Am. Chem. Soc.* **2000**, *122*, 1937–1944. https://doi.org/10.1021/ja993766b.

40) Wang, S.; Goronzy, D. P.; Young, T. D.; Wattanatorn, N.; Stewart, L.; Baše, T.; Weiss, P. S. Formation of Highly Ordered Terminal Alkyne Self-Assembled Monolayers on the Au{111} Surface through Substitution of 1-Decaboranethiolate. *J. Phys. Chem. C* **2019**, *123* (2), 1348–1353. https://doi.org/10.1021/acs.jpcc.8b11033.

41) Zhang, S.; Chandra, K. L.; Gorman, C. B. Self-Assembled Monolayers of Terminal Alkynes on Gold. *J. Am. Chem. Soc.* **2007**, *129*, 4876–4877. https://doi.org/10.1021/ja0704380.

42) Periasamy, M.; Srinivas, G.; Karunakar, G. V.; Bharathi, P. Reductive Coupling of Aromatic Aldehydes and Imines by the Low Valent Titanium Species Generated in the Reaction of TiCI4 with Et3N. 4. *Tet. Let.* **1999**, *40*, 7577 – 7580. https://doi.org/10.1016/S00404039(99)01609-3

43) Shimizu, T.; Miyasaka, D.; Kamigata, N. Synthesis and Reactivity of Allenes Substituted by Selenenyl Groups at 1- and 3-Positions. *J. Org. Chem.* **2001**, *66*, 1787–1794. https://doi.org/10.1021/jo001483s.

44) Barluenga, J.; de la Rúa, R. B.; de Sáa, D.; Ballesteros, A.; Tomás, M. Formal Alkyne Insertion into Alkoxycarbene Complexes: Simple Access to Enantiopure Group 6

Alkynyl(Alkoxy)Carbene Complexes. *Angew. Chem.* **2005**, *117* (31), 5061–5063. https://doi.org/10.1002/ange.200501400.

45) Periasamy, M.; Karunakar, G. V.; Bharathi, P. Synthesis of Enynones from Alkynes, Alkynyl Ketones and Aromatic Aldehydes Using the TiCl4/Et3N Reagent System.

46) Henkelman, G.; Arnaldsson, A.; Jónsson, H. A Fast and Robust Algorithm for Bader Decomposition of Charge Density. *Computational Materials Science* **2006**, *36* (3), 354–360. https://doi.org/10.1016/j.commatsci.2005.04.010.

47) Yu, M.; Trinkle, D. R. Accurate and Efficient Algorithm for Bader Charge Integration. *The Journal of Chemical Physics* **2011**, *134* (6), 064111. https://doi.org/10.1063/1.3553716.

48) Tang, W.; Sanville, E.; Henkelman, G. A Grid-Based Bader Analysis Algorithm without Lattice Bias. *J. Phys.: Condens. Matter* **2009**, *21* (8), 084204. https://doi.org/10.1088/0953-8984/21/8/084204.

49) Hopf, H.; Jones, P. G.; Bubenitschek, P.; Werner, C. para- and ortho-Quinodimethane Intermediates with Cumulative Double Bonds. *Angew. Chem., Int. Ed.* **1995**, *34*, 2367 – 2368. https://doi.org/10.1002/anie.199523671

50) Kinikar, A.; Di Giovannantonio, M.; Urgel, J. I.; Eimre, K.; Qiu, Z.; Gu, Y.; Jin, E.; Narita, A.; Wang, X.-Y.; Müllen, K.; Ruffieux, P.; Pignedoli, C. A.; Fasel, R. On-Surface Polyarylene Synthesis by Cycloaromatization of Isopropyl Substituents. *Nat. Synth* **2022**, *1*, 289–296. https://doi.org/10.1038/s44160-022-00032-5.

51) Yakutovich, A. V.; Eimre, K.; Schütt, O.; Talirz, L.; Adorf, C. S.; Andersen, C. W.; Ditler, E.; Du, D.; Passerone, D.; Smit, B.; Marzari, N.; Pizzi, G.; Pignedoli, C. A. AiiDAlab – an

Ecosystem for Developing, Executing, and Sharing Scientific Workflows. *Computational Materials Science* **2021**, *188*, 110165. https://doi.org/10.1016/j.commatsci.2020.110165.

52) Pizzi, G.; Cepellotti, A.; Sabatini, R.; Marzari, N.; Kozinsky, B. AiiDA: Automated Interactive Infrastructure and Database for Computational Science. *Computational Materials Science* **2016**, *111*, 218–230. https://doi.org/10.1016/j.commatsci.2015.09.013.

53) Hutter, J., Iannuzzi, M., Schiffmann, F. & VandeVondele, J. cp2k: atomistic simulations of condensed matter systems. *Wiley Interdisciplinary Reviews: Computational Molecular Science* **4**, 15–25 (2014). https://doi.org/10.1002/wcms.1159

54) VandeVondele, J., Hutter, J. Gaussian basis sets for accurate calculations on molecular systems in gas and condensed phases. *The Journal of Chem. Phys.* **127**, 114105 (2007). https://doi.org/10.1063/1.2770708. https://doi.org/10.1103/PhysRevB.54.1703

55) Goedecker, S., Teter, M.; Hutter, J. Separable dual-space gaussian pseudopotentials. *Physical Review B* **54**, 1703 (1996). https://doi.org/10.1103/PhysRevB.54.1703.

56) Perdew, J. P.; Burke, K.; Ernzerhof, M. Generalized Gradient Approximation Made Simple. *Phys. Rev. Lett.* **1996**, *77*, 3865–3868.
https://doi.org/10.1103/PhysRevLett.77.3865.

57) Grimme, S., Antony, J., Ehrlich, S.; Krieg, H. A consistent and accurate ab initio parametrization of density functional dispersion correction (dft-d) for the 94 elements h-pu. *The Journal of chemical physics* **132**, 154104 (2010). https://doi.org/10.1063/1.3382344.

58) Hanke, F.; Björk, J. Structure and Local Reactivity of the Au(111) Surface Reconstruction. *Phys. Rev. B* **2013**, *87*, 235422.
https://doi.org/10.1103/PhysRevB.87.235422.

59) Hapala, P.; Kichin, G.; Wagner, C.; Tautz, F. S.; Temirov, R.; Jelinek, P. The Mechanism of High-Resolution STM/AFM Imaging with Functionalized Tips. *Phys. Rev. B* **2014**, *90* (8), 085421. https://doi.org/10.1103/PhysRevB.90.085421.

60) Laio, A.; Parrinello, M. Escaping Free-Energy Minima. *Proc. Natl. Acad. Sci. U.S.A.* **2002**, *99* (20), 12562–12566. https://doi.org/10.1073/pnas.202427399.

61) Henkelman, G.; Uberuaga, B. P.; Jónsson, H. A Climbing Image Nudged Elastic Band Method for Finding Saddle Points and Minimum Energy Paths. *The Journal of Chemical Physics* **2000**, *113*, 9901–9904. https://doi.org/10.1063/1.1329672.

62) E, W.; Ren, W.; Vanden-Eijnden, E. String Method for the Study of Rare Events. *Phys. Rev. B* **2002**, *66*, 052301. https://doi.org/10.1103/PhysRevB.66.052301.

63) R.S. Jordan. Setting the Record Straight: Bottom-Up Carbon Nanostructures via Solid-State Reactions. Doctoral Dissertation, University of California Los Angeles, Los Angeles, CA **2017**.

64) Jones, G. B.; Wright, J. M.; Plourde, G. W.; Hynd, G.; Huber, R. S.; Mathews, J. E. A Direct and Stereocontrolled Route to Conjugated Enediynes. *J. Am. Chem. Soc.* **2000**, *122*, 1937–1944. https://doi.org/10.1021/ja993766b.

CHAPTER 3. LOW TEMPERATURE FORMATION OF CONJUGATED AROMATIC POLYMERS ON GOLD SURFACE

3.1. Background

Ullman couplings can typically form one- or two-dimensional structures on a gold(111) surface, thanks to a judicious placement of halogens on the molecular precursor. The type of halogen also plays an important role in the design, orientation, and extent of surface coverage.[1] This first step in this reaction is the thermal carbon-halogen cleavage. Next, a coupling of diradical intermediates takes place.[2]

This reaction is currently referred to as an Ullman coupling when performed on a metal surface; however, it should not be confused with a formal Ullman coupling that conventionally takes place in solution. In the formal process, an electron transfer takes place, and the halogen is removed as a halide anion. However, the on-surface reaction takes place via a homolytic carbon-halogen bond cleavage giving two radicals, both a carbon-based and a halogen radical. This leads to carbon radicals that are stabilized by the presence of the metal surface under ultra-high vacuum conditions. These radicals can then undergo homocoupling to form covalent bonds.

3.1.1. Reactivity of Iodine-Containing Molecular Precursors

Inclusion of two chemically identical halogen units on the precursor monomer should cause the molecules to undergo Ullman coupling when deposited on Au(111).[3] This reaction has been demonstrated a number of times before and is typically used to polymerize halogenated polyaromatic hydrocarbons on surface. However, depending on the molecular precursor design, such polymerization reactions have been observed at varying temperatures.

99

In 2001, research by Koel and co-workers shows that iodobenzene chemisorbs on Au(111) and is partially irreversibly adsorbed below room temperature.[4] Heating this precursor monomer to temperatures slightly higher than this (-73 ˚C to -23 ˚C), but still below room temperature afforded coupled products. Additionally in 2010, Fasel and co-workers showed that the macrocycle hexaiodo-cyclohexa-m-phenylene (CHP) on Cu(111), Au(111), and Ag(111) could form covalently bonded *m*-polyphenylene networks.[5] The authors used scanning tunnelling microscopy (STM), X-ray photoelectron spectroscopy (XPS), and density functional theory (DFT) to reveal room temperature dehalogenation on all surfaces, leading to surface stabilized radicals and coadsorbed iodine. All three metals followed the same dissociative pathway, with C-I cleavage and the formation of stabilized radicals. However, the three different metals dictated different subsequent polymer formation morphologies at different temperatures. While Ag gave highly ordered networks, Cu produced more branched networks, and Au resulted in an in-between situation. Furthermore, polymerization temperatures on Cu, Au, and Ag were 202 ˚C, 252 ˚C, and 302 ˚C respectively. Fasel *et al*. therefore concluded that there is a balance between the diffusion and coupling steps. On Cu, the radicals spontaneously form covalent bonds, leading to less diffusion time of the radicals, and therefore the formation of more highly branched structures. On Ag however, diffusion lasts longer, allowing more time for an organized network formation, but this requires the highest temperatures. Finally, Au(111) shows the best potential for Ullman coupling because it allows for a balance between diffusion time and coupling reactivity. By allowing molecules adequate time to diffuse across the surface, but not too much time as to require higher temperatures, iodinated molecular precursors on Au(111) are ideal for exploitation in polymer synthesis.

Work by Lackinger and co-workers in 2012 has shown that iodinated precursors are easily dehalogenated at room temperature by the catalytic properties of an Au(111) noble metal surface.[6] By using 1,3,5-triiodobenzene (TIB), benzene tris-radicals were observed to be mobile at room temperature. Thus, polymerization could take place without any thermal activation. When using 1,3,5-tris(4′-iodophenyl)benzene (TIPB) at room temperature, only oligomers were observed. The authors point out two important facts as a result of their work. Smaller precursor monomers with iodine are capable of polymerizing at room temperature, while larger ones require additional heating to 110 ˚C due to their higher surface adhesion through π-Au interactions. Also, while smaller precursors can be beneficial, those that are too small result in a higher concentration of co-formed iodine atoms, and thus can hampers the polymerization by steric shielding.

In 2014, Lackinger and co-workers also showed that 1,3-bis(p-bromophenyl)-5-(*p*-iodophenyl)benzene, a molecular precursor containing both iodine and bromine atoms, could be used to be selectively dehalogenated at different temperatures.[7] Coupling of this precursor at room temperature takes place because only iodine is selectively cleaved off. Due to the temperature dependance on the halogen, the C-Br bond requires higher temperatures (185 ˚C) for the cleavage to take place.

In 2016, work by Silly and co-workers revealed that star-shaped 1,3,5-tris(4-iodophenyl)benzene molecules could be used to form covalent polygonal nanoarchitectures.[8] However, while polymerization was expected to take place at room temperature, STM images reveal bright spots that correspond to molecular iodine atoms. This again indicates that, due to the size of the selected molecular precursor, iodine atoms can render precursors unable to systemically associate into large structures.

In 2017, work by Crommie and co-workers monitored the difference for de-iodination and de-bromination of intact monomers on surface to produce surface-stabilized radicals, monomers and polymers.[9] Using 6,11-dibromo-1,2,3,4-tetraphenyltriphenylene and 6,11-diiodo-1,2,3,4-tetraphenyltriphenylene, they demonstrated the differences that exist between molecular precursors of larger size that are based on either Ullman coupling of iodine or bromine-bearing carbons. While it was expected that iodine-precursors should polymerize at room temperature, these authors observed de-iodination produced surface stabilized radicals instead of spontaneous coupling. Because these radicals are tightly bound to the gold surface at room temperature, they have reduced diffusivity and are unable to polymerize. Polymerization of their monomer started to occur only around 100 ˚C, while surface-stabilized radicals were generally observed below 80 ˚C. Between these temperatures, mixtures of monomers and polymers were observed. On the other hand, intact monomers of the bromine analog were observed at temperatures below 80 ˚C, rather than surface stabilized radicals. Around 80 ˚C, monomers and polymers were observed and any higher temperature resulted in the formation of polymers. These results again show that there can be vast differences in behavior between bromine and iodine-based molecular precursors.

In 2017, work by Saywell and co-workers showed that the use of 4,4″-diiodo-*m*-terphenyl (DITP) on Ag(111) and Ag(110).[10] Here, room temperature deposition resulted in dissociation of iodine and formation of metal-organic structures bearing Ag adatoms. Different structures could be observed depending on the metal surface used. To produce polymers from this molecular precursor, heating to 187 ˚C was required. Again, this works points to the use of Au(111) surface instead for the low temperature formation of polymers.

Additionally in 2019, work by Lackinger and co-workers also showed the difference between Ag(111) and Au(111) with 1,3,5-tris(4-bromophenyl)benzene as a molecular precursor.[11] The authors of this work stated that Ag(111) offers kinetic control, while Au(111) allows for thermodynamic control. On Ag(111), debromination at room temperature was exothermic because of interactions between surface stabilized radicals and chemisorbed bromine. However, heating to 277 ˚C was required to form covalent linkages. This was justified through the high diffusion, rotation, and coupling barriers presented on Ag(111). Bromine desorption from the surface took place at temperatures starting at 177 ˚C. On the other hand, Au(111) required higher temperatures to remove bromine (50 ˚C) and produce surface-stabilized radicals. Debromination also took place over a larger temperature interval (50 ˚C – 185 ˚C) due to the fact that radicals could reversibly react with bromine atoms still present on the surface. While bromine desorption occurred at a lower temperature on Au(111), higher temperatures were required to induce covalent coupling (227 ˚C – 277 ˚C). Overall, this work showed that a combination of surface and halogen choice was required to produce polymers.

Overall research in this area has pointed to the use of diiodo molecular precursors for the room or low temperature synthesis of polymers on Au(111). Au(111) allows for low temperature deiodination, followed by surface stabilized radicals that react to form covalent linkages. On the other hand, Cu(111) offers low temperature dehalogenation but a higher barrier to movement of surface stabilized radicals across the surface. This results in high reactivity to form covalent bonds, but allows no time for organized self-assembly. Ag(111) requires higher temperatures for dehalogenation, but allows for more mobility. As a result of these prior findings, Au(111) is the perfect choice for polymer formation. Adequate molecular precursor design is also necessary to achieve this aim. For one, a molecular precursor that is still relatively small should be used,

instead of a large molecular precursor, to avoid a high barrier to diffusivity. On the other hand, too small of a molecular precursor will result in difficulties in polymerization due to high-diffusion and the presence of too many iodine atoms.

Thus, a diiodinated version of our tetraphenyl *trans*-3-hexene-1,5-diyne (enediyne, Fig. 21) should give easy polymer formation on Au(111) at room temperature. The low temperature would be beneficial to study the following stepwise cyclodehydrogenation at higher temperatures (discussed in Chapter 2), while avoiding molecular desorption.

3.1.2. ITPE for Graphene Nanoribbon Synthesis
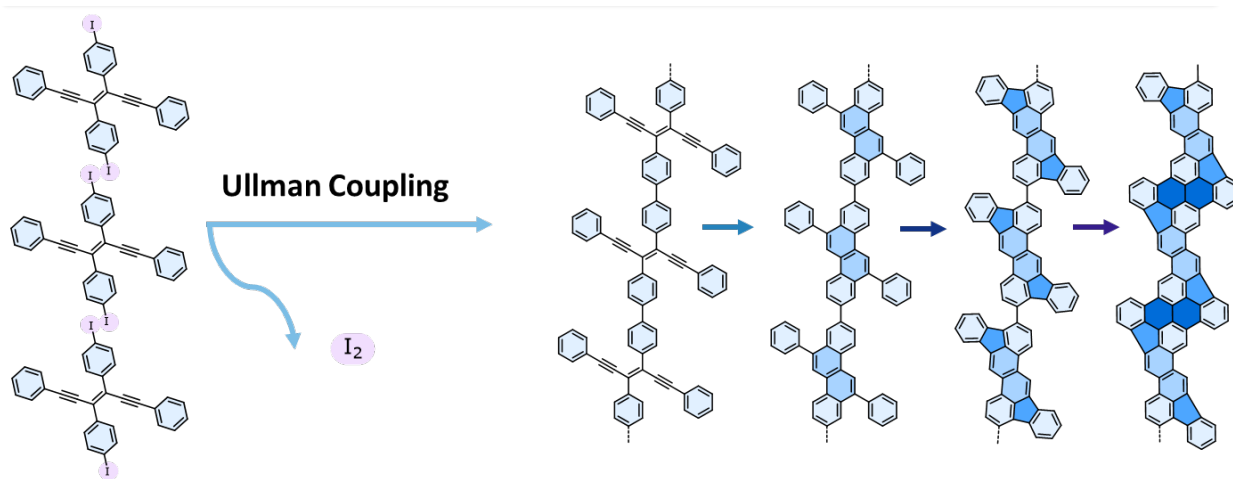
Figure 30. Proposed synthesis of graphene nanoribbons from diiodo-tetraphenyl *trans*-3-hexene-1,5-diyne (ITPE). Deiodination of ITPE on Au(111) would result in surface-stabilized radicals that form covalent bonds through Ullman couplings; further heating should result in a series of Hopf cyclizations and cyclodehydrogenation reactions.

An iodine derivative, diiodinated tetraphenyl *trans*-3-hexene-1,5-diyne (ITPE) could be synthesized via an analogous method to our previously reported TPE molecule. By replacing benzaldehyde with 4-iodobenzaldehyde, the iodine containing precursor monomer ITPE can be synthesized (Fig. 31).

3.2. Methods

3.2.1. Synthesis of iodo-tetraphenyl *trans*-3-hexene-1,5-diyne 3c (ITPE)
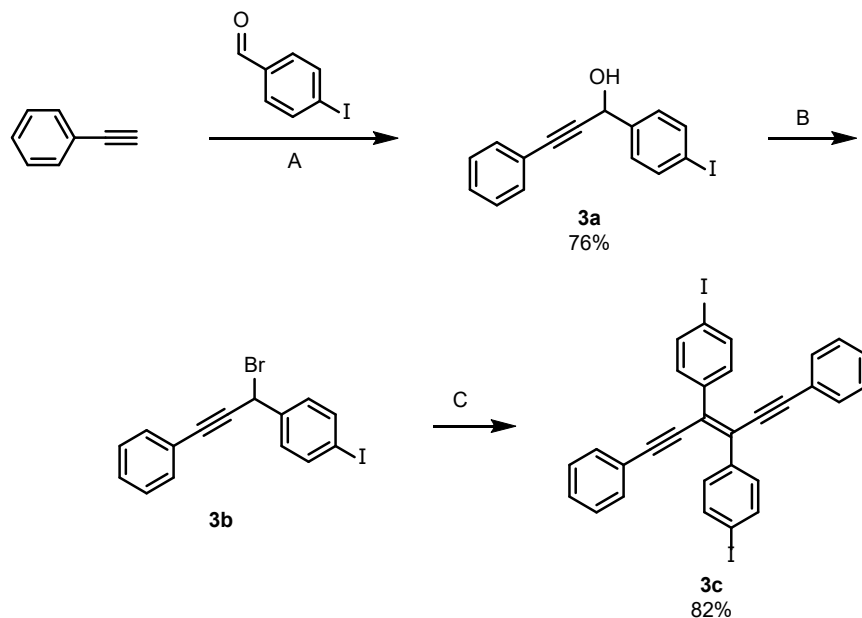
Figure 31. Synthetic scheme for the synthesis of diiodo-tetraphenyl *trans*-3-hexene-1,5-diyne 3c (ITPE). a) 1. *n*-BuLi, THF 0 °C, 30 min, 2. Benzaldehyde, 2 h (3a, 76%); b) PBr$_3$, Et$_2$O, 0 °C, 30 min, (3b, not isolated); (C) LiHMDS, HMPA, THF, -90 °C to RT, (3c, 82%).

To synthesize the diiodo-tetraphenyl *trans*-3-hexene-1,5-diyne **3c** (ITPE), a similar reaction pathway to that described in Chapter 2 was followed (Fig. 32). Phenylacetylene was deprotonated with *n*-butyllithium in THF. The corresponding acetylide anion was reacted with 4-iodobenzaldehyde. This resulted in the propargyl alcohol **3a** (76%), which could be subsequently converted to the corresponding propargylic bromide using PBr$_3$ in diethyl ether. Similar to compound **2b** in Chapter 2, compound **3b** was not isolated due to its high sensitivity to hydrolysis. Instead, propargyl bromide **3b** was dried under vacuum overnight and reacted the subsequent day.
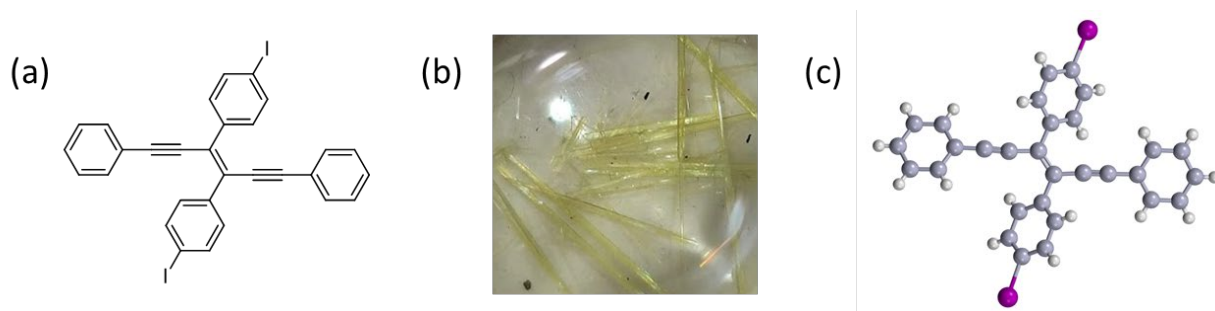
Figure 32. Crystallization of ITPE. a) Chemical structure of ITPE, b) pale-yellow needles formed by layering hexanes over chloroform, (c) crystal structure of ITPE.

The same procedure as described in Chapter 2 was used for the last step. Propargyl bromide **3b** was cooled to -90 °C, then a lithium bis(trimethylsilyl)amide (LiHMDS) and hexamethylphosphoramide (HMPA) mixture was either syringed in or cannula transferred dropwise. The crude reaction mixture has initially a dark-red color, then briefly turns green in the area drops are added when the LiHMDS/HMPA mixture hits the solution. This continues until almost all the mixture is added, and then the reaction becomes entirely dark green colored. A yellow precipitate begins to appear in solution. The reaction is worked up by addition of saturated NH$_4$Cl and extracted with chloroform. From here, the compound can be precipitated out of chloroform with hexanes and washed with diethyl ether, giving a relatively pure product. Diiodo-tetraphenyl *trans*-3-hexene-1,5-diyne **3c** (ITPE) is obtained in 82% yield. The compound can be crystallized by layering hexanes over chloroform (see Experimental Section). Figure 33 shows a) the chemical structure of ITPE, b) the yellow needle like crystals that are formed, and (c) its single crystal structure.

3.2.2. Vapor Deposition and Reaction on Gold(111) in Ultra High Vacuum
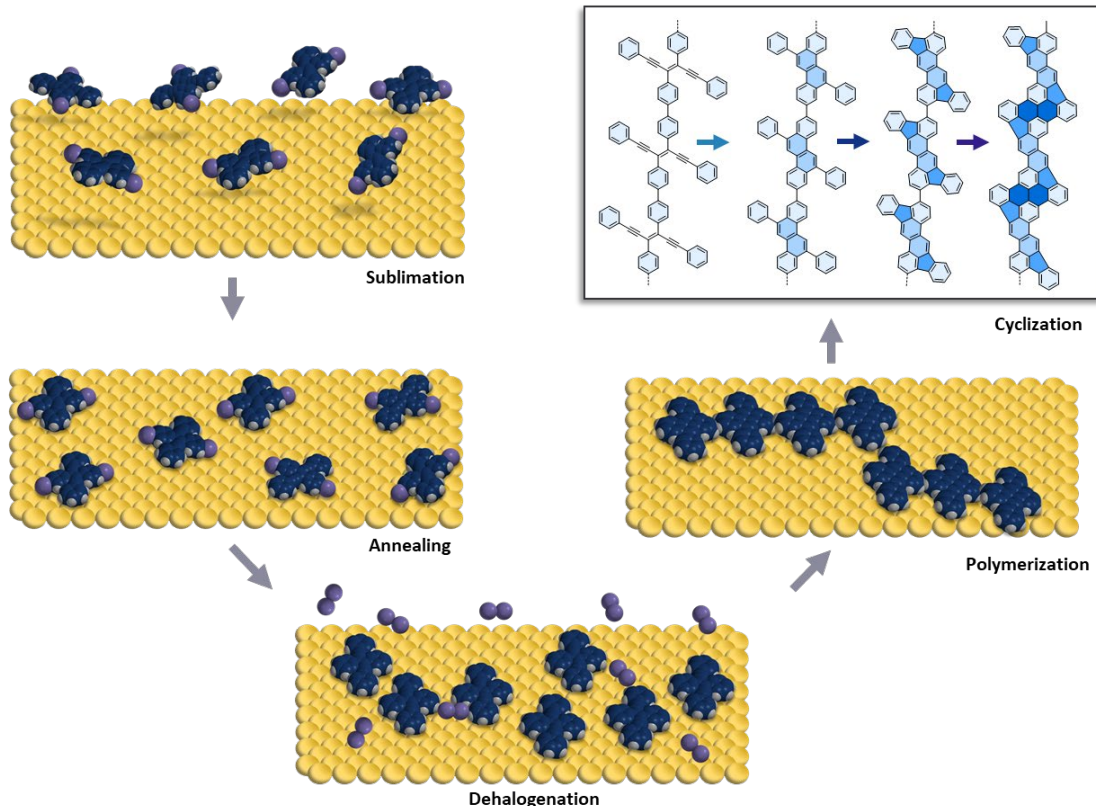
Figure 33. Schematic representation of graphene nanoribbon formation from ITPE. *Sublimation*: molecular precursor is heated to vapor; *annealing*: deposition of molecules onto a gold(111) surface held at constant temperature; *dehalogenation*: iodine dissociates from carbon, forming surface-stabilized radicals; *polymerization*: diradicals covalently couple to polymerize via carbon-carbon bonds; *cyclization*: subsequent Hopf cyclizations and cyclodehydrogenation reactions form graphene nanoribbons.

From here, the diiodo derivative **3c** was used as a precursor for graphene nanoribbon fabrication. Chapter 2 showed that, thanks to unusually low conversion of the enediyne backbone, tetraphenyl *trans*-3-hexene-1,5-diyne can undergo two different types of cyclizations. The first step is a double Hopf cyclization that occurs at the two dienyne portions within the molecule. The second is a cyclodehydrogenative step that results from C-C bond formation at

two of the phenyl substituents. To test if this compound could be a suitable prototype for graphene nanoribbon synthesis, it was deposited and studied on surface.

3.3. Results and Discussion

3.3.1. ITPE Ullman Coupling During Room Temperature Deposition
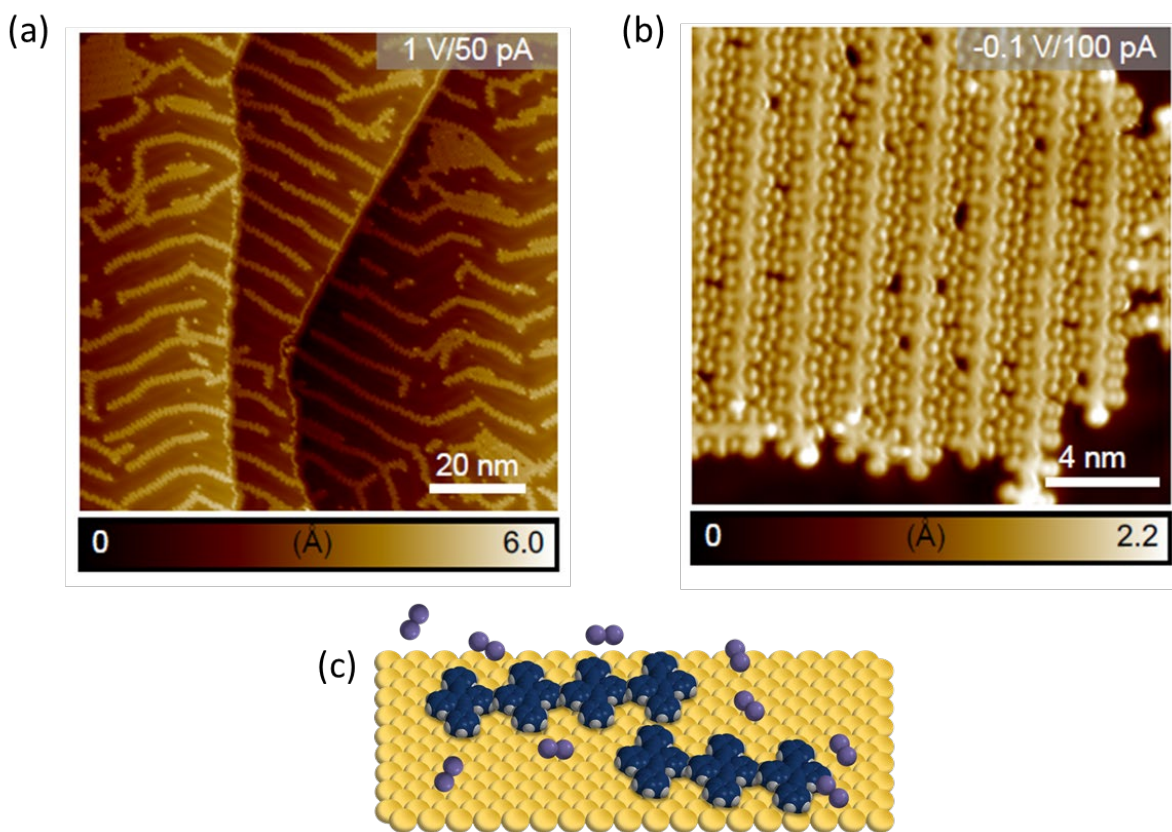
Figure 34. Room temperature (RT) deposition of ITPE 3c on Au(111). (a) STM image of Ullman-coupled 3c (ITPE) after RT deposition on Au(111), which results in self-assembled ribbons; scale bar: 20 nm; (b) close up STM image of polymerized ITPE at RT, scale bar: 4 nm; (c) schematic representation of resulting structure after deiodination, movement of surface stabilized radicals, and subsequent polymerization.

First, diiodo-tetraphenyl *trans*-3-hexene-1,5-diyne **3c** (ITPE) was deposited onto an Au(111) surface held at constant temperature according to Figure 34. This is done through sublimation of the molecules of **3c** onto a gold(111) surface held at room temperature.

From here, STM images were recorded at increasing temperatures. Figure 35 shows the resultant STM images after deposition at room temperature. Diiodo-tetraphenyl *trans*-3-hexene-1,5-diyne **3c** (ITPE) undergoes Ullman couplings already at room temperature, similar to previous reports.[6,7] No iodine or surface-stabilized radicals were observed at room temperature. Fig. 35a shows an STM image of self-assembled polymeric structures across the metal surface. Fig. 35b shows a close-up version in a high-density area of these long polymer chains. Interestingly enough, most polymerization steps that take place in published graphene nanoribbon syntheses require heating to at least 150 ˚C. This is because of the higher temperatures required to remove halogens such as chlorine and bromine. In most cases, bromine is used, however introduction of iodine moiety shows that it is possible to polymerize these structures at temperatures as low as 20 ˚C. This proves that designing a precursor monomer of this size with iodine is beneficial for the industrialization of graphene nanoribbon synthesis.
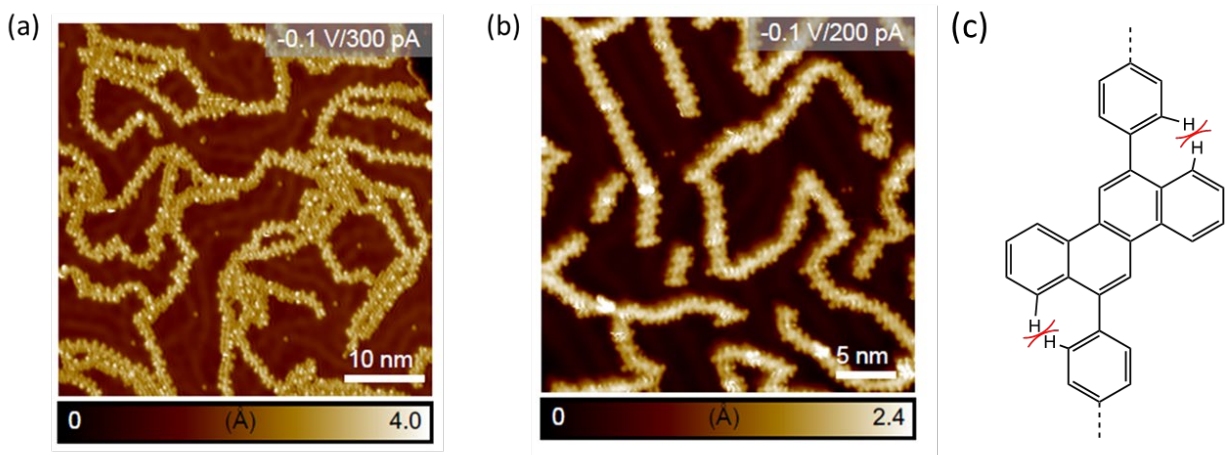
Figure 35. Heating of polymerized ITPE to 210 ˚C on Au(111) achieves the sequential, multiple Hopf cyclization to give non-planar polymers. (a) STM image of twisted and bent polymers observed after heating, during with the proposed Hopf cyclizations take place, scale bar: 10 nm; (b) close up STM image of observed polymers, scale bar: 5 nm; (c) steric clash from resulting Hopf cyclized structure (2e).

3.3.2. ITPE Nanoribbon Formation via Hopf Cyclizations

Similar to our Chapter 2 findings, ITPE undergoes multiple Hopf cyclizations. Even though this requires higher temperatures than in Chapter 2 (210 ˚C), polymeric structures result as predicted; however, they appear irregular (Fig. 36). This is an indication that the products of Hopf cyclization are not planar. Instead, they bent and twisted by a number of steric clashes between diphenyl-chrysene units (Fig. 36c). These irregularities can be observed throughout, but some regions of the hypothesized polymeric structures can be observed more clearly by STM.

3.3.3. ITPE Nanoribbon Formation via Cyclodehydrogenation

After heating to 370 ˚C, images become more difficult to analyze. This occurs because of the steric clash and phenyl twisting (Fig. 36c). However, segments of fully annulated polymers are also observed by STM. Fig. 37a shows more rigid chains of polymers on Au(111). Fig. 37b shows an STM image of a segment of carbon polymer with precise structure. This structure

matches the hypothesized 5-membered cyclodehydrogenated structure discussed in Fig. 30, which is also shown in Fig. 37c. Furthermore, Fig. 37d shows a beautiful non-contact atomic force microscopy (nc-AFM) image of the intact chiral structure that was proposed earlier. Interestingly, previous work for a similar chiral polymer was conducted by Müllen in 2020 (see Chapter 1, Figure 7, entry 15).[12] These authors here stated that when their polymer was heated to temperatures above 370 ˚C, five-membered rings could also be formed, similar to our work here. Our data therefore demonstrates that diiodo-tetraphenyl *trans*-3-hexene-1,5-diyne **3c** (ITPE) can be polymerized on surface at room temperature and subsequently annulated through further cyclizations (Hopf and cyclodehydrogenation) to form nanoribbon structures.
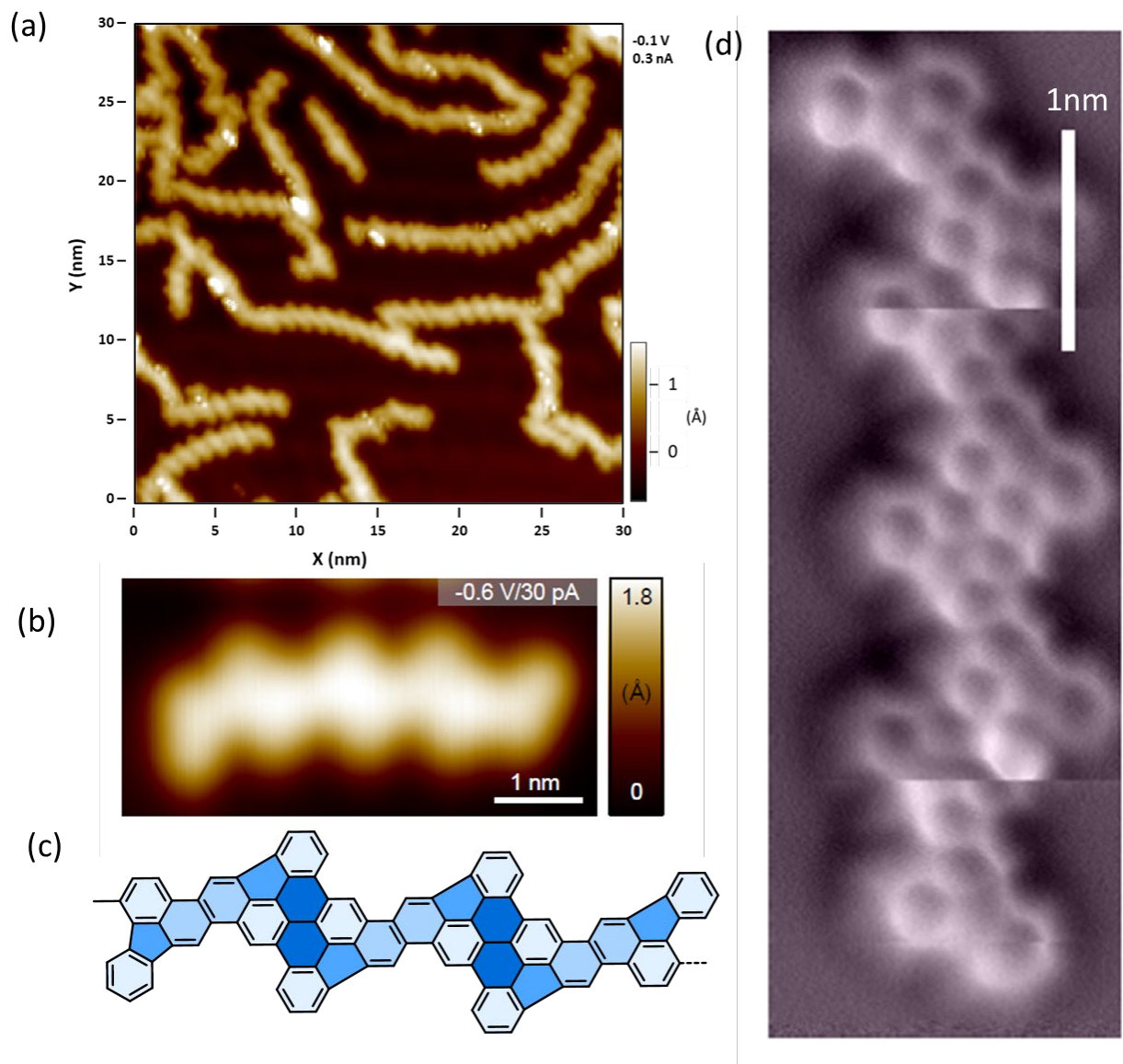
Figure 36. Proposed nanoribbon formation of ITPE. (a) STM image of carbon polymers after heating to 370 ˚C, scale bar: 5 nm; (b) STM image of intact region of proposed cyclized polymer from ITPE, scale bar: 1 nm; (c) schematic representation of observed nanoribbon; (d) non-contact atomic force microscopy (nc-AFM) image of intact proposed nanoribbon from ITPE.

112

3.3.4. Other Designed Precursors
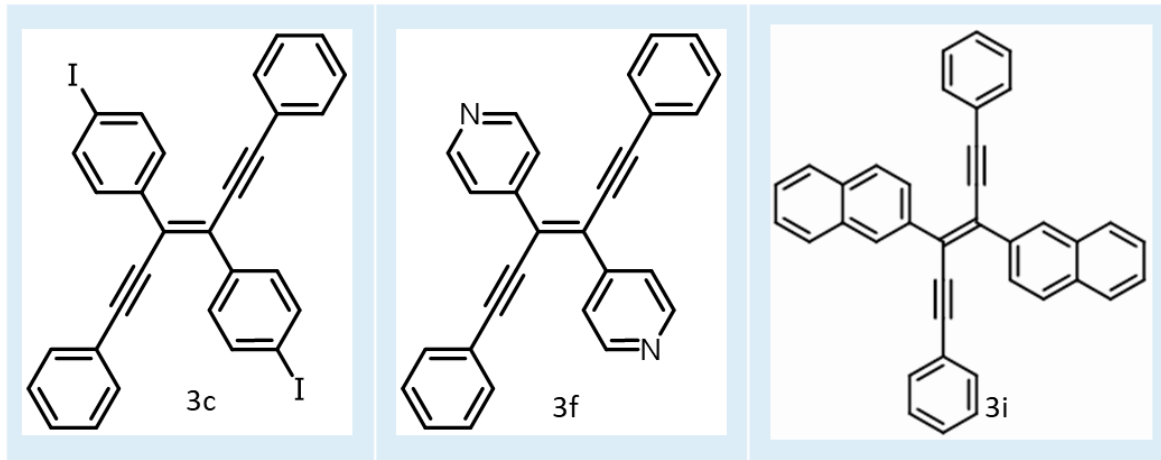
Figure 37. Other derivatives of TPE synthesized. (left) iodo-tetraphenyl *trans*-3-hexene-1,5-diyne (ITPE, 3c); (middle) nitrogen doped (N-doped TPE, 3f). (right) 1-naphthyl-tetraphenyl *trans*-3-hexene-1,5-diyne (NTPE, 3i);

In addition to ITPE **3c**, analogous nitrogen (N-doped TPE, **3f**) and naphthalene (NTPE, **3i**) derivatives were synthesized as potential candidates for graphene nanoribbon synthesis. This was done by replacing the aldehyde precursor with either 2-naphthaldehyde or isonicotinaldehyde (Fig. 38). Thus, this approach to this series of enediynes shows that we can exploit our method to synthesize TPE and ITPE to produce a large number of different structures, in similarly high yields. Although their use on gold(111) surface has not been studied yet, future work on these derivatives will help understand the cyclization parameters and reaction outcomes. We are also excited by the possibility of creating novel electronic structure of graphene nanoribbons. Their synthesis is described in the Experimental Section of Chapter 3.

3.4. Conclusion

Chapter 2 pointed to investigating the polymerization of a halogenated derivative of TPE. Chapter 3 has shown the potential of these derivatives for low-temperature graphene nanoribbon formation by using diiodo-tetraphenyl *trans*-3-hexene-1,5-diyne **3c** (ITPE) as the molecular precursor. Room temperature deposition of ITPE shows that this molecular precursor is reactive enough to undergo Ullman couplings at room temperature. This is useful because very few examples in the literature have shown to utilize this specialized precursor monomer for graphene nanoribbon synthesis Even more so, heating of these polymers induces a series of Hopf cyclizations, shown with STM images that detail bent and twisted polymer chains. Further heating causes these polymer chains to undergo cyclodehydrogenation, resulting in a planar-chiral graphene nanoribbon.

3.5. Experimental

Synthetic Procedures for Diiodo-tetraphenyl *trans*-3-hexene-1,5-diyne 3c (ITPE)
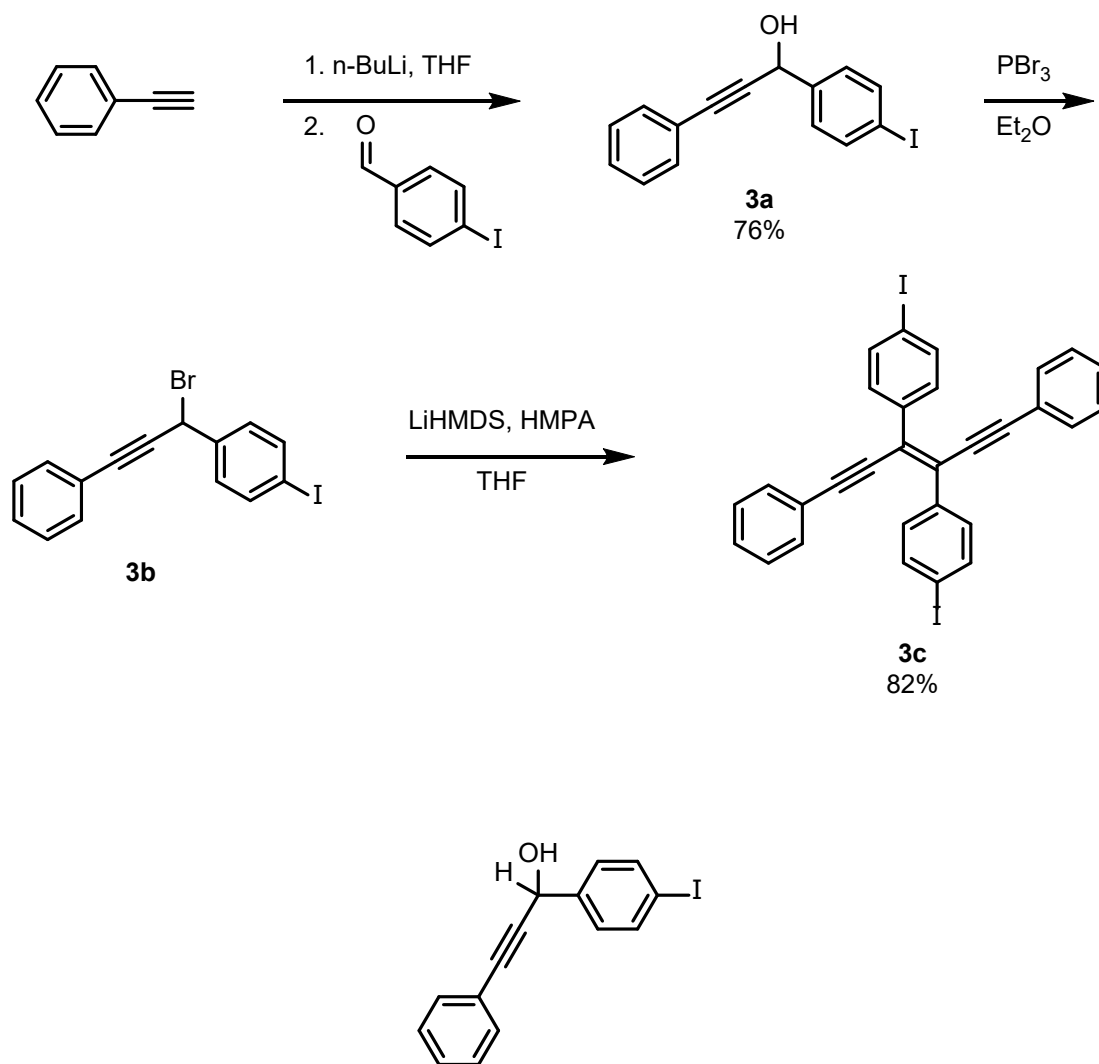
1-(4-iodophenyl)-3-phenylprop-2-yn-1-ol (3a)

Dry THF (15 mL) was added to a flame-dried 50 mL round bottom flask containing a magnetic stirring bar and placed under argon. Phenylacetylene (1.0 mL, 9.1 mmol, 1.0 eq) was added via syringe. The reaction was cooled to 0 °C to generate the lithium acetylide. A total of 6.7 mL (10.0 mmol, 1.1 eq) of 1.5 M *n*-BuLi was added dropwise via syringe. The bath was removed, allowing the reaction to warm up to room temperature. After 30 minutes, the reaction

was cooled back down to –78 ˚C. 0.45 M 1,4 iodo-benzaldehyde / THF (20 mL, 1.0 eq) was added dropwise via syringe. Once added, the bath was removed, and the reaction was left stirring at RT for 2 hours. The reaction was quenched with saturated NH$_4$Cl (20 mL). The crude organic product was extracted with EtOAc, washed with brine, dried with anh. MgSO$_4$, and then evaporated on the Rotavap. The residual oil was dried under vacuum overnight. The product was purified as an oil via column chromatography (100% hexanes to 100% DCM; rf = 0.45, 100% DCM) to give 2.3 gram of pure 1-(4-iodophenyl)-3-phenylprop-2-yn-1-ol **3a** in 76% yield. ^{1}H NMR (500 MHz, CDCl$_3$) δ (ppm) 7.74 (d, J = 8.5 Hz, 2H), 7.46 (d, J = 6.0 Hz, 2H), 7.41 – 7.30 (m, 5H), 2.3 (bs, 1H)

1-(4-Iodophenyl)-3-phenylprop-2-yn-1-bromide (3b).

Dry Et$_2$O (150 mL) was added to a flame-dried 500 mL round bottom flask containing a magnetic stirring bar and **3a** (1.0 g, 3.0 mmol, 1 eq). The flask was cooled to 0 ˚C using an ice bath. PBr$_3$ (0.57 mL, 6.0 mmol, 2 eq) was added dropwise via syringe under argon and the reaction was stirred for 30 minutes. The reaction was quenched with sat. NaHCO$_3$, (30 mL). The crude organic product was extracted with Et$_2$O, washed with brine, the separated organic layer dried with anh. MgSO$_4$, and the residual oil dried overnight under high vacuum. Compound **3b** is unstable on silica gel. Thus, this crude material was carried onto the next step.

(*E*)-1,6-(bis-4-iodophenyl)-3,4-diphenyl-3-hexen-1,5-diyne (3c).

Dry THF (45 mL) and a magnetic stirring bar were added to the flask containing 1.4 g (3 mmol, 1 eq) of crude propargylic bromide **3b**. Dry THF (20 mL) was added to a separate, flame-dried 250 mL round bottom flask containing a magnetic stirring bar. The reaction was cooled to –10 ˚C and LiHMDS (0.6 mL, 2.8 mmol, 1.1 eq) and HMPA (0.5 mL, 2.8 mmol, 1.1 eq) were added via syringe and the reaction was cooled to –90 ˚C using a frozen hexanes slurry generated with liquid nitrogen. The LiHMDS and HMPA mixture was added dropwise over 30 minutes and the reaction was left to stir and warm to room temperature. The reaction was quenched with saturated NH_4Cl (100 mL). The crude organic product was extracted with chloroform, washed with brine, and dried under vacuum. Pure pale-yellow needles of **3c** were isolated by slow evaporation of chloroform, giving 650 mg (82%). ^{1}H NMR (500 MHz, CDCl$_3$): δ (ppm) 7.78 (d, *J* = 8.7 Hz, 2H), 7.71 (d, *J* = 8.1 Hz, 4H), 7.41 (t, *J* = 7.4 Hz, 4H), 7.34 – 7.28 (m, 10H). ^{13}C-NMR (500 MHz, CDCl$_3$): δ (ppm) 128.4, 137.0, 131.4, 131.0, 128.9, 128.5, 127.6, 122.8, 99.48.
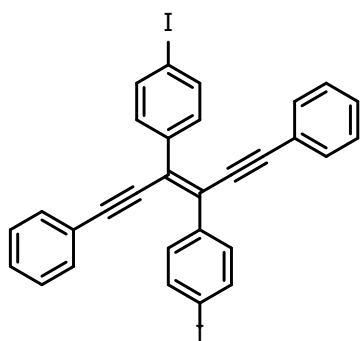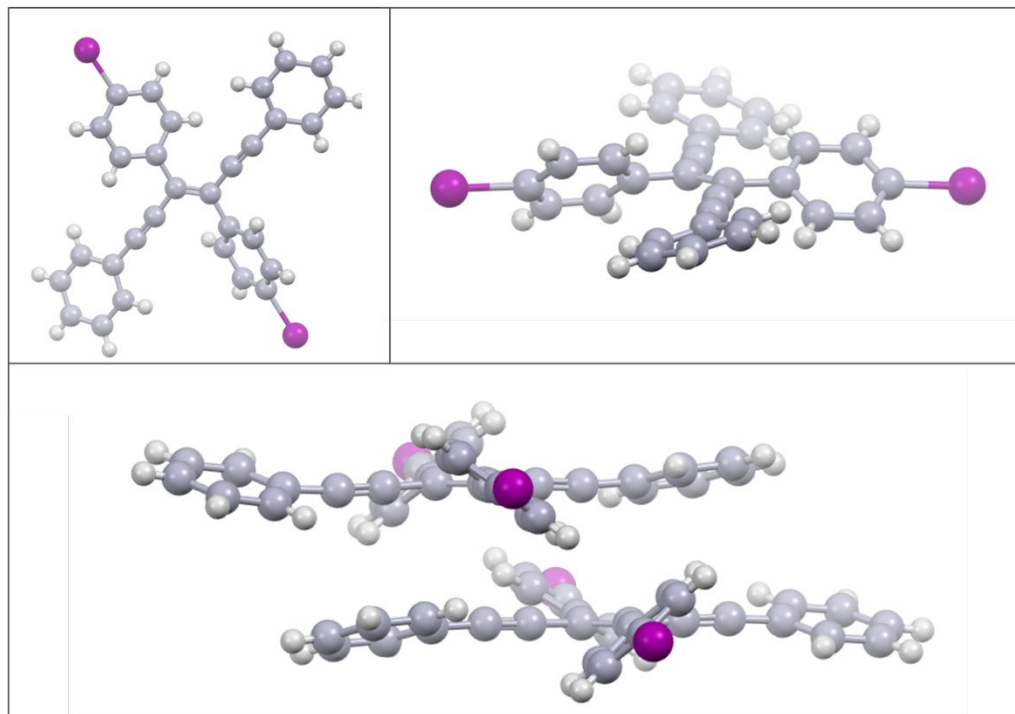
Synthetic Procedure for (E)-3,4-(bis-4-pyridyl)-1,6-diphenyl-3-hexen-1,5-diyne 3f.
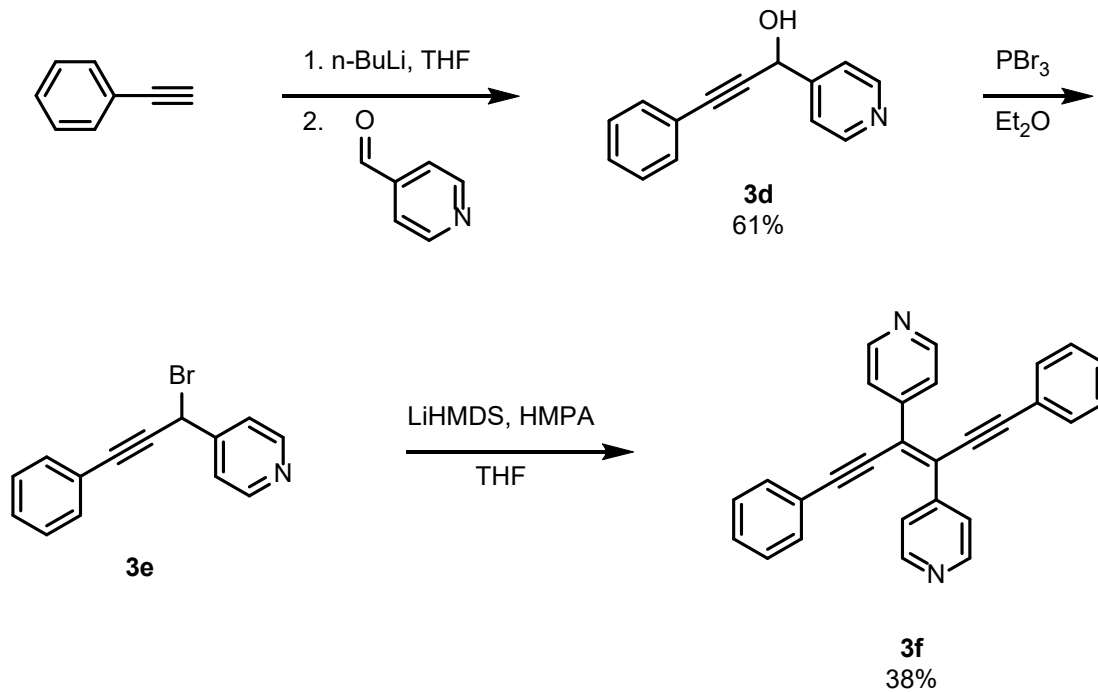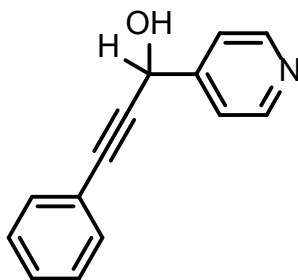
3-Phenyl-1-(4-pyridyl)prop-2-yn-1-ol (3d)

Dry THF (15 mL) was added to a flame-dried 50 mL round bottom flask containing a magnetic stirring bar and placed under argon. Phenylacetylene (1.0 mL, 9.1 mmol, 1.0 eq) was added via syringe. The reaction was cooled to 0 ˚C to generate the lithium acetylide. A total of 6.7 mL (10.0 mmol, 1.1 eq) of 1.5 M *n*-BuLi was added dropwise via syringe. The bath was removed, allowing the reaction to warm up to room temperature. After 30 minutes, the reaction was cooled back down to –78 ˚C. Isonicotinaldehyde (**2c**) (0.86 mL, 9.1 mmol, 1.0 eq) was added dropwise via syringe. Once added, the bath was removed, and the reaction was left stirring at RT for 2 hours. The reaction was quenched with saturated NH4Cl (20 mL). The crude organic product was extracted with EtOAc, washed with brine, dried with anh. MgSO4, and then evaporated on the Rotavap. The final product was purified via column chromatography (100% hexanes to 100% DCM; rf = 0.47, 100% DCM) to give 1.3 gram of pure 3-phenyl-1-(4-pyridyl)prop-2-yn-1-ol (**3d**) in 61% yield. ^{1}H NMR (500 MHz, CDCl3) δ (ppm): 8.85 (d, J = 5.5 Hz, 2H), 7.80 (d, J = 6.4 Hz, 2H), 7.65 (d, J = 6.9 Hz, 2H), 7.45 (m, 5H). ^{13}C-NMR (500 MHz, CDCl3) δ (ppm): 189.8, 150.7, 146.9, 144.5, 134.2, 131.2, 129.1, 128.7, 121.6, 121.2.
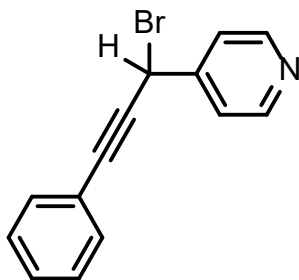
1-Bromo-3-phenyl-1-(4-pyridyl)-2-propyne (3e)

Dry Et$_2$O (150 mL) was added to a flame-dried 500 mL round bottom flask containing a magnetic stirring bar and **3d** (1.0 g, 4.8 mmol, 1 eq). The flask was cooled to 0 ˚C using an ice bath. PBr$_3$ (0.91 mL, 9.6 mmol, 2 eq) was added dropwise via syringe under argon and the reaction was stirred for 30 minutes. The reaction was quenched with sat. NaHCO$_3$, (30 mL). The crude organic product was extracted with Et$_2$O, washed with brine, the separated organic layer dried with anh. MgSO$_4$, and the residual oil dried overnight under high vacuum. Compound **3e** is unstable on silica gel. The crude material was carried onto the next step.
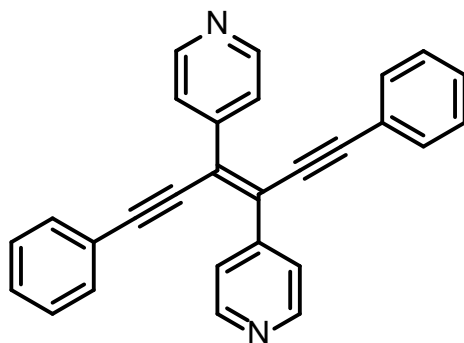
(E)-3,4-(bis-4-pyridyl)-1,6-diphenyl-3-hexen-1,5-diyne (3f)

Dry THF (45 mL) and a magnetic stirring bar were added to the flask containing 1.2 gram of crude propargylic bromide (**3e**). Dry THF (20 mL) was added to a separate flame-dried 250 mL round bottom flask containing a magnetic stirring bar. The reaction was cooled to –10 ˚C and

LiHMDS (1.0 mL, 5.3 mmol, 1.1 eq) and HMPA (0.9 mL, 5.3 mmol, 1.1 eq) were added via syringe. The reaction containing the starting material was cooled to –90 ˚C using a frozen hexanes slurry generated with liquid nitrogen. The LiHMDS and HMPA mixture was added dropwise over 30 minutes and the reaction was left to stir and warm to room temperature. The reaction was quenched with saturated NH_4Cl (100 mL). The crude organic product was extracted with chloroform, washed with brine, and dried under vacuum. A tan solid was obtained by washing with diethyl ether to afford 0.7 grams of pure (*E*)-3,4-(bis-4-pyridyl)-1,6-diphenyl-3-hexen-1,5-diyne **3f** in 38% yield. ^{1}H NMR (500 MHz, CDCl$_3$) δ (ppm): 7.08 (d, *J* = 5.1 Hz, 2H), 7.41 (d, *J* = 7.0 Hz, 2H), 7.7 (m, 3H), 7.24 (t, *J* = 1.6 Hz, 1H).

Synthetic Procedures for (*E*)-3,4-(bis-1-naphthyl)-1,6-diphenyl-3-hexen-1,5-diyne 3i.
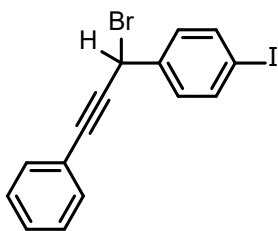

3g
44%

3h

LiHMDS, HMPA

THF

3i
49%
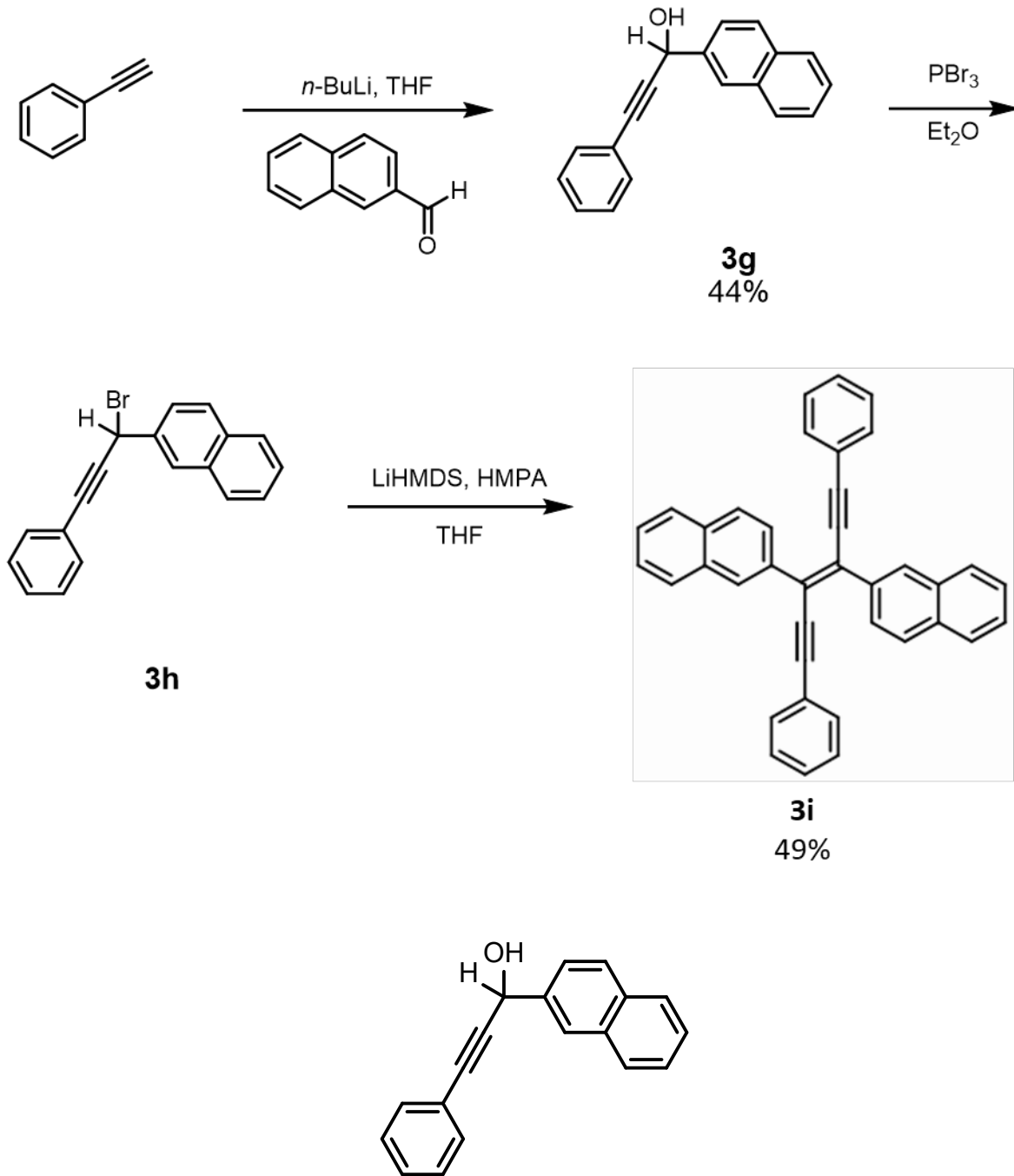
1-(2-Naphthyl)-3-phenylprop-2-yn-1-ol 3g.

Dry THF (15 mL) was added to a flame-dried 50 mL round bottom flask containing a magnetic stirring bar and placed under argon. Phenylacetylene (1.0 mL, 9.1 mmol, 1.0 eq) was

added via syringe. The reaction was cooled to 0 ˚C to generate the lithium acetylide. A total of 6.7 mL (10.0 mmol, 1.1 eq) of 1.5 M *n*-BuLi was added dropwise via syringe. The bath was removed, allowing the reaction to warm up to room temperature. After 30 minutes, the reaction was cooled back down to –78 ˚C. 2-Naphthaldehyde (1.42 g, 9.1 mmol, 1.0 eq) / 5 mL THF was added dropwise via syringe. Once added, the bath was removed, and the reaction was left stirring at RT for 2 hours. The reaction was quenched with saturated NH_4Cl (20 mL). The crude organic product was extracted with EtOAc, washed with brine, dried with anh. $MgSO_4$, and then evaporated on the Rotavap. The final product was purified via column chromatography (100% hexanes to 100% DCM; rf = 0.58, 100% DCM) to give 1.1 gram of pure 1-(2-naphthyl)-3-phenylprop-2-yn-1-ol **3g** in 44% yield. ^{1}H NMR (500 MHz, CDCl$_3$) δ (ppm): 8.85 (dd, *J* = 21.1, *J* = 4.2 Hz, 2H), 7.99 (dd, *J* = 4.35, *J* = 1.7 Hz, 1H), 7.83 (d, *J* = 16.4 Hz, 1H), 7.76 (dd, *J* = 4.8, 1.8 Hz, 1H), 7.70 (dt, J = 7.5, 1.9 Hz, 1H), 7.65 (m, 1H), 7.53 (tt, *J* = 7.7, 1.7 Hz, 1H), 7.45 (t, *J* = 5.2 Hz, 3H). ^{13}C-NMR (500 MHz, CDCl$_3$) δ (ppm): 150.9, 150.7, 146.9, 144.5, 134.3, 133.4, 131.5, 131.2, 129.1, 128.9, 128.3, 122.0, 121.6, 121.2.
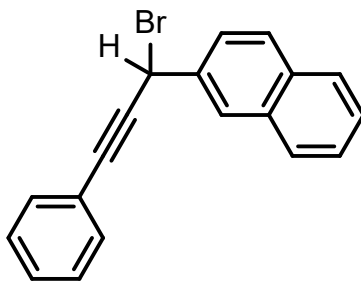
1-Bromo-3-phenyl-1-(2-naphthyl)-2-propyne (3h)

Dry Et_2O (150 mL) was added to a flame-dried 500 mL round bottom flask containing a magnetic stirring bar and **3g** (1.0 g, 3.9 mmol, 1 eq). The flask was cooled to 0 ˚C using an ice bath. PBr$_3$ (0.44 mL, 7.8 mmol, 2 eq) was added dropwise via syringe under argon and the

reaction was stirred for 30 minutes. The reaction was quenched with sat. NaHCO₃, (30 mL). The crude organic product was extracted with Et₂O, washed with brine, the separated organic layer dried with anh. MgSO₄, and the residual oil dried overnight under high vacuum. Compound **3h** is unstable on silica gel. Crude material was carried on to next step.
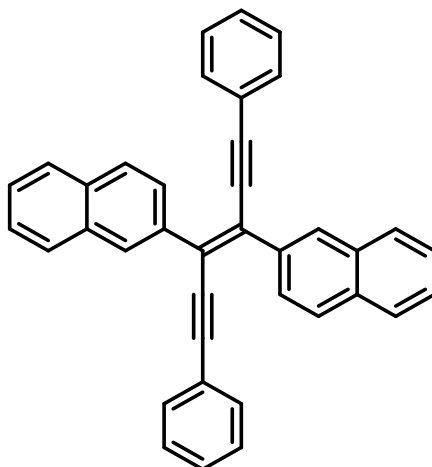


(*E*)-3,4-(bis-2-naphthyl)-1,6-diphenyl-3-hexen-1,5-diyne (3i)

Dry THF (45 mL) and a magnetic stirring bar were added to the flask containing 1.2 gram of crude propargylic bromide (**3h**). Dry THF (20 mL) was added to a separate flame-dried 250 mL round bottom flask containing a magnetic stirring bar. The reaction was cooled to –10 ˚C and LiHMDS (0.8 mL, 4.3 mmol, 1.1 eq) and HMPA (0.7 mL, 4.3 mmol, 1.1 eq) were added via syringe. The reaction containing the starting material was cooled to –90 ˚C using a frozen hexanes slurry generated with liquid nitrogen. The LiHMDS and HMPA mixture was added dropwise over 30 minutes and the reaction was left to stir and warm to room temperature. The reaction was quenched with saturated NH₄Cl (100 mL). The crude organic product was extracted with chloroform, washed with brine, and dried under vacuum. A pale-yellow powder was obtained by washing with ether to give 0.92 gram of pure (*E*)-3,4-(bis-2-naphthyl)-1,6-diphenyl-

3-hexen-1,5-diyne (**3i**) in 49% yield. ^{1}H NMR (500 MHz, CDCl$_3$) δ (ppm): 8.54 (s, 1H), 8.1 (dd,

J = 8.5, 1.7 Hz, 1H), 7.93 (d, J = 8.3 Hz, 2H), 7.91 (m, 1H), 7.52 (d, J = 3.6 Hz, 2H), 7.27 (m,

5H). ^{13}C NMR (500 MHz, CDCl$_3$) δ (ppm) 136.6, 133.2, 133.0, 131.5, 128.8, 128.5, 128.4,

128.3, 127.7, 127.3, 126.5, 126.2, 123,2, 98.9, 91.0.

3.6. References

1) Galeotti, G.; Di Giovannantonio, M.; Lipton-Duffin, J.; Ebrahimi, M.; Tebi, S.; Verdini, A.; Floreano, L.; Fagot-Revurat, Y.; Perepichka, D. F.; Rosei, F.; Contini, G. The Role of Halogens in On-Surface Ullmann Polymerization. *Faraday Discuss.* **2017**, *204*, 453–469. https://doi.org/10.1039/C7FD00099E.

2) Grill, L.; Dyer, M.; Lafferentz, L.; Persson, M.; Peters, M. V.; Hecht, S. Nano-Architectures by Covalent Assembly of Molecular Building Blocks. *Nat. Nanotech.* **2007**, *2*, 687–691. https://doi.org/10.1038/nnano.2007.346.

3) Clair, S.; de Oteyza, D. G. Controlling a Chemical Coupling Reaction on a Surface: Tools and Strategies for On-Surface Synthesis. *Chem. Rev.* **2019**, *119*, 4717–4776. https://doi.org/10.1021/acs.chemrev.8b00601.

4) Syomin, D.; Koel, B. E. Adsorption of Iodobenzene (C6H5I) on Au(111) Surfaces and Production of Biphenyl (C6H5–C6H5). *Surface Science* **2001**, *490*, 265–273. https://doi.org/10.1016/S0039-6028(01)01319-X.

5) Bieri, M.; Nguyen, M.-T.; Gröning, O.; Cai, J.; Treier, M.; Aït-Mansour, K.; Ruffieux, P.; Pignedoli, C. A.; Passerone, D.; Kastler, M.; Müllen, K.; Fasel, R. Two-Dimensional Polymer Formation on Surfaces: Insight into the Roles of Precursor Mobility and Reactivity. *J. Am. Chem. Soc.* **2010**, *132*, 16669–16676. https://doi.org/10.1021/ja107947z.

6) Schlögl, S.; Heckl, W. M.; Lackinger, M. On-Surface Radical Addition of Triply Iodinated Monomers on Au(111)—the Influence of Monomer Size and Thermal Post-Processing. *Surface Science* **2012**, *606*, 999–1004. https://doi.org/10.1016/j.susc.2012.02.011.

7) Eichhorn, J.; Nieckarz, D.; Ochs, O.; Samanta, D.; Schmittel, M.; Szabelski, P. J.; Lackinger, M. On-Surface Ullmann Coupling: The Influence of Kinetic Reaction Parameters on the Morphology and Quality of Covalent Networks. *ACS Nano* **2014**, *8*, 7880–7889. https://doi.org/10.1021/nn501567p.

8) Peyrot, D.; Silly, F. On-Surface Synthesis of Two-Dimensional Covalent Organic Structures versus Halogen-Bonded Self-Assembly: Competing Formation of Organic Nanoarchitectures. *ACS Nano* **2016**, *10*, 5490–5498.

https://doi.org/10.1021/acsnano.6b01938.

9) Bronner, C.; Marangoni, T.; Rizzo, D. J.; Durr, R. A.; Jørgensen, J. H.; Fischer, F. R.; Crommie, M. F. Iodine versus Bromine Functionalization for Bottom-Up Graphene Nanoribbon Growth: Role of Diffusion. *J. Phys. Chem. C* **2017**, *121*, 18490–18495. https://doi.org/10.1021/acs.jpcc.7b02896.

10) Judd, C. J.; Haddow, S. L.; Champness, N. R.; Saywell, A. Ullmann Coupling Reactions on Ag(111) and Ag(110); Substrate Influence on the Formation of Covalently Coupled Products and Intermediate Metal-Organic Structures. *Sci Rep* **2017**, *7*, 14541. https://doi.org/10.1038/s41598-017-13315-1.

11) Fritton, M.; Duncan, D. A.; Deimel, P. S.; Rastgoo-Lahrood, A.; Allegretti, F.; Barth, J. V.; Heckl, W. M.; Björk, J.; Lackinger, M. The Role of Kinetics versus Thermodynamics in Surface-Assisted Ullmann Coupling on Gold and Silver Surfaces. *J. Am. Chem. Soc.* **2019**, *141*, 4824–4832. https://doi.org/10.1021/jacs.8b11473.

12) Keerthi, A.; Sánchez-Sánchez, C.; Deniz, O.; Ruffieux, P.; Schollmeyer, D.; Feng, X.; Narita, A.; Fasel, R.; Müllen, K. On-surface Synthesis of a Chiral Graphene Nanoribbon with Mixed Edge Structure. *Chem. Asian J.* **2020**, *15*, 3807–3811. https://doi.org/10.1002/asia.202001008.

CHAPTER 4. ANNULATED DIIODO-TETRAARYL ENEDIYNES FOR GRAPHENE NANORIBBON SYNTHESIS ON GOLD SURFACE

4.1. Background

In an effort to utilize the findings from Chapters 2 and 3, a proposed annulated system is planned to be used for novel graphene nanoribbon formation. Chapter 2 discusses the synthesis and studies of tetraphenyl *trans*-3-hexene-1,5-diyne **2c** (TPE). It was found that the conjugated enediyne backbone can efficiently undergo two consecutive Hopf cyclizations on Au(111) in ultrahigh vacuum. Further heating provided a cyclodehydrogenation product with five-membered rings. Following this finding, an iodine derivative (ITPE) was synthesized in effort to create polymers that could react under the same conditions. Chapter 3 discusses the formation of more highly conjugated polymers on Au(111) that undergo a Hopf cyclization when heated and subsequently cyclodehydrogenate to form fully conjugated graphene nanoribbons.

Chapter 4 looks at problems encountered in extending this principle to the formation of polymers with extended π-conjugation, and efforts to create a new precursor system, which when reacted under the same conditions, can form uniformly structured graphene nanoribbons (GNRs).

4.1.1. Occurrence of Different Rotamers

(a)

(b)

(c)

(d)

non-planar
conformation
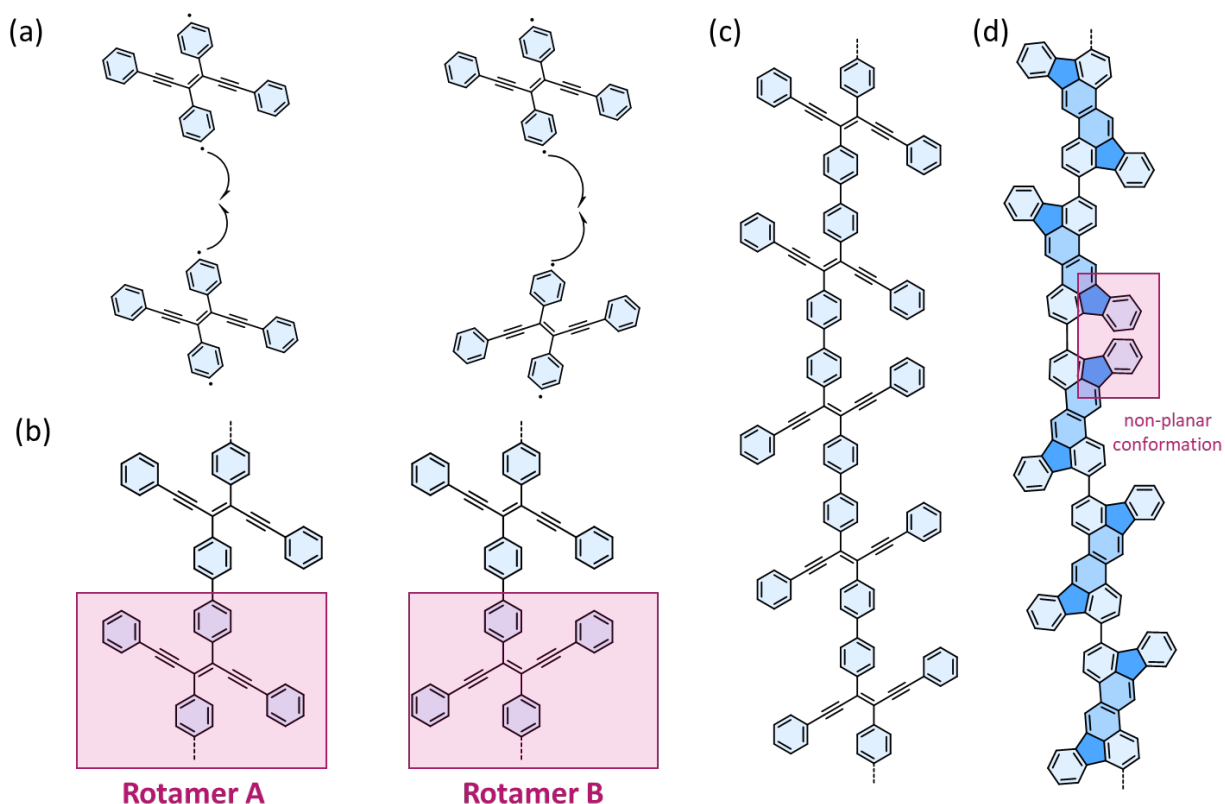
Rotamer A   **Rotamer B**

Figure 38. Diiodo-tetraphenyl *trans*-3-hexene-1,5-diyne (ITPE) couples on Au(111) to form different rotamers. (a) Diradicals of ITPE couple at room temperature on Au(111); (b, rotamer A) symmetrical coupling of diradicals; (b, rotamer B) asymmetrical coupling of diradicals; (c) structure of ITPE polymer on Au(111) after Hopf cyclization; (d) structure of ITPE polymer on Au(111) after cyclodehydrogenation step, nonplanar structure occurs.

The occurrence of different rotamers was observed by STM in Chapter 3. Iodo-tetraphenyl *trans*-3-hexene-1,5-diyne was shown to polymerize on Au(111). Some segments of this polymer produced uniform π-conjugated polymers. This was achieved through Hopf cyclizations and cyclodehydrations steps. Even then, heating of carbon polymers produced annulated structures that had uniform definition, most polymers resulted in ill-defined structures that were not characterizable by STM and AFM.

It was determined that this was due to the occurrence of different rotamers when TPE was sublimed onto the Au(111) surface. A rotamer is a molecule that can be interconverted by the rotation of single bonds. While this is true in the case of traditional organic chemistry in solution, on-surface synthesis requires different structural definitions. The molecules that contain sigma bonds are nonetheless confined to 2-D platform through van-der-Waals interactions, and therefore experience restricted rotation when on-surface.

Typically, polymers that are formed via sigma bond linkages of monomers can rotate freely in solution. Monomeric units within a polymer will align in a way that minimizes steric hindrance, meaning that the monomers will evenly space apart.[1] When synthesized on-surface, monomers are deposited and reacted on a metal surface. This hinders their ability to freely rotate and assemble in an energetically favorable confirmation. Instead, molecules must lay flat on the surface.[2] In the case of Chapter 3, iodo-tetraphenyl *trans*-3-hexene-1,5-diyne was shown to polymerize but in a way that produced inconsistent and uncharacterizable structures. It was realized that this was because monomers were not polymerizing in a uniform fashion. Figure 39a shows the how different rotamers of ITPE can form on surface and through an Ullman coupling of surface stabilized radicals. If purely consistent polymers were formed, monomers would be aligning and polymerizing in a symmetrical fashion only from rotamer A (Fig. 39b, left). However, monomers were also shown to align and assemble in an asymmetric fashion, i.e., rotamer B, (Fig. 39b, right). This propensity to polymerize either from rotamer A or rotamer B causes the polymers to become non-uniform overall. This is particular to the case of iodine-substituted precursors because initial deposition at room temperature forms surface-stabilized radicals that do not desorb, but quickly couple to form well-defined polymers. Polymers typically align in a symmetrical fashion; however, some poorly fitting asymmetrical segments

can be observed throughout. Initial heating does induce a Hopf cyclization, which results in the polymers becoming twisted and bent on the gold surface. This is because after the Hopf cyclization step, phenyl rings adopt a conformation where they are bent away from the surface (see Chapter 2). Thus, further heating produces polymers that are a result of the cyclodehydrogenation step. However non-planar segments within the molecule that occur from rotamer B, cause the polymer to bend and twist. This is depicted schematically in Fig. 39d, where portions of polymer result in a non-planar conformation, highlighted in red. Therefore, polymers that are heated at higher temperatures result in non-uniform structures and are hard to characterize and study with STM and AFM.
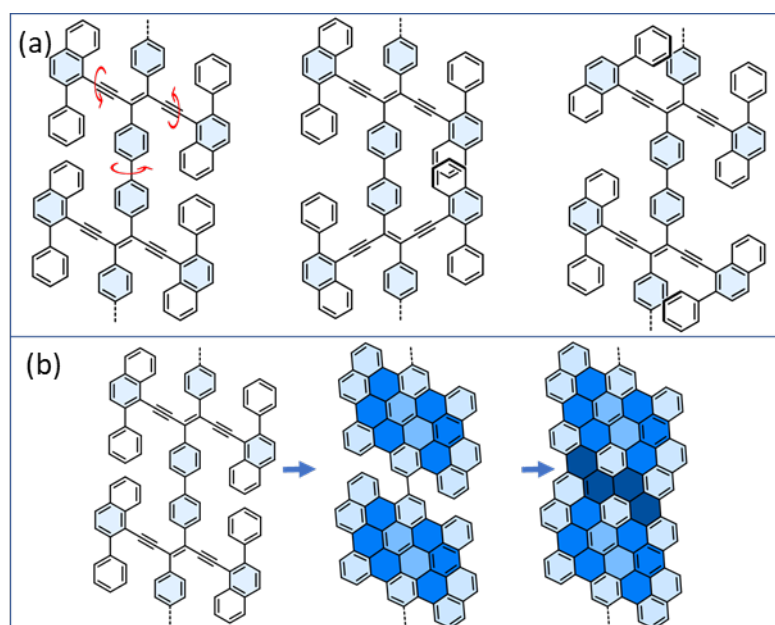
Figure 39. Hypothesized annulated system to produce graphene nanoribbons. (a) polymers of diiodo-2-phenyl-naphthalene-enediyne (I2PNE), steric hindrance occurs from any other rotamer or possible conformation; (b) symmetrical polymerization of 12PNE as a result of only one possible rotamer and subsequent cyclization products.

To bypass this problem, a more highly annulated system, similar to the diiodo-tetraphenyl *trans*-3-hexene-1,5-diyne (ITPE) was suggested. (E)-3,4-(Bis-2-phenyl-naphthyl)-1,6-(bis-4-iodophenyl)-3,4-diphenyl-3-hexen-1,5-diyne (**4g**, I2PNE) (Fig. 40) was proposed as a precursor molecule, as well as analogous methyl precursor (E)-3,4-(bis-2-phenyl-3-methyl-naphthyl)-1,6-(bis-4-iodophenyl)-3,4-diphenyl-3-hexen-1,5-diyne (**4m**, I2P3MNE). It was hypothesized that by extending the system with phenyl rings on the sides of the molecule, rotations that are permitted in the ITPE system would be restricted in these due to steric clashes (Fig. 40a). Ullman coupling resulting in different rotamers would be prevented because the bond linkages between asymmetrically aligned monomers would be prevented by steric hindrance (Fig. 40a, middle). This would be caused by an overlapping of the neighboring 1-ethynyl-2-phenyl-naphthyl units in Rotamer B. Rotamer A should then be the predominant structure formed on-surface. Because of the added aromatic units, this makes the molecule asymmetrical and adds the possibility of a second rotation. Rotations around the alkyne section of the molecule after deposition could therefore also result in inconsistent monomer formation on the gold surface. However, the rotation of the 1-ethynyl-2-phenyl-naphthyl unit is also limited because of steric hindrance. The resulting structure would have interactions between the side naphthyl units and the phenyl units connected (Fig. 40a, right). Additionally Figure 40b shows how asymmetrical alignment to form consistent polymers, could produce graphene nanoribbons through subsequent cyclizations.

4.2. Methods

To synthesize the two variations of the annulated systems, two different starting iodinated precursors were first made. These were made by following combinatorial work of González (2003) and Yan (2020), according to the synthetic scheme in Figure 41.[3,4] 2-Hexynyl-

benzaldhyde (**4a**) was synthesized in 93% via Sonogashira coupling between 2-bromobenzal-dehyde and 1-hexyne in water.[5]

4.2.1. Synthesis of Annulated Naphthyl Iodides
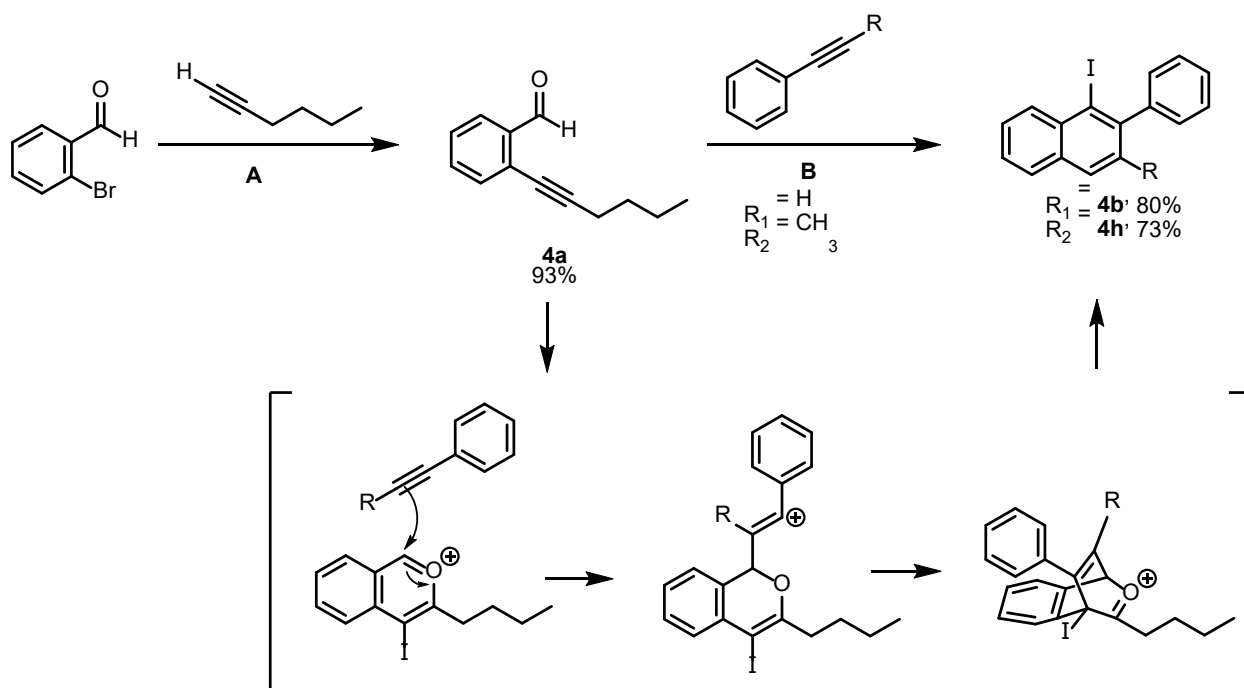
Figure 40. Synthesis of iodo-compounds for annulated systems. (A) 1-hexyne, Pd(PPh3)4, CuI, pyrrolidine, H2O, 80 °C, 24 h (4a, 93%); (B) (R_1 = H) phenylacetylene, I2, DCM, 1.5 h (4b, 80%), (R_2 = CH3) 1-phenylprop-1-yne, I2, DCM, 1.5 h (4b, 80%; 4h, 73%); (bottom)

It should be noted that use of this reaction does not require the additional steps that involve drying solvent, since the reaction is carried out in aqueous conditions. At first, typical Sonogashira reaction conditions were used to couple the alkyne and aryl motif (Fig. 41). This involved using rigorously dried tetrahydrofuran, catalytic amounts of bis(triphenylphosphine)-palladium(II) dichloride (Pd(PPh3)2Cl2), and copper iodide (CuI) under air-free conditions.

Reactions were refluxed overnight, but it was found that a residual amount of 2-bromo-benzaldehyde always persisted, meaning that the reaction never went to completion. Additionally, separating the starting material, 2-bromobenzaldhyde, from the product, 2-hexynyl-benzaldehyde, proved to be too difficult to achieve. Both compounds had very similar Rf$_s$ on silica gel thin layer chromatography in 100% hexanes, thus they would be very difficult to separate via silica-gel column chromatography. It was only through ^{1}H nuclear magnetic resonance (^{1}H-NMR) spectroscopy that concentrations of both products could be determined, and the reaction could be monitored for completion that way. For the starting material 2-bromo-benzaldehyde, the aldehyde proton has a peak in ^{1}H-NMR at 10.37 ppm. In comparison, the product 2-hexynyl benzaldehyde has its aldehyde proton show up slightly more downfield at 10.54 ppm.

Initially, this reaction was scaled up in an attempt to purify at least five grams of product. However, ^{1}H -NMR always showed the presence of both 10.54 ppm and 10.37 ppm peaks.

To bypass this problem, alternative reactions that produced higher yields were investigated. After running this reaction according to Bhattacharya (2004), crude ^{1}H -NMR showed quantitative conversion of the starting material. The only observable aldehyde peak was at 10.54; therefore, this reaction was chosen as the best route moving forward. Additionally, this reaction requires a very simple procedure, since the reaction is done in water.

This reaction uses pyrrolidine as well as catalytic tetrakis(triphenylphosphine)palladium(0) (Pd(PPh$_3$)$_4$) and copper iodide (CuI). Initial trials for this reaction resulted in complete consumption of starting material but resulted in yields below 70%. It was found, that by deoxygenating the water through sparging, yields were increased to 93%. Sparging was done by using a long needle connected to an argon line and a venting needle. The long needle was

submerged into the solution, and while stirring, the water, base, and catalysts were sparged by passing argon through the flask.

Barluenga and co-workers showed that iodine could be used to form naphthalene-based molecules starting from **4a** and the corresponding aryl alkyne. The mechanism is depicted in the bottom of Figure 41. In this mechanism, the iodine first adds to the alkyne causing a bond to be formed between the alkyne and neighboring aldehyde oxygen. The second alkyne then adds to the alpha carbon, generating a carbocation on the alkene. From here, the lone pair on the oxygen then moves towards the hexynyl chain, causing the double bond to connect to the carbocation. This forms the second ring of the naphthyl unit. After this intermediate, a retro-Diels Alder reaction takes place, causing pentanal to be expelled from the molecule. From here, 1-iodo-2-phenylnaphthalene (**4b**) and 1-iodo-2-phenyl-3-methylnaphthalene (**4h**) were obtained in 80 and 73% yields, respectively.

By reacting either phenylacetylene or 1-phenylpropyne with 1-hexyne-benzaldehyde, **4b** or **4h** are obtained, respectively. This is because, while the iodine always ends up in position 1' of the naphthyl unit, the phenyl group on the alkyne always ends up in position 2'. Furthermore, the proton or methyl group from the alkyne always ends up in position 3' of the naphthyl unit. This mechanism makes for the perfect pathway for discovering new derivatives of this annulated system.

4.2.2. Synthesis of Annulated Diiodo-tetraphenyl *trans*-3-hexene-1,5-diyne Compounds
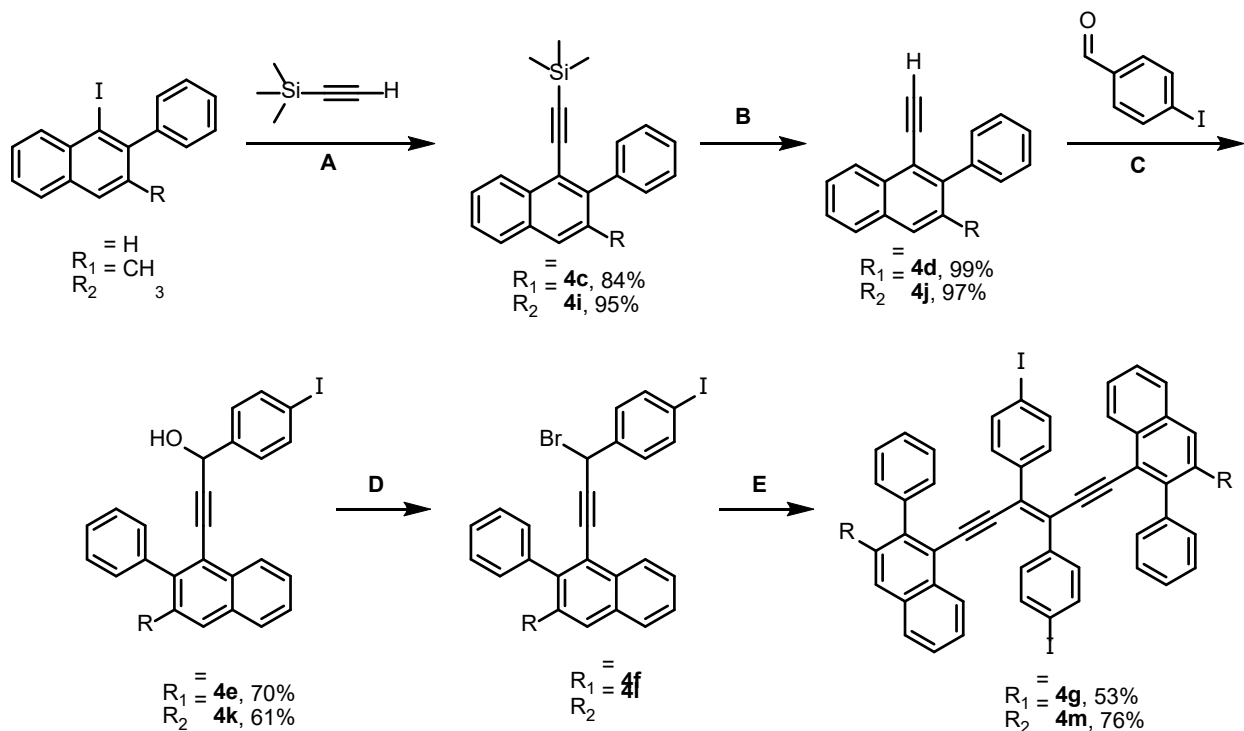
Figure 41. Synthetic scheme for methyl and non-methyl 2-phenyl-napthlene enediynes (I2PNE and I2P3MNE). (A) Trimethylsilylacetylene, PdCl$_2$(PPh$_3$)$_2$, CuI, Et$_3$N, 85 °C, 24 h (4c, 84%; 4i, 95%); (B) K$_2$CO$_3$, MeOH, 2h (4d, 99%; 4j, 97%); (C) 1. *n*-BuLi, THF, 2. 1,4-iodobenzaldehyde (4e, 70%; 4k, 61%); (D) PBr$_3$, Et$_2$O, 2h (4f, 4l); (E) LiHMDS, HMPA, -90 °C, THF (4g, 53%; 4m, 76%).

After achieving the iodine-precursor for both systems, the rest of the synthesis was carried out to afford final annulated compounds **4g** and **4m,** according to Figure 42. First, the corresponding aryl iodide was reacted with trimethylsilyl acetylene (TMS) via a Sonogashira reaction. This version of the Sonogashira reaction uses standard conditions (non-aqueous) and was run using triethylamine as the solvent. Palladium tetrakis(triphenylphosphine) (Pd(PPh$_3$)$_4$) and CuI were used as the catalysts, and the reaction was run overnight while refluxing under argon. This produced the protected alkyne product in high yields, both of which could be

purified via silica gel column chromatography. Compounds **4c** and **4i** were synthesized in 84 and 95%, respectively. From here, a simple deprotection step using catalytic amounts of potassium carbonate (K_2CO_3) in methanol was conducted. This reaction needed about two hours to complete and produced the terminal alkyne product. Compound **4d**, 1-ethynyl-2-phenylnaphthalene, and **4j**, 1-ethynyl-2-phenyl-3-methylnaphthalene were synthesized in 99 and 97%, respectively. Both of these products could also be recrystallized or precipitated from any of the starting material by adding hexanes.

From here, the propargyl alcohols were synthesized. It should be noted that the propargyl product does not show up as strongly on thin layer chromatography under 254 nm UV, a method used to monitor most of the synthesized products to this point. This made initial purifications and monitoring of the reaction difficult. However, both propargyl alcohols **4e** and **4k** were synthesized in 70 and 61%, respectively. After this, the propargyl alcohols could be converted to their respective propargyl bromides by brominating with phosphorus tribromide (PBr_3) in diethyl ether. This produced compounds **4f** and **4l**, which are shown in Figure 42. Just as in Chapters 2 and 3, it should be noted that these compounds cannot be isolated due to the rapid heterolysis of the C-Br bond upon exposure to moisture.

To prepare for the next step, the crude material was then dissolved in dry THF under argon. In a separate flask cooled to 0 °C, tetrahydrofuran (THF), lithium bis(trimethylsilyl)amide (LiHMDS), and hexamethylphosphoramide (HMPA) were added under argon. From here, the crude material flask was cooled to –90 °C. The LiHMDS and HMPA mixture was transferred in, and the crude mixture changed from dark red to dark green.

From here, a yellow precipitate was noted to form from the solution. The resulting mixture was then dissolved in chloroform and extracted. Both compounds were difficult to dissolve in

chloroform entirely, so it is likely that some of the material was lost in this step. To avoid this, three times the amount of solvent used in the reactions was used to extract the compound. After drying down, pure product could be obtained by washing with diethyl ether. Overall, annulated hydro (**4g**) and methyl (**4m**) iodo-2-phenyl-naphthalene enediyne molecules were synthesized in 53 and 76% yield, respectively.
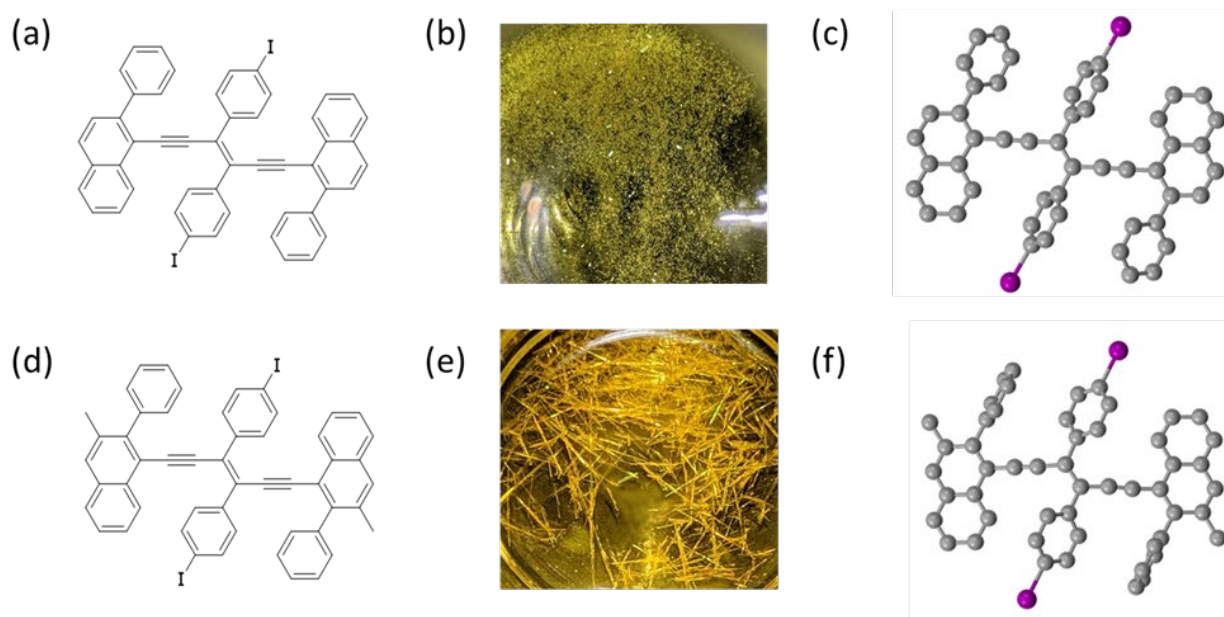
Figure 42. Recrystallization of I2PNE and I2P3MNE. (a-c): diiodo-2-phenyl-naphthalene enediyne (I2PNE), (a) chemical structure of, (b) crystals, (c) crystal structure; (d-f): diiodo-2-phenyl-3-methyl-naphthalene enediyne (I2P3MNE), (d) chemical structure, (e) crystals, (f) crystal structure.

Crystal structures of both final compounds I2PNE (**4g**) and 12P3MNE (**4m**) were obtained (Figure 43). Compound **4g** has only low solubility in chloroform. Although the compound appears to dissolve when heated in chloroform, no spectra could be obtained by NMR at room temperature (i.e., the compound crystallized out in the NMR tube). To bypass this problem, several solvents were tested for solubility. It was found that compound **4g** has a much better

solubility in 1,1,2,2-tetrachloroethane ($C_2H_2Cl_4$) when heated. Therefore, ^{1}H-NMR and ^{13}C-NMR spectra could be obtained by running the sample in deuterated 1,1,2,2-tetrachloroethane ($C_2D_2Cl_4$). This is somewhat peculiar because no other final compound discussed in this work had this poor solubility in chloroform. It is obvious that the annulated system increases the non-polar nature of the aromatic system and further induced *pi*-stacking between molecules, making it difficult to solubilize. Compound **4g** could therefore be recrystallized by dissolving it in 1,1,2,2-tetrachloroethane, and layering it with hexanes. On the other hand, compound **4m** could be analyzed via NMR in deuterated chloroform. This is because the methyl group hinders the π-stacking that would typically occur.[6] Thus, the intermolecular forces between the molecules are weakened and can solubilize in chloroform like the previously discussed molecules. Crystals of this compound were obtained by dissolving compound **4m** in chloroform and layering hexanes on top. Compound **4g** produces smaller and pale-yellow square-like crystals, while compound **4m** produces larger bright orange needles.

4.3. Results and Discussion

Figure 44 shows how the annulated system for **4g** is expected to react on gold surface. The extended π-systems and additional aromatic units should enable the molecules to only favor one rotamer confirmation. Before synthesizing this, collaboration studies allowed for density functional theory (DFT) calculations of the proposed graphene nanoribbon (GNR) structure (Figure 44, top structure). Figure 44 (top, left calculation) shows the structure optimization and band structure without spin, whereas Figure 44 (top, right calculation) shows the structure optimization and band structure with the associated free spin. The e/bohr^3 value for highlighted

red regions is 4.0 x 10^{-9}, which is considered too small. The absolute magnetization is also 0.0 which means that the GNR is not spin-polarized.
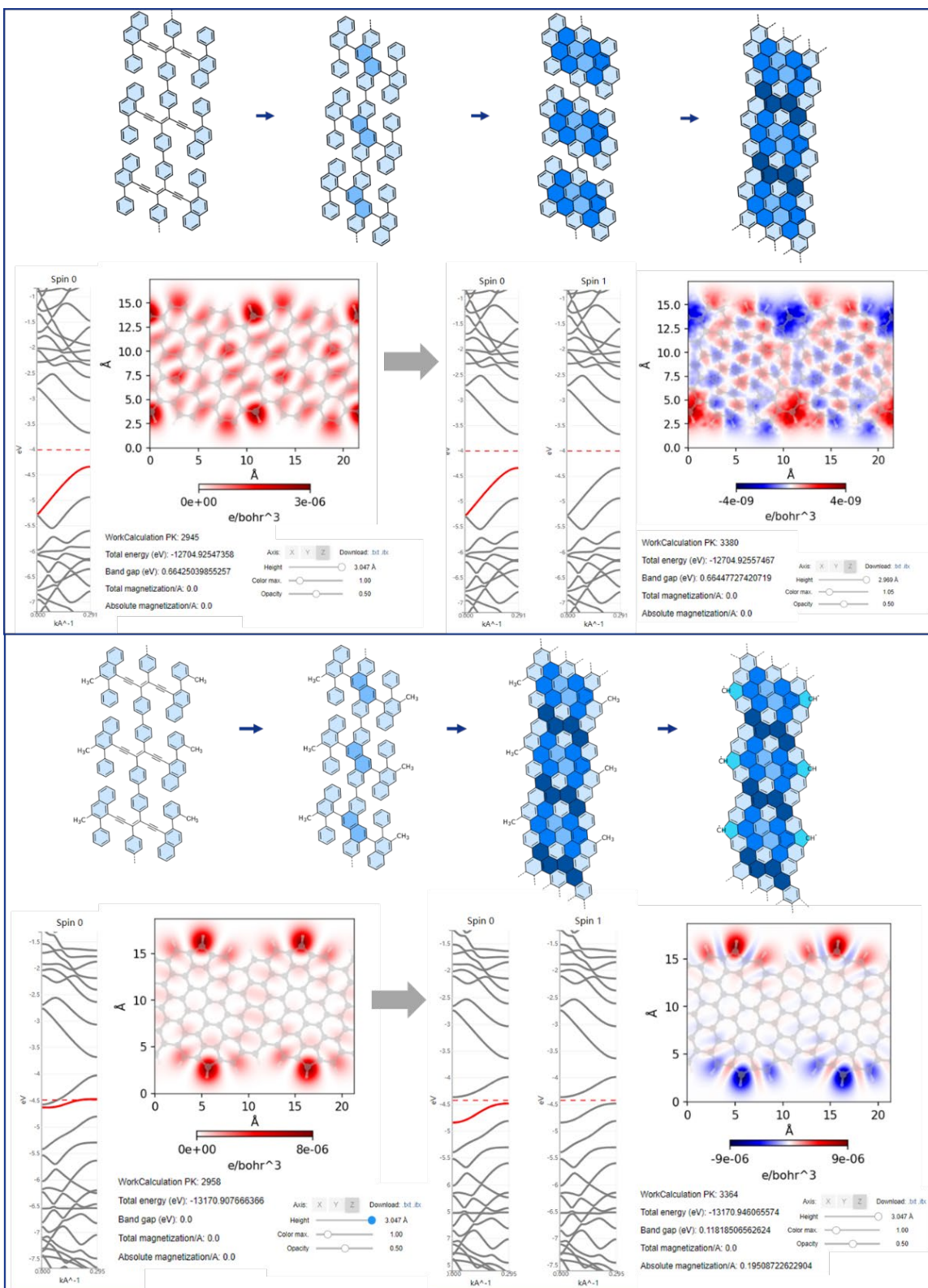
Figure 43. DFT calculations for annulated systems. (top) I2PNE's hypothesized progression GNRs Au(111); (bottom) I2P3MNE hypothesized progression to GNR on Au(111), metallic.

142

Figure 44 (bottom structure) shows how the annulated system for the alternative methyl version would convert to a novel GNR on surface. It is still expected to align properly on gold surface, while the extended π-system and additional aromatic units should favor a single rotamer confirmation. Due to the inclusion of the methyl group, **4m** would undergo one additional cyclization step to form a 5-membered ring. This would be achieved by C-H activation and cyclization of benzylic methyl groups, which has been demonstrated in other work.[7,8,9] In work by Narita and co-workers in 2021, the authors showed that *ortho*-tolyl-substituted 9,9'-dibromobianthryl could form methylene-bridged pentagons along the edges of the GNR. Furthermore, heating of these structures resulted in some sites that had singly-hydrogenated apexes.

DFT calculations were also conducted for the GNR structure **4m** as a comparison to the non-methyl version above. Figure 44 (bottom, left calculation) shows the structure optimization and band structure without spin, where Figure 44 (bottom, right calculation) shows the structure optimization and band structure considering spin. The band gap calculated for **4m** is 0.0 which means that the chain would be considered metallic. Furthermore, the absolute magnetization is approximately 0.195, which means that this structure hould be spin-polarized, owing to the localized CH radical sites.

4.4. Conclusion

In conclusion, two diiodo-tetraphenyl *trans*-3-hexene-1,5-diyne (ITPE, Chapter 3) derivatives were synthesized for on-surface studies. Diiodo-2-phenylnaphthalene enediyne (I2PNE) and diiodo-2-phenyl-3-methylnaphthalene enediyne (12P3MNE) were synthesized in effort to produce polymers that would give symmetrical structures as a result of only one rotamer

occurrence. Predicted GNR structures of each final compound are expected to have different electronic properties. This is because of the different edge structure that can be afforded via benzylic cyclization of methyl groups. These compounds will be used in future studies in an effort to produce novel GNRs with magnetic properties.

4.5. Experimental

Synthetic Procedures for (E)-3,4-(bis-2-phenyl-naphthyl)-1,6-(bis-4-iodophenyl)-3,4 diphenyl-3-hexen-1,5-diyne (4g)
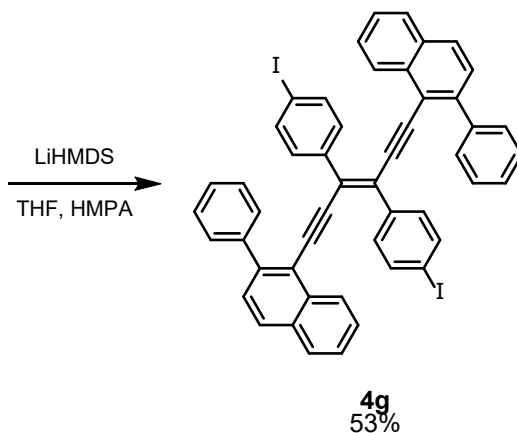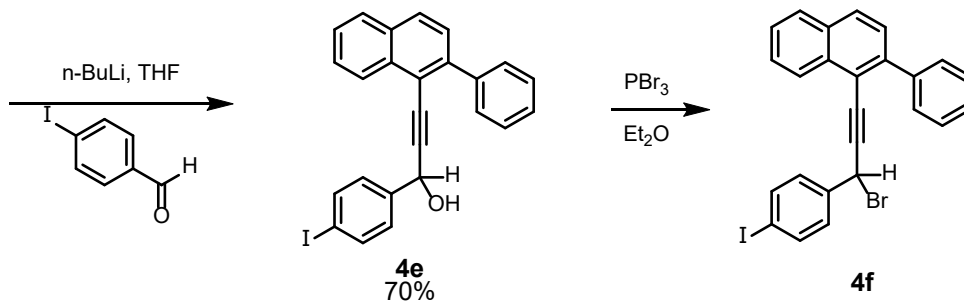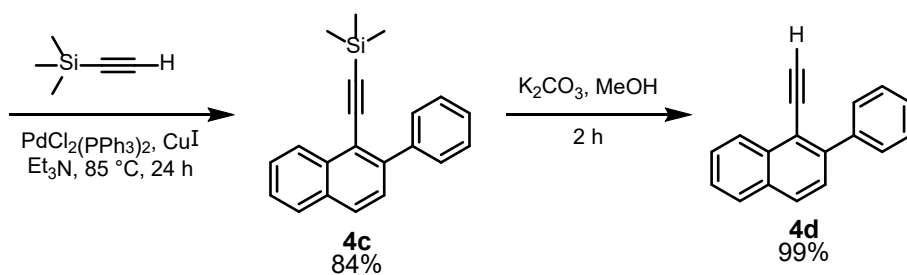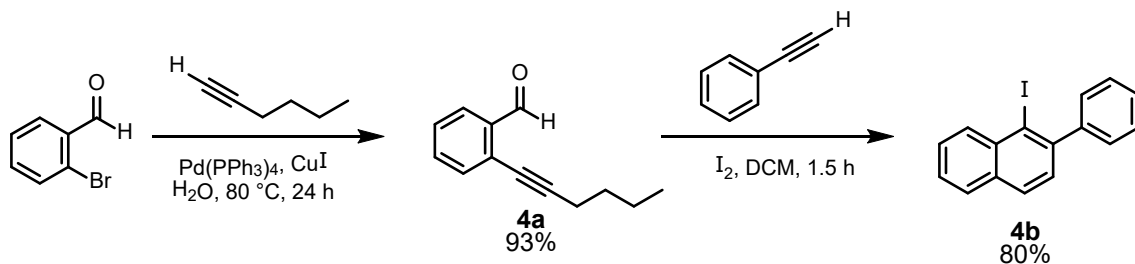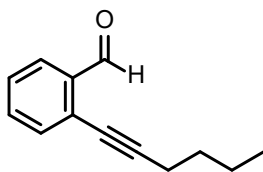
2-(Hex-1-yn-1-yl)benzaldehyde (4a)[5]

To a two-neck round bottom flask was added deionized water (250 mL, 0.2M), 2-bromobenzaldehyde (5.83 mL, 50 mmol, 1.0 eq), and pyrrolidine (6.12 mL, 75 mmol, 1.5 eq). The reaction was sparged with argon for 10 minutes. Pd(PPh$_3$)$_4$ (175 mg, 0.5 mol%) and CuI (95.2 mg, 1.0 mol%) were added to the flask under argon. 1-hexyne (10.4 mL, 180 mmol, 1.8 eq) was added dropwise. The reaction was heated to 80 ˚C for 16 hours. The reaction was cooled to room temperature and the crude organic mixture was extracted with chloroform, washed with brine, and dried under vacuum. The pure organic product was isolated via column chromatography (100% chloroform; rf = 0.75, 100% chloroform) to afford a dark yellow oil, **4a** (8.6 grams, 93% yield. ^{1}H NMR (500 MHz, CDCl$_3$) δ (ppm) 10.54 (s, 1H), 7.88 (d, J = 7.8 Hz, 1H), 7.51 – 7.49 (m, 2H), 7.38 (t, J = 6.4 Hz, 1H), 2.49 (t, J = 7.21 Hz, 2H), 1.64 – 1.58 (m, 2H), 1.53 – 1.48 (m, 2H), 0.96 (t, J = 7.3 Hz, 3H). ^{13}C-NMR (500 MHz, CDCl$_3$) δ (ppm) 192.3, 136.0, 133.7, 133.3, 127.9, 127.0, 98.1, 53.4, 30.6, 23.4, 22.1, 19.3, 13.6.
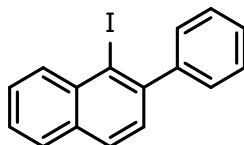
1-Iodo-2-phenylnaphthalene (4b)[3,4]

To a round-bottom flask equipped with a stirring bar, was added CH_2Cl_2 (0.1 M), **4a** (2 grams, 10.7 mmol, 1 eq), I_2 (1.1 grams, 10.7 mmol, 1 eq), and phenylacetylene (1.2 mL, 10.7 mmol, 1 eq). The reaction was stirred for 1.5 hours at room temperature and then quenched by the addition of sat. aq. $Na_2S_2O_3$ solution. The crude organic mixture was extracted with chloroform, washed with brine, and dried under vacuum. The pure organic compound, **4b**, was isolated via column chromatography (10 (ppm)1 hexanes (ppm) dichloromethane; rf = 0.5, 100% hexanes) to afford a dark red oil (2.8 grams, 80% yield). ^{1}H NMR (500 MHz, CDCl₃) δ (ppm) 8.33 (d, J = 8.5 Hz, 1H), 7.84 (t, J = 8.6 Hz, 2H), 7.62 (t, J = 7.7 Hz, 2H), 7.54 (t, J = 7.6 Hz, 1H), 7.49 – 7.38 (m, 6H). ^{13}C-NMR (500 MHz, CDCl₃) δ (ppm) 146.2, 146.1, 135.0, 133.5, 133.0, 130.0, 128.5, 128.3, 128.1, 128.0, 127.6, 126.6, 104.1.
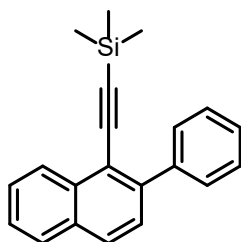
Trimethyl((2-phenylnaphthalen-1-yl)ethynyl)silane (4c)[10]

To a flame dried round-bottom flask equipped with a stirring bar was added triethylamine (42 mL, 0.1 M) and **4b** (1.36 grams, 4.12 mmol, 1 eq)**.** The mixture was sparged for 10 minutes. Following this, Pd(PPh₃)₂Cl₂ (57 mg, 2 mol%), CuI (39 mg, 5 mol%), and trimethylsilyl acetylene (0.61 mL, 4.9 mmol, 1.2 eq) were added. The reaction was heated to 90 ˚C for 12

hours. The crude mixture was filtered through celite and concentrated under vacuum. The pure organic compound, **4c**, was isolated via column chromatography (100% petroleum ether; rf = 0.40) to afford a dark yellow oil (1.0 gram, 84%). ^{1}H NMR (500 MHz, CDCl$_3$) δ (ppm) 8.47 (d, J = 8.4 Hz, 1H), 7.85 (t, J = 8.7 Hz, 2H), 7.72 (d, J = 7.6 Hz, 2H), 7.61 (t, J = 7.9 Hz, 1H), 7.54 – 7.39 (m, 6H), 0.2 (s, 9H). DART-MS calcd for C$_{21}$H$_{20}$Si·H+: 301.1413; found: 301.1436.
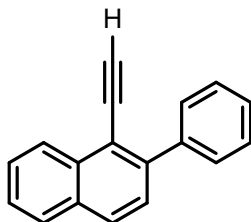
1-Ethynyl-2-phenyl-naphthalene (4d)

To a round-bottom flask equipped with a stirring bar was added MeOH (87 mL, 0.05 M) and **4c** (1 gram, 4.4 mmol, 1 eq), followed by the addition of K$_2$CO$_3$ (60 mg, 0.44 mmol, 0.1 eq). The reaction was stirred at RT for 2 hours. The crude mixture was extracted with chloroform, washed with brine, and concentrated under vacuum. The pure organic compound was isolated via column chromatography (100% petroleum ether; rf = 0.35, 100% petroleum ether) to afford a pale-yellow solid, **4d** (985 mg, 99%). Pure white needle-like crystals were obtained by slow evaporation from dichloromethane. ^{1}H NMR (500 MHz, CDCl$_3$) δ (ppm) 8.49 (d, J = 8.4 Hz, 1H), 7.88 (t, J = 8.7 Hz, 2H), 7.69 (d, J = 7.6 Hz, 2H), 7.62 (t, J = 7.2 Hz, 1H), 7.56 – 7.49 (m, 2H), 7.48 (t, J = 7.7 Hz, 2H), 7.41 (t, J = 7.1 Hz, 1H), 3.45 (s, 1H). ^{13}C-NMR (500 MHz, CDCl$_3$) δ (ppm) 143.5, 140.9, 134.0, 132.1, 129.7, 129.0, 128.1, 128.0, 127.6, 127.5, 127.4, 126.6, 126.4, 117.2, 85.5, 80.9; DART-MS calcd for C$_{18}$H$_{12}$·H+: 229.1012; found: 229.1017.
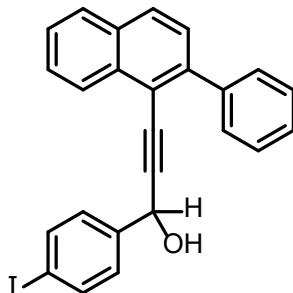
1-(4-Iodophenyl)-3-(2-phenylnaphthalen-1-yl)prop-2-yn-1-ol (4e)

Dry THF (15 mL) was added to a flame-dried 50 mL round bottom flask containing a magnetic stirring bar and placed under argon. 1-Ethynyl-2-phenyl-naphthalene (**4d**) (1.0 g, 4.4 mmol, 1.0 eq) was added via syringe. The reaction was cooled to 0 ˚C to generate the lithium acetylide. A total of 3.2 mL (4.8 mmol, 1.1 eq) of 1.5 M *n*-BuLi was added dropwise via syringe. The bath was removed, allowing the reaction to warm up to room temperature. After 30 minutes, the reaction was cooled back down to –78 ˚C. 0.45 M 1,4 iodo-benzaldehyde / THF (10 mL, 1.0 eq) was added dropwise via syringe the reaction was left stirring at RT for 2 hours. The reaction was quenched with saturated NH₄Cl (20 mL). The crude organic product was extracted with EtOAc, washed with brine, dried with anh. MgSO₄, and then evaporated on the Rotavap. The residual oil was dried under vacuum overnight. The final product, **4e**, was purified as an oil via column chromatography (100% hexanes to 100% CHCl₃; rf = 0.35, 100% CHCl₃) to give 1.4 gram of pure 1,3-diphenylprop-2-yn-1-ol in 70% yield. ^{1}H NMR (500 MHz, CDCl₃) δ (ppm) 8.41 (d, *J* = 7.35 Hz, 1H), 7.9 (t, *J* = 7.8 Hz, 2H), 7.66 – 7.57 (m, 5H), 7.53 (t, *J* = 7.4 Hz, 1H), 7.51, (d, *J* = 4.9 Hz, 1H), 7.43 – 7.39 (m, 3H), 7.13 (d, *J* = 8.49 Hz, 2), 5.6 (d, *J* = 5.8 Hz, 1H), 2.2 (d, *J* = 6.3 Hz, 1H). ^{13}C-NMR (500 MHz, CDCl₃) δ (ppm) 143.4, 141.1, 140.2, 137.6, 133.6, 132.2129.6, 129.0, 128.7, 128.2, 128.1, 127.6, 127.4, 126.5, 117.496.194.1, 84.8, 64.8; DART-MS calcd for C₂₅H₁₇IO·H+: 461.0397; found: 443.0305 [M-H₂O]⁺.
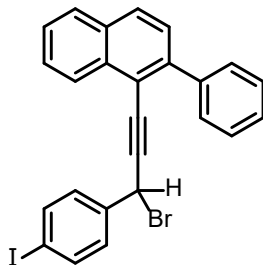
1-(4-Iodophenyl)-3-(2-phenyl-naphthalen-1-yl)prop-2-yn-1-bromide (4f)

Dry Et₂O (150 mL) was added to a flame-dried 500 mL round bottom flask containing a magnetic stirring bar and **4e** (1.0 g, 2.2 mmol, 1 eq). The flask was cooled to 0 ˚C using an ice bath. PBr₃ (0.42 mL, 4.4 mmol, 2 eq) was added dropwise via syringe under argon and the reaction was stirred for 30 minutes. The reaction was quenched with sat. NaHCO₃, (30 mL). The crude organic product was extracted with Et₂O, washed with brine, the separated organic layer dried with anh. MgSO₄, and the residual oil dried overnight under high vacuum. Compound **4f** is unstable on silica gel. Crude material was carried on to next step.
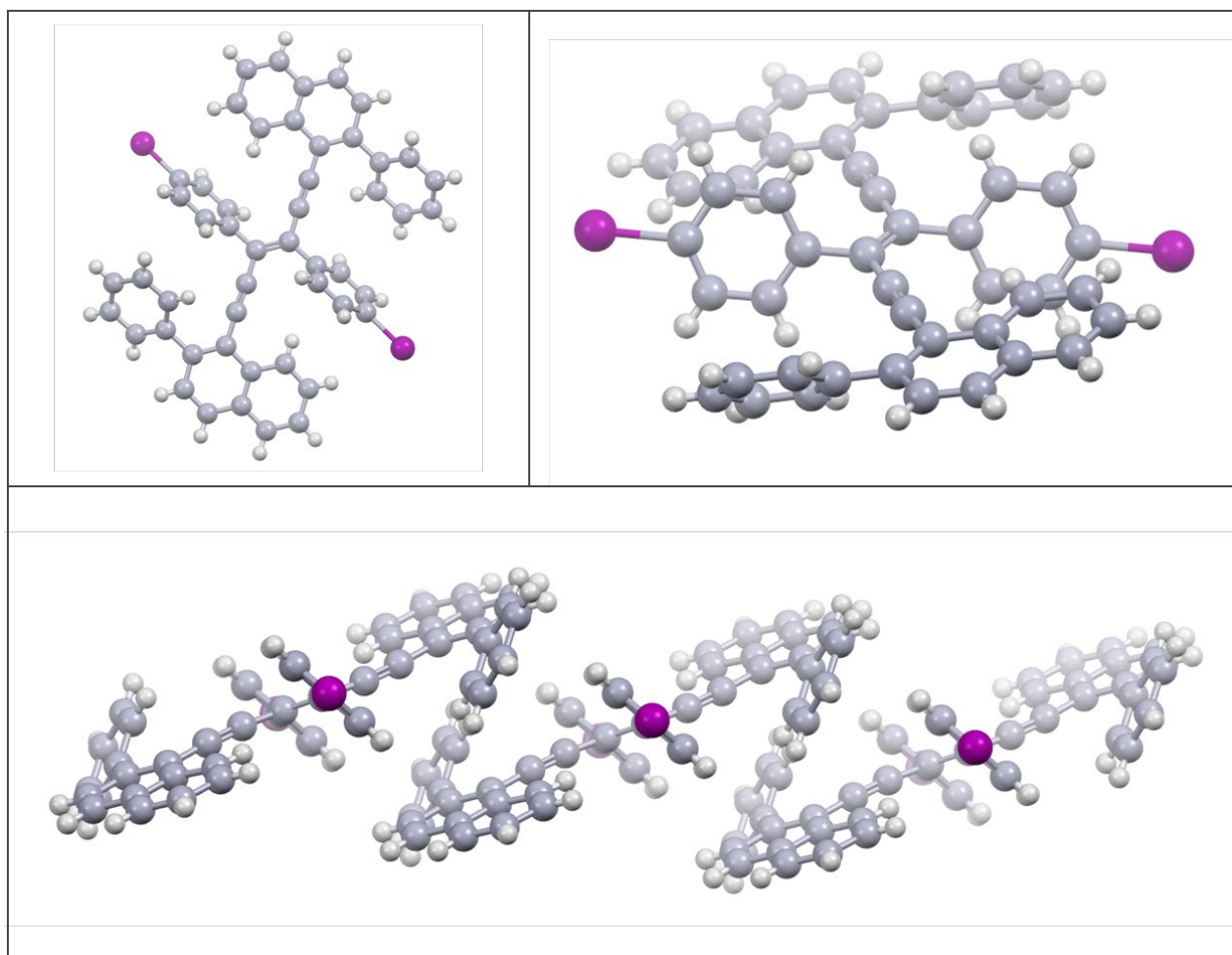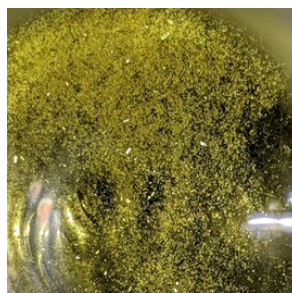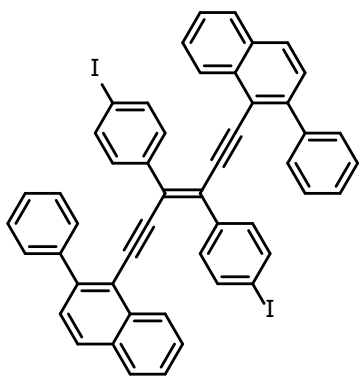
(E)-3,4-(bis-2-phenyl-naphthyl)-1,6-(bis-4-iodophenyl)-3,4-diphenyl-3-hexen-1,5-diyne (4g)

Dry THF (45 mL) and a magnetic stirring bar were added to the flask containing 1.0 gram of crude propargylic bromide (**4f**). Dry THF (20 mL) was added to a separate flame-dried 250 mL round bottom flask containing a magnetic stirring bar. The flask was cooled to –10 ˚C and 1 M

LiHMDS (2.1 mL, 2.1 mmol, 1.1 eq) and HMPA (0.4 mL, 2.1 mmol, 1.1 eq) were added via syringe. The reaction containing the starting material was cooled to –90 ˚C using a frozen hexanes slurry generated with liquid nitrogen. The LiHMDS and HMPA mixture was added dropwise over 30 minutes and the reaction was left to stir and warm to room temperature. The reaction was quenched with saturated NH_4Cl (100 mL). The crude organic product was extracted with chloroform, washed with brine, and dried under vacuum. The pure compound, **4g**, was isolated as a yellow solid by washing with ether. (890 mg, 53% yield). ^{1}H NMR (500 MHz, $C_2D_2Cl_4$) δ (ppm) 7.88 (dd, J_a = 8.5, J_b = 3.1 Hz, 4H), 7.71 (d, J = 8.7 Hz, 2H), 7.63 (d, J = 8.1 Hz, 4H), 7.59 – 7.46 (m, 10H), 7.40 (t, J = 7.11, 2H), 7.36 (d, J = 9.0 Hz, 4H), 7.31 (t, J = 7.4 Hz, 4H). ^{13}C-NMR (500 MHz, $C_2D_2Cl_4$) δ (ppm) 143.3, 140.7, 138.4, 137.5, 133.5, 132.1, 131.0, 129.6, 129.4, 128.3, 128.3, 127.8, 127.6, 126.8, 126.6, 120.4, 118.1, 98.4, 97.8, 94.3; DART-MS calcd for $C_{52}H_{34}I_2 \cdot H+$: 913.0823; found: 913.0885.

Synthetic Procedures for (E)-3,4-(bis-2-phenyl-3-methyl-naphthyl)-1,6-(bis-4-iodophenyl)-3,4-diphenyl-3-hexen-1,5-diyne (4m).
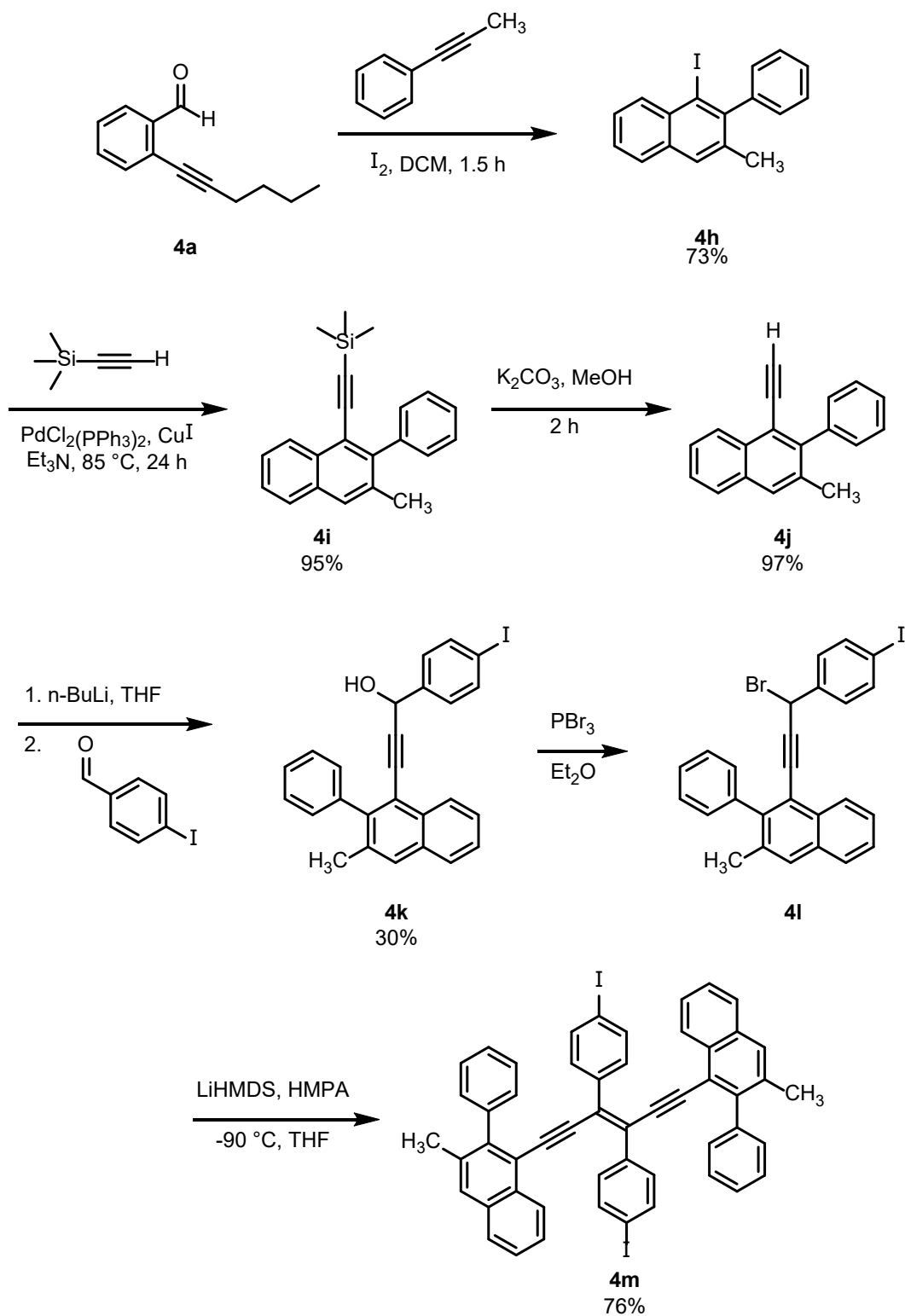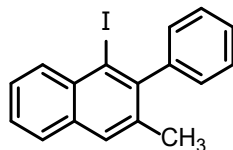
1-Iodo-2-phenyl-3-methyl-naphthalene (4h)

To a round-bottom flask equipped with a stirring bar, was added CH_2Cl_2 (0.1 M), **4a** (2.4 grams, 13 mmol, 1 eq), I_2 (1.5 grams, 13 mmol, 1 eq), and 1-phenyl-1-propyne (1.6 mL, 13 mmol, 1 eq). The reaction was stirred for 1.5 hours at room temperature and then quenched by the addition of sat. aq. $Na_2S_2O_3$ solution. The crude organic mixture was extracted with chloroform, washed with brine, and dried under vacuum. The pure organic compound, **4h**, was isolated via column chromatography (10 (ppm)1 hexanes (ppm) dichloromethane; rf = 0.35, 100% hexanes) to afford pale yellow solid (2.8 grams, 73% yield) Additionally, it was found that the pure product could be isolated by triturating with methanol. ^{1}H NMR (500 MHz, CDCl3) δ (ppm) 8.27 (d, J = 8.0 Hz, 1H), 7.75 (d, J = 8.3 Hz, 1H), 7.70 (s, 1H), 7.59 – 7.49 (m, 4H), 7.47 (tt, J_a = 7.2 Hz, J_b = 2.3 Hz, 1H), 7.20 (dt, J_a = 7.4 Hz, J_b = 1.6 Hz, 2H), 2.25 (s, 3H). 13C-NMR (500 MHz, CDCl3) δ (ppm) 147.1, 145.9, 135.0, 133.7, 133.7, 133.4, 129.0, 128.7, 128.5, 127.6, 127.5, 127.2, 126.7, 106.1, 20.8.
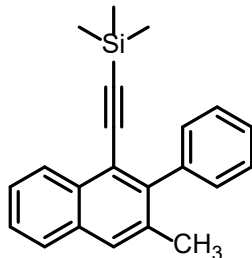
Trimethyl((2-phenylnaphthalen-1-yl)ethynyl)silane (4i)

To a flame dried round-bottom flask equipped with a stirring bar was added triethylamine (30 mL, 0.1 M) and **4h** (1.0 grams, 3.0 mmol, 1 eq). The mixture was sparged for 10 minutes. Following this, Pd(PPh₃)₂Cl₂ (40 mg, 2 mol%), CuI (27 mg, 5 mol%), and trimethylsilyl acetylene (0.43 mL, 3.5 mmol, 1.2 eq) were added. The reaction was heated to 90 ˚C for 12 hours. The crude mixture was filtered through celite and concentrated under vacuum. The pure organic compound, **4i**, was isolated via column chromatography (100% hexanes to 100% CH₂Cl₂; rf = 0.25, 100% hexanes) to afford a dark yellow oil (900 mg, 95%). ^{1}H NMR (500 MHz, CDCl₃) δ (ppm) 8.34 (d, J = 8.1 Hz, 1H), 7.78 (d, J = 7.1 Hz, 1H), 7.70 (s, 1H), 7.54 – 7.40 (m, 5H), 7.31 (d, J = 7.40 Hz), 2.24 (s, 3H), 0.05 (s, 9H).
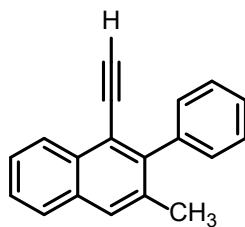
1-Ethynyl-2-phenyl-3-methyl-naphthalene (4j)

To a round-bottom flask equipped with a stirring bar was added MeOH (63 mL, 0.05 M). **4i** (1 gram, 3.2 mmol, 1 eq) was added, followed by the addition of K₂CO₃ (44 mg, 0.32 mmol, 0.1

eq). The reaction was stirred for 2 hours. The crude mixture was extracted with chloroform, washed with brine, and concentrated under vacuum. The pure organic compound was isolated via column chromatography (100% hexanes to 100% chloroform; rf = 0.65, 100% hexanes) to afford a clear oil **4j** (750 mg, 97%). ^{1}H NMR (500 MHz, CDCl$_3$) δ (ppm) 8.37 (d, J = 8.5 Hz, 1H), 7.80 (d, J = 8.2 Hz, 1H), 7.73 (s, 1H), 7.56 – 7.44 (m, 4H), 7.42 (d, J = 7.5 Hz, 1H), 7.33 (d, J = 7.2 Hz, 2H), 3.29 (s, 1H), 2.23 (s, 3H). ^{13}C-NMR (500 MHz, CDCl$_3$) δ (ppm) 145.2, 140.4, 134.1, 132.5, 132.4, 129.4, 129.0, 128.1, 127.4, 127.3, 126.4, 126.4, 126.3, 118.8, 85.5, 80.9, 21.4.
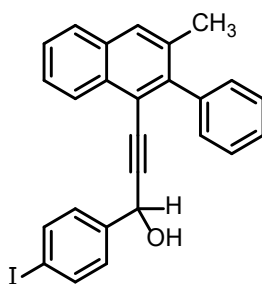
1-(4-Iodophenyl)-3-(2-phenyl-3-methyl-naphthalen-1-yl)prop-2-yn-1-ol (4k)

Dry THF (15 mL) was added to a flame-dried 50 mL round bottom flask containing a magnetic stirring bar and placed under argon. 1-Ethynyl-2-phenyl-3-methyl-naphthalene (**4j**) (0.34 g, 1.5 mmol, 1.0 eq) was added via syringe. The reaction was cooled to 0 ˚C to generate the lithium acetylide. A total of 1.1 mL (1.6 mmol, 1.1 eq) of 1.5 M *n*-BuLi was added dropwise via syringe. The bath was removed, allowing the reaction to warm up to room temperature. After 30 minutes, the reaction was cooled back down to –78 ˚C. 0.5 M 1,4 iodo-benzaldehyde / THF (3 mL, 1.0 eq) was added dropwise via syringe the reaction was left stirring at RT for 2 hours. The reaction was quenched with saturated NH$_4$Cl (20 mL). The crude organic product was extracted with chloroform, washed with brine, dried with anh. MgSO$_4$, and then evaporated on the

Rotavap. The residual oil was dried under vacuum overnight. The final product was purified as an oil via column chromatography (100% hexanes to 100% CH$_2$Cl$_2$; rf = 0.40, 100% CH$_2$Cl$_2$) to give 0.25 gram of pure 1-(4-iodophenyl)-3-(2-phenyl-3-methyl-naphthalen-1-yl)prop-2-yn-1-ol, **4k**, in 30% yield. ^{1}H NMR (500 MHz, CDCl$_3$) δ (ppm) 8.30 (d, J = 7.3 Hz, 1H), 7.80 (d, J = 7.7 Hz, 1H), 7.73 (s, 1H), 7.58 (d, J = 8.2 Hz, 2H), 7.55 – 7.42 (m, 5H), 7.33 (J = 7.1 Hz, 1H), 7.31 – 7.27 (m, 1H), 6.90 (d, J = 7.6 Hz, 2H), 5.50 (d, J = 7.4 Hz, 1H), 2.23 (s, 3H), 1.97 (d, J = 7.5 Hz). ^{13}C-NMR (500 MHz, CDCl$_3$) δ (ppm) 144.9, 140.7, 140.1, 137.6, 134.2, 132.5, 131.9, 129.4, 129.0, 128.7, 128.2, 127.4, 127.3, 126.5, 126.4, 126.2, 118.9, 96.3, 93.9, 85.0, 64.7, 21.3.
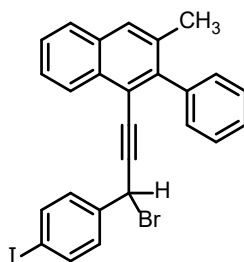
1-(4-Iodophenyl)-3-(2-phenyl-3-methyl-naphthalen-1-yl)prop-2-yn-1-bromide (4l)

Dry Et$_2$O (50 mL) was added to a flame-dried 500 mL round bottom flask containing a magnetic stirring bar and **4k** (0.25 g, 0.52 mmol, 1 eq). The flask was cooled to 0 ˚C using an ice bath. PBr$_3$ (0.11 mL, 1.1 mmol, 2 eq) was added dropwise via syringe under argon and the reaction was stirred for 30 minutes. The reaction was quenched with sat. NaHCO$_3$, (20 mL). The crude organic product was extracted with Et$_2$O, washed with brine, the separated organic layer dried with anh. MgSO$_4$, and the residual oil dried overnight under high vacuum. Compound **4l** is unstable on silica gel. Crude material was carried on to next step.
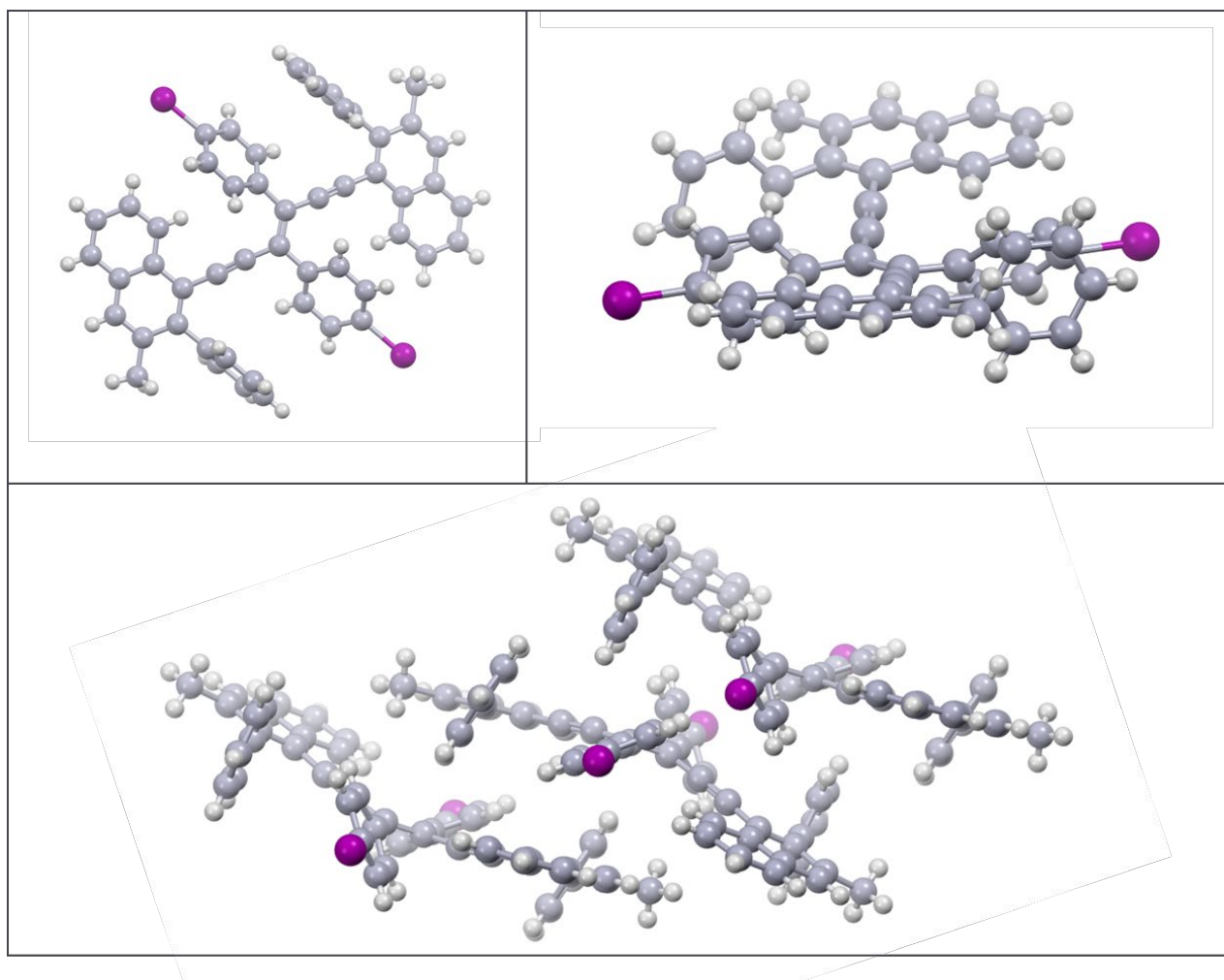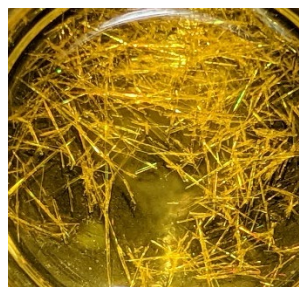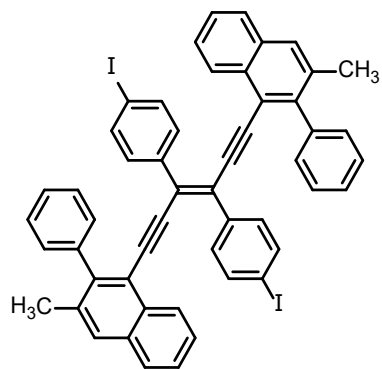
(E)-3,4-(bis-2-phenyl-3-methyl-naphthyl)-1,6-(bis-4-iodophenyl)-3,4-diphenyl-3-hexen-1,5 diyne (4m).

Dry THF (25 mL) and a magnetic stirring bar were added to the flask containing 0.27 gram of crude propargylic bromide (**4l**). Dry THF (20 mL) was added to a separate flame-dried 50 mL

158

round bottom flask containing a magnetic stirring bar. The flask was cooled to –10 ˚C and 1M LiHMDS in THF (0.6 mL, 0.6 mmol, 1.1 eq) and HMPA (0.1 mL, 0.6 mmol, 1.1 eq). The flask containing the starting material was cooled to –90 ˚C using a frozen hexanes slurry generated with liquid nitrogen. The LiHMDS and HMPA mixture was added dropwise over 30 minutes and the reaction was left to stir and warm to room temperature. The reaction was quenched with saturated NH_4Cl (25 mL). The crude organic product was extracted with chloroform, washed with brine, and dried under vacuum. The pure compound was isolated as a yellow solid, **4m**, by washing with ether. (180 mg, 76% yield). ^{1}H NMR (500 MHz, $CDCl_3$) δ (ppm) 7.73 (d, J = 8.6 Hz, 2H), 7.66 (s, 2H), 7.56 (dt, J_a = 8.4 Hz, J_b = 2.32 Hz, 4H), 7.50 (d, J = 8.4 Hz, 2H), 7.46 (dd, J_a = 7.0, J_b = 1.0 Hz, 2H), 7.38 – 7.30 (m, 8H), 7.19 (dt, J_a = 7.7 Hz, J_b = 1.6 Hz, 4H), 7.06 (dt, J_a = 8.3 Hz, J_b = 1.6 Hz, 4H), 2.16 (s, 6H). ^{13}C-NMR (500 MHz, $CDCl_3$) δ (ppm) 144.6, 140.3, 138.6, 137.3, 134.3, 132.4, 131.8, 130.7, 129.3, 129.2, 128.2, 127.9, 127.3, 127.2, 126.5, 126.3, 126.3, 119.5, 98.4, 97.9. 93.6, 21.3.

4.6. References

1) Fan, Q.; Gottfried, J. M.; Zhu, J. Surface-Catalyzed C–C Covalent Coupling Strategies toward the Synthesis of Low-Dimensional Carbon-Based Nanostructures. *Acc. Chem. Res.* **2015**, *48* (8), 2484–2494. https://doi.org/10.1021/acs.accounts.5b00168.

2) Yortanlı, M.; Mete, E. Common Surface Structures of Graphene and Au(111): The Effect of Rotational Angle on Adsorption and Electronic Properties. *J. Chem. Phys.* **2019**, *151* (21), 214701. https://doi.org/10.1063/1.5127099.

3) Tan, Y.; Zhao, Z.; Chen, Z.; Huang, S.; Jia, S.; Peng, L.; Xu, D.; Qin, W.; Yan, H. *N*-Iodosuccinimide-Mediated Dimerization of 2-Alkynylnaphthols: A Highly Diastereoselective Construction of Bridged Polycyclic Compounds via Vinylidene *Ortho*-Quinone Methide Intermediates. *Org. Lett.* **2020**, *22*, 4461–4466. https://doi.org/10.1021/acs.orglett.0c01458.

4) Barluenga, J.; Vázquez-Villa, H.; Ballesteros, A.; González, J. M. Regioselective Synthesis of Substituted Naphthalenes: A Novel de novo Approach Based on a Metal-Free Protocol for Stepwise Cycloaddition of *o*-Alkynylbenzaldehyde Derivatives with Either Alkynes or Alkenes. *Org. Lett.* **2003**, *5*, 4121–4123. https://doi.org/10.1021/ol035691t.

5) Bhattacharya, S.; Sengupta, S. Palladium Catalyzed Alkynylation of Aryl Halides (Sonogashira Reaction) in Water. *Tetrahedron Lett.* **2004**, *45*, 8733–8736. https://doi.org/10.1016/j.tetlet.2004.09.131.

6) Shetty, A. S.; Zhang, J.; Moore, J. S. Aromatic π-Stacking in Solution as Revealed through the Aggregation of Phenylacetylene Macrocycles. *J. Am. Chem. Soc.* **1996**, *118* (5), 1019–1027. https://doi.org/10.1021/ja9528893.

7) Ruffieux, P.; Wang, S.; Yang, B.; Sánchez-Sánchez, C.; Liu, J.; Dienel, T.; Talirz, L.; Shinde, P.; Pignedoli, C. A.; Passerone, D.; Dumslaff, T.; Feng, X.; Müllen, K.; Fasel, R. On-Surface Synthesis of Graphene Nanoribbons with Zigzag Edge Topology. *Nature* **2016**, *531*, 489–492. https://doi.org/10.1038/nature17151.

8) Di Giovannantonio, M.; Chen, Q.; Urgel, J. I.; Ruffieux, P.; Pignedoli, C. A.; Müllen, K.; Narita, A.; Fasel, R. On-Surface Synthesis of Oligo(Indenoindene). *J. Am. Chem. Soc.* **2020**, *142*, 12925–12929. https://doi.org/10.1021/jacs.0c05701.

9) Xu, X.; Di Giovannantonio, M.; Urgel, J. I.; Pignedoli, C. A.; Ruffieux, P.; Müllen, K.; Fasel, R.; Narita, A. On-Surface Activation of Benzylic C-H Bonds for the Synthesis of Pentagon-Fused Graphene Nanoribbons. *Nano Res.* **2021**, *14*, 4754–4759. https://doi.org/10.1007/s12274-021-3419-2.

10) Jones, G. B.; Wright, J. M.; Plourde, G. W.; Hynd, G.; Huber, R. S.; Mathews, J. E. A Direct and Stereocontrolled Route to Conjugated Enediynes. *J. Am. Chem. Soc.* **2000**, *122*, 1937–1944. https://doi.org/10.1021/ja993766b.

CHAPTER 5. BIS-PHENYL DIYNE MODEL PRECURSOR FOR HOPF CYCLIZATION

5.1. Background

Chapter 2 of this work described the solid-state synthesis of graphene nanoribbons obtained by Rubin *et al.*[1,2,3] This was done by using 1,4-diphenyl-1,4-butadiyne derivatives that could crystallize in the solid state and topochemically polymerize due to hydrogen-bonding interactions between neighboring amide substituents. Work in this area showed that within the crystal structure, the 1,4-butadiyne units undergo a polymerization step to afford a polydiacetylene (PDA). Conversion of the diynes to PDAs cause the crystals to become deep blue. Heating of these PDAs then causes the material to graphitize through Hopf cyclizations and subsequent cyclodehydrogenation reactions. Chapter 2 and 3 of this work introduced the potential for a model compound, a hexa-1,3-dien-5-yne, to undergo Hopf cyclization into an aromatic ring on an Au(111) surface. To better understand this system, similar analogues capable of undergoing a Hopf cyclization should be studied. Chapter 5 of this work looks at the synthesis of 1,4-bis(2,5-dibromophenyl)buta-1,3-diyne for its potential to polymerize and cyclize to [8]AGNR on Au(111).

5.1.1. Molecular Precursor Design

A symmetrical molecular precursor containing a hexa-1,3-dien-5-yne was proposed for coupling studies. This molecular precursor contains four bromine atoms, so that two Ullman couplings could take place to form a polymeric structure connected by two C-C covalent bonds (Fig. 45a). Additionally, proper alignment of the molecular precursors on the metal surface could induce a topochemical polymerization to take place between the units (Fig. 45b). This has been

demonstrated before by the solid-state conversion of butadiynes to PDAs. Through either of these mechanisms, polymeric structures will be formed. Figure 45a depicts a Hopf cyclization that would take place between the hexa-1,3-dien-5-yne backbone created from the side aryl rings and the alkyne units. Figure 45b depicts a Hopf cyclization that could instead take place on the hexa-1,3-dien-5-yne backbone created from the polymerization to PDA. Both mechanisms would end in a cyclodehydrogenation step. The differences in ring formation are highlighted in green, with the lightest green coming from the starting materials aromatic rings, the medium green indicating the Hopf cyclization, and the darkest green indicating the final cyclodehydrogenation step. Overall, 1,4-bis(2,5-dibromophenyl)buta-1,3-diyne (**5c**) was synthesized as a potential precursor to fabricate N=8 Armchair GNRs on a gold surface.

Previous work has shown that 1,4-diphenylbutadiyne undergoes a dehydro-Diels Alder reaction to form graphitic nanoribbons when pressurized at 10–20 GPa.[4] Here the work by Mao and co-workers showed that this reaction is "distance-selected." This means that a close distance of 3.2 Å between the phenyl and phenylethynyl moieities helps facilitate this reaction. Therefore, using a derivative of this precursor on-surface could provide additional reactions to induce cyclization to the graphene nanoribbon. Additionally, work by Aono and co-workers in 2007 used AFM to characterize a diacetylene compound of 10,12-pentacosadiynoic acid.[5]
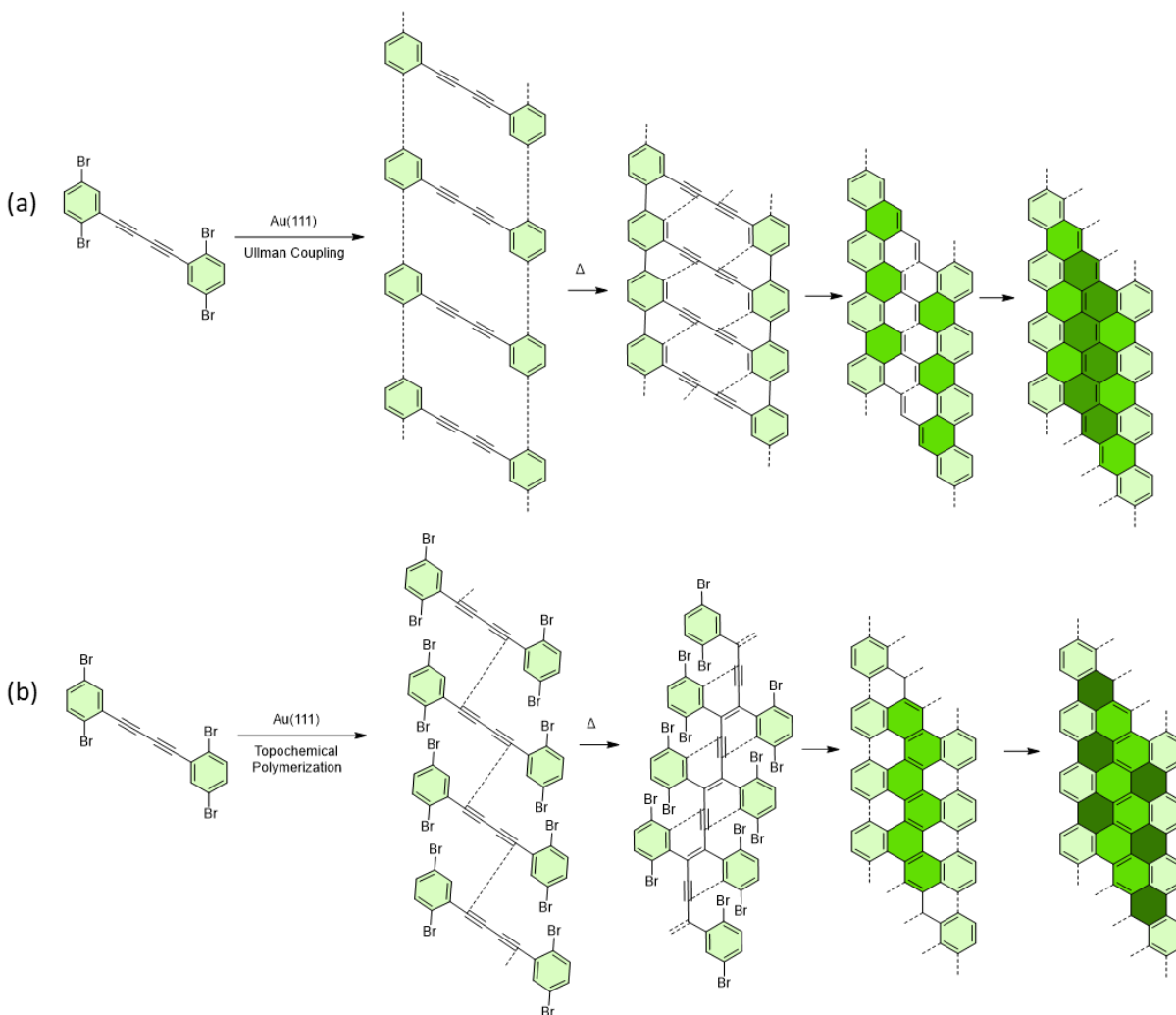
Figure 44. Proposed reactivity of 1,4-bis(2,5-dibromophenyl)buta-1,3-diyne (5c) on Au(111). Compound 5c will be deposited on Au(111); heating will cause (a) Ullman coupling (b) topochemical polymerization to take place, forming a polymeric structure; a Hopf cyclization should take place between the hexa-1,3-dien-5-yne backbone; cyclodehydrogenation and complete aromatization affords the final Armchair [8] GNR

5.2. Methods, Results and Discussion
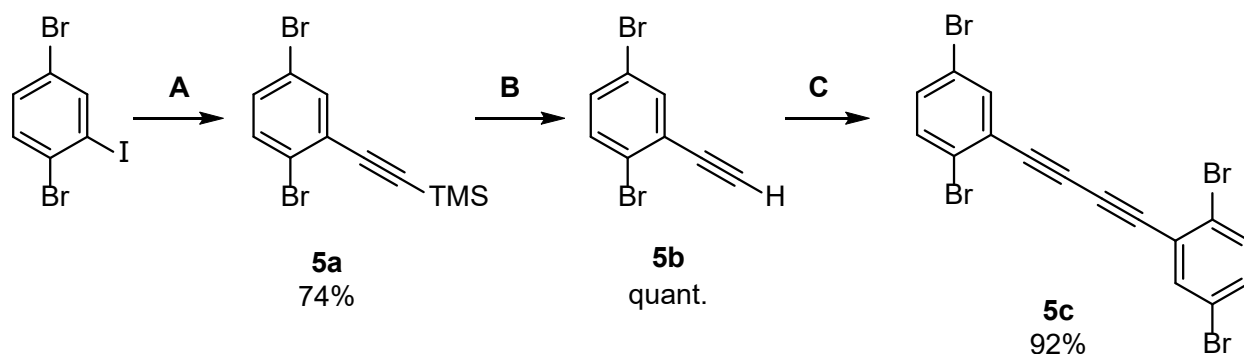
Figure 45. Synthesis of 1,4-bis(2,5-dibromophenyl-1,3-diyne). (A) TMS acetylene, PdCl$_2$(PPh$_3$)$_2$, DIPA, THF, reflux (**5a**, 74%); K$_2$CO$_3$, MeOH, THF (**5b**, quant.); CuI, TMEDA, O$_2$, DCM (**5c**, 92%).

Synthesis of Bis-phenyldiyne Model Precursor

Compound **5c** was synthesized according to Figure 46. To synthesize this molecular precursor, a simple three step route was followed. First 1-iodo-2,5-dibromobenzne was treated with trimethylsilyl (TMS) acetylene, bis(triphenylphosphine)palladium(II) dichloride (PdCl$_2$(PPh$_3$)$_2$), N,N-diisopropylethylamine (DIPA) in THF. The Sonogashira reaction was refluxed to afford **5a,** (2,5-dibromophenyl)ethynyl)trimethylsilane, in 74% yield. From here, the protected alkyne was deprotected with potassium carbonate (K$_2$CO$_3$) in methanol (MeOH)/tetrahydrofuran (THF) to afford **5b**, 1,4-dibromo-2-ethynylbenzene, in quantitative yield. The final compound **5c**, 1,4-bis(2,5-dibromophenyl)buta-1,3-diyne, was obtained in 92% yield via Glaser coupling. This was done by treating **5b** with copper iodide (CuI), N,N,N′,N′-tetramethylethylenediamine (TMEDA), and oxygen in dichloromethane (CH$_2$Cl$_2$). Overall, the

progression of starting material to product could be followed by ^{1}H NMR (see Chapter 5 Experimental).

5.3. Conclusion

In conclusion, novel compound 1,4-bis(2,5-dibromophenyl)buta-1,3-diyne was synthesized in effort to produce graphene nanoribbons through on-surface cyclizations. The polymerization of this precursor on gold(111) will be studied in the near future with our collaborators in the Fasel group.

5.4. Experimental

Synthetic Procedures for 1,4-Bis(2,5-dibromophenyl)buta-1,3-diyne (4p)

5a
74%

5b
quant.

5c
92%
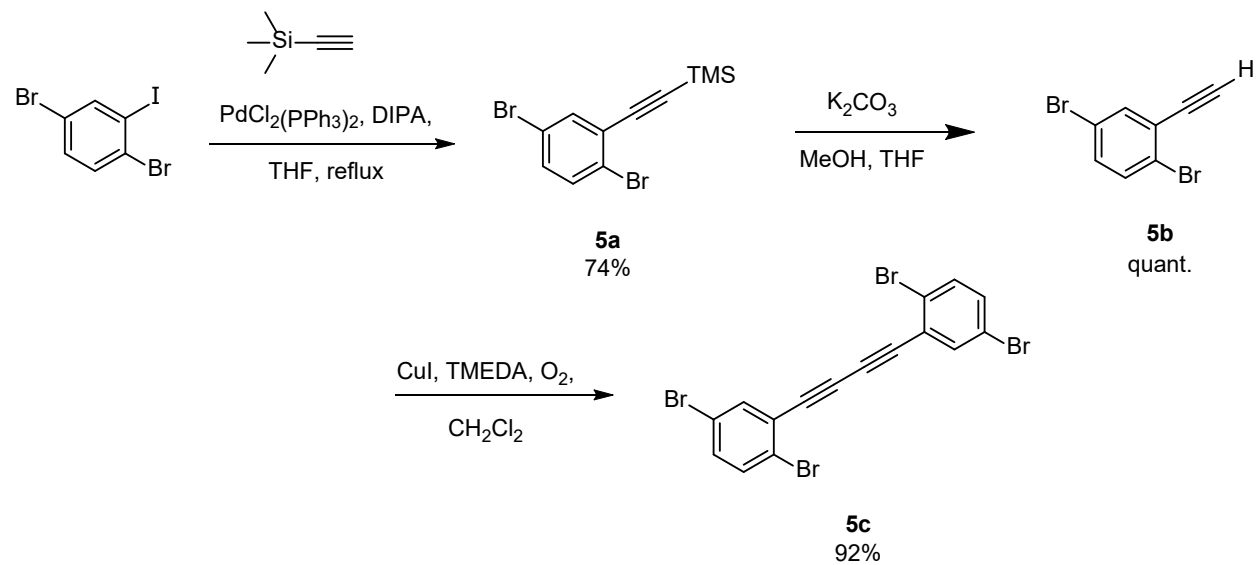
^{1}H NMR Spectra Comparison of Starting Materials and Products
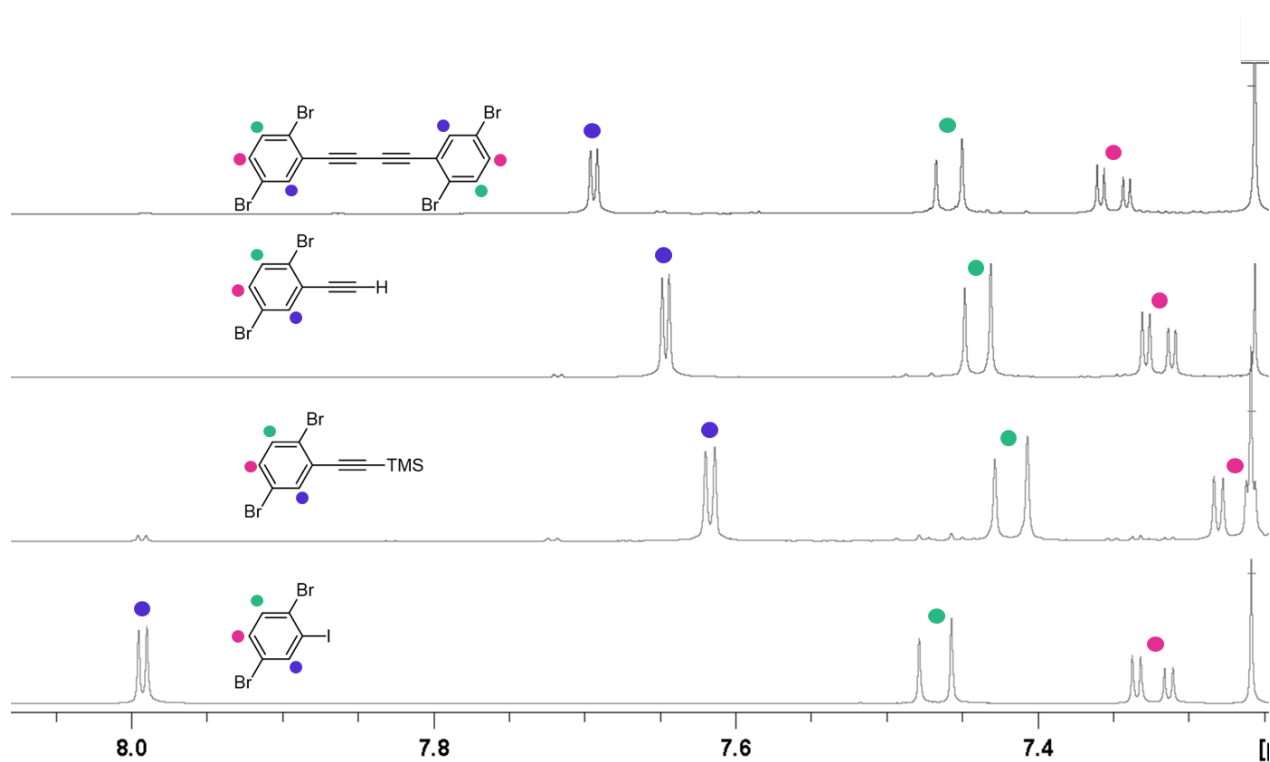
The above depicts the ^{1}H NMR spectrum of all the compounds synthesized for this work. The blue dots depict the peaks that correspond to the original proton between the bromine and iodine atom. This proton should appear as a singlet, but because of the *meta* coupling to the proton indicated by the green dot, it appears as a doublet. Additionally, because it is in-between two halogens, the starting material peak (bottom) appears more downfield in comparison to the rest. After the Sonogashira reaction, replacement with the TMS alkyne causes the shift to move up field. The green dot indicates the peak that corresponds to the proton *meta* to the alkyne and ortho to one bromine atom. Because of this, the peak is only split by one adjacent proton (pink dot) and appears as a doublet as well. The green dot proton has a chemical shift in-between the blue and pink proton. This is because the proton is still close to one electronegative bromine atom but still further away from the iodine/alkyne. Lastly the pink dot corresponds to the proton *para* to the iodine/alkyne. This proton appears as a doublet of doublets because it is split by the neighboring green dot proton and *meta* coupled to the blue dot proton. This peak appears as the most up field since it is next to one bromine atom and furthest away from the position of the iodine/alkyne.
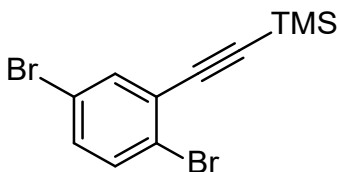
((2,5-Dibromophenyl)ethynyl)trimethylsilane (5a)

1,4-Dibromo-iodobenzene (500 mg, 1.92 mmol, 1 eq) was added to a flame-dried round bottom flask. Copper iodide (7.2 mg, 0.038 mmol, 2 mol%) and palladium bis-triphenylphosphine dichloride (40 mg, 0.06 mmol, 3 mol%) was added to the flask. Tetrahydrofuran (25 mL) was added to the flask followed by dimethylamine (0.2 mL, 1.92 mmol, 1 eq). The mixture was

sparged with argon and then trimethylsilylacetylene (0.24 mL, 1.92 mmol, 1 eq) was added

dropwise to the mixture. The reaction was refluxed at 60 ˚C for 6 hours. The crude reaction

mixture was washed with water and extracted with chloroform. The pure compound **4n** was

isolated as an oil via silica gel column chromatography (100% hexanes to 100% CH_2Cl_2; rf =

0.85, 100% hexanes) to give 346 mg, 74%. ^{1}H NMR (500 MHz, $CDCl_3$) δ (ppm) 7.61 (d, J =

2.46 Hz, 1H), 7.42 (d, J = 8.6 Hz, 1H), 7.27 (dd, J_a = 8.9, J_b = 2.46 Hz, 1H), 0.27 (s, 9H). [13]C-

NMR (500 MHz, $CDCl_3$) δ (ppm) 136.1, 133.6, 132.6, 127.1, 124.4, 120.4, 101.6, 101.4, 77.3,

77.0, 76.7, -0.2.
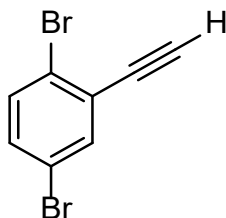
1,4-Dibromo-2-ethynylbenzene (5b)

Compound **4n** (300 mg, 0.9 mmol, 1 eq) was dissolved in a 30 mL mixture of 1:1 methanol:

tetrahydrofuran. To this mixture was added a catalytic amount of potassium carbonate (12 mg,

0.09 mmol, 0.1 eq). The reaction was left to stir for two hours at room temperature. The crude

mixture was extracted with chloroform, washed with brine, and concentrated under vacuum. The

pure organic compound was isolated via column chromatography (100% hexanes to 100%

chloroform; rf = 0.80, 100% hexanes) to afford 230 mg (quantitative yield) of **4o**. ^{1}H NMR (500

MHz, $CDCl_3$) δ (ppm) 7.64 (d, J = 2.5 Hz, 1H), 7.44 (d, J = 8.6 Hz, 1H), 7.31 (dd, J_a = 8.5, J_b =

169

2.3 Hz, 1H), 3.42 (s, 1H). ^{13}C NMR (500 MHz, CDCl$_3$) δ (ppm) 136.6, 133.7, 133.1, 126.1, 124.3, 120.6, 83.1, 80.6.
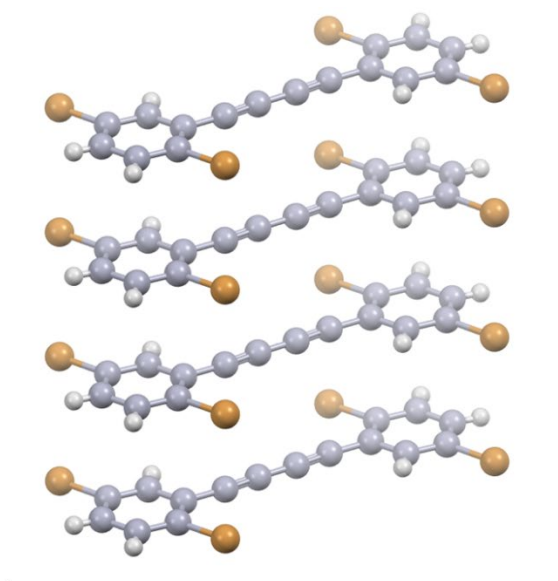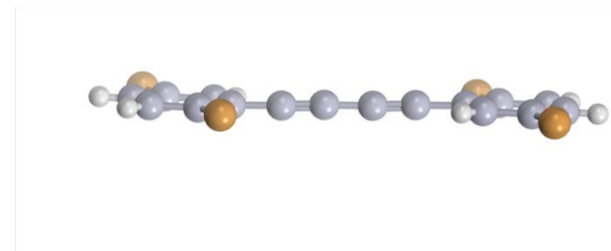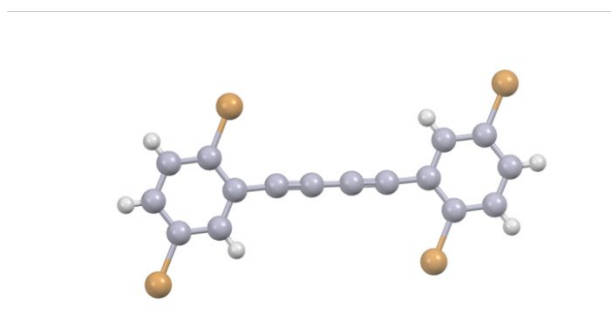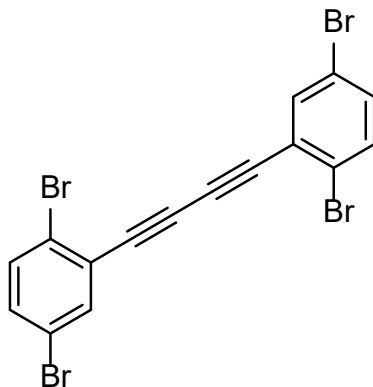
1,4-Bis(2,5-dibromophenyl)buta-1,3-diyne (5c)

Compound **4o** (250 mg, 1 mmol, 1 eq) was dissolved in 10 mL dichloromethane. To this was added copper iodide (18 mg, 0.1 mmol, 10 mol%) and N,N,N′,N′-tetramethylethylenediamine (0.01 mL, 0.1 mmol, 10 mol%). The reaction was bubbled with air for 10 minutes. This was done by attaching a short pipette to a fitted hose. The pipette was submerged into the solution and the air flow was regulated for continuous bubbling. After this, the pipette was removed the reaction was left to stir for four hours. Water was added to quench the reaction. The crude reaction mixture was washed with water and extracted with dichloromethane. The crude organic product was concentrated down. Residual impurities were decanted with ether and the final product was washed with more ether. The pure organic compound, **4p**, was isolated in as 230 mg in 92% yield. ^{1}H NMR (500 MHz, CDCl$_3$) δ (ppm) 7.70 (d, J = 2.3 Hz, 1H), 7.46 (d, J = 8.9 Hz, 1H), 7.35 (dd, J_a = 8.6, J_b = 2.4 Hz, 1H), 3.42 (s, 1H). ^{13}C-NMR (500 MHz, CDCl$_3$) δ (ppm) 136. 8, 133.8, 133.7, 125.7, 125.0, 120.7, 80.3, 78.6.

5.5. References

1) Li, Y. L.; Zee, C.-T.; Lin, J. B.; Basile, V. M.; Muni, M.; Flores, M. D.; Munárriz, J.; Kaner, R. B.; Alexandrova, A. N.; Houk, K. N.; Tolbert, S. H.; Rubin, Y. Fjord-Edge Graphene Nanoribbons with Site-Specific Nitrogen Substitution. *J. Am. Chem. Soc.* **2020**, *142* (42), 18093–18102. https://doi.org/10.1021/jacs.0c07657.

2) Jordan, R. S.; Li, Y. L.; Lin, C.-W.; McCurdy, R. D.; Lin, J. B.; Brosmer, J. L.; Marsh, K. L.; Khan, S. I.; Houk, K. N.; Kaner, R. B.; Rubin, Y. Synthesis of $N = 8$ Armchair Graphene Nanoribbons from Four Distinct Polydiacetylenes. *J. Am. Chem. Soc.* **2017**, *139* (44), 15878–15890. https://doi.org/10.1021/jacs.7b08800.

3) Jordan, R. S.; Wang, Y.; McCurdy, R. D.; Yeung, M. T.; Marsh, K. L.; Khan, S. I.; Kaner, R. B.; Rubin, Y. Synthesis of Graphene Nanoribbons via the Topochemical Polymerization and Subsequent Aromatization of a Diacetylene Precursor. *Chem* **2016**, *1* (1), 78–90. https://doi.org/10.1016/j.chempr.2016.06.010

4) Zhang, P.; Tang, X.; Wang, Y.; Wang, X.; Gao, D.; Li, Y.; Zheng, H.; Wang, Y.; Wang, X.; Fu, R.; Tang, M.; Ikeda, K.; Miao, P.; Hattori, T.; Sano-Furukawa, A.; Tulk, C. A.; Molaison, J. J.; Dong, X.; Li, K.; Ju, J.; Mao, H. Distance-Selected Topochemical Dehydro-Diels–Alder Reaction of 1,4-Diphenylbutadiyne toward Crystalline Graphitic Nanoribbons. *J. Am. Chem. Soc.* **2020**, *142* (41), 17662–17669. https://doi.org/10.1021/jacs.0c08274.

5) Okawa, Y.; Takajo, D.; Tsukamoto, S.; Hasegawa, T.; Aono, M. Atomic Force Microscopy and Theoretical Investigation of the Lifted-up Conformation of Polydiacetylene on a Graphite Substrate. *Soft Matter* **2008**, *4* (5), 1041. https://doi.org/10.1039/b718402f.

EXPERIMENTAL SPECTRA FOR ALL CHAPTERS

^{1}H NMR of 1,3-Diphenylprop-2-yn-1-ol (2a)
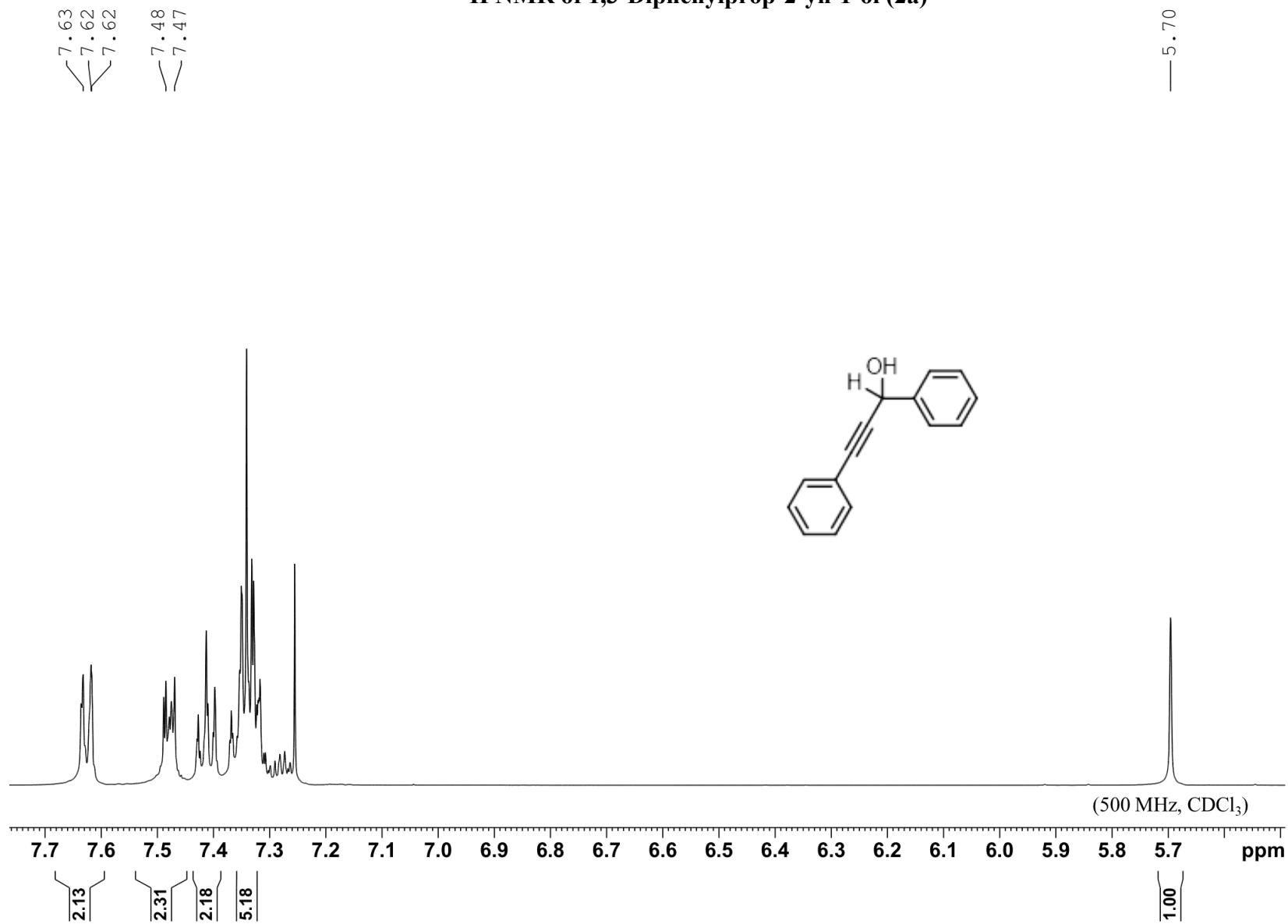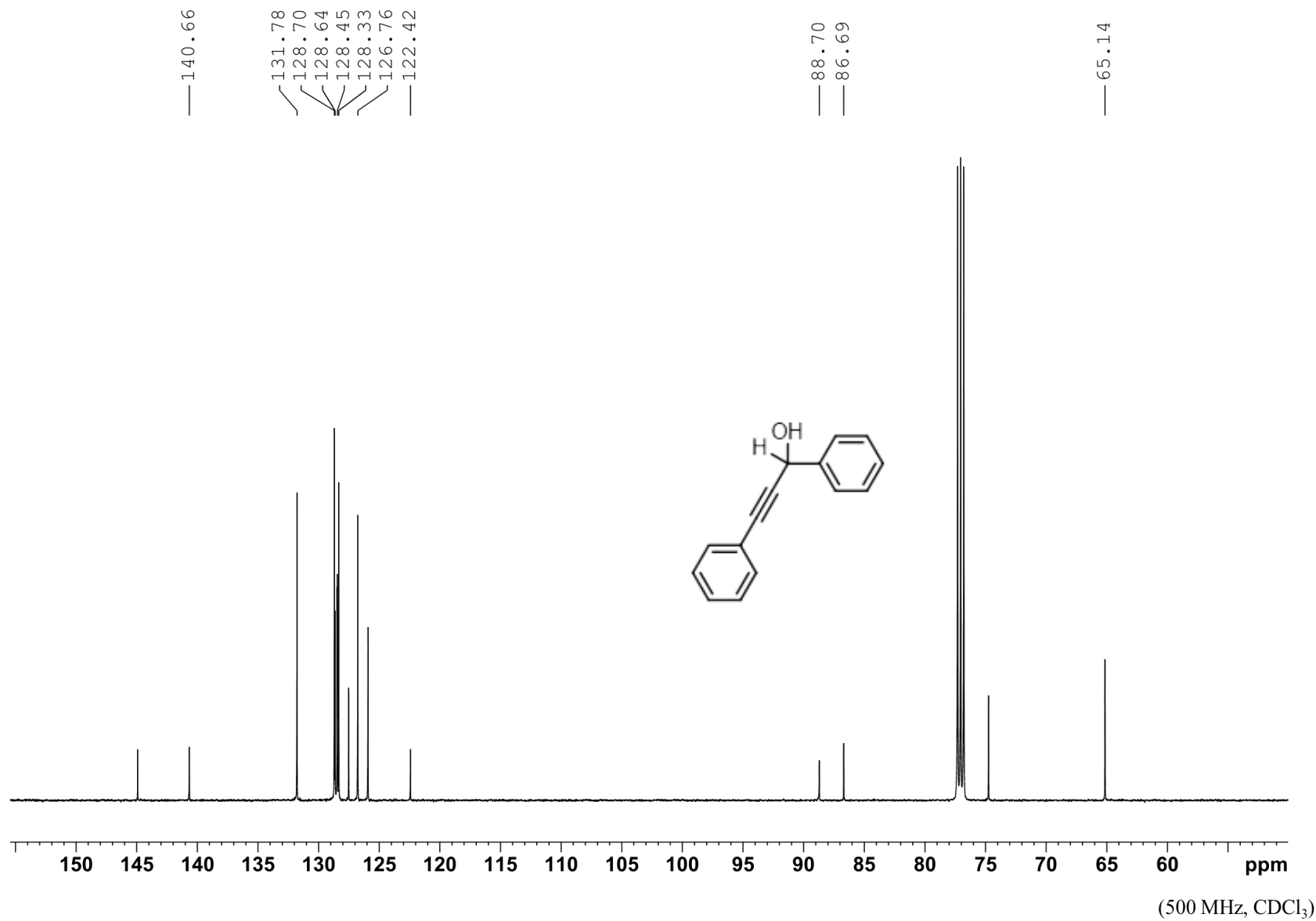
7.63
7.62
7.62
7.48
7.47

5.70

OH

H

(500 MHz, CDCl$_3$)

| 7.7 | 7.6 | 7.5 | 7.4 | 7.3 | 7.2 | 7.1 | 7.0 | 6.9 | 6.8 | 6.7 | 6.6 | 6.5 | 6.4 | 6.3 | 6.2 | 6.1 | 6.0 | 5.9 | 5.8 | 5.7 | ppm |

2.13
2.31
2.18
5.18
1.00

¹³C NMR of 1,3-Diphenylprop-2-yn-1-ol (2a)

(500 MHz, CDCl₃)

¹H NMR of (*E*)-1,3,4,6-tetraphenyl-hex-3-en-1,5-diyne (2c)

7.99
7.99
7.97

7.47
7.41
7.40
7.36
7.29

8.1   8.0   7.9   7.8   7.7   7.6   7.5   7.4   7.3   7.2   ppm

4.00

4.18   2.08   10.10

(500 MHz, CDCl₃)

176

¹³C NMR of *(E)*-1,3,4,6-tetraphenyl-hex-3-en-1,5-diyne (2c)

139.05

131.43
129.27
128.64
128.48
128.31
127.86

123.26

98.57

90.93

(500 MHz, CDCl₃)

^{1}H NMR of (*E*)-1,4-diiodobenzene-3,6-biphneyl- hex-3-en-1,5-diyne (3c)

(500 MHz, CDCl$_3$)

7.79
7.77
7.71
7.70
7.31
7.30

7.90 7.85 7.80 7.75 7.70 7.65 7.60 7.55 7.50 7.45 7.40 7.35 7.30 7.25 ppm

4.00   4.02   10.08

¹³C-NMR of (*E*)-1,4-diiodobenzene-3,6-biphneyl- hex-3-en-1,5-diyne (3c)

138.42
137.02
131.44
131.00
128.87
128.47
127.62
122.74
99.47
94.34
90.00

(500 MHz, CDCl₃)

140 135 130 125 120 115 110 105 100 95 ppm
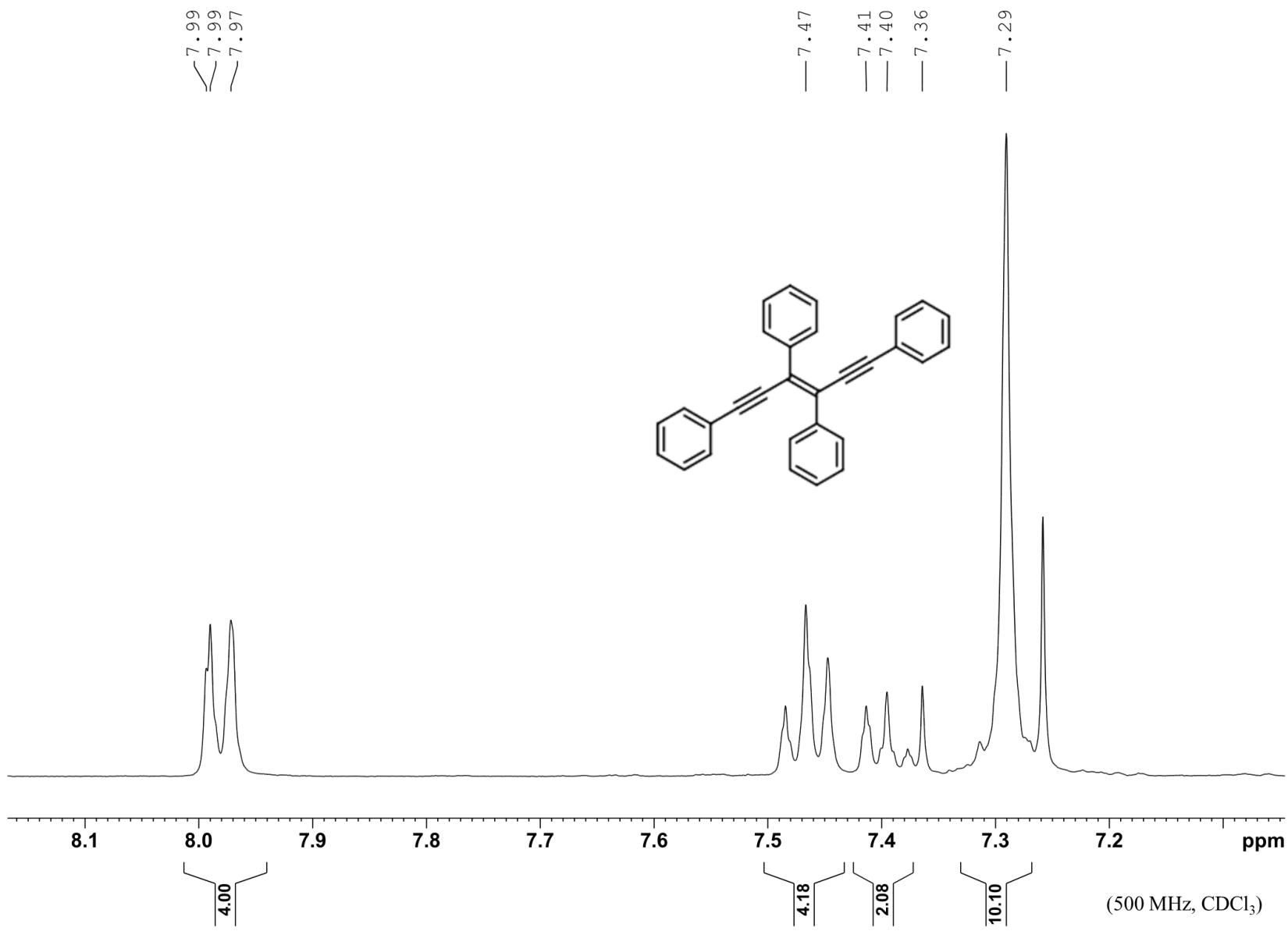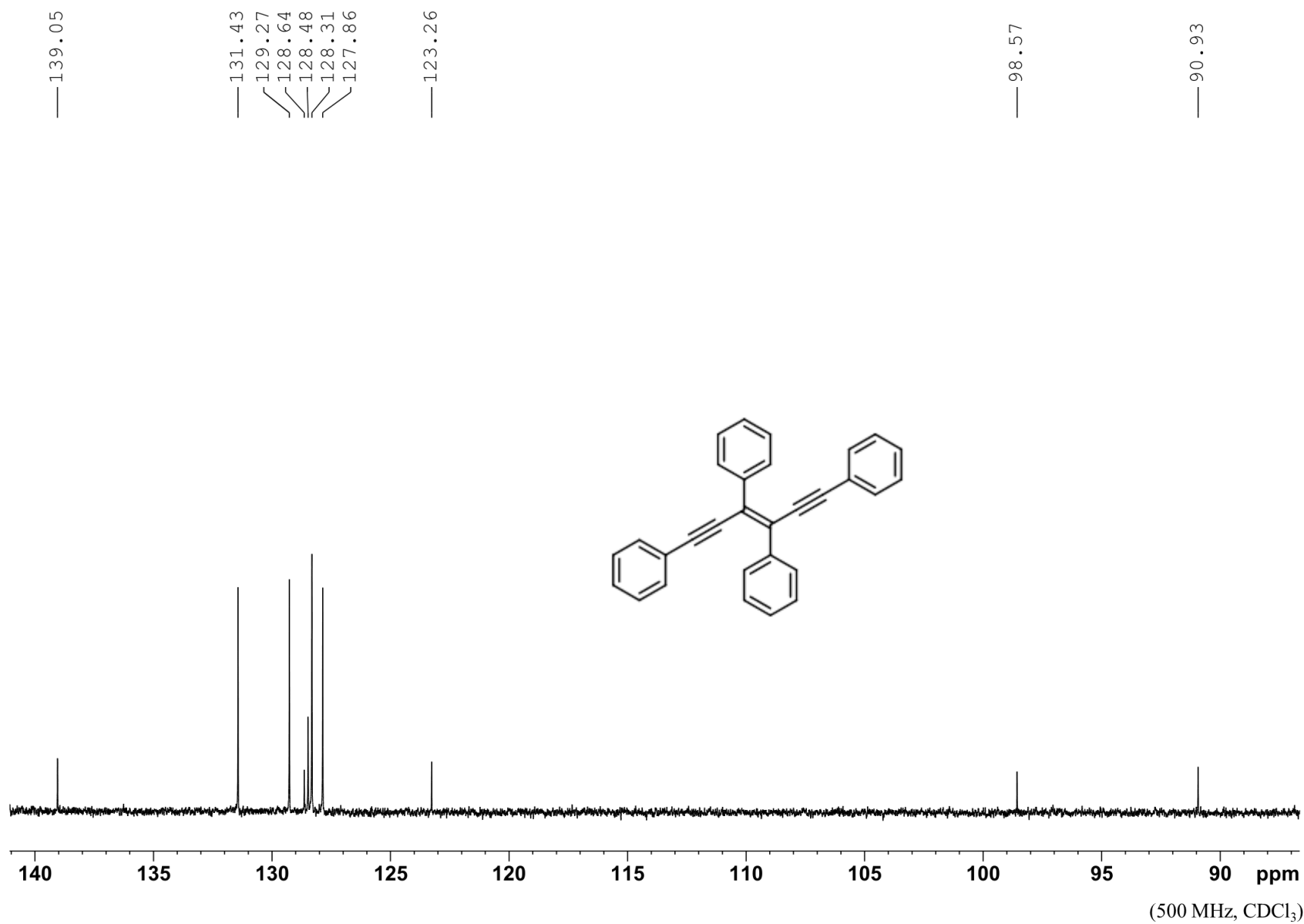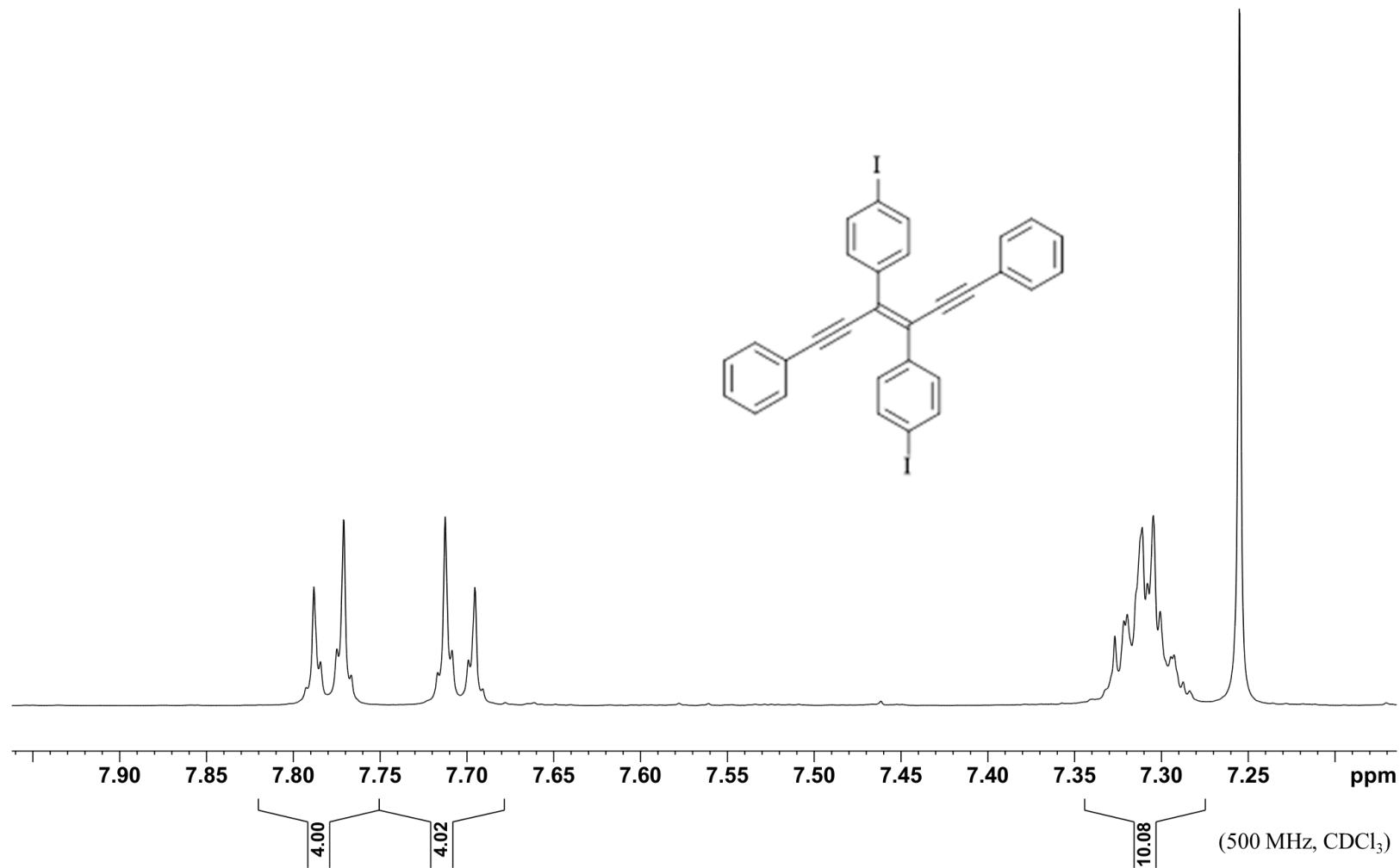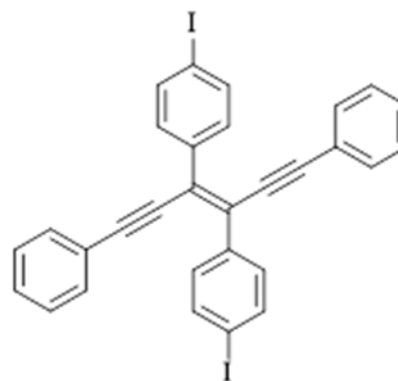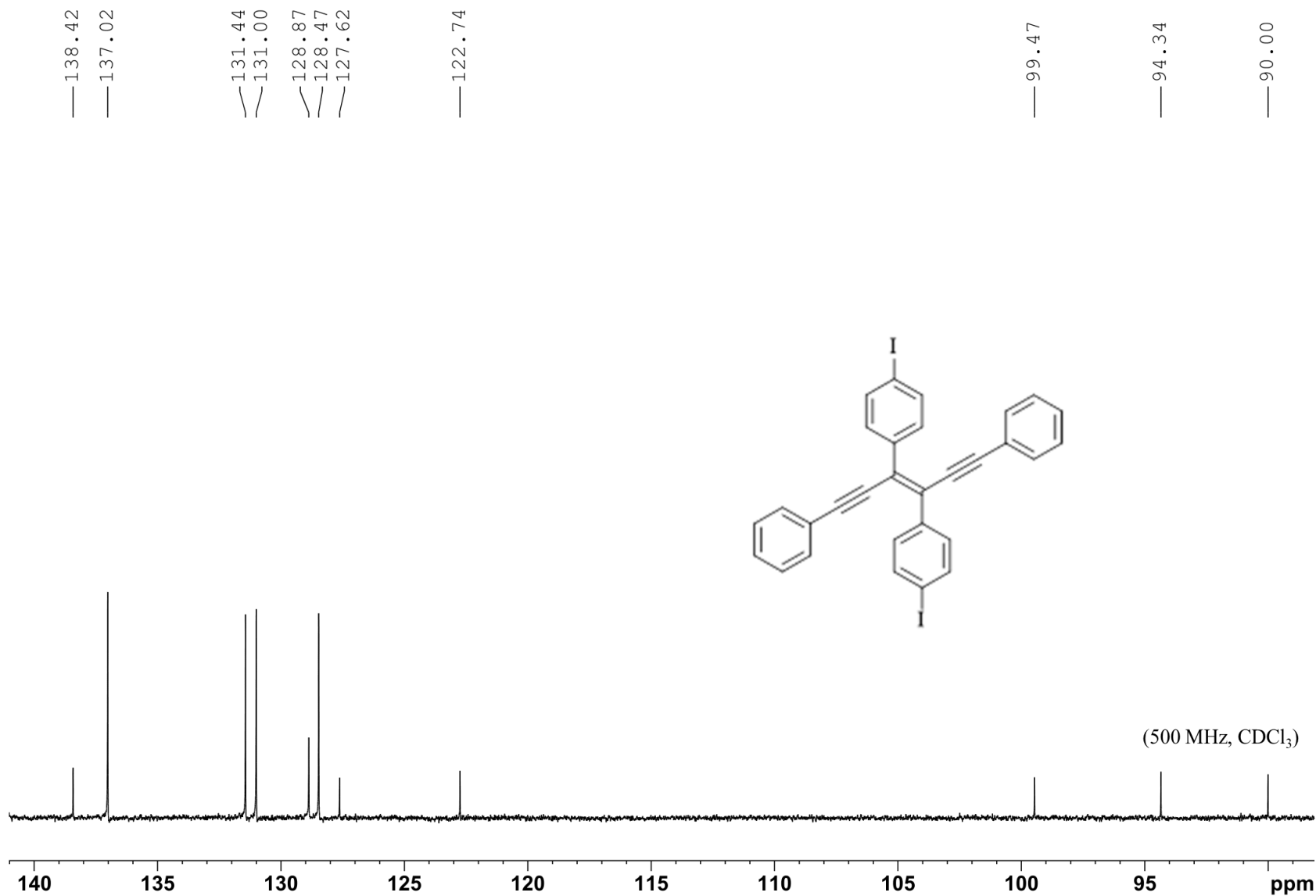
^{1}H NMR of (E)-2,3-dinaphthyl-4,6-diphenyl-hex-3-en-1,5-diyne (3i)

8.54
8.54

8.16
8.16
8.14
8.14

7.95
7.94
7.93
7.91
7.90

7.55
7.54
7.54
7.53
7.53
7.52
7.52

7.28
7.27
7.26

8.6   8.5   8.4   8.3   8.2   8.1   8.0   7.9   7.8   7.7   7.6   7.5   7.4   7.3   7.2   ppm

1.00   1.02   3.07   2.14   3.16   (500 MHz, CDCl$_3$)
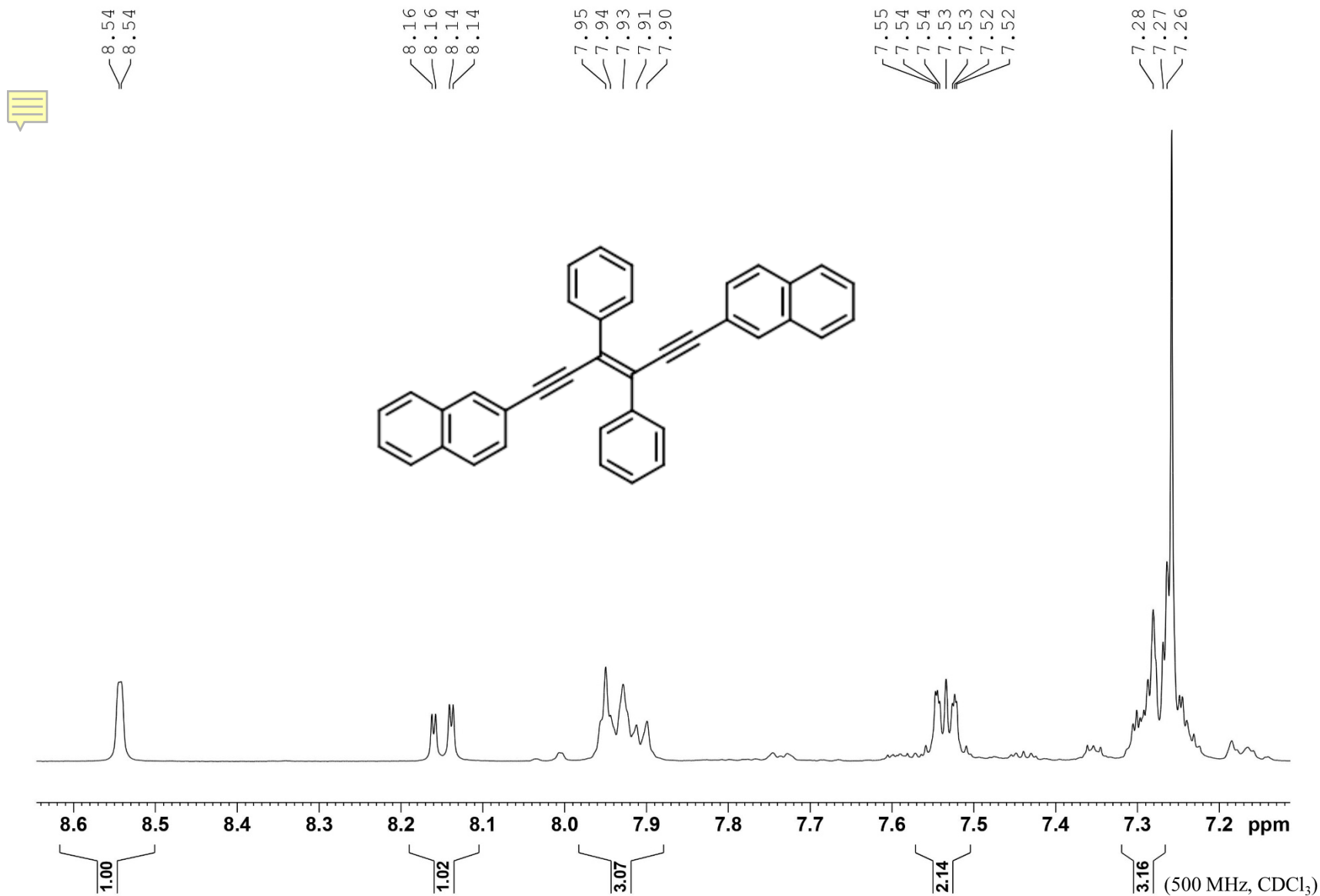
^{13}C-NMR of (E)-1, 3-dinaphtyl-4,6-diphenyl-hex-3-en-1,5-diyne (3i)

136.57
133.24
133.05
131.46
128.75
128.54
128.46
128.33
127.69
127.27
127.13
126.47
126.18
123.17
98.94
91.13
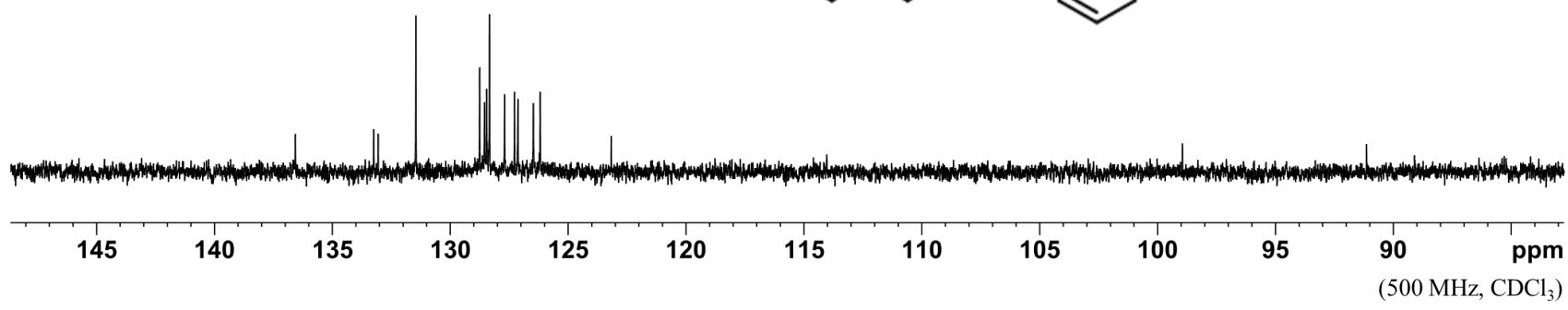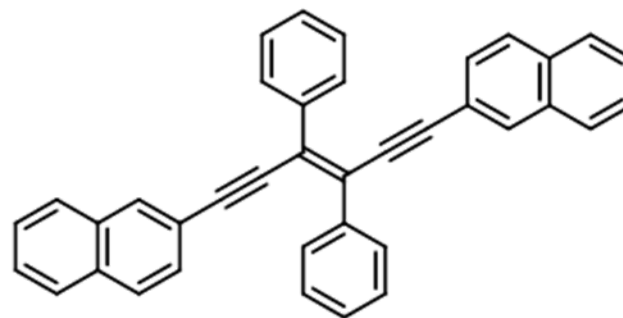
145   140   135   130   125   120   115   110   105   100   95   90   ppm
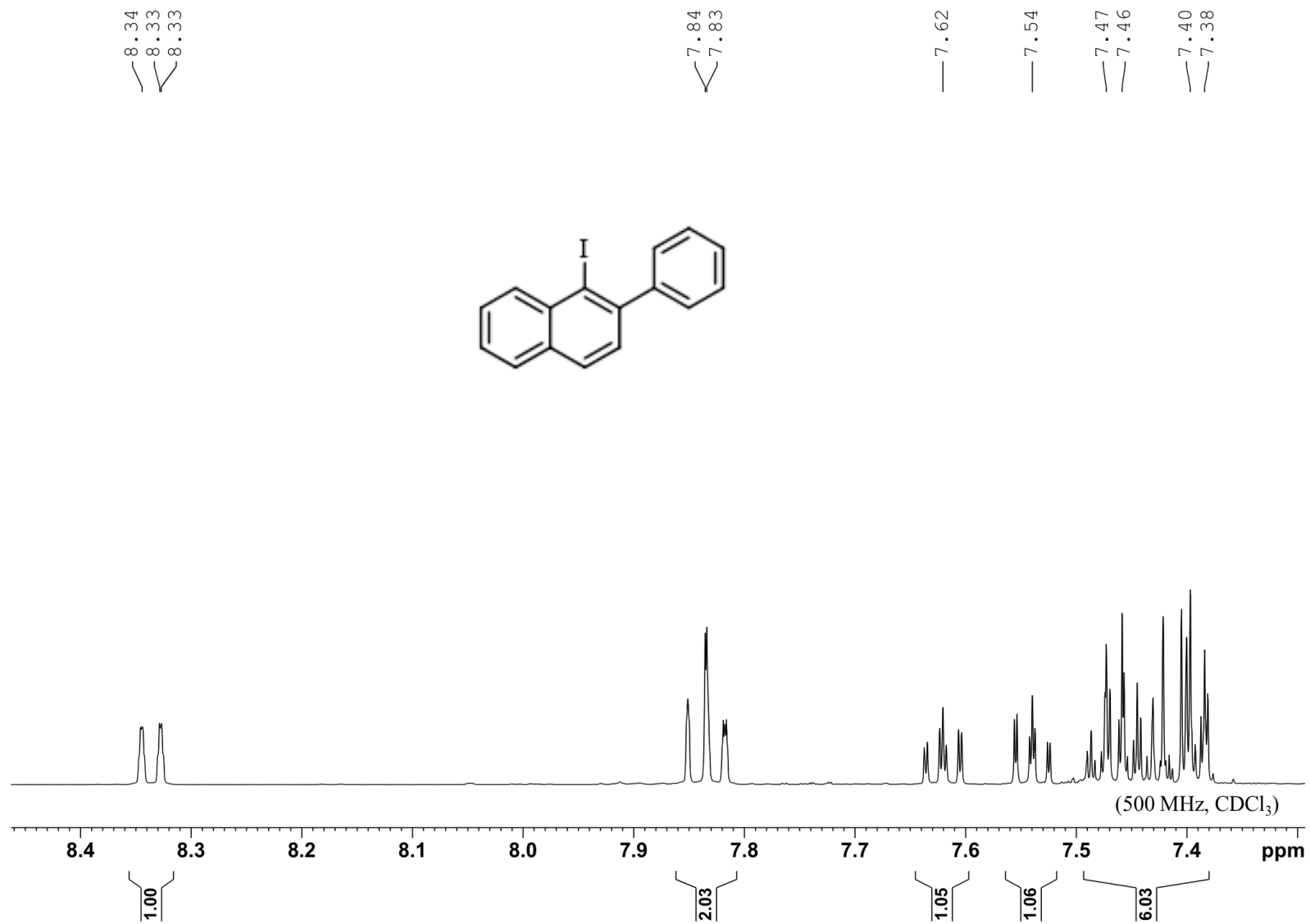
(500 MHz, CDCl$_3$)

181

^{1}H NMR of 1-iodo-2-phenylnaphthalene (4b)

8.34
8.33
8.33

7.84
7.83

7.62

7.54

7.47
7.46

7.40
7.38

(500 MHz, CDCl$_3$)

| 8.4 | 8.3 | 8.2 | 8.1 | 8.0 | 7.9 | 7.8 | 7.7 | 7.6 | 7.5 | 7.4 | ppm |

1.00

2.03

1.05

1.06

6.03

^{13}C NMR of 1-iodo-2-phenylnaphthalene (4b)

146.24
146.09
134.98
133.47
132.97
129.53
128.47
128.26
128.13
127.98
127.61
126.57
104.05

(500 MHz, CDCl$_3$)

145   140   135   130   125   120   115   110   ppm

¹H NMR of 1-ethynyl-2-phenyl-naphthalene (4d)

8.51
8.49
7.91
7.89
7.87
7.70
7.70
7.68
7.62
7.54
7.52
7.51
7.49
7.48
7.46
7.42
7.41
3.45

(500 MHz, CDCl₃)

8.5
8.4
8.3
8.2
8.1
8.0
7.9
7.8
7.7
7.6
7.5
ppm

1.00
2.05
2.02
1.03
2.04
2.04
1.04

8.5
8.0
7.5
7.0
6.5
6.0
5.5
5.0
4.5
4.0
ppm

1.00
2.05
2.02
1.03
2.04
2.04
1.04
0.98
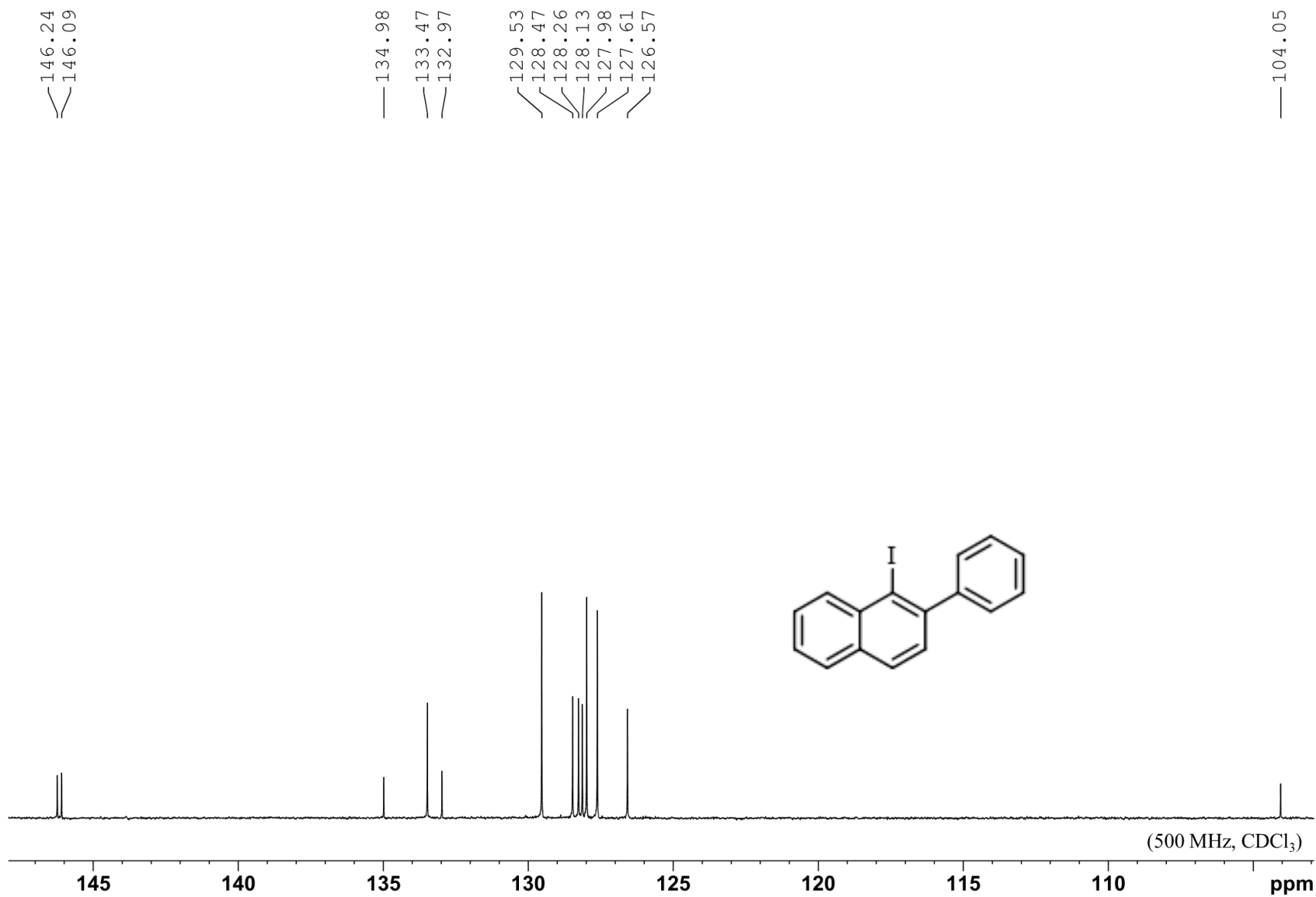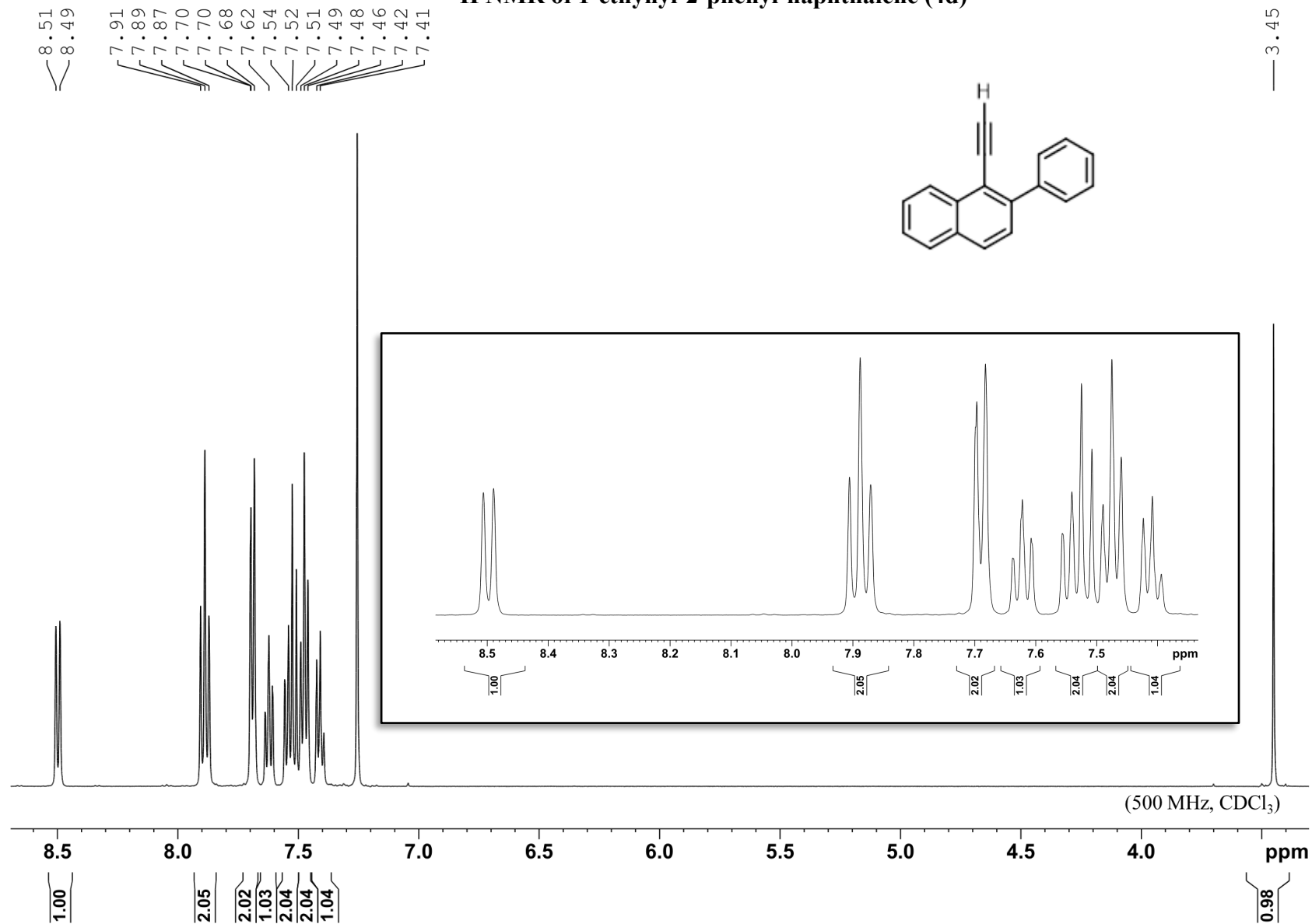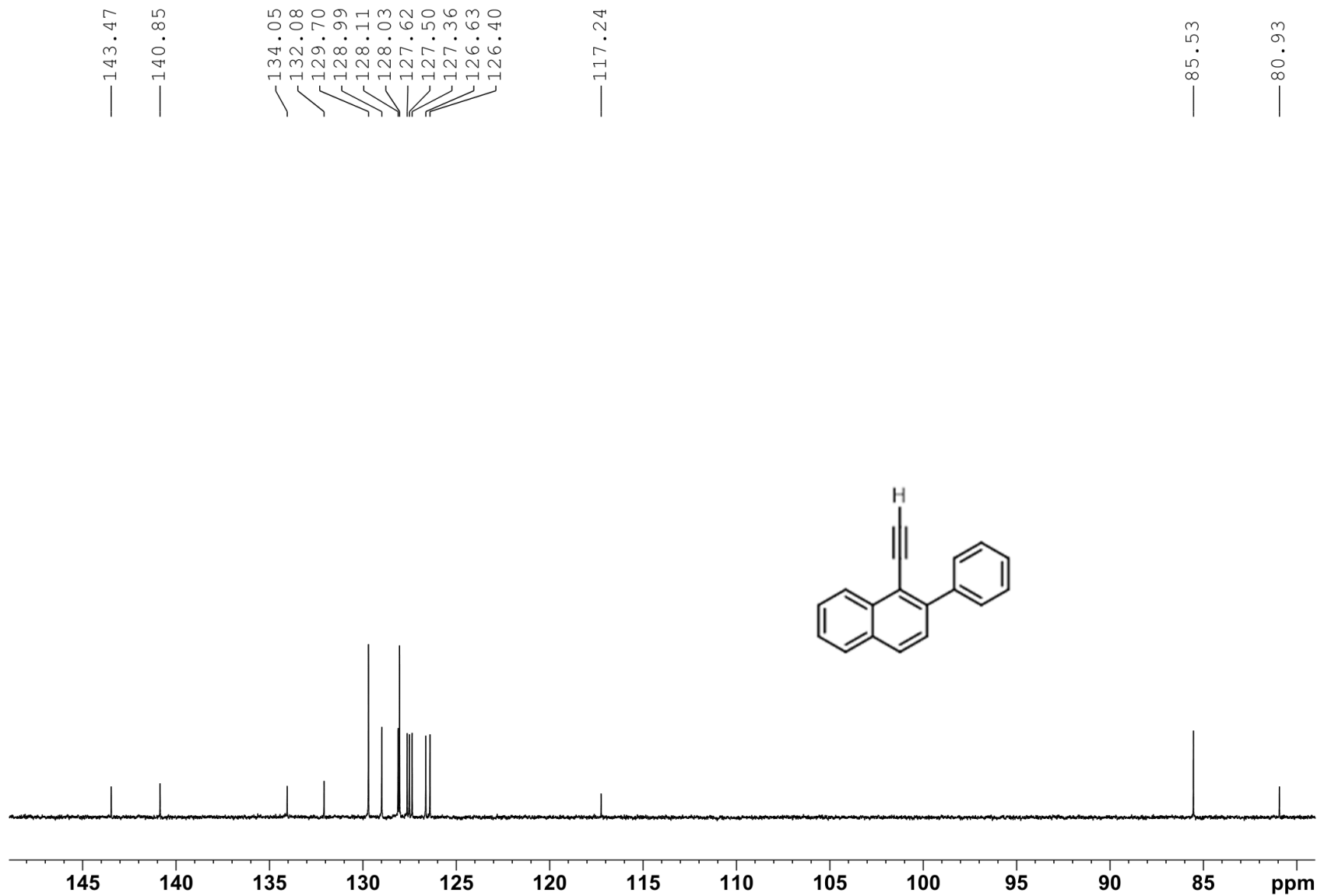
(500 MHz, CDCl₃)

¹H NMR of 1- (4-iodophenyl)-3-(2-phenylnaphthalen-1-yl)prop-2-yn-1-ol (4e)

8.42
8.40

7.88
7.65
7.63
7.61
7.52
7.41
7.41
7.14
7.12

5.63

2.25
2.24

(500 MHz, CDCl₃)
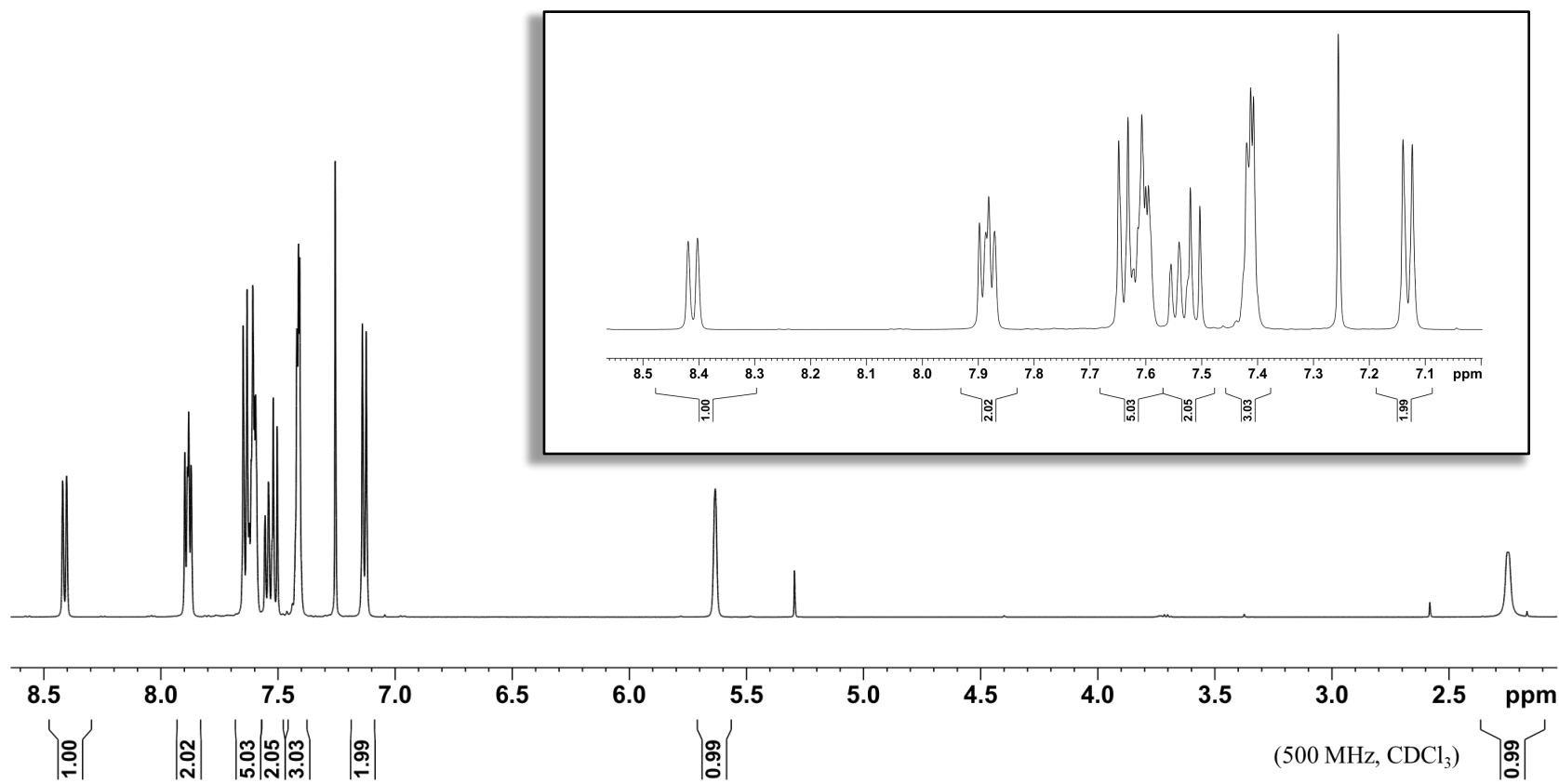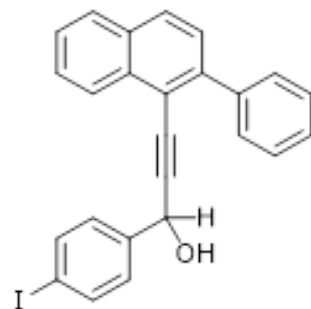
^{13}C NMR of 1-(4-iodophenyl)-3-(2-phenylnaphthalen-1-yl)prop-2-yn-1-ol (4e)

143.36
141.05
140.14
137.63
133.62
132.14
129.66
129.01
128.69
128.19
128.10
127.63
127.41
126.47
117.40
96.06
94.01
84.77
64.81

(500 MHz, CDCl$_3$)

150 145 140 135 130 125 120 115 110 105 100 95 90 85 80 75 70 65 60 ppm
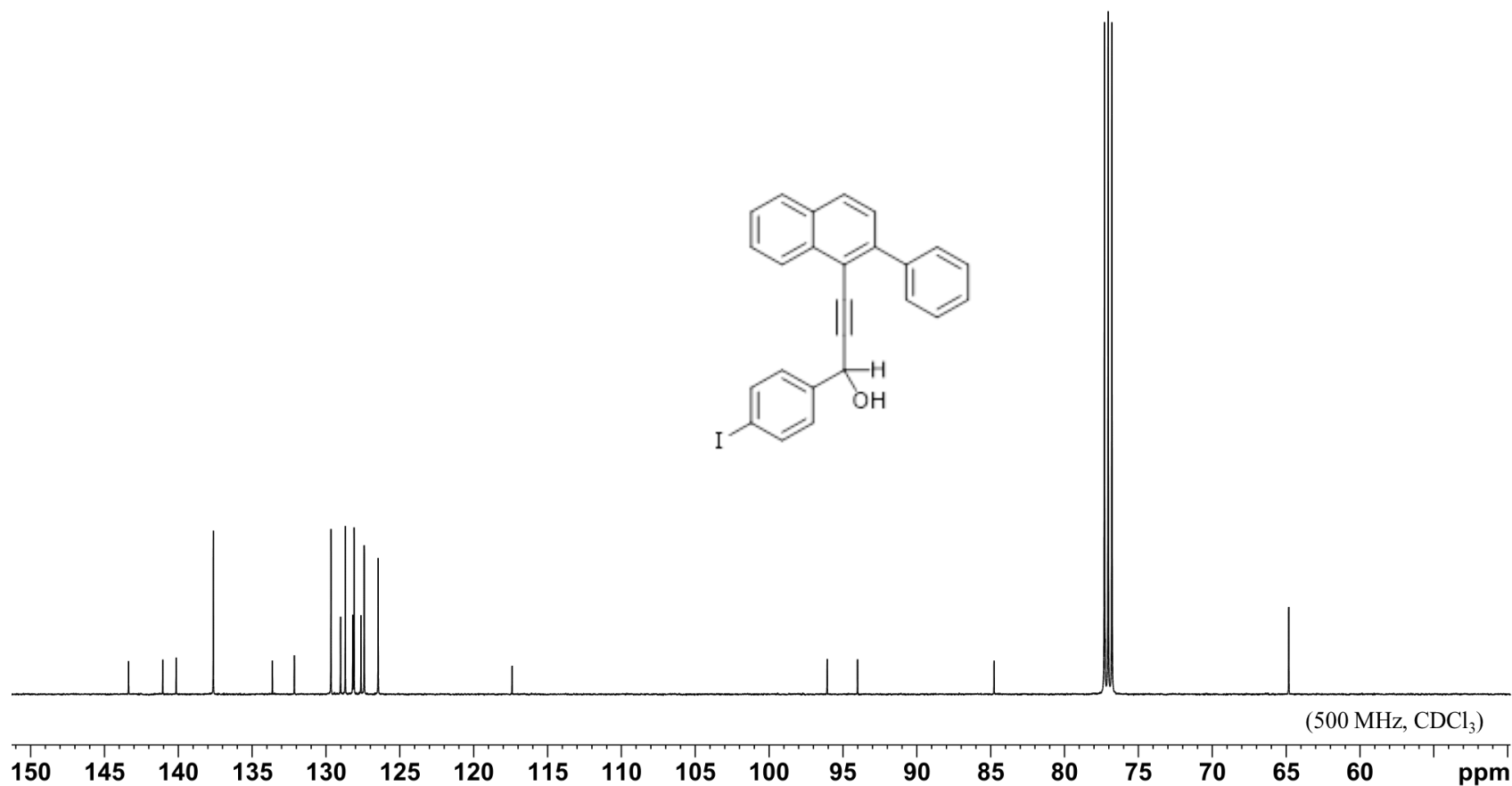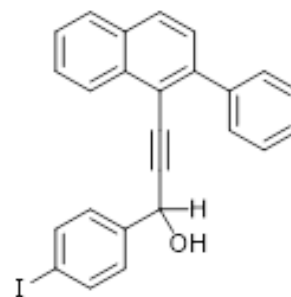
¹H NMR of (E)-1,3-(2-phenylnaphtyl)-4,6-diiodophenyl-hex-3-en-1,5-diyne (4g)

7.90
7.89
7.88
7.87

7.71
7.70

7.64
7.62

7.55
7.54
7.53
7.50

7.40

7.37
7.35

7.31
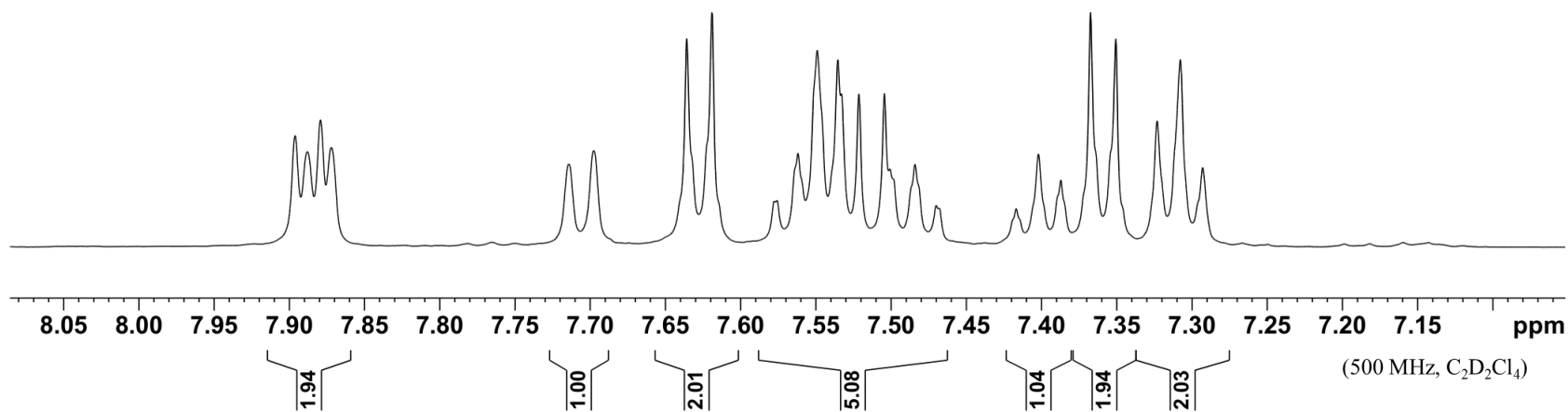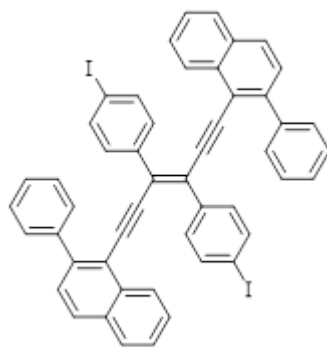
8.05 8.00 7.95 7.90 7.85 7.80 7.75 7.70 7.65 7.60 7.55 7.50 7.45 7.40 7.35 7.30 7.25 7.20 7.15   ppm

1.94   1.00   2.01   5.08   1.04   1.94   2.03

(500 MHz, C₂D₂Cl₄)

^{13}C NMR of (E)-1,3-(2-phenylnaphtyl)-4,6-diiodophenyl-hex-3-en-1,5-diyne (4g)

143.33
140.70
138.37
137.49
133.49
132.07
130.95
129.60
129.37
128.27
127.82
127.78
127.58
126.75
126.59
120.45
118.11
98.47
97.76
94.33

(500 MHz, C₂D₂Cl₄)

150   145   140   135   130   125   120   115   110   105   100   95   ppm

^{1}H NMR of 1-iodo-2-phenyl-3-methyl-naphthalene (4h)
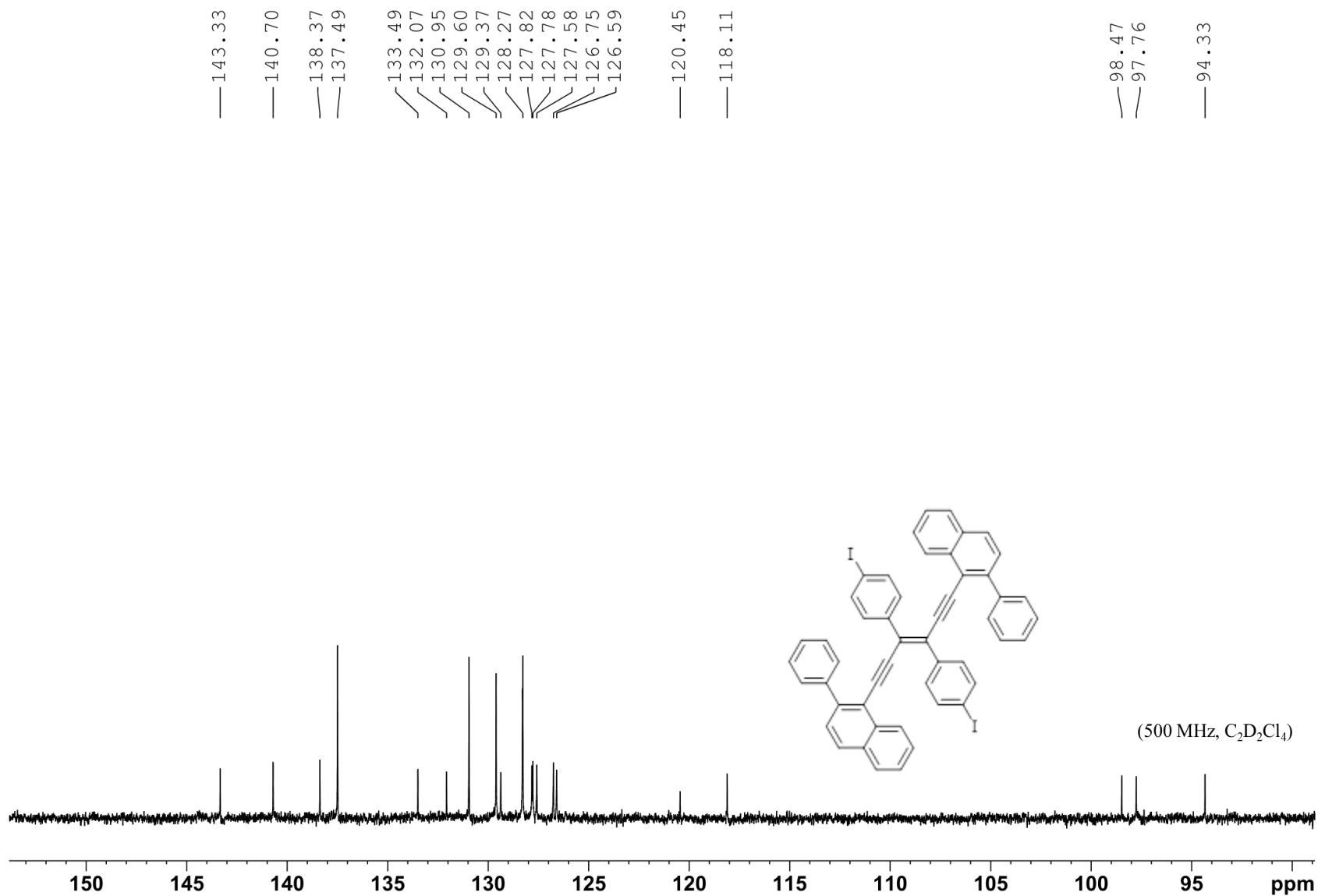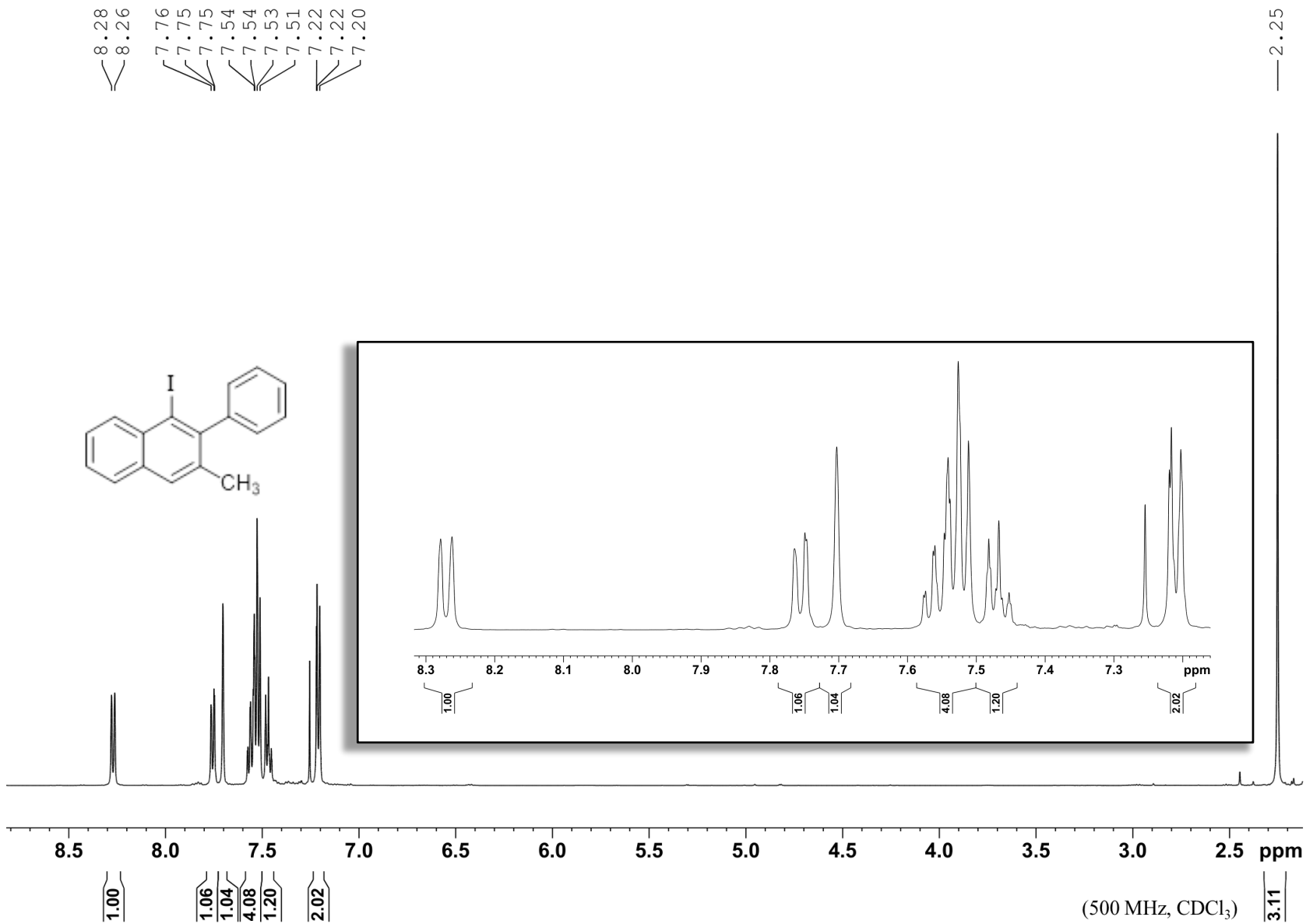
(500 MHz, CDCl$_3$)

^{13}C NMR of 1-iodo-2-phenyl-3-methyl-naphthalene (4h)

147.10
145.95

135.06
133.73
133.70
133.38
129.08
128.74
128.49
127.58
127.53
127.16
126.66

106.10
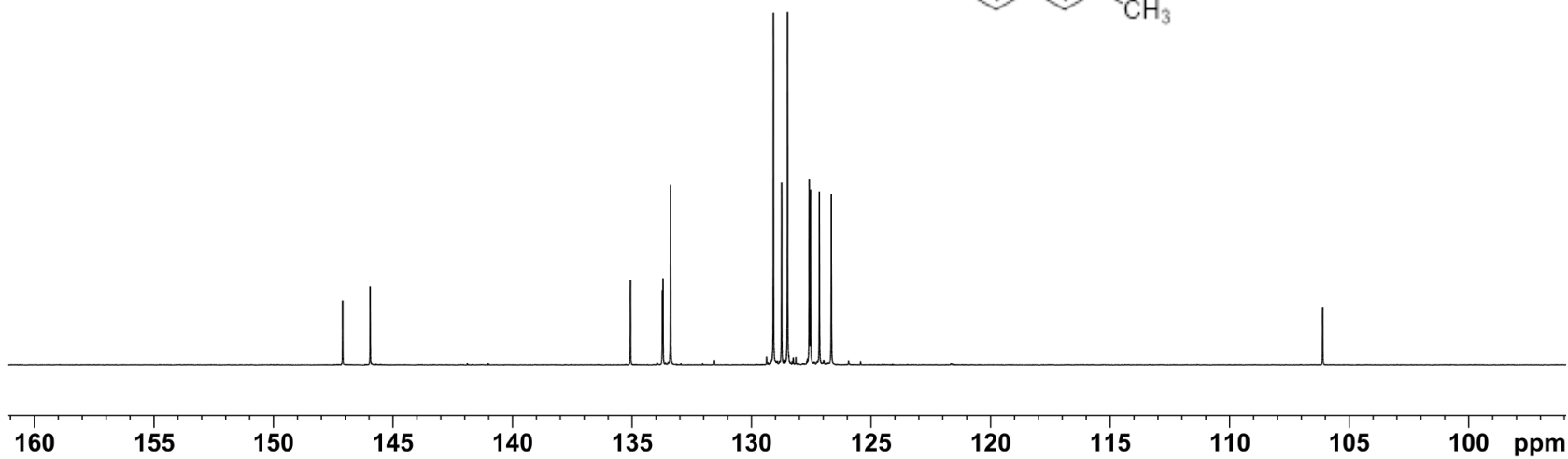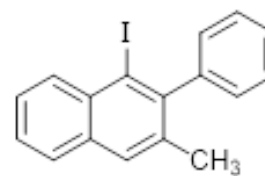
(500 MHz, CDCl$_3$)

^{1}H NMR of 1-ethynyl-2-phenyl-3-methyl-naphthalene (4j)

8.36

7.73
7.52
7.47
7.45
7.32
7.25

3.29

2.23

(500 MHz, CDCl$_3$)
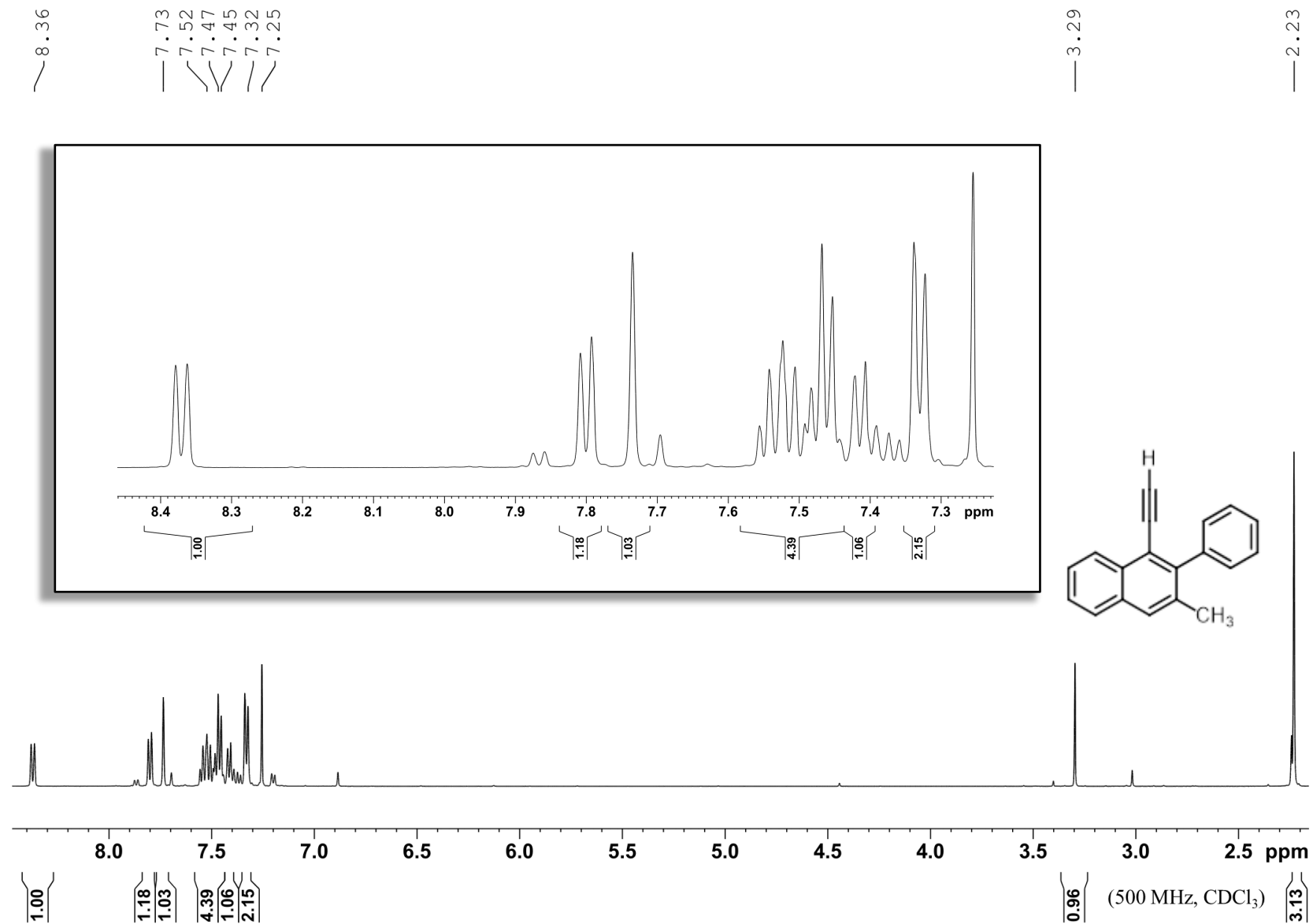
^{13}C-NMR Spectrum of 1-ethynyl-2-phenyl-3-methyl-naphthalene (4j)

145.17
140.37
134.15
132.47
132.35
129.36
129.00
128.09
127.37
127.26
126.42
126.41
126.31
118.79

85.48
80.91

21.44

150   140   130   120   110   100   90   80   70   60   50   40   30   ppm

(500 MHz, CDCl$_3$)

^{1}H NMR of 1-(4-iodophenyl)-3-(2-phenyl-3-methyl-naphthalen-1-yl)prop-2-yn-1-ol (4k)

8.31, 8.29

7.73, 7.59, 7.58, 7.52, 7.44, 7.33, 7.32, 7.30, 7.30, 7.29, 7.29, 6.91, 6.89

5.51, 5.50

2.23

1.98, 1.96

(500 MHz, CDCl$_3$)

1.00 1.04 1.05 2.03 2.11 3.06 2.13 2.02 1.00 3.10 1.01

^{13}C NMR of 1-(4-iodophenyl)-3-(2-phenyl-3-methyl-naphthalen-1-yl)prop-2-yn-1-ol (4k)

140.68
140.12
137.53
134.16
132.53
131.89
129.43
129.00
128.66
128.25
127.43
127.31
126.49
126.43
126.16
118.88

96.34
93.89

84.97

64.66

21.35

140 130 120 110 100 90 80 70 60 50 40 30 20 ppm

(500 MHz, CDCl$_3$)

195

^{1}H NMR of (E) -1,3-(2-phenyl-3-methyl-naphtyl)-4,6-diiodophenyl-hex-3-en-1,5-diyne (4m)

7.55
7.51
7.50
7.47
7.46
7.36
7.36
7.35
7.35
7.35
7.34
7.32
7.20
7.20
7.19
7.08
7.06

2.16

(500 MHz, CDCl$_3$)

7.75 7.70 7.65 7.60 7.55 7.50 7.45 7.40 7.35 7.30 7.25 7.20 7.15 7.10 ppm

1.00
1.03
1.93
1.03
1.19
3.97
1.86
1.81

8.0   7.5   7.0   6.5   6.0   5.5   5.0   4.5   4.0   3.5   3.0   2.5   ppm

1.00
1.03
1.93
1.03
1.19
3.97
1.86
1.81

3.15

¹³C NMR of (E)-1,3-(2-phenyl-3-methyl-naphtyl)-4,6-diiodophenyl-hex-3-en-1,5-diyne (4m)

140.27
138.51
137.35
134.27
132.43
131.84
130.70
129.26
129.18
128.17
127.87
127.28
127.24
126.48
126.32
126.28
119.55
98.38
97.93
93.64
21.30

1.00

(500 MHz, CDCl₃)

^{1}H NMR of ((2,5-dibromophenyl)ethynyl)trimethylsilane
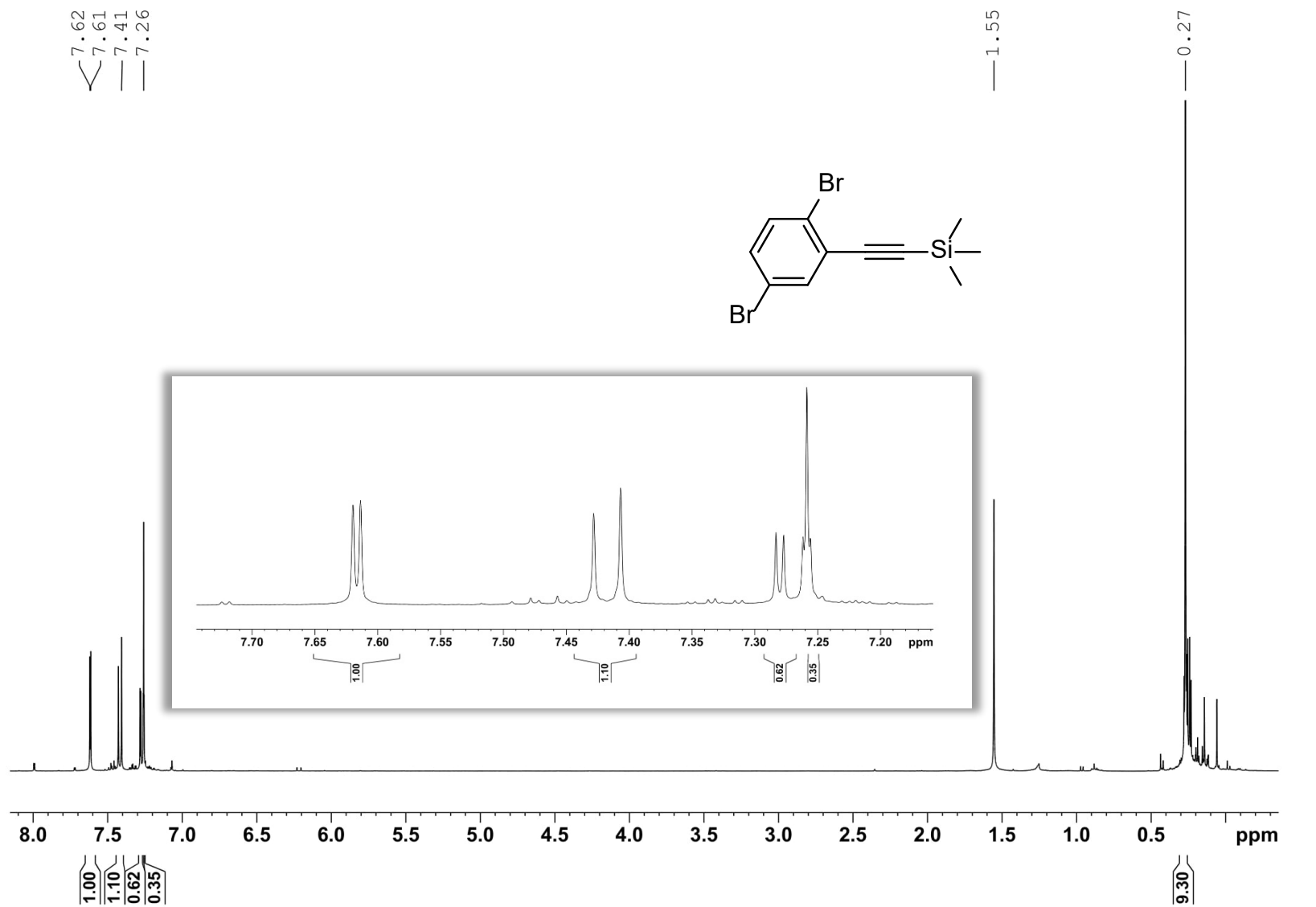
7.62
7.61
7.41
7.26

1.55

0.27

(500 MHz, CDCl$_3$)

136.55
133.74
133.14
126.15
124.32
120.59
83.14
80.61

(500 MHz, CDCl$_3$)

135 130 125 120 115 110 105 100 95 90 85 ppm

^{1}H NMR of 1,4-dibromo-2-ethynylbenzene (4o)

7.70
7.69

7.47
7.45

7.36
7.36
7.34
7.34

(500 MHz, CDCl$_3$)

1.00

1.07

1.03

7.70   7.65   7.60   7.55   7.50   7.45   7.40   7.35   7.30   ppm

200
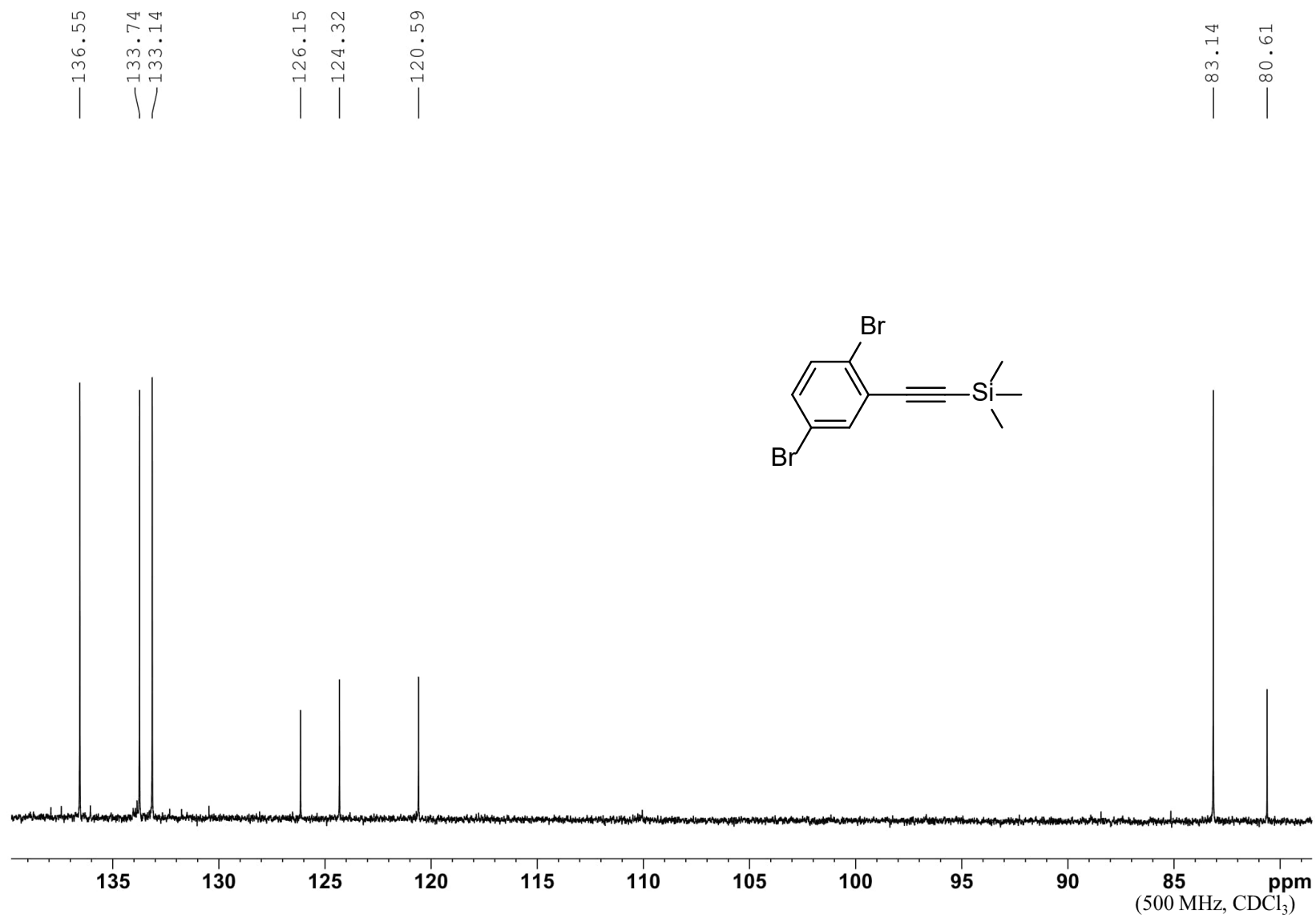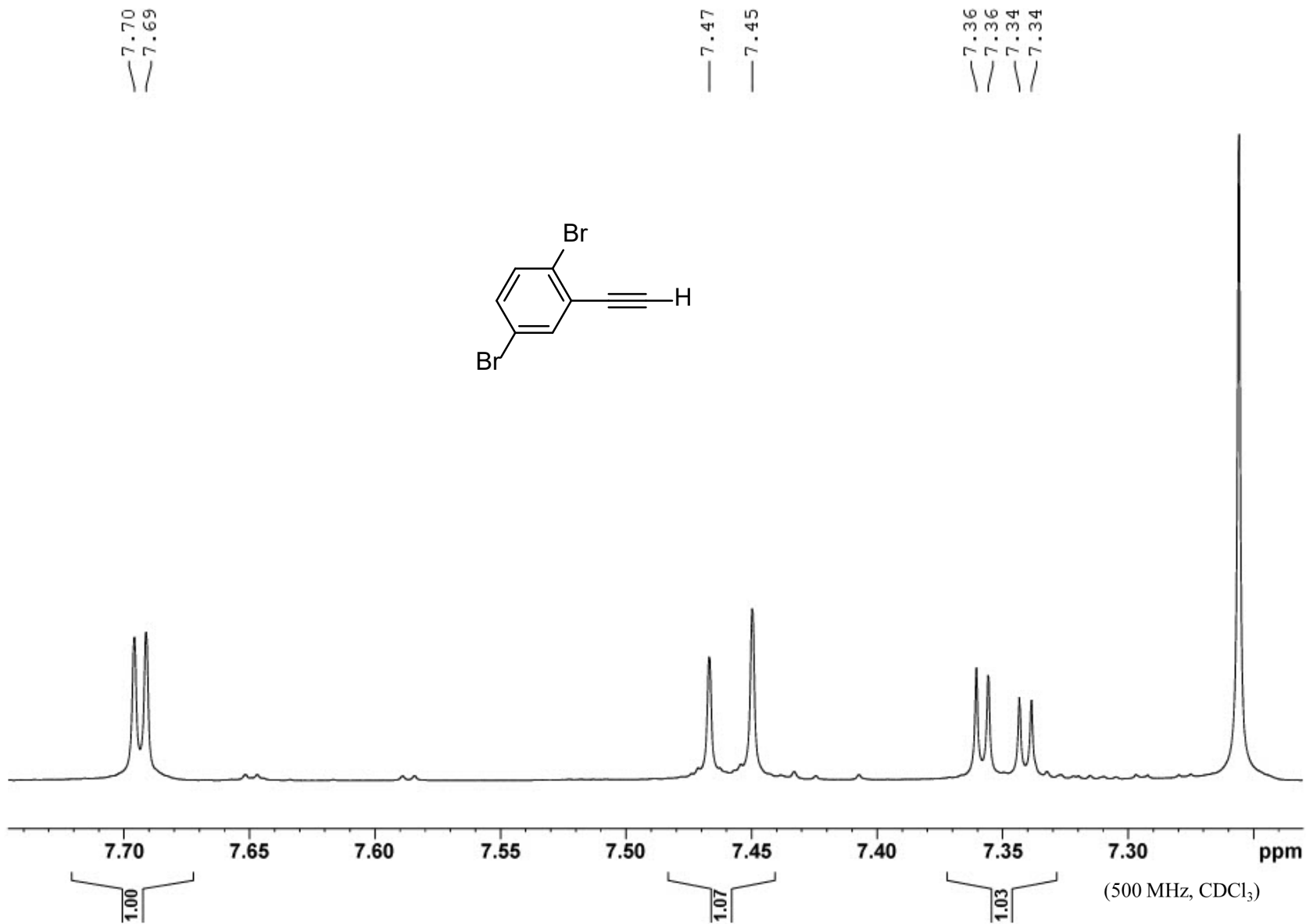
¹³C NMR Spectrum of 1,4-dibromo-2-ethynylbenzene (4o)

189.84

150.73
146.90
144.47

134.29
131.24
129.12
128.72

121.58
121.18

190 180 170 160 150 140 130 120 110 100 90 80 ppm

(500 MHz, CDCl₃)

201

^{1}H NMR of 1,4-bis(2,5-dibromophenyl)buta-1,3-diyne (4p)

7.70
7.69

7.47
7.45

7.36
7.36
7.34
7.34

1.00

1.07

1.03

7.75   7.70   7.65   7.60   7.55   7.50   7.45   7.40   7.35   ppm

(500 MHz, CDCl$_3$)
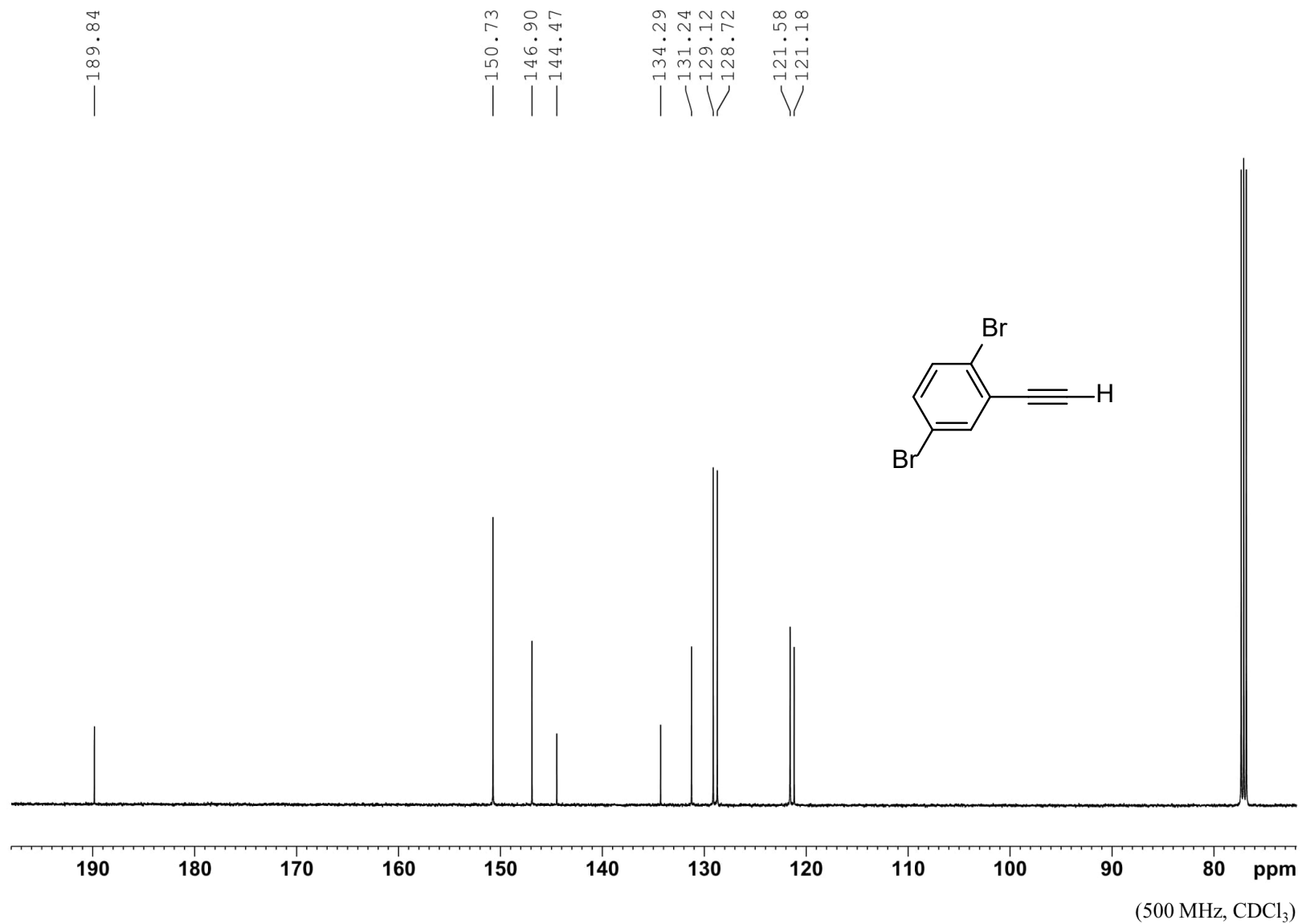
¹³C NMR of 1,4-bis(2,5-dibromophenyl)buta-1,3-diyne (4P)

136.87
133.88
133.68
125.71
124.95
120.70
80.31
78.64

(500 MHz, CDCl₃)
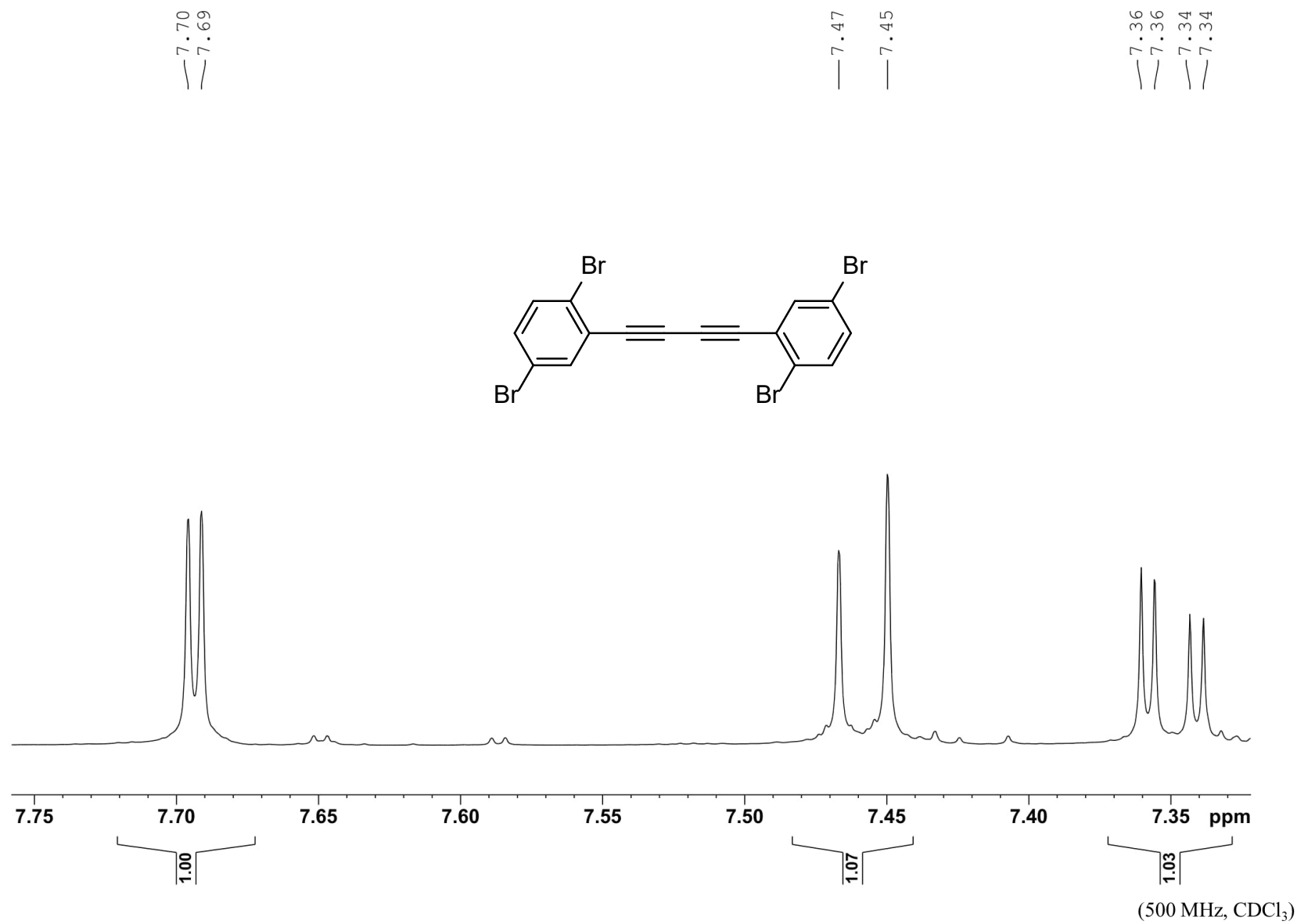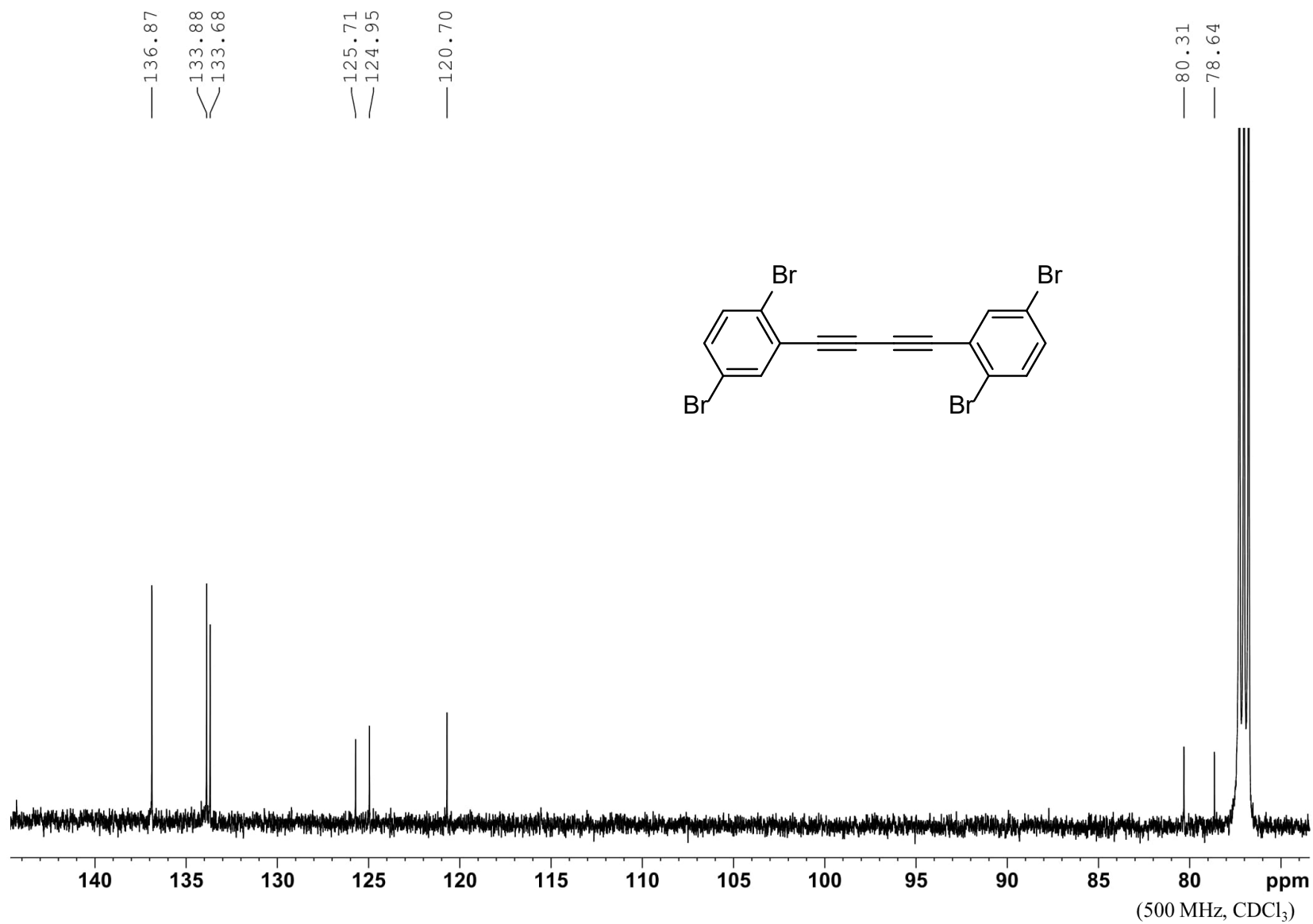
CHAPTER 6. CHEMICAL EDUCATION: STRUCTURED REMOTE CLASSES REFLECT HIGH STUDENT ENGAGEMENT IN DISCUSSION SECTIONS

6.1. Introduction

With the shift to remote instruction, chemical education research has noted the recent disparities in student performance in an online setting. To help create equitable remote learning environments, a closer analysis of students' activity within a remote setting is necessary. Herein, quantitative measurements on camera usage and student interaction in Zoom breakout rooms for Fall 2020 (F20), Winter 2021 (W21), and Summer 2021 (S21) courses were collected and analyzed.

Results indicate that "structured," remote courses are correlated with increased student engagement within breakout rooms of a discussion section. A structured course was characterized by tallying specific requirements for how group facilitation was conducted. Observational measurements that counted (1) student interaction and (2) general camera usage were used to monitor overall engagement. This was done by surveying almost 1,000 induvial students across nine different courses in F20 and W21 at random timepoints. During W21, survey responses were also considered to determine students' sense of inclusion and the relationship to engagement. Here, the results indicate that there is a positive trend between the courses' structure and students' sense of belonging and connectedness. Additionally, in S21, a single high structured course, with approximately 120 students, was observed at interval time points to determine the overall trend of engagement, and further validate the previous findings.

In conclusion, the overall results presented here indicate that an enhanced course structure leads to higher rates of student engagement and sense of inclusion in remote courses. Suggested

methods for designing a successful remote course include the following: required attendance, assigned groups, 4 students per group, assigned roles for each student in a group, assistance mobility between groups, and assigned worksheets.

6.2. Background

On March 6, 2020, University of Washington became the first university in the United States to announce the move to remote instruction as an emergency response to the COVID-19 pandemic[1]. Universities across the country followed suit and pivoted from offering in-person classes to remote online instructions within a matter of weeks. This presented a major challenge for large enrollment STEM courses, especially in chemistry classes where visual demonstrations were integral to portraying molecular structure and other chemical concepts. The challenges that ensued from this sudden transition were documented in The Journal of Chemical Education special edition.[2] A majority of the discussion revolved around the decline in student engagement during remote learning and its subsequent impact on student performance.[3,4,5,6,7] This work aims to divulge trends in students' sense of community and inclusivity in online classrooms as a result of the COVID-19 pandemic. Herein, we have quantitatively monitored student engagement within large enrollment introductory chemistry courses during the Fall 2020, Winter 2021, and Summer 2021 quarters.

Previous work has used a mixed methods approach to define the relationship between student engagement and persistence in introductory STEM courses. To aid student success in these "gatekeeper" courses, suggestions were made for increasing student engagement and interactions overall[8]. Furthermore, STEM students who received a D, F, or W in these classes were more likely to leave a STEM degree program after their first two years.[9,10] This is especially

concerning for persons excluded because of their ethnicity or race (PEERs); "in US Science, this includes persons who identify as Black or African American, Latinx or Hispanic, and peoples indigenous to the spaces comprising the US and its territories."[11] Both PEERs and non-PEERs enter STEM at comparable rates[12], however PEERs leave at disproportionately higher rates.[13] Furthermore, A 2019 study found that the exclusion of PEERs is not found in non-STEM fields.[14] Therefore, to discern approaches that make science inclusive, methods aimed at increasing PEER participation rates in early STEM courses should be closely addressed.

Inclusion and a sense of belonging are two important contributors that increase student engagement and persistence through STEM courses. Fink et. al. has shown that belonging predicts first-year undergraduates' performance and attrition in general chemistry.[15] Belonging has also been studied through various lenses including first-year students,[16,17] college-wide level,[18,19] and most importantly with PEERs.[20,21,22,23,24] A 2015 multi-institute study surveyed over 1500 students and found that belonging level in STEM classroom was key to student engagement.[25] Moreso, creating a classroom environment that increases inclusion, belonging, and engagement is multifaceted and most successful with intentional design to facilitate positive interactions among peers[19] and between faculty and students.[8]

Two strategies to create this environment are highly structured courses and incorporating peer learning. High structure courses incorporate multiple facets for students to interact with the material through active learning[26] inside and outside of class. This contrasts with low structure courses which rely mainly on lecture and major summative assessments. Studies have demonstrated improvements in student performance in highly structured biology [27,28] and organic chemistry[29] courses. Furthermore, a study by Eddy and Hogan found that increasing a course's

structure closes the achievement gap between white and black students and first-generation and continuing-generation students in a general introduction to Biology course.[30]

The second strategy that reinforces inclusion and belonging in the classroom is the addition of peer learning[31] through the use of Learning Assistants (LAs). LAs, as described by the Colorado Learning Assistant Model,[32] are undergraduate students who are trained to support student learning through various pedagogical methods. In studies, peer learning has been shown to increase sense of belonging by using LAs[33] which increase student reasoning and problem solving through cooperative group work.[34,35] Therefore, it is important to determine how to adapt these known best practices to an online space while maintaining feelings of belonging and inclusion.

Creating a Successful Online Learning Community through Enhanced Instructional Design

In the last decade, there has been an expansion of online learning spaces and recent research indicates that enrollment in online courses is continuing to grow. As of 2014, it was estimated that 5.8 million students were enrolled in at least one online course in the United States higher education system. Additionally, online education is being supported by many higher education academic leaders (63.3%)[36]. In 2008, 96% of public two-year colleges and 86% of public four-year colleges offered online courses[37].

Extensive research on learning advocates that students learn best when they construct new knowledge by forming a classroom community where they interact with each other and share common goals, values, and language.[38,39] *Garrison et al.* has expanded and applied the social views of learning to an online learning context and developed a theoretical framework,

Community of Inquiry (CoI). CoI supports building an online community where students can have a meaningful educational experience through social interaction.[40] Furthermore, research regarding online learning evidenced that an effective online education required the development of a learning community.[41,42,43] The collaborative and constructive CoI framework consists of three core and interdependent elements - cognitive presence, social presence, and teaching presence. Cognitive presence is defined as the ability of learners to construct meaning through sustained communication and reflection. Social presence includes a supportive and collaborative online setting where students can express emotions, communicate openly, and create a sense of belonging through discussion and reflection. Additionally, high social presence increases students' motivation to participate, improves learners' satisfaction with the instructor, and betters the students' actual and perceived learning in an online environment.[44,45,46,47,48] The third element of CoI, *teaching presence*, involves the design, direction, and facilitation of cognitive and social processes to maximize learning.[40] Therefore, carefully designed instructional methods or activities to facilitate discourse to develop a social and cognitive presence in online learning are of utmost importance. Several studies have shown that structured collaborative peer teams, problem-solving tasks, collaborative projects, and group discussion can help students effectively achieve learning objectives in online environments.[49,50, 51] Therefore, it is necessary for educators to explore different frameworks and theories to focus their attention on students' learning experience and needs with respect to online environments.

6.3. Motivation

Initial data collection for this study began through observations as a Teaching Assistant for *Life Sciences: Introduction to Collaborative Learning Theory and Practice* at University of

California, Los Angeles (UCLA) in Fall 2020. This role required each assigned TA to support all

LAs in their respective departments. While different institutions utilize LAs in various capacities,

UCLA primarily utilizes LAs in supporting discussion sections, lectures, and assisting TAs and

instructors in office hours, or laboratory courses. Specifically, in the chemistry department, prior

in-person discussion sections utilized LAs to assist groups of students throughout the classroom.

6.4. Research Design
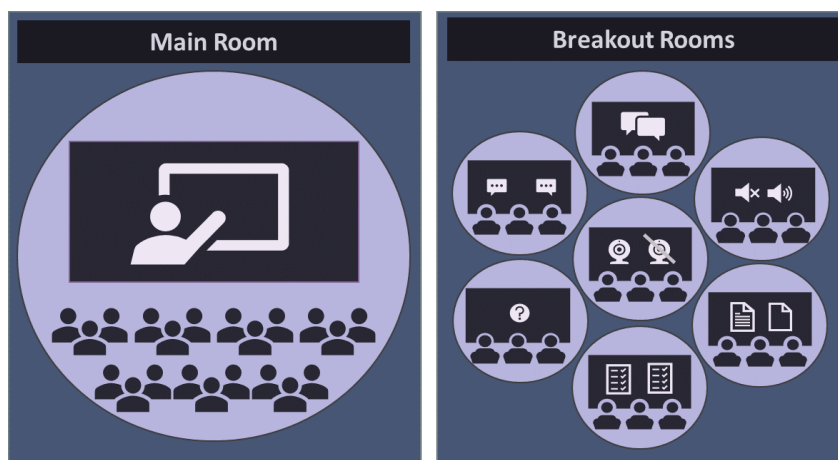
Figure 46. Zoom's Main Room and Breakout Room Depiction of Remote Learning. All
students are able to view and listen to the Teaching Assistant (TA), students are engaged through
TA facilitation (Left); Zoom's Breakout Room Depiction: Groups of students are divided into
induvial rooms where facilitation relies on instruction, TA does not have access to all rooms at
once, and therefore cannot observe how each group is performing with given instruction (Right).

Initial surveying of discussion sections in F20, quickly revealed that total student

engagement had decreased significantly in comparison to previous, in-person classes. This was a

result of the breakout rooms used within a remote discussion section, where students could not

be all monitored at once. Figure 46 describes how breakout rooms would engage differently in

respect to the main room. To survey classes and gather data about the best practices that were

improving student engagement in remote chemistry courses, a careful monitoring of discussion

section in Zoom breakout rooms supported by LAs across F20 and W20 was conducted. This strategy produced a robust model to study how remote learning affected themes around course-facilitated student engagement and sense of inclusion. In addition to this, S21 data was collected for one class at different time points to survey the overall trends of a high structured course.

6.5. Methods

The UCLA Office of the Human Research Protection Program has determined that data collection and analysis from F20 and W21 does not meet the definition of human subjects research under IRB#21-000551 protocol. Additionally, the UCLA Office of the Human Research Protection Program has determined that data collection and analysis from S21 does not meet the definition of human subjects research under IRB#22-001216

Classes

The following lists all courses surveyed for this study. All courses taught at UCLA between F20 and S21 under remote instruction. It is noted that UCLA uses the quarter system , where each of these courses takes place over a 10-week period (F20 and W21), with the exception of summer courses. Additionally, different series of classes were observed. Classes beginning with "14" denotes courses designed for life science and pre-med majors while classes beginning with "20" or "30" are denotes courses designed for physical sciences and engineering majors. Classes ending in "E" indicated "enhanced." These class times are usually doubled and have a highly ordered discussion section which requires total student participation. S21 used observations from a six-week summer course, consisting of twelve classes.

The following classes are also listed as *low*, *medium*, or *high* to indicate the level of structure associated with the discussion section. This was done by counting the number of requirements for the discussion section (see Analyzing Discussion Section Structure)

F20

- 14AE - General Chemistry for Life Scientists I – Enhanced (*high*)

- 14C - Structure of Organic Molecules (*medium*)

- 14D - Organic Reactions and Pharmaceuticals (*medium*)

- 20A - Chemical Structure (*high*)

- 30A - Organic Chemistry I: Structure and Reactivity (*low*)

W21

- 14BE - General Chemistry for Life Scientists II – Enhanced (*high*)

- 14C - Structure of Organic Molecules (*medium*)

- 14D - Organic Reactions and Pharmaceuticals (*low*)

- 20B - Chemical Energetics and Change (*medium*)

S21

- 14AE - General Chemistry for Life Scientists I – Enhanced (*high*)

Analyzing Discussion Section Structure

Realizing the variability throughout student engagement, discussion sections were characterized for both F20 and W21. For S21, a particular class with all the above characteristics was chosen for this study. Chosen criteria included analyzing the following elements specific to each course's remote discussion section structure:

- Assigned Groups – Student groups are assigned and remain the same throughout

- Assigned Roles – Each student is assigned a specific role within the group

- Group Size – Each group consists of about 4 students, but often does not have more

- TA Mobility - Teaching Assistant/Learning Assistant can move between breakout rooms

- Assigned Worksheets – Assigned worksheets are counted for class credit

- Mandatory Attendance – Discussion attendance affects overall grade

Quantifying Student Engagement in Discussion Sections

Preliminary observational data across chemistry courses during the first half of F20 revealed significant variability in student engagement. To better understand this discrepancy, discussion sections were monitored. These results summarize key findings about camera usage and student interaction (Table S1). It is noted that none of these courses required cameras nor offered incentives for turning them on as an equity consideration within remote learning. However, recent data suggests that quantifying camera usage under LA presence can help discern successful practices in remote education[3]. Therefore, in parallel to measuring student interactions in breakout rooms, camera usage was also monitored.

Surveying Discussion Sections and Breakout Rooms

Observations of discussion sections from various chemistry lectures required coordinating single access to all Zoom links. For this, permission was granted through the Common Collaboration and Learning Environment (CCLE) and therefore classes could be observed at random timepoints. Discussion section observations commenced at periodic times throughout the class and all breakout rooms for each discussion were observed. (F20 and W21). For S21, all

students were observed over multiple classes. This course consisted of three different sections, each with about 10 groups of students, one group for each breakout room.

Measuring Camera Use and Student Interaction in Breakout Rooms

Each breakout room was observed for about 3 minutes. In that time, several data points were collected. This included counting the number of students, the number of cameras turned on, and noting interactions between students, all of which were used to determine student engagement. The authors' definition of engagement was deliberated and revised for this study. For both F20 and W21, camera usage was determined by comparing the number of students with cameras on to the total number of students present (grey, Fig. 47-48; CAM (%) Table S1-S2). Initial measurements in F20 defined student interaction as the number of breakout rooms where any student directly interacted with another student compared to the total number of breakout rooms observed for the course (purple, Fig. 47; BR[SS] (%), Table S1). However, due to the limited student-student interaction observed, this definition was revised to include any student interaction (i.e. speaking to/chatting with TAs or LAs) in W21. Thus, W21 results in two different measurements of student interaction - a) the number of students with any observed interaction compared to the total number students present (light blue, Fig. 48; BR[AS] (%), Table S2), b) the number of breakout rooms with any observed student interaction compared to the total number of breakout rooms (dark blue, Fig. 48; NS[AS] (%), Table S2). In S21, this definition was further revised to include any student interaction as the overall measure (Table S4 and Table S5).

Student Inclusion Survey

After seeing the trend apparent between course structure and student engagement, a final survey was administered to W21 students at the end of the quarter to probe their sense of inclusion. The utilized survey typically gauges performance of the Learning Assistant program, however inclusion of three more questions on this survey were meant to probe trends in student inclusion that could be related to course structure. Student agreement rates were calculated and summarized for the following questions. Both questions were inspired by work from the Project for Education Research That SCALES (PERTS - https://www.perts.net/orientation/ascend).

1. **"My group in the discussion section helped me feel more like I belong in the class."**
   This question is meant to probe uncertainty about the quality of students' social bonds in their group and how it affects motivation.[22]

2. **"My group in the discussion section helped me feel more like I can rely on other students for academic support."** This question was meant to probe how remote learning impacts social connectedness and motivation.[52]

In addition to these two questions, students were given an optional question which asked them to list groups that they identify with. This data provided the initial background for further studies regarding PEERs participation in remote courses.

6.6. Results and Discussion

Observational data was collected across chemistry breakout rooms for two quarters (Fig. 47 and 48). For F2020, 14AE had the highest measurement of engagement with 85% of students with cameras ON and 81% of breakout rooms with observed student-student interaction. Similarly, for W2021, 14BE had the highest measurement of engagement with 78% of students with cameras ON, 95% of breakout rooms with any interaction, and 65% of students with any

observed interaction. These results are contrasted to the lower structured courses for each quarter, where 30A had no camera use while 14D had 9% of students with cameras on. Both classes had the lowest measurements of overall engagement. A clear trend between course structure and total engagement can be interpreted from Figure 45 and 46. Results from both quarters indicate that student engagement in breakout rooms increases with discussion section structure.
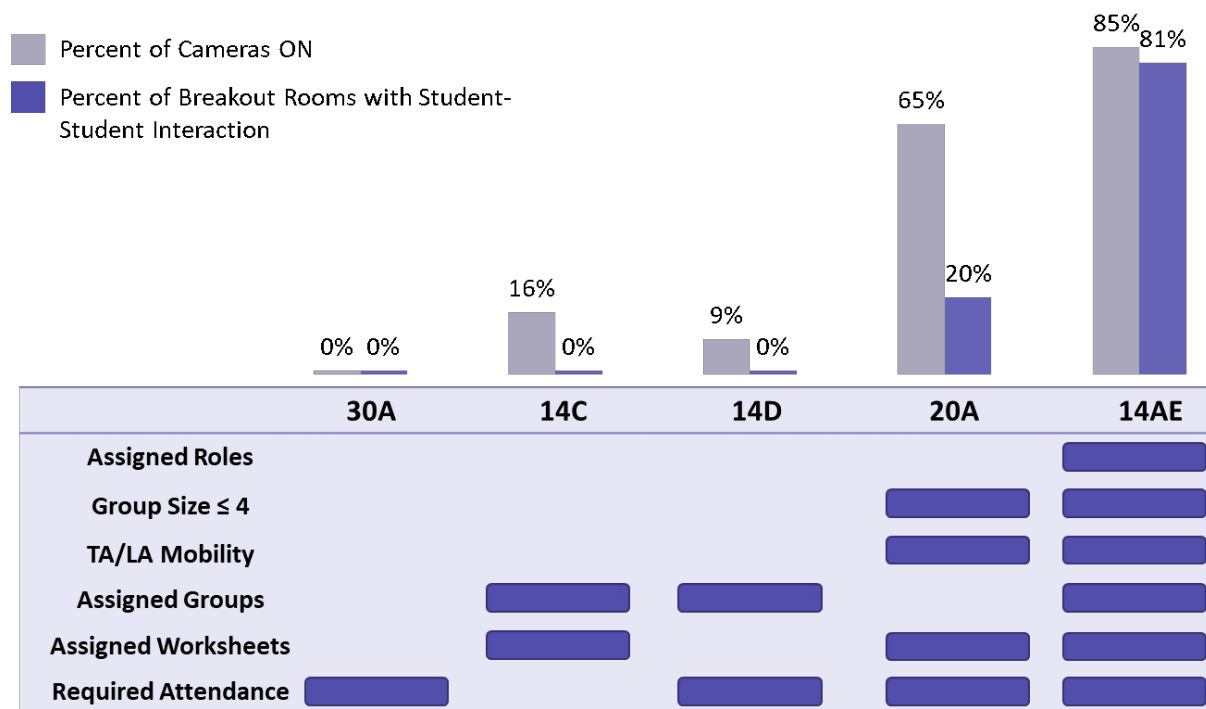
Figure 47. Comparison of Engagement Measurements to Discussion Structure for F2020. Here preliminary results indicate an increase in camera use with increased course structure. 30A, 14C and 14D were considered lower ordered courses in comparison to 20A and 14AE. 14AE is an enhanced course that requires active participation from each group member. Alongside this, percent of student interaction also matches this trend. Student interaction here is defined as number of breakout rooms where any student-student interaction was observed.
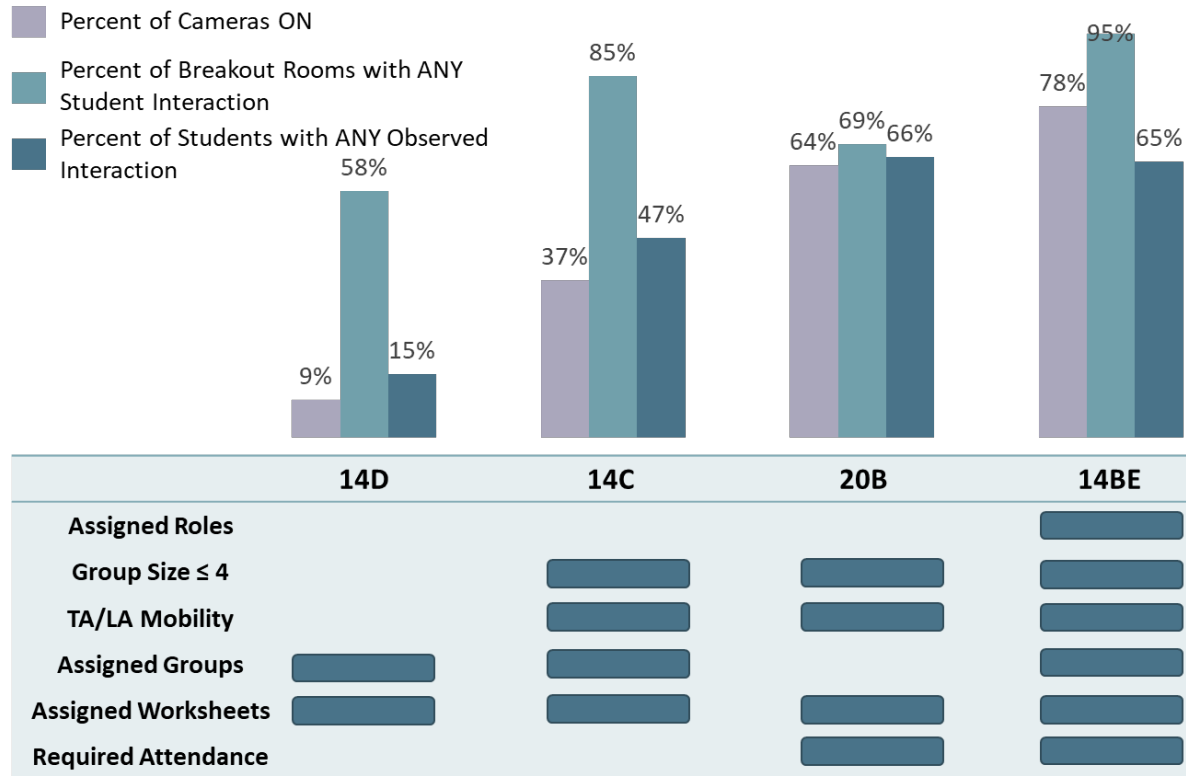
Figure 48. Comparison of Engagement Measurements to Discussion Structure for W2021. As course structure increases all total engagement increases. Note that 14C and 14BE are equal in terms of structure and grouped according to the trend from F2020. Camera use increases in this order along with defined interaction for this quarter. Interaction was measured by counting the number of students who interacted with anyone else (TA, LA, or student) at any point during the observation. This was compared against the number of breakout rooms that had any interaction and the total number of students present.

Post-quarter survey results from W2021 have been broken down to show the percentages of PEER students and non-PEER students who selected "Strongly Agree" in response to the previously mentioned questions regarding belonging and connectedness (Fig. 49). Courses are ordered by increasing course structure determined in Fig 48. Results indicate that increased course structure results in an overall higher sense of belonging and connectedness among students, two factors that contribute to inclusion. Further analysis also indicates that there is no significant discrepancy between PEER and non-PEER percentages. With the exception of 20B, which had a larger gap between PEER and non-PEER students for both Q1 and Q2, the remaining three courses show a strong trend for both PEER and non-PEER inclusion and course structure.
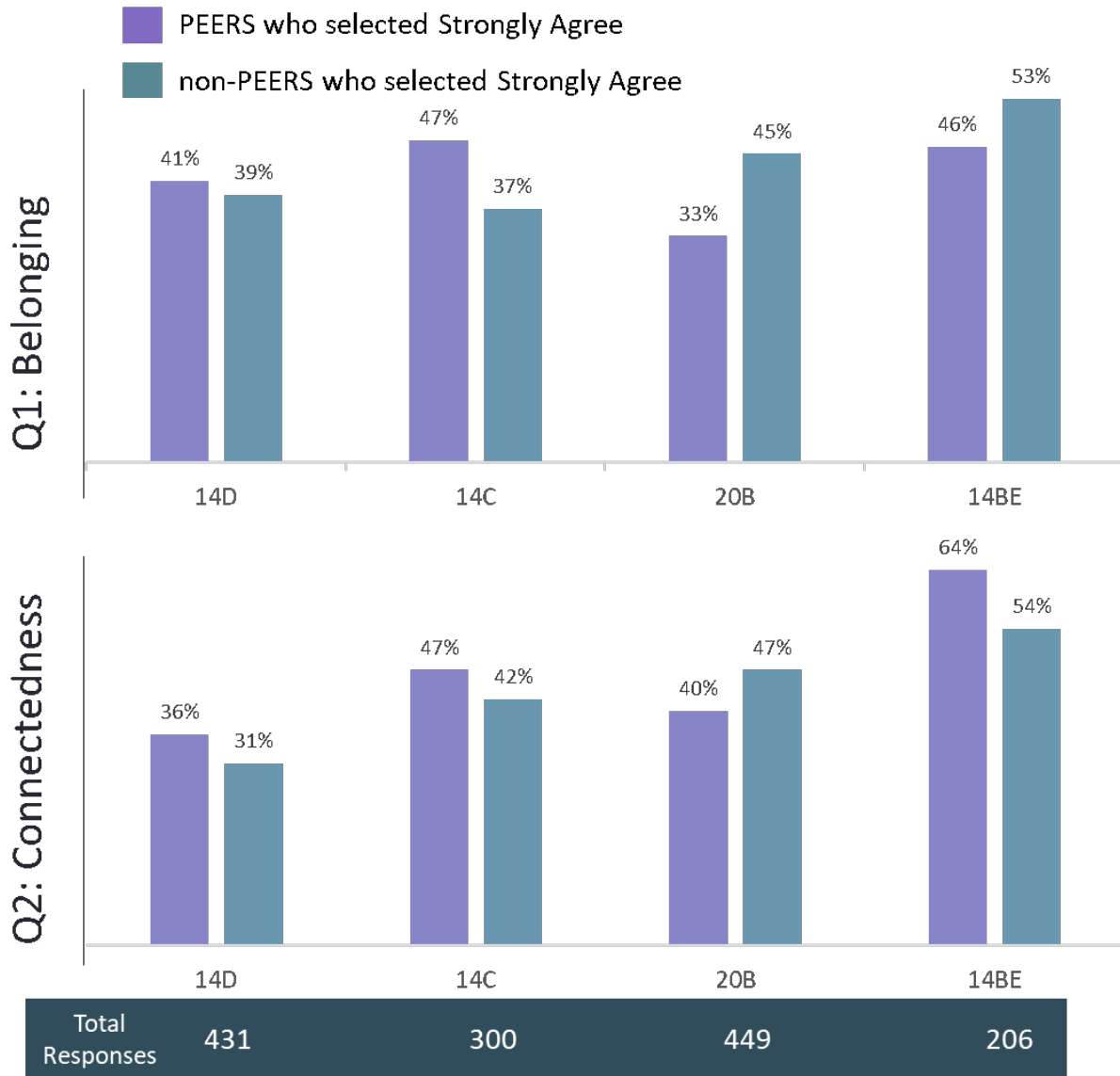
Figure 49. Inclusion Survey Results for W2021. Percentages of Students who Selected "Strongly Agree" in response to Q1 and Q2. Purple indicates students who identified as a PEER (person excluded due to ethnicity or race). Blue indicates non-PEER. No significant gaps between PEER and non-PEER measurements are observed. Students report a higher rate of belonging and connectedness as course structure increases. X-Axis is in order of increasing course structure (left to right). Total student responses collected from each course depicted below.
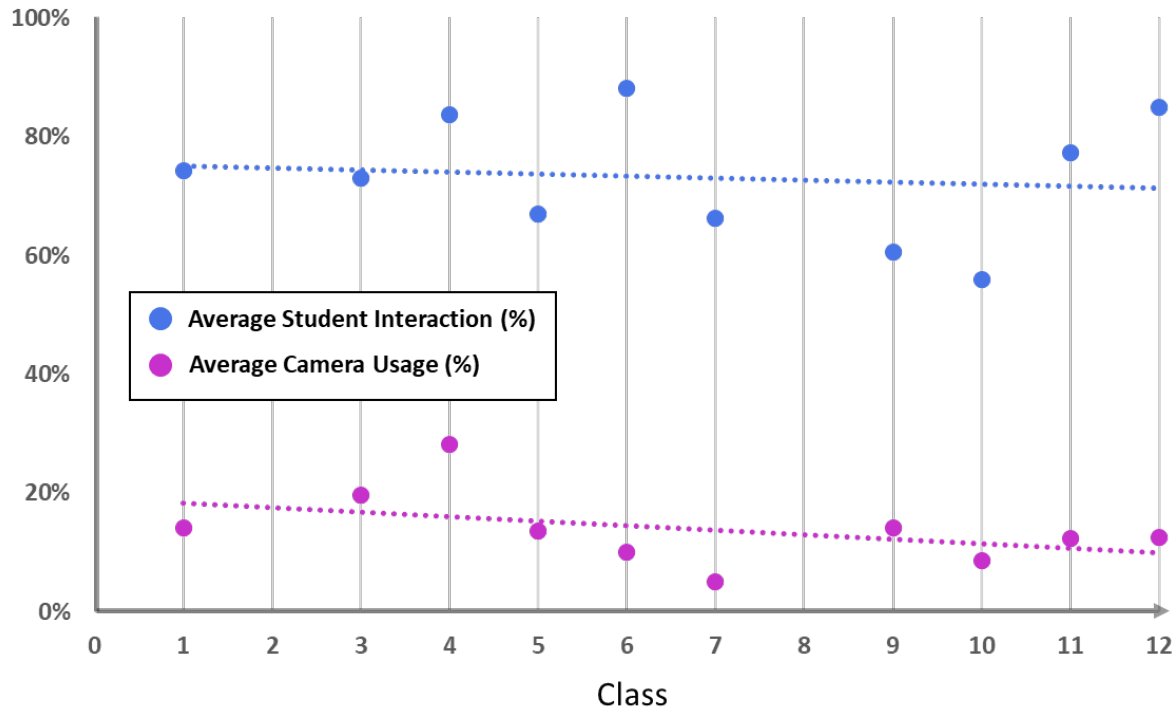
Figure 50. Average Student Interaction and Camera Usage for S21. (pink) average percent camera usage, remains below 30% across course; (blue) average percent student interaction, remains between 50% and 90% across course.

In addition to the results from F20 and W21, results from S21 were also considered. Figure 50 shows the overall trend across twelve classes for average student interaction (blue) and average camera usage (pink). The percentage (%) determined for each class was calculated by dividing the sum of all student interaction by the sum of total students observed (See Table S4-S5). Here the data shows that student engagement remains high for this high-structured course, throughout the six weeks/twelve classes. Camera usage, however, remained low throughout. From this it was determined that the camera usage is indeed not representative of overall student engagement.

6.7. Conclusions

To divulge trends in student engagement and inclusion, course structure was compared to camera use, student interaction, and survey results. Results indicate course structure positively effects student engagement and inclusion. For both F2020 and W2021, increased structural elements of a course resulted in a higher percentage of engagement in the discussion with cameras ON. Additionally, there is also a positive correlation between three different measurements of student interaction and course structure. Survey results also indicate that students feel a heightened sense of belonging and connectedness, two important elements of inclusion, with increased course structure. This trend is also apparent when responses from PEER and non-PEER students were also analyzed, suggesting no significant discrepancy in sense of inclusion with increased course structure. Originally it was thought that camera usage could be indicative of student engagement, however S21 shows that even though camera usage remained low throughout, student interaction was still high. Nonetheless, this still concludes that high structured courses leads to high student engagement in a remote setting.

Conclusions for this work aim to suggest methods for designing remote discussion sections that can increase student engagement and sense of inclusion. Suggested strategies can be found in Fig. 51 and include the following: required attendance, assigned groups, limiting groups to 4 at a maximum, assigned roles for each student in a group, assistance mobility between groups, and assigned worksheets.
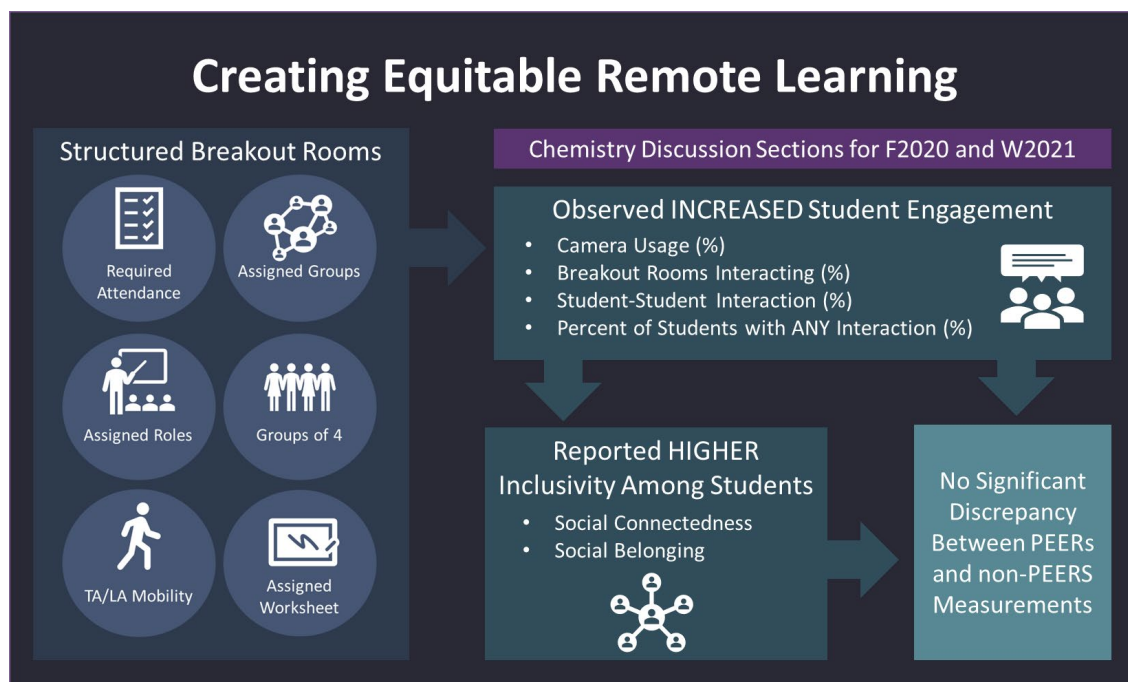
Figure 51. Structured Breakout Rooms for Creating Equitable Remote Learning. Structured courses with (1) required attendance, (2) assigned groups, (3) assigned roles, (4)

Limitations

Limitations for this paper are acknowledged by the authors. Camera use is not a direct measurement of a single student's engagement, rather an assessment of the overall engagement of the class/group. Additionally, not all discussion sections for each class were observed. The administered survey provided students an optional question to self-identify groups they belong in. From this, the authors grouped student responses into PEER and non-PEER categories.

Preliminary observational data for W2021 aimed to analyze engagement between PEER and non-PEER students. This work was limited by the inability of the authors to clearly identify students as PEER or non-PEER in breakout rooms. Data was collected only through analysis of

names and appearances. Future work in this area aims to analyze engagement with self-reported

student PEER and non-PEER identification results.

6.8. Experimental Data

Observational Data

Table S1. Total Observational Data for F2020

Class	NS	NBR	NS/BR	CAM	CAM (%)	BR[SS]	BR[SS] (%)
14AE	82	21	4	70	85%	17	81%
14C	114	17	7	18	16%	0	0%
14D	93	9	10	8	9%	0	0%
20A	26	5	5	17	65%	1	20%
30A	37	9	4	0	0%	0	0%

NS = Total Number of Students Observed, NBR = Total Number of Breakout Rooms Observed, NS/BR = Average Student Per Breakout Room, CAM = Total Number of Cameras Observed "On", BR[SS] = Total Number of Breakout Rooms with Observed Student-Student Interaction

Table S2. Total Observational Data for W2021

Class	NS	NBR	NS/BR	CAM	CAM (%)	BR[AS]	NS[AS]	BR[AS] (%)	NS[AS] (%)
14BE	333	88	4	26	78%	84	215	95%	65%
14C	98	27	4	36	37%	23	46	85%	47%
14D	312	36	9	29	9%	21	47	58%	15%
20A	13	5	3	3	23%	2	4	40%	31%
20B	176	62	3	112	64%	43	117	69%	66%

NS = Total Number of Students Observed, NBR = Total Number of Breakout Rooms Observed, NS/BR = Average Student Per Breakout Room, CAM = Total Number of Cameras Observed "On", BR[AS] = Total Number of Breakout Rooms with ANY Observed Student Interaction, NS[AS] = Total Number of Students Observed with ANY Interaction

Preliminary PEERs Data

"PEERs" is defined as the following: in US Science, this includes persons who identify as Black or African American, Latinx or Hispanic, and peoples indigenous to the spaces comprising the US and its territories.[53]

Table S3. Preliminary Data Collected on PEERs Engagement in Breakout Rooms for W2021

Class	Structure	NS	CAM (%)	NS[EN] (%)	PEER[EN] (%)	non-PEER[EN] (%)
Chemistry 14BE	high	333	78%	65%	69%	64%
Chemistry 14C	med	98	37%	47%	58%	43%
Chemistry 14D	low	312	9%	15%	24%	13%
Chemistry 20A	low	13	23%	31%	0%	37%
Chemistry 20B	high	176	64%	67%	56%	70%
Physics 5C	high	185	52%	73%	61%	75%

NS = Total Number of Students Observed, CAM (%) = Percent of Cameras Observed "On", NS[EN] (%) = Percent of Students Engaging, PEER[EN] (%) = Percent of Identifiable PEER students Engaging, non-PEER[EN] (%) = Percent of Identifiable Non-Peer Students and Non-Identifiable Students Engaging

Table S4. Observational Data Timeline for Highly Structured Sum. 14A Class.

A	CLASS 1			CLASS 2			CLASS 3			CLASS 4			CLASS 5			CLASS 6		
	NS	CAM	SS	NS	CAM	SS	NS	CAM	SS	NS	CAM	SS	NS	CAM	SS	NS	CAM	SS
A1	5	4	5	-	-	-	5	4	4	5	4	5	5	4	5	5	4	5
A2	5	0	3	-	-	-	4	0	3	5	1	4	-	-	-	4	0	3
A3	5	0	4	-	-	-	5	0	4	5	0	3	5	0	3	5	0	5
A4	4	2	4	-	-	-	4	3	3	4	4	3	4	0	3	4	0	4
A5	5	0	4	-	-	-	5	0	4	5	0	4	5	0	3	5	0	4
A6	3	0	3	-	-	-	4	0	2	3	0	3	3	0	3	3	0	3
A7	4	0	4	-	-	-	4	0	4	4	0	3	4	0	3	4	0	3
A8	4	1	3	-	-	-	4	1	3	4	1	4	4	1	3	4	0	3
B																		
B1	5	2	4	-	-	-	5	1	4	-	-	-	5	1	3	-	-	-
B2	4	0	0	-	-	-	-	-	-	-	-	-	5	0	0	-	-	-
B3	5	0	3	-	-	-	5	0	4	-	-	-	5	0	3	-	-	-
B4	6	4	5	-	-	-	5	4	4	-	-	-	5	3	4	-	-	-
B5	4	0	3	-	-	-	3	0	3	-	-	-	3	0	0	-	-	-
B6	0	0	0	-	-	-	4	4	3	-	-	-	4	3	3	-	-	-
B7	3	0	3	-	-	-	3	0	2	-	-	-	3	0	3	-	-	-
B8	4	0	4	-	-	-	4	0	3	-	-	-	4	0	3	-	-	-
C																		
C1	5	2	4	-	-	-	4	2	3	-	-	-	5	2	3	-	-	-
C2	4	0	2	-	-	-	4	0	1	-	-	-	5	0	0	-	-	-
C3	6	0	0	-	-	-	5	1	2	-	-	-	-	-	-	-	-	-
C4	3	0	3	-	-	-	3	0	2	-	-	-	4	0	4	-	-	-
C5	4	1	4	-	-	-	4	0	3	-	-	-	4	0	4	-	-	-
C6	5	0	3	-	-	-	4	0	4	-	-	-	4	0	3	-	-	-
C7	4	0	2	-	-	-	4	0	2	-	-	-	4	0	3	-	-	-
C8	4	0	3	-	-	-	4	0	3	-	-	-	3	0	2	-	-	-

Summer 14A observational data. Class 1 through 6 indicated on top. Classes = A, B, and C; Breakout rooms indicated by Class and then number (i.e. A1 = Class A, Group 1); NS = Total Number of Students Observed; CAM = Total Number of Cameras Observed "On"; SS = Total Number of Observed Student Interaction.

Table S4. Observational Data Timeline for Highly Structured Sum. 14A Class (continued).

A	CLASS 7			CLASS 8			CLASS 9			CLASS 10			CLASS 11			CLASS 12		
	NS	CAM	SS	NS	CAM	SS	NS	CAM	SS	NS	CAM	SS	NS	CAM	SS	NS	CAM	SS
A1	-	-	-	-	-	-	5	4	4	5	3	4	5	4	4	4	3	4
A2	-	-	-	-	-	-	-	-	-	4	0	2	4	0	0	-	-	-
A3	-	-	-	-	-	-	-	-	-	5	0	3	5	0	4	5	0	3
A4	-	-	-	-	-	-	4	0	0	4	0	0	4	0	2	3	0	3
A5	-	-	-	-	-	-	5	0	2	5	0	3	4	0	3	4	0	2
A6	-	-	-	-	-	-	-	-	-	-	-	-	-	-	-	-	-	-
A7	-	-	-	-	-	-	2	0	2	3	0	2	3	0	3	3	0	3
A8	-	-	-	-	-	-	4	0	0	4	0	3	3	0	3	2	0	2
B																		
B1	-	-	-	-	-	-	4	0	4	-	-	-	4	0	4	-	-	-
B2	-	-	-	-	-	-				-	-	-	5	0	5	-	-	-
B3	-	-	-	-	-	-	5	0	4	-	-	-	4	0	2	-	-	-
B4	-	-	-	-	-	-	5	3	3	-	-	-	5	3	5	-	-	-
B5	-	-	-	-	-	-	2	0	0	-	-	-	3	0	3	-	-	-
B6	-	-	-	-	-	-	4	3	4	-	-	-	2	2	2	-	-	-
B7	-	-	-	-	-	-	2	0	2	-	-	-	3	0	2	-	-	-
B8	-	-	-	-	-	-	4	0	2	-	-	-	4	0	0	-	-	-
C																		
C1	5	2	3	-	-	-	5	2	4	-	-	-	3	1	3	-	-	-
C2	4	0	2	-	-	-	4	0	2	-	-	-	4	0	2	-	-	-
C3	5	0	1	-	-	-	4	0	2	-	-	-	4	0	3	-	-	-
C4	3	0	3	-	-	-	-	-	-	-	-	-	-	-	-	-	-	-
C5	4	0	3	-	-	-	-	-	-	-	-	-	3	0	3	-	-	-
C6	4	0	2	-	-	-	4	0	2	-	-	-	3	0	3	-	-	-
C7	4	0	3	-	-	-	4	0	3	-	-	-	4	0	3	-	-	-
C8	3	0	3	-	-	-	4	0	3	-	-	-	4	0	4	-	-	-

Summer 14A observational data. Class 7 through 12 indicated on top. Classes = A, B, and C; Breakout rooms indicated by Class and then number (i.e. A1 = Class A, Group 1); NS = Total Number of Students Observed; CAM = Total Number of Cameras Observed "On"; SS = Total Number of Observed Student Interaction.

6.9. References

1) Gourley 2021: Gourley, R. A Year with COVID-19: A Chronology of How the UW Adapted - and Responded - to the Pandemic. UW News. *https://www.washington.edu/news/2021/03/04/a-year-with-covid-19-a-chronology-of-how-the-uw-adapted-and-responded-to-the-pandemic/* (accessed Mar. 2021).

2) Holme, T. A. Introduction to the Journal of Chemical Education Special Issue on Insights Gained While Teaching Chemistry in the Time of COVID-19. *J. Chem. Educ.* **2020**, *97*, 2375– 2377, https://doi.org/10.1021/acs.jchemed.0c01087

3) Emenike, M. E.; Schick, C. P.; Van Duzor, A. G.; Sabella, M. S.; Hendrickson, S. M.; Langdon, L. S. Leveraging Undergraduate Learning Assistants to Engage Students during Remote Instruction: Strategies and Lessons Learned from Four Institutions. *J. Chem. Educ.* **2020**, *97* (9), 2502−2511. https://doi.org/10.1021/acs.jchemed.0c00779

4) Miltiadous, A.; Callahan, D. L.; Schultz, M. Exploring Engagement as a Predictor of Success in the Transition to Online Learning in First Year Chemistry. *J. Chem. Educ.* **2020**, *97* (9), 2494− 2501. https://doi.org/10.1021/acs.jchemed.0c00794

5) Perets, E. A.; Chabeda, D.; Gong, A. Z.; Huang, X.; Fung, T. S.; Ng, K. Y.; Bathgate, M.; Yan, E. C. Y. Impact of the Emergency Transition to Remote Teaching on Student Engagement in a Non-STEM Undergraduate Chemistry Course in the Time of COVID-19. *J. Chem. Educ.* **2020**, *97* (9), 2439– 2447, https://doi.org/10.1021/acs.jchemed.0c00879

6) Reynders, G.; Ruder, S. M. Moving a Large-Lecture Organic POGIL Classroom to an Online Setting. *J. Chem. Educ.* **2020**, *97* (9), 3182-3187, https://doi.org/10.1021/acs.jchemed.0c00615

7) Baldock, B. L.; Fernandez, A. L.; Franco, J.; Provencher, B. A.; McCoy, M. R. Overcoming the Challenges of Remote Instruction: Using Mobile Technology to Promote Active Learning. *J. Chem. Educ.* **2021**, *98* (3), 833– 842, https://doi.org/10.1021/acs.jchemed.0c00992

8) Gasiewski, J. A.; Eagan, M. K.; Garcia, G. A.; Hurtado, S.; Chang, M. J. From Gatekeeping to Engagement: A Multicontextual, Mixed Method Study of Student Academic Engagement in Introductory STEM Courses *Res. High. Educ.* **2012**, *53*, 229– 261, https://doi.org/10.1007/s11162-011-9247-y

9) Chen, X.; Soldner, M. *STEM Attrition: College Students' Paths Into and Out of STEM Fields* (NCES 2014-001); National Center for Education Statistics, Institute of Education Sciences, U.S. Department of Education Sciences: Washington DC, 2013

10) Chang, M. J.; Cerna, O.; Han, J.; Sàenz, V. The contradictory roles of institutional status in retaining underrepresented minorities in biomedical and behavioral science majors. *Rev. High. Educ.* **2008**, *31*, 433– 64. https://doi.org/10.1353/rhe.0.0011

11) Asai, D. J. Race Matters. *Cell* **2020**, *181* (4), 754-757. https://doi.org/10.1016/j.cell.2020.03.044

12) Women, Minorities, and Persons with Disabilities in Science and Engineering: 2019. *Special Report to the National Science Foundation* 19-304; National Center for Science and Engineering Statistics: Alexandria, VA, 2019.

13) Huang, G.; Taddese, N.; Walter, E. *Entry and Persistence of Women and Minorities in College Science and Engineering, Education*; U.S. Department of Education, Office of Educational Research and Improvement: Washington, DC, USA, 2000.

14) Riegle-Crumb, C.; King, B.; Irizarry, Y. Does STEM Stand Out? Examining Racial/Ethnic Gaps in Persistence Across Postsecondary Fields. *Educ. Res.* **2019**, *48* (3), 133– 144, https://doi/org/10.3102/0013189X19831006

15) Fink, A.; Frey, R. F.; Solomon, E. D. Belonging in general chemistry predicts first-year undergraduates' performance and attrition. *Chem. Educ. Res. Pract.* **2020**, *21*, 1042-1062, https://doi.org/10.1039/D0RP00053A

16) Hoffman, M.; Richmond, J.; Morrow, J.; Salomone, K. Investigating "Sense of Belonging" in First-Year College Students. *J. Coll. Stud. Ret.* **2002**, *4* (3), 227– 256, https://doi.org/10.2190/DRYC-CXQ9-JQ8V-HT4V

17) Freeman, T. M.; Anderman, L. H.; Jensen J. M. Sense of Belonging in College Freshmen at the Classroom and Campus Levels. *J. Exp. Educ.* **2007**, *75*, 203-220. http://www.jstor.org/stable/20157456

18) O'Keeffe, P. A Sense of Belonging: Improving Student Retention. *Coll. Stud. J.* **2013**, *47* (4), 605-613.

19) Zumbrunn, S.; McKim, C.; Buhs, E; Hawley, L.R. Support, belonging, motivation, and engagement in the college classroom: A mixed method study. *Instr. Sci.* **2014**, *42* (5), 661-684. https://doi.org/10.1007/s11251-014-9310-0

20) Hurtado, S.; Carter, D. F. Effects of College Transition and Perceptions of the Campus Racial Climate on Latino Students' Sense of Belonging. *Sociol. Educ.* **1997**, *70* (4), 324–45. https://doi.org/10.2307/2673270

21) Hausmann L. R. M.; Schofield J. W.; Woods R. L. Sense of Belonging as a Predictor of Intentions to Persist Among African American and White First-Year College Students. *Res. High. Educ.* **2007**, *48*, 803-839. https://doi.org/10.1007/s11162-007-9052-9

22) Walton, G. M.; Cohen, G. L. A Question of Belonging: Race, Social Fit, and Achievement. J. Person. *Soc. Psy.* **2007**, *92* (1), 82– 96. https://doi.org/10.1037/0022-3514.92.1.82

23) Rahman, K. Belonging and Learning to Belong in School: The Implications of the Hidden Curriculum for Indigenous Students. *Dis. Stud. Cult. Pol. Educ.* **2013**, *34* (5), 660-672. https://doi.org/10.1080/01596306.2013.728362

24) Murphy, M. C.; Zirkel, S. Race and Belonging in School: How Anticipated and Experienced Belonging Affect Choice, Persistence, and Performance. *Teach. Coll. Rec.* **2014**, *117* (12), 1-40. https://doi.org/10.1177/016146811511701204

25) Wilson D.; Jones D.; Bocell F.; Crawford J.; Kim M. J.; Veilleux N.; Floyd-Smith T.; Bates R.; Plett M. Belonging and Academic Engagement Among Undergraduate STEM Students: A Multi-Institutional Study *Res. High. Educ.* **2015**, *56*, 750-776. https://doi.org/10.1007/s11162-015-9367-x

26) Freeman, S.; Eddy, S. L.; McDonough, M.; Smith, M. K.; Okoroafor, N.; Jordt, H.; Wenderoth, M. P. Active Learning Increases Student Performance in Science, Engineering,

and Mathematics *Proc. Natl. Acad. Sci. U. S. A.* **2014**, *111*, 8410– 8415, https://doi.org/10.1073/pnas.1319030111

27) Freeman, S.; Haak, D.; Wenderoth, M. Increased Course Structure Improves Performance in Introductory Biology. *CBE Life Sci. Educ.* **2011**, *10*, 175– 186, https://doi.org/10.1187/cbe.10-08-0105

28) Haak, D. C.; HilleRisLambers, J.; Pitre, E.; Freeman, S. Increased Structure and Active Learning Reduce the Achievement Gap in Introductory Biology. *Science* **2011**, *332*, 1213– 1216, https://doi.org/10.1126/science.1204820

29) Crimmins, M. T.; Midkiff, B. High Structure Active Learning Pedagogy for the Teaching of Organic Chemistry: Assessing the Impact on Academic Outcomes. *J. Chem. Educ.* **2017**, *94* (4), 429– 438, https://doi.org/10.1021/acs.jchemed.6b00663

30) Eddy, S. L.; Hogan, K. A. Getting Under the Hood: How and for Whom Does Increasing Course Structure Work? *CBE-Life Sci. Educ.* **2014**, *13*, 453– 468, https://doi.org/10.1187/cbe.14-03-0050

31) Topping, K. J. Trends in Peer Learning. *Educ. Psych.* **2005**, *25* (6), 631– 645. https://doi.org/10.1080/01443410500345172

32) Otero, V.; Pollock, S.; Finkelstein, N. A Physics Department's Role in Preparing Physics Teachers: The Colorado Learning Assistant Model *Am. J. Phys.* **2010**, *78* (11), 1218– 1224, https://doi.org/10.1119/1.3471291

33) Price, S.; Wallace, K.; Verezub, E.; Sinchenko, E. Student Learning Assistants: The Journey from Learning Advice to Creating Community. *J. Fur. High. Educ.* **2019**, *43* (7), 914-928, https://doi.org/10.1080/0309877X.2018.1425379

34) Crouch, C.; Mazur, E. Peer Instruction: Ten Years of Experience and Results. *Am. J. Phys.* **2001**, 69 (9), 970– 977, https://doi.org/10.1119/1.1374249

35) Nicol, D. J.; Boyle, J. T. The Influence of Group Discussion on Students' Responses and Confidence During Peer Instruction. *Stud. High. Educ.* **2003**, *28*, 457– 473. https://doi.org/10.1021/ed101066x.

36) Allen, I. E., & Seaman, J. *Online report card: Tacking online education in the United States. Newburyport*, MA: Babson Survey Research Group, **2016**.

37) Parsad, B., and Lewis, L. *Distance Education at Degree-Granting Postsecondary Institutions: 2006–07* (NCES 2009–044). National Center for Education Statistics, Institute of Education Sciences, U.S. Department of Education. Washington, DC. **2008**.

38) Dewey, J. *Experience and education* New York: Macmillan, **1938**.

39) Lipmann, M. *Thinking in Education.* New York: Cambridge University Press, **2003**.

40) Garrison, D. R., Anderson, T., & Archer, W. Critical inquiry in a text-based environment: Computer conferencing in higher education. *Internet High Edu.* **2000** *2*(2-3), 87-105. https://doi.org/10.1016/S1096-7516(00)00016-6

41) Rovai, A. P. Sense of community, perceived cognitive learning, and persistence in asynchronous learning networks. *Internet High Edu*., **2002** *5*, 319e332. https://doi.org/10.1016/S1096-7516(02)00130-6

42) Shea, P. A study of students' sense of learning community in online environments. *JALN*, **2006** *10* (1), 35-44. https://doi.org/10.24059/olj.v10i1.1774

43) Thompson, T.L. & MacDonald, C.J. Community building, emergent design and expecting the unexpected: Creating a quality eLearning experience. *Internet High Edu*. **2005** *8*(3), 233-249. https://doi.org/10.1016/j.iheduc.2005.06.004

44) Richardson, J. C., & Swan, K. Examining social presence in online courses in relation to students' perceived learning and satisfaction. *JALN*, **2003** *7*(1), 68−88. https://doi.org/10.24059/olj.v7i1.1864

45) Tao, Y. *The Relationship between motivation and online social presence in an online class* (Doctoral dissertation) 2009.

46) Kang, M., & Im, T. Factors of learner-instructor interaction which predict perceived learning outcomes in online learning environment. *J. Comput. Assist. Learn*. **2013** *29*, 292e301. https://doi.org/10.1111/jcal.12005

47) Joksimovic, S., Gasevic, D., Kovanovic, V., Riecke, B. E., & Hatala, M. Social presence in online discussions as a process predictor of academic performance. *J. Comput. Assist. Learn*. **2015.** https://doi.org/10.1111/jcal.12107

48) Richardson, J. C., Maeda, Y., Lv, J., & Caskurlu, S. Social presence in relation to students' satisfaction and learning in the online environment: A meta-analysis. *Comput. Hum. Behav.* **2017** *71*, 402-417. https://doi.org/10.1016/j.chb.2017.02.001

49) Fiock, H. Designing a Community of Inquiry in Online Courses. *IRRODL.* **2020** *21*(1), 135-153. https://doi.org/10.19173/irrodl.v20i5.3985

50) Richardson J.C., Arbaugh J.B., Cleveland-Innes M., Ice P., Swan K.P., Garrison D.R. Using the Community of Inquiry Framework to Inform Effective Instructional Design. In: Moller L., Huett J. (eds) *The Next Generation of Distance Education*. Springer, Boston, MA, 2012. https://doi.org/10.1007/978-1-4614-1785-9_7

51) Charity Flener-Lovitt, Karl Bailey, and Rui Han Using Structured Teams to Develop Social Presence in Asynchronous Chemistry Courses. *J. Chem. Educ.* **2020** *97* (9), 2519-2525. https://doi.org/10.1021/acs.jchemed.0c00765

52) Walton, G. M., Cohen, G. L., Cwir, D., & Spencer, S. J. Mere belonging: The power of social connections. *J Pers Soc Psychol.* **2012** *102*(3), 513–532. https://doi.org/10.1037/a0025731